UNIVERSITAT DE BARCELONA

Active nematic turbulence: An experimental study

Berta Martínez Prat

ACTIVE NEMATIC TURBULENCE:

An experimental study

BERTA MARTÍNEZ PRAT

UNIVERSITAT DE BARCELONA

DOCTORAT EN NANOCIÈNCIES

Active nematic turbulence: An experimental study

Berta Martínez Prat

Ph.D. Advisors:

Dr. Jordi Ignés Mullol [1,2]
Dr. Francesc Sagués Mestre [1,2]

Tutor:

Dr. Jordi Ignés Mullol [1,2]

[1]Departament de Ciència dels Materials i Química Física
[2]Institut de Nanociència i Nanotecnologia de la Universitat de Barcelona (IN^{2}UB)

September 2022

UNIVERSITAT DE BARCELONA

The work described in this thesis has been financially supported by the Generalitat de Catalunya through an FI-2018 Ph.D. Fellowship and by MINECO (No. FIS2016-78507-C2-1-P, AEI/ FEDER, EU, and No. PID2019–108842 GB-C22).

Abstract

One of the most striking phenomena of active fluids, i.e., fluids composed of self-propelled constituents, is the emergence of chaotic spatiotemporal flows. "This regime, reminiscent of inertial turbulence but happening at low Reynolds numbers, has become to be known as active turbulence. It has been observed in a variety of systems, such as bacterial suspensions or epithelial tissues. Despite the visual similarities, active turbulent flows possess fundamental differences from classical turbulent flows. The differences essentially emanate from the fact that active turbulence originates at vanishing Reynolds numbers from the self-organization of the fluid constituents, which move coordinately at distances much larger than their own size. As a result, active chaotic flows are endowed with a characteristic length scale.

In this thesis, working with an experimental active system displaying nematic order, i.e., head-to-tail orientational order, and composed of proteins from the cytoskeleton, we address some still-standing open questions regarding active turbulence. More specifically, since our experimental system is two-dimensional and has nematic order, we study 2D active nematic turbulence. We begin this thesis by unveiling the pathway followed by the active fluid with an imposed radial alignment to its final characteristic chaotic state. More in particular, we demonstrate that the AN in the aster configuration is intrinsically unstable to buckling. In turn, a characteristic length scale already emerges at the instability's early stages. Interestingly, the instability of the aligned active nematic can be characterized in terms of a growth rate that exhibits a quadratic or quasi-quadratic dependence on the leading wavenumber. Our experimental results are then compared with predictions obtained from linear stability analysis. This enables us to see that the coupling of the active nematic with adjacent fluid layers precludes long wavelength fluctuations, imposing in this way a genuine wavelength selection mechanism.

In the second project, we measure the active liquid crystal's flow field and the associated kinetic energy spectrum. In this way, we verify the existence of scaling regimes, some of which feature exponents previously predicted through theory and simulations , together with new ones. To understand the newly-discovered scaling regimes, we exploit a theory that includes the hydrodynamic coupling of the active nematic with the two contacting passive fluid layers. This theory assesses the range of validity of the identified scaling regimes, and permits

to extract information on important rheological parameters of the active fluid.

In the final project, still in progress, we address the presence of energy cascades in active nematic turbulence. Preliminary experimental results, supported with simulations, suggest that even though the free energy balance does not entirely vanish at all length scales, we cannot indeed conclude that there is energy transfer between scales. A significant limitation we encounter when computing the free energy balance of the active nematic is that most of the material parameters still need to be determined. Therefore, further research research devoted to the evaluation of such parameters may shed light on this respect.

On top of the above fundamental studies, we also demonstrate two implementations of polarimetry measurements coupled with fluorescence imaging, with which we can simultaneously measure the director and velocity fields of the active nematic. The first arrangement is based on a liquid crystal slab, whose retardance can be easily commanded with a computer. By measuring the light intensity reaching the detector at different configurations of the liquid crystal retarder, we can unequivocally and continuously know the sample's local orientation. The alternative implementation incorporates a polarization camera, a device composed of subpixels with different polarizations. This arrangement allows us to obtain exceptional birefringence measurements at significantly high frame rates, even with very low-birefringent samples, as it is common for the active nematic.

Resum

Els fluids actius, com les suspensions de bactèries o els teixits, són fluids compostos per moltes unitats capaces de propulsar-se contínuament. Aquests fluids presenten propietats molt interessants i radicalment oposades a les que s'observen quan una d'aquestes unitats actives es mou individualment. Un exemple és el que es coneix com a turbulència activa, on els fluids actius es mouen caòticament i que emergeix inclús a números de Reynolds baixos, quan la inèrcia es menyspreable. Aquest fenomen es diu així perquè visualment recorda a la turbulència inercial clàssica. Tot i així, hi ha diferències fonamentals entre aquests dos tipus de turbulència, els quals ens interessa discernir.

En aquesta tesi es presenten estudis experimentals, duts a terme amb una suspensió de proteïnes del citoesquelet, i amb els quals abordem algunes qüestions encara obertes sobre la turbulència activa i les seves similituds i diferències amb la turbulència inercial. Més concretament, com el nostre sistema experimental és 2D i presenta simetria nemàtica, nosaltres estudiem la turbulència nemàtica activa.

En primer lloc, revelem el camí que segueix el nemàtic actiu alineat radialment fins que arriba al seu estat turbulent. Més concretament, demostrem que la geometria d'àster és inestable; en conseqüència, el fluid actiu comença a deformar-se i llavors emergeix una escala de longitud característica. Després duem a terme estudis on l'actiu nemàtic ja es troba plenament en el seu estat turbulent. En aquest sentit, demostrem l'existència de règims d'escala en l'espectre d'energia cinètica del nemàtic actiu i abordem la presència o no presència de cascades d'energia en el context de la turbulència nemàtica activa. Finalment, descrivim dues tècniques de polarimetria acoblades a fluorescència amb les quals podem mesurar simultàniament la orientació i el camp de velocitats del nemàtic actiu i que ens permeten dur a terme les mesures experimentals presentades en aquesta tesi.

Pels yayos: l'Amador i la María.

Acknowledgements

Even though it seems incredible, this Ph.D. thesis is finally getting to an end. These last months practically only devoted to writing have been harsh and exhausting, more than I had expected. However, I would still choose to pursue this Ph.D. over and over again. Now, I would like to thank all the people that have made this possible.

First, I want to thank my two advisors, Francesc and Jordi, who gave me the tremendous opportunity to join the SOC& SAM group seven (or eight?) years ago. Also, they have always helped me find the way and supported me through the different projects presented here. Francesc, moltes gràcies per haver-me convençut a quedar-me a fer una beca de col·laboració en el vostre grup i acabar fent el màster i el doctorat. Gràcies a tu vaig poder conèixer al món tan fascinant de la biofísica. A més, sempre has intentat motivar-me i t'has obsessionat fins i tot més que jo en els meus problemes per poder ajudar-me. A tu Jordi, gràcies per tots els invents que has fet i m'has ajudat a fer per poder fer els meus experiments. També, gràcies per tota la paciència que tens per ajudar-nos i ensenyar-nos a fer experiments, per l'optimisme que sempre transmets. Sempre recordaré el primer dia que vaig "ficar la pota" i vaig llençar uns nanofils al bany d'ultrasons. Tot espantada vaig anar a explicar-t'ho i l'únic que vas fer va ser riure i explicar-me la teva primera "ficada de pota". Tots dos heu sigut una gran inspiració per a mi. Formeu un gran tàndem. Finalment voldria agrair-vos haver-me permès i suportat les meves lluites pels drets dels doctorands i haver-me donat l'oportunitat de seguir un any més sense morir-me de gana.

I must also thank Prof. Julia Yeomans, Prof. Ignacio Pagonabarraga, Prof. Teresa López-León, Prof. Laura Casanellas, and Prof. Demian Lewis for kindly accepting to be my jury members. Additionally, I want to thank my Ph.D. Research Monitoring Committee: Prof. Jaume Casademunt, Prof. Miquel Pons, and Prof. Francesc Mas.

Since research is impossible without collaborators, I must acknowledge Jaume Casademunt for performing the linear stability analysis described in Chapter 2 and more in detail in Appendix A.2, and Ricard Alert for doing the stability analysis with the axial symmetry in Appendix A.3. Additionally, I want to acknowledge Ricard Alert and Fanlong Meng, who derived the theory presented in Appendix B, and Jean-François Joanny, Jaume Casademunt, and Ramin Golestanian, who also participated in the project in Chapter 3 by guiding, su-

pervising, and assessing all the study. Regarding the analysis in Chapter 4, I must thank Daniel Pearce for providing us with simulations to help us shed light on our experimental results. Furthermore, I would like to acknowledge Oriol Arteaga for helping us to assemble the two polarimeters presented in Chapter 5. Also, I must thank Miquel Pons for allowing us to express the protein in his lab and Guillermo Iruela, Irrem-Laareb Mohammad Jabeen, and Hector Fuentes for their assistance during the protein expression. Last but not least, I would also like to thank Tyler Ross for helping us in the expression of the photodimerizable proteins, even though I have not finally used them during my thesis.

During my Ph.D. I have had the huge pleasure of meeting incredible people and, even better, working alongside them. El primer que vaig conèixer va ser el Pau. Gràcies per ensenyar-me a preparar l'active nematic i per ensenyar-me tant, ets un gran exemple a seguir. També volia agrair-te que em deixessis el teu ordinador quan jo estava desesperada amb el meu, no podia escriure sad... Una mica a la vegada que vaig entrar jo al lab va arribar el Joseph (o la Josefina). Tot i que el primer dia no em vas ni saludar, ràpidament vas passar a ser un gran amic. Conjuntament amb el Pau vam viure moments molt divertits al lab i fora. De fet, gràcies a vosaltres dos el meu TFG no va ser un complet desastre. And Jérôme, with your sometimes crazy ideas, thank you for always inspiring me, transmitting your calmness, and advising me regarding my uncertain future. Més tard van arribar l'Igni, el Raimon i el Ramon, amb qui també he pogut viure moments inoblidables com a Brussel·les, fent esport durant la quarentena..., han fet molt més fàcil el doctorat i s'han convertit en uns molt bons amics. A year later, Olgui arrived at the lab. You have constantly challenged me at trying to do my best at explaining to you the codes and the few physics I know. També he d'agraïr a tots els bons amics que he pogut fer durant el doctorat i que m'han acompanyat a les hores de dinar. Raul, Genís, Martí, Oriol, Dani, Roger: gràcies. Evidentment no puc oblidar-me d'agrair a la Lorena i la Cristina, que han sigut dos pilars durant la tesi i m'han donat forces per poder seguir endavant amb el doctorat. Fora de la facultat, però encara en el sí de la universitat, he pogut conèixer molta gent amb la qual he compartit molts bons moments. Aquí vull destacar tota la gent de Doctorandes en Lluita, especialment a la Raquel, i del comitè.

També vull agrair a tots els companys del grau que van fer que aquells anys fossin increïbles i que han passat a ser imprescindibles en la meva vida, especialment l'Andrea, la Marta i la Irene, amb qui tinc la sort d'encara poder compartir tants moments amb elles, l'Anna Perelló, l'Anna Martín i la Mireia. I no puc oblidar el Martí, que encara que m'abandonés a principis de la carrera, va seguir delectant-se amb les meves fantàstiques bromes. También quiero agradecer a mis compañeros de máster todos los momentos de locura y risas. Álvar, Javi, Pablo y Juan: gracias por todas las risas compartides durante las comidas

en la UAM. Durante el màster pude vivir en Madrid durante unos meses y allí conocí a grandes amigos. Primero conocí a Antoinette, quien fue una compañera de piso ejemplar y que se ha convertido en una grandísima amiga. Our chaotic apartment also led me to meet Ladina, with whom we lived crazy moments, and also I had the pleasure of travelling with. Y a Javi, mi amigo más majo.

Fora de la universitat i del món acadèmic, no he pogut estar més ben acompanyada. Ja des dels 3 anys m'han acompanyat incondicionalment la Paula i la Cèlia. També m'han acompanyat l'Anna i les nostres tardes de diumenge, tota la gent de Martinet i la Inés. Evidentment aquí no podia faltar tota la gent de Crossfit, que han ajudat que la meva salut mental es mantingués raonablement bé durant la tesi, aquí he de mencionar especialment a la Laura, la Raquel, la Ghiza, l'Alberto, l'Aleix, la Roser, la Laura B., el Marco (intentando igualar mis bromas), la Júlia i el Pol i, obviament a la Marta la millor coach del món.

Finalment, vull agrair a la meva família per ser sempre allà incondicionalment i per animar-me a realitzar aquesta tesi. Sense vosaltres no hagués sigut possible. Mai hagués triat una millor família. Us estimo. Als yayos per preocupar-se sempre tan per mi. Gràcies yaya pel ciri perquè acabi la tesi. Gràcies al Jordi, a l'Emma, a la Toni, a la Pili, a l'Óscar, a la Núria i al Tomàs per animar-me. No puc deixar d'agrair als que ja no són aquí: a l'avi i a l'àvia. Gràcies àvia per acollir-me a casa teva durant uns mesos i per ser un exemple a seguir per mi. Y a ti Javi, gracias por seguir incondicionalmente a mi lado estos meses aunque yo no lo haya puesto nada fácil, gracias por sacarme siempre una sonrisa y por cuidarme pasara lo que pasara.

Contents

Publications

The work presented in this thesis has been published in the following articles:

- Guillamat, P., Hardoüin, J., Martínez-Prat, B., Ignés-Mullol, J & Sagués, F. *Features of interfaced and confined experimental active nematics*, chapter from Active Matter and Nonequilibrium Statistical Physics: Lecture Notes of the Les Houches Summer School (Oxford University Press, 2022)

- Martínez-Prat, B.*, Alert, R*. et al. Scaling Regimes of Active Turbulence with External Dissipation. Phys. Rev. X 11, 031065 (2021) – Chapter 3

- Martínez-Prat, B., Ignés-Mullol, J., Casademunt, J. & Sagués, F. Selection mechanism at the onset of active turbulence. Nat. Phys. 15, 362–366 (2019) **(Appearing on the cover)** – Chapter 2

- Guillamat, P., Hardoüin, J., Prat, B. M., Ignés-Mullol, J. & Sagués, F. Control of active turbulence through addressable soft interfaces. J. Condens. Matter Phys. 29, 504003 (2017) – Chapter 2

There is one more article in preparation:

- Martínez-Prat, B., Arteaga, O., Sagués, F. & Ignés, J. Multimodal fluorescence microscope with fast adaptive polarimetry. – Chapter 5

Additionally, a research regarding chromonic liquid crystals and that is not included in this thesis has been published in:

- Ignés-Mullol, J., Mora, M., Martínez-Prat, B. et al. Stable and metastable patterns in chromonic nematic liquid crystal droplets forced with static and dynamic magnetic fields. Crystals 10, 138 (2020)

* Equal contribution

List of Figures

List of Tables

List of Videos

The videos can be found by scanning the following QR-code or by clicking here.

List of Codes

The codes can be found by scanning the following QR-code or by clicking here.

List of abbreviations

ADP adenosine 5′-diphosphate 113, 114

AN active nematic 32, 40, 43, 44, 48–50, 52, 58, 59, 70, 72, 74–77, 82, 84, 88, 94, 95, 99, 100, 117–119, 122, 123, 129, 133, 134, 139–141, 153, 159, 165, 170

ATP adenosine 5′-triphosphate 14, 32, 34, 35, 109, 113, 114

DFT Discrete Fourier Transform 132, 175, 177–179, 181, 182

DTT dithiothreitol 112–114

FFT Fast Fourier Transform 32–34, 125, 127, 132, 177, 180–182

iFFT Inverse Fast Fourier Transform 180

IW interrogation window 120–122

LC liquid crystal 74, 82, 92, 94, 95, 104

LCR liquid crystal retarder 80, 82–84, 87, 89–93, 96, 99, 193–195

LHP linear horizontal polarizer 96, 188, 189, 191, 194

LP linear polarizer 90, 197

LR linear retarder 89, 90, 99, 193, 194, 198

LVP linear vertical polarizer 83, 90, 191, 194

MT microtubule 12–17, 20, 21, 30, 32, 35, 37, 39, 44, 50, 58, 66, 73, 79, 82, 94, 110, 111, 113, 114, 116–118, 120–123, 144, 147

OW Okubo-Weiss 129

PAM polyacrylamide 116, 117

PDMS polydimethylsiloxane 116, 117

PEG polyethylene glycol 13, 32, 37, 113, 114

PEP phosphoenol-pyruvate 114

PIV particle image velocimetry 50, 63, 66, 82, 117, 120, 121, 130, 133, 137

PK pyruvate kinase 114

POM polarized optical microscope 79–81, 84, 95

QWP quarter waveplate 82, 84, 88–90, 96, 99, 191, 194, 195, 197, 198

List of symbols

Symbol	Description	Unit
i	imaginary number $\sqrt{-1}$	
M	Mueller matrix	
$\boldsymbol{S}$	Stokes vector	
$\boldsymbol{n}$	Nematic director vector	
η	Dynamic viscosity	Pa·s
η_{N}	2D dynamic viscosity of the active nematic	Pa·s·m
γ	Rotational viscosity	Pa·s
γ_{N}	2D rotational viscosity of the active nematic	Pa·s·m
$\mathcal{F}$	fourier transform	
$\mathbf{Q}$	Nematic tensor	
S	Scalar order parameter	
$q_{\alpha\beta}$	Nematic tensor with fixed order parameter $S = 1$	
θ	Nematic orientation	rad
ν	Flow alignment parameter	
$\boldsymbol{h}$	Molecular field (2D)	
F_n	Frank elastic energy (2D)	N·m
K	Elastic constant (2D)	N·m
K_1	Splay elastic constant (2D)	N·m
K_3	Bend elastic constant (2D)	N·m
α	Activity coefficient (2D)	N/m≡Pa·m
ρ	Mass density (2D)	$\mathrm{kg/m^2}$
$\boldsymbol{\sigma}$	Symmetric stress tensor (2D)	N/m≡Pa·m

Symbol	Description	Unit
$\boldsymbol{\sigma}^{\mathrm{a}}$	Antisymmetric stress tensor (2D)	N/m≡Pa·m
P	Hydrodynamic pressure (2D)	N/m≡Pa·m
$\delta_{\alpha\beta}$	Dirac delta	
$\boldsymbol{v}$	Velocity	m/s
$v_{\alpha\beta}$	Symmetric part of the strain rate tensor	s^{-1}
$\omega_{\alpha\beta}$	Antisymmetric part of the strain rate tensor	s^{-1}
ω	Vorticity	s^{-1}
E	Kinetic energy density per unit mass (2D)	$\mathrm{m}^4{\cdot}\mathrm{s}^{-2}$
$\boldsymbol{q}$	Wave number	m^{-1}
q	Wave number modulus	m^{-1}
$E(q)$	Kinetic energy density spectrum per unit mass (2D)	$\mathrm{m}^3{\cdot}\mathrm{s}^{-2}$
q^*	Characteristic wave number	m^{-1}
Ω	Growth rate	s^{-1}
Ω^*	Characteristic growth rate	m^{-1}
R_*	Mean vortex radius	m
R_*^{s}	Mean vortex radius extracted from the kinetic energy spectrum	m
R_*^{v}	Mean vortex radius extracted from the distribution of vortex areas	m
I	Energy injection	N/(m·s)
D_s	Viscous energy dissipation	N/(m·s)
D_r	Rotational energy dissipation	N/(m·s)
T	Energy transfer	N/(m·s)
$\mathcal{A}$	Area	m^2
φ	Azimuth	rad
w	Winding number	
m	Topological charge	
Re	Reynolds number	
H	Height or layer thickness	m
$\boldsymbol{u}$	3d fluid velocity	m/s
$\boldsymbol{E}$	Electric field	V/m

Symbol	Description	Unit
δ_x, δ_y	x and y phase constants	rad
δ	phase shift	rad
χ	Ellipticity angle	rad
ψ	Retarance of the variable liquid crystal retarder	rad
α	Fast axis orientation	rad or degrees (^{o})
Δn	Birefringence	rad
n	Refractive index	rad
V	Voltage	V

Chapter 1

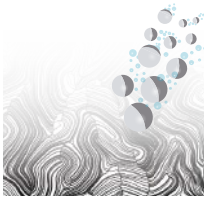

Introduction

1.1 Active matter

Flocks of birds, colonies of ants, large groups of people or dense suspensions of swimming bacteria are all encompassed within what is known as **active matter**. Active matter refers to systems composed of units, each capable of transforming stored or ambient energy into constant movement [2, 3, 4, 5, 6]. These systems can be found in a vast spectrum of length scales: from the micron scale up to some tens of meters (see Fig. 1.1).

Interestingly, interactions of the constituents with their neighbors and the surrounding medium trigger the appearance of collective motion, where large groups of these active particles move as a one, without the need for a leader [9]. Moreover, this collective behavior and the non-equilibrium environment give rise to striking phenomena. Some examples include pattern formation [8, 10, 11, 12, 13, 14], unusual mechanical and rheological properties [15], and chaotic flows even when inertia is negligible [16, 17, 18, 19, 20], all sharing that they are not observed for individual constituents.

Throughout this thesis, we have been mainly concerned about active colloidal systems. The latter refer to suspensions with non-soluble particles with a typical size ranging between the nano and the micron scales. Given the particles' small scales, these systems are at low *Re*. This number relates inertial forces with viscous forces:

$$Re = \frac{L\rho u}{\eta} \tag{1.1}$$

where ρ and η are the fluid's density and viscosity, respectively, and L and u are the swimmer's typical size and velocity. Then, hydrodynamics at low

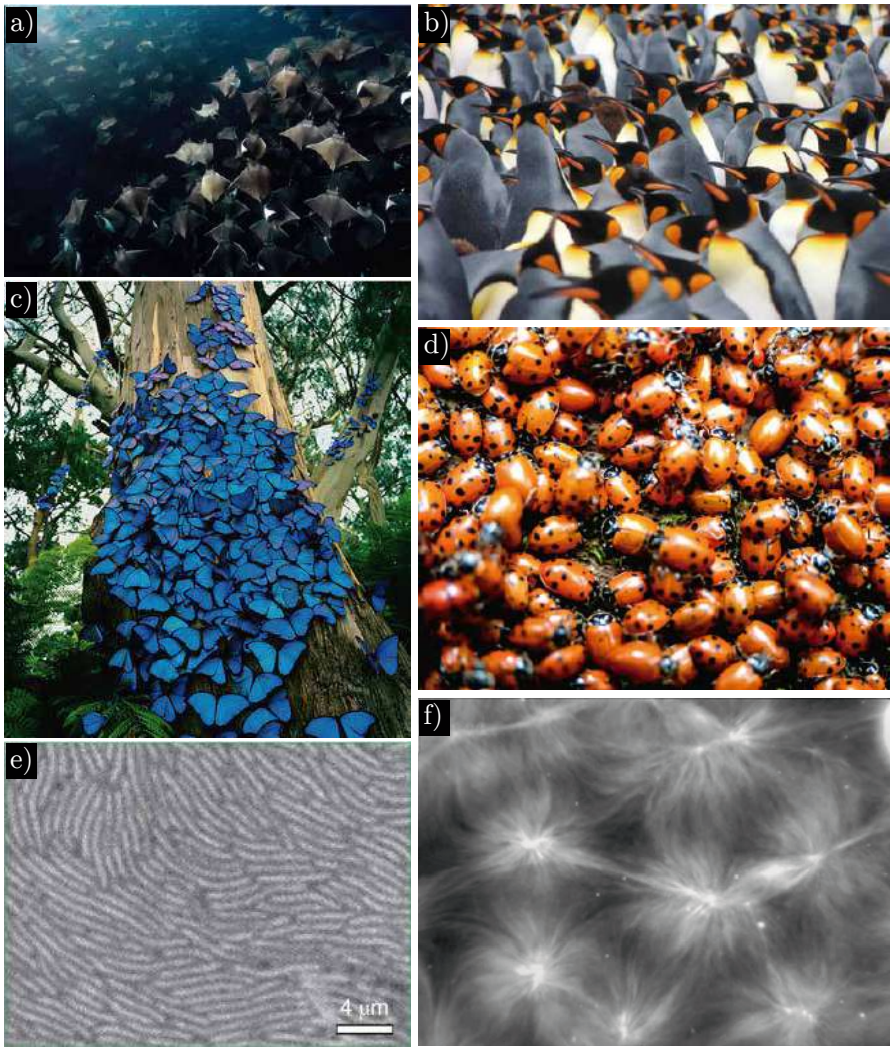

Figure 1.1: Examples of active systems at different length scales. **a**) Giant school of mobulas swimming in Mexico. Image from Pier Nirandara adapted under Attribution-NonCommercial-NoDerivs 2.0 license (CC BY-NC-ND 2.0). **b**) Penguin waddle. Image available at Rawpixel under CC0 1.0 Universal (CC0 1.0) Public Domain Dedication. **c**) A swarm of Blue Morpho butterflies. Image courtesy of Kelvin Hudson. **d**) Swarms of ladybugs. Image from Amit Patel under Creative Commons Attribution 2.0 Generic (CC BY 2.0 license). **e**) A dense colony of *Myxococcus xanthus* forming an active nematic layer. Image adapted from [7] with permission from Springer Nature. **f**) Pattern of asters formed through the self-organization of microtubules and kinesins. Image adapted from [8] with permission from Springer Nature.

Reynolds numbers are governed by viscosity rather than inertia. As we will see in the next section, swimming at a low Reynolds number has far-reaching consequences because not all ways of swimming produce net movement under these conditions. Accordingly, in this introductory chapter, we will first cover different active colloidal particles able to move at low *Re*. Then we will focus on highly packed systems of such active entities and their striking phenomena.

1.2 Active particles

In this section, we specifically concentrate on active colloidal particles, whose motion can arise from either self-propulsion mechanisms or interactions with external fields [21]. It is true that if one takes the definition of an active system strictly, particles driven by external fields should not be considered active. Other names, such as driven or activated particles, could be used instead. Nonetheless, these entities still capture the essence of their self-propelled counterparts. Indeed, their study can lead to the engineering of new applications for medical purposes, such as drug delivery to targeted regions [22].

Regardless of the phoretic mechanism, all particles moving at low Reynolds numbers in a Newtonian fluid need to swim in a non-invariant way under time reversal. This is because if a swimmer at low Reynolds number deforms its body in a particular way and then deforms back to the original shape by following the same sequence, but in reverse, it will not move. This idea was first introduced by Purcell as the Scallop's theorem in his celebrated article *Life at low Reynolds number* [23]. Such conclusion was derived from the Navier-Stokes equation in the Stokes limit, which neglects the inertial terms:

$$-\boldsymbol{\nabla} p + \eta \nabla^2 \mathbf{u} = \mathbf{0} \tag{1.2}$$

where p, η, and $\mathbf{u}$ are the fluid's pressure, viscosity and velocity, respectively. Dropping all the inertial terms, leads to a non-time dependant velocity. Consequently, if an animal at low *Re* swims in a reciprocal motion, it will exactly go back to the starting point. Notice that Purcell's theorem only holds for Newtonian fluids. For instance, Qiu et al. [24] have reported a symmetric 'micro-scallop' moving in a reciprocal motion that can self-actuate in shear thickening and shear thinning, which are fluids with shear-dependent viscosities (non-Newtonian). Thus, as the authors reported, the micro-scallop can self-propel by setting different opening and closing rates. Reviews regarding this issue can be found in [25, 26]. Also, a very detailed review dedicated to microswimmers can be found in [27].

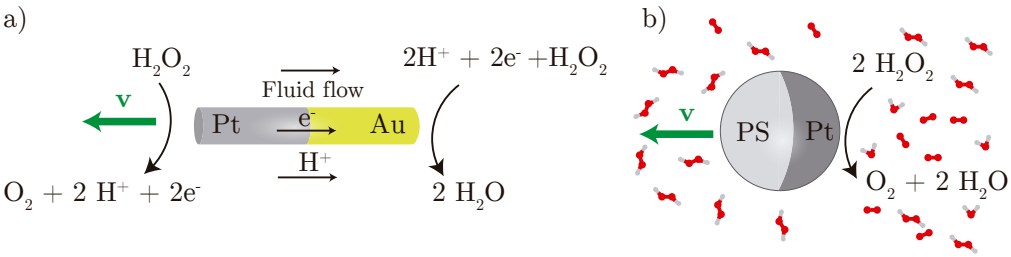

Figure 1.2: Schematic representation of two artificial swimmers with self-phoresis. **a**) Bimetallic rod (self-electrophoresis) and **b**) Janus polystyrene (PS) particle half-coated with a platinium (Pt) layer that catalyzes the disproportionation of H_2O. Solute gradients drive the particle (self-diffusiophoresis).

1.2.1 Experimental realizations

1.2.1.1 Artificial microswimmers

Inspired by living systems, researchers have created synthetic microswimmers that, with few building blocks, grasp the dynamics of their more complex living analogues. Here I list and introduce som examples.

Bimetallic nanorods

The first synthesized self-propelled particles were reported by Paxton et al. [28], who prepared self-motile bimetallic rods with one platinum and one gold part. The former metal catalyzes the oxidation of H_2O, whereas the latter catalyzes the H_2O reduction. These electrical processes generate an electron transport from the platinum to the gold end, which translates into a potential difference that triggers the proton migration along the rod-solution interface. The movement of protons produces, in turn, the flow of water molecules from Pt to Au, which propels the rod (see Fig. 1.2a). This motion process is known as **self-electrophoresis** [29, 30, 31]. Other colloidal particles actuated through self-electrophoresis also include enzymatic reactions.

Janus particles

We cannot go trough this section without mentioning Janus particles (see Info Box 1.1). These self-phoretic colloids are split into at least two regions with differentiated physical and/or chemical properties. In this way, the symmetry is broken so that they can self-propel. The most simplified version of a Janus particle is a sphere with its surface divided into two parts, with one of them catalyzing a given reaction, such as the redox disproportionation of H_2O in the surrounding media. This chemical reaction locally produces O_2 and H_2O, leading to a concentration gradient and, thus, to **self-diffusiophoresis** (see

Fig. 1.2b). Howse et al. [32] engineered the first realization of such self-motile inclusions, which contained platinum or palladium as catalytic materials.

Infobox 1.1: Where does the name Janus particle come from?

Leonard Wibberley, in his novel *The Mouse on the Moon* (1962), was the first person who coined the term Janus to refer to a science-fictional device for space travel propelled with wine. The author used this name after the roman god Janus [33], who is usually depicted with two faces (see Fig. 1.3).

Figure 1.3: Statue representation of the roman god Janus in Museo Chiaramonti (Vatican Museums). Janus, usually represented two-faced, is the god of the beginnings, gates, and endings. This is why January is named after Janus [34]. Image from Marie-Lan Nguyen [35] under Attribution 3.0 Unported license (CC BY 3.0).

The term Janus was not used in a scientific context until 1988 by C. Casagrande et al., who synthesized glass spherical particles, featuring one hemisphere hydrophilic, and the other one hydrophobic [36].

Other artificial self-proppeled colloids

Apart from the already mentioned synthetic self-propelled particles, researchers have also synthesized many others, like those moving from the production of bubbles, or through Marangoni stresses originating from surface tension gradients localized at the colloid surface.

1.2.1.2 Driven or activated particles

As aforementioned, colloidal particles can also be propelled through external fields. This can be very interesting because external actuation enables finely tuning and controlling the motility, at least in some cases. In the literature, many different experimental realizations of externally-driven colloids exist. Here

we will only mention some of them. For a thorough review concerning driven active particles, refer to [37].

Janus-based driven particles

First, we can find Janus-based driven particles whose underlying working principle is the same as in the autonomous Janus particles, but in this case, an external laser or force is applied to the particle to initiate and trigger the propulsion mechanism. An example is the colloids Palacci et al. synthesized with hematite, which catalyzes the H_2O_2 decomposition under blue light [38]. These colloids, as their autonomous counterparts, also move by diffusiophoresis. Alternatively to this phoresis, as Jiang et al. proposed [39], Janus particles can also be propelled by means of **self-thermophoresis**. In this case, silica particles are half-coated with a gold layer that, upon laser beam irradiation, produce a local thermal gradient leading to net propulsion.

Particles driven by magnetic and electric fields

Then, we can find colloidal particles actuated through magnetic fields. Some remarkable examples include the Dreyfus et al. [40] sperm-like particles constructed by the DNA-mediated linking of colloidal magnetic particles attached to a red blood cell. By means of external magnetic field, the researchers align the colloids and produce a beating pattern that propels the swimmer. Other magnetically-actuated particles are based on rotary particles [41] and axially symmetric particle spinners [42, 43].

Alternatively, electric fields have also been proven effective in propelling colloids. For example, Quincke rollers are colloids made of dielectric spheres or cylinders that start to spin when immersed in a slightly conducting fluid and a DC field is applied. If such colloids are near a substrate, this rotation causes the translation of the particles [44]. Also, some colloidal particles have been driven by what is known as induced-charge electrophoresis. In this case, asymmetric particles in a solvent under an AC field produce an imbalanced migration of charged ions or molecules, resulting in net particle propulsion [37, 44].

1.2.1.3 Biological microswimmers

Living systems are the prototypical example of entities capable of self-propelling. At the colloidal scale, one can find microorganisms like bacteria, eukaryotic cells, algae, or proteins from the cytoskeleton. All of them, constrained by the Scallop theorem, have evolved to create propulsion strategies, successfully overcoming and exploiting viscosity.

Bacteria

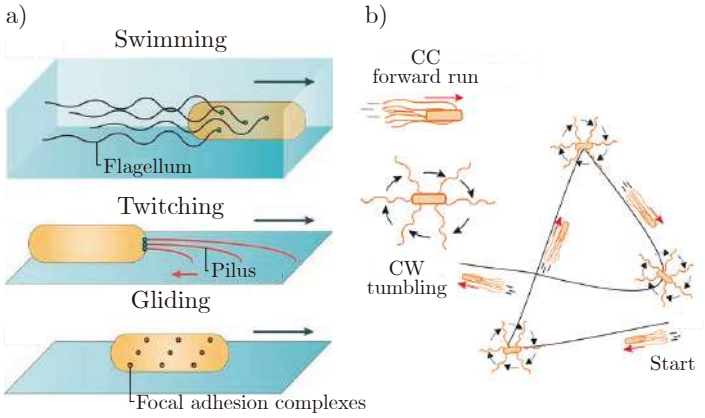

Figure 1.4: Bacterial motion. **a**) The different locomotion mechanisms of individual bacteria. Swimming is attained with helical flagella. Conversely, bacteria can move on a substrate through twitching with pilus or gliding with focal-adhesions. Image adapted from Kearns [46] with permission from Springer Nature. **b**) The run-and-tumble in *Escherichia Coli*. Image adapted from Bastos-Arrieta et al. [47] under Creative Commons Attribution License (CC BY).

Most bacteria swim thanks to helical filaments, known as flagella, protruding from the cell envelope (Fig. 1.4a). The helical structure of flagella ensures the broken time-reversal symmetry. The number and arrangement of flagella can vary among different species of bacteria. For example, some bacteria possess multiple flagella localized at a particular spot, whereas others can be covered by multiple flagella randomly oriented. Flagella are then spun by motor complexes either clockwise or counterclockwise, inducing in this way the bacterium's propulsion [27, 45].

Flagellated bacteria generally present two differentiated motion phases: the run and tumble phases. In the run phase, the bacteria move forward in one direction, whereas in the tumbling phase, the microswimmers change their orientation randomly (Fig. 1.4b). By tuning the shift from one phase to the other, bacteria can explore the surroundings in the seek of food or ideal environmental conditions. [27].

Other forms of bacterial locomotion include gliding either through proteins (adhesins) that attach to the substrate and move across the length of the cell, or pili, which are thin filaments acting like grappling hooks: they extend, attach to the substrate and then retract, pulling the cell forward. The latter way of motility is known as twitching (Fig. 1.4a). Finally, some pathological bacteria, when they infect a eukaryotic cell, induce the polymerization of the eukaryotic actin, a component of the cytoskeleton (see Info Box 1.2) to propel themselves

[45, 48].

Infobox 1.2: The cytoskeleton

The cystokeleton is a complex of network-forming filamentous proteins involved in many cell functions. This protein complex is ubiquitous: it can be found in almost all cells, from bacteria and archae to eukaryotic cells.
The proteins of the cytoskeleton are involved in a multitude of functions [49, 50, 51]:

- Preserve and change the cell's shape
- Secure a specific position of some organelles
- Enable the active transport of vesicles and cytoplasm (cytoplasmic streaming)
- Enable the cell's movement
- Assist with cell division

In the case of eukaryotic cells, one can find the intermediate filaments, composed of keratin, the microfilaments, composed of tubulin, and microtubules, composed of actin (Fig. 1.5). The two latter ones work together with molecular motors: myosins, dyneins, and kinesins.

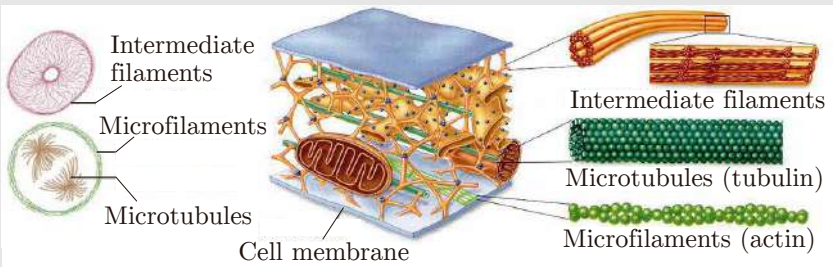

Figure 1.5: The cytoskeleton of an eukaryotic cell. Microfilaments thicken the cortex around the inner edge of a cell; like rubber bands, they resist tension. Microtubules are found in the interior of the cell where they maintain cell shape by resisting compressive forces. Intermediate filaments are found throughout the cell and hold organelles in place. Image and caption adapted avialable in OpenStax [49] under Creative Commons Attribution 4.0 License (CC BY 4.0).

Eukaryotic cells

The locomotion mechanism of eukaryotic cells is very diverse. Nevertheless, the two prevailing ones are flagellar-dependent swimming and actin-dependent cell migration (crawling) (Fig. 1.6). These two types of motility are both used by animal cells and unicellular eukaryotic organisms [52].

Flagellar motility in eukaryotic cells is akin to flagellar motility in bacteria. However, in eukaryotic cells, apart from actin, flagella also contain microtubules, which are absent in prokaryotic cells (like bacteria). Moreover, motion of bacteria through flagella is attained through the filaments rotation, whereas flagella in eukaryotic cells exhibit a beating model resulting in the cell's propulsion.

Actin-dependent cell migration relies on the dynamic turnover of actin networks, which pull and push the cell across solid surfaces. Some cells can also crawl by exploiting the flows created at the cell's rear by the myosin-mediated contraction of actin filaments.

Other biological microswimmers

Nature offers us a huge catalogue of microswimmers. Apart from the already explained bacteria and eukaryotic cells, there are some that are worth-mentioning. The first one is the single-celled algae *Chlamydomonas reinhardtii*, which swims with two flagella and are the typical example of a puller microswimmer [27].

Motility assays

Actin and microtubules are essential for the life of eukaryotic cells. These filamentous proteins are not only involved in the cells' motility but also many other functions, such as intracellular transport or the divisions of chromosomes during mitosis. In pursuit of understanding these proteins' mechanical and kinetic properties, researchers have devised techniques to measure the molecular motors' movement. First, Sheetz et al. [53] constructed myosin proteins bonded to fluorescent beads that were then deposited onto a Nitella axillaris cell, which features actin cables. Myosin can then move along such well-aligned structures carrying the beads. Later, Kron et al. [54], inspired by Sheetz et al. investigation, developed a system based on a myosin-decorated substrate that induces movement to actin filaments under the presence of ATP (Fig. 1.7). This pioneering study led to many others devoted to deciphering the self-organization and the collective behavior of motile actin filaments [11, 12] and microtubules [55].

Alternatively to motility assays, motion translocation from molecular motors to actin filaments or microtubules can also be attained by using crosslinking molecular motors. For instance, Verde et al. [57] used dynein to dynamically self-organize microtubules into asters and Kumar et al. [58] used myosin II to prepare an active system. Also, Nédélec et al. [8] succeeded in preparing clus-

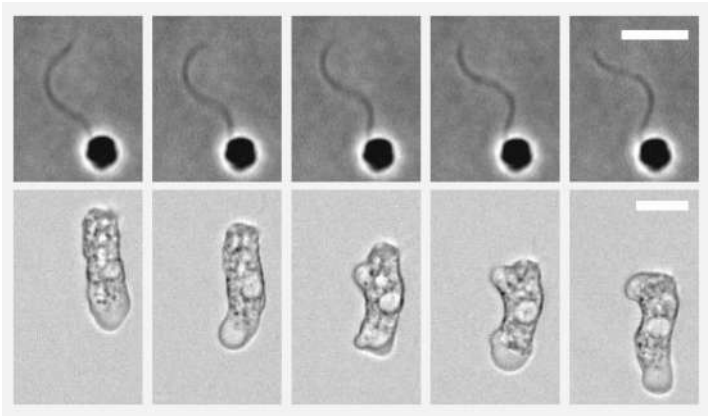

Figure 1.6: Flagellar-based swimming and actin-dependent crawling are the two predominant forms of eukaryotic cell motility. (Top) Species from every branch of the eukaryotic tree use flagella to swim through liquids. Some cells, including human sperm and the *Batrachochytrium dendrobatidis* fungal cells shown here, use flagella to push cells. Other cells, like *Chlamydomona*s and *Naegleria* flagellates, use flagella to pull themselves through liquid. Flagellar motility is often very rapid; these cells were imaged once every millisecond. (Bottom) The other predominant form of eukaryotic cell motility is the actin-dependent crawling motility used by cells to crawl across or between solid surfaces. In contrast to the rigid and stable microtubules that are the basis of flagellar motility, crawling motility relies on the dynamic turnover of ephemeral actin polymer networks. Many eukaryotic species take advantage of the ability to crawl on solid surfaces and swim through liquids, including this *Naegleria gruberi* cell (here imaged every 2 seconds) that eats and replicates as a crawling amoeba, but under stress can differentiate into a swimming flagellate. Both scale bars represent 5 µm. Image and caption adapted from Fritz-Laylin [52] with permision from Elsevier.

tered kinesins, which are very similar to the ones we have used in the experiments presented in this thesis and that we will introduce in Section 1.4.1.

1.3 Active fluids

In the previous section, we have seen different self-propelled and driven particles. When they are densely packed, forming an active fluid, these entities start self-organizing, giving rise to emergent collective phenomena.

Pattern formation

In some scenarios, large collections of active particles can self-organize, giving rise to structures with an order that propagates to scales much larger than the

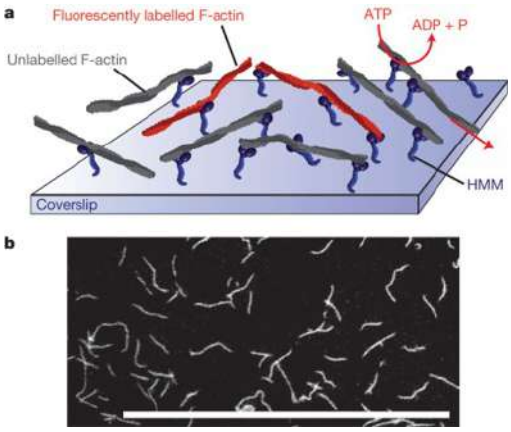

Figure 1.7: Schematic of the high-density motility assay. **a**) The molecular motor heavy meromyosin (HMM) is immobilized on a coverslip and the filament motion is visualized by the use offluorescently labelled reporter filaments with a ratio of labelled to unlabelled filaments of ∼1:200 to 1:320. **b**) For low filament densities, a disordered phase is found. The individual filaments perform persistent random walks without any specific directional preferences. Encounters between filaments lead to crossing events with only slight reorientations. Scale bar, 50 µm. Image adapted from Shaller et al. [56] with permision from Springer Nature.

particle size. Depending on the symmetries of the system, one can find polar patterns, where active entities move in the same direction producing active transport, or nematic patterns, which form in systems where particles align but move indistinctively back and forth.

Motility-induced phase separation

Systems of self-propelled particles can undergo liquid-phase separation. Remarkably, such phase separation happens even when the interactions between particles are repulsive. It, therefore, stems from the motility of the particles [59].

Giant number fluctuactions

One of the hallmarks of collective motion is the presence of giant number fluctuations, a phenomenon characterized by abnormally large fluctuations in particle density [60, 61]. They are abnormal because they are far larger than those for particles in thermal equilibrium.

Chaotic flows. Active turbulence

One of the most striking behaviors seen in active systems is the presence of

chaotic spatiotemporal flows, even at low Reynolds numbers. The study of the statistical properties of this chaotic state has been the main focus of this thesis. Therefore, to contextualize the concept of active turbulence better, we will not enter into more detail here and devote Section 1.5 to explaining active turbulence thoroughly.

1.4 Active systems based on cytoskeletal proteins

Dealing with cells to prepare in vitro reconstitution of active systems can be complex and time-consuming. Working instead with in vitro active materials composed of proteins from the cytoskeleton effectively reduces the system's complexity and, at the same time, enables the study of self-organization. Remarkably, with only a few building blocks, these protein-based systems show a vast plethora of dynamic states. Indeed, these in vitro systems do not only reproduce behaviors seen in some living systems but also uncover new phenomena, leading to a significant betterment in bioinspired material science.

As earlier explained in Section 1.2, these synthetic protein-based materials are mainly comprised of either **actin filaments** or **microtubules** driven far from equilibrium by their corresponding molecular motors, which are proteins capable of converting chemical energy into mechanical work. In general, to do so, they hydrolyze ATP, the fuel of the cell. In eukaryotic cells, one can find three different types of molecular motors: **myosins**, which are the ones associated with actin filaments and **dyneins** and **kinesins**, both associated with microtubules.

1.4.1 The Dogic group active system

Back in 2012, Sanchez et al. [17], in the Dogic group, revolutionized the field of active bioinspired systems by presenting an assemblage of stabilized-MT with kinesin, ATP, and a depletant (or crowding agent). This protein suspension leads to the spontaneous formation of a percolating network of continuously breaking and self-healing MT-bundles.

The typical preparation of the protein suspension includes 1 µm-longMTs, stabilized with the GTP analog GMPCPP (see Info Box 1.3), and bundled thanks to the depleting action of the non-adsorbing polymer polyethylene glycol (PEG) (Fig. 1.8). The system is driven far from equilibrium with clustered kinesins (see inset in Fig. 1.9), which crosslink multipleMTs. These kinesin clusters, fueled by ATP hydrolysis, walk along two neighboring microtubules towards the plus-end. If such microtubules are antiparallely aligned (they have opposite polarity), such movement results in a relative sliding of the two filaments (Fig. 1.9).

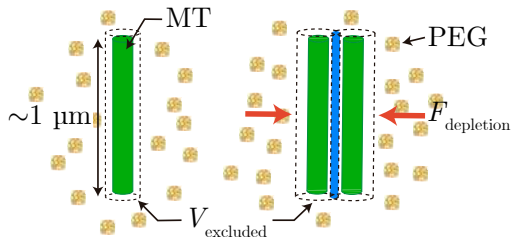

Figure 1.8: PEG drives the formation of bundles trhough depletion forces. The addition of a non-adsorbing polymer, like polyethylene glycol (PEG), induces an effective attraction of the ∼1 µm-microtubules (MTs), leading to the formation of bundles. There is a volume around the filament (the excluded volume, V_{excluded}, indicated with dashed lines) unavailable for the PEG molecules. As two filaments get closer, there is an overlap between their V_{excluded} (indicated in blue). This originates an imbalance of osmotic pressure and an attractive force between theMTs ($F_{\text{depletion}}$). This phenomena is the so-called depletion. The PEG molecules have been created using Biorender.

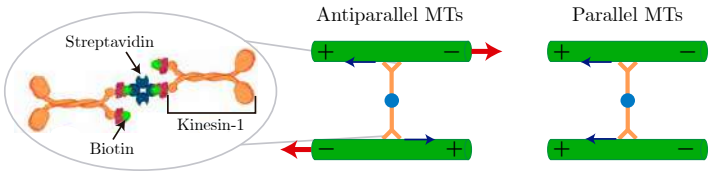

Figure 1.9: Kinesin clusters induce the sliding of antiparallely aligned MTs. Kinesins-1 walk alongMTs towards the filament's plus end (kinesins' directions are marked with blue arrows) as they hydrolyze ATP into ADP and a phosphate (P_i). When a kinesin cluster crosslinks two antiparrallely aligned MTs, it produces a relative movement of the filamentous proteins (red arrows indicateMTs' displacement). If the MTs are polarity sorted, no sliding is produced. The insets shows a representation of the kinesin clusters, which are prepared through the binding of (in average) two kinesins-1 with the tetrameric protein streptavidin via biotin molecules. The the inset has been created using Biorender.

Infobox 1.3: The dynamic instability of microtubules

The length of microtubules is not constant inside the cell because they constantly suffer from polymerization and depolymerization events. Such processes are regulated by the nucleotide GTP, which binds to tubulin (the MT's subunit), triggering the attachment of the subunit to the filament growing side. This binding requires energy supplied by the GTP hydrolysis into GPD + a phosphate after the tubulin's incorporation. Tubulins at the end of the filament linked to a GTP are stable and do not detach from the microtubule. However, if the hydrolysis catches up to the tip, it originates a rapid depolymerization and shrinkage (see Fig. 1.10). The polymerization and depolymerization phenomena allow the cell to reorganize microtubules rapidly when necessary [62].

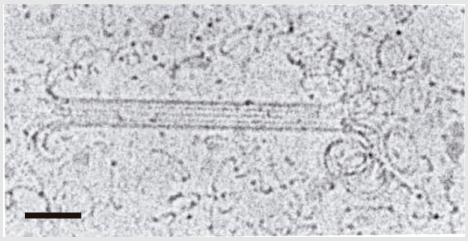

Figure 1.10: Shrinking microtubule. Cryo-electron micrograph of a microtubule during its depolymerization. Image adapted from Mandelkow et al. [63] with permision from Elsevier.

The depolymerization of microtubules can be hampered using other molecules, such as GMPCPP or the stabilizing agent Taxol.

In this system, the active stresses that the kinesin clusters produce are extensile in the sense that they tend to extend the bundles' length (Fig. 1.11a). This is in contrast to other systems, such as the actin-myosin preparation in [64], that feature contractile stresses, which shorten the filamentous bundles (Fig. 1.11b). It is worth mentioning that the molecular motor's nature is not the only determinant of the type of stress. As a matter of fact, clusters of kinesin-1 have been shown to produce many different dynamic patterns compatible with both types of stresses [8, 17, 55, 65, 66]. According to computer simulations and experiments, molecular motors in contractile systems tend to accumulate at the end of the filaments [10, 67], be they microtubules or actin filaments. This capacity to remain bound upon reaching the filament ends enables multiple filament ends to be brought together, forming an aster. For stabilized

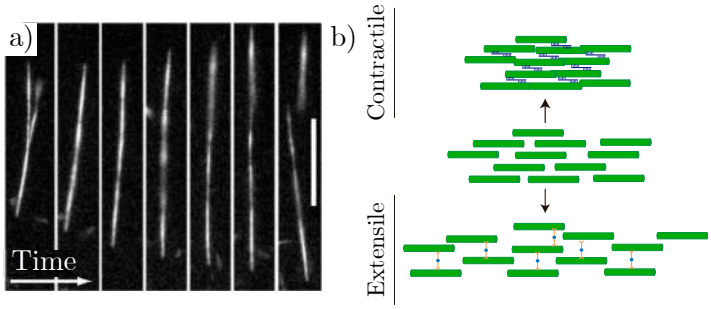

Figure 1.11: The kinesin clusters in this preparation produce extensile stresses. **a**) Fluorescence micrographs of two microtubule bundles merging and immediately extending, eventually falling apart. Time interval, 5 s; scale bar 15 µm. Image adapted from Sanchez et al. [17] with permission from Springer Nature. **b**) Schematic of a filaments' bundle experiencing contraction (top) and extension (bottom). In contractile systems, the bundles' length shortens, whereas in extensile systems, it lengthens.

filaments, the inter-filament attractive interactions and the filament length and density seem to be key in dictating the stresses generated by the molecular motors [11, 65, 68, 69, 70, 71]. Large atractive forces promote the formation of bundles, thereby precluding aster formation

The extension of long filament MT-bundles causes their buckling and posterior fracture into smaller fragments, which can recombine with a surrounding bundle. If such recombination produces regions with mixed polarity, the bundle extends, buckles and fractures back again (Fig. 1.12a). When the concentration of MT-bundles is high enough, these cycles of polarity sorting, extension, buckling, and fracturing drive the formation of an active network pervaded with large-scale chaotic flows (Fig. 1.12b).

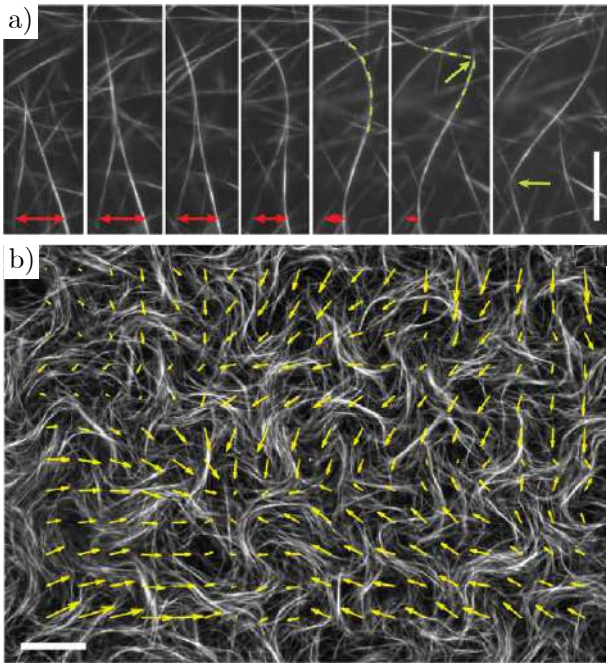

Figure 1.12: The dynamics of the MT-bundles. **a**) In a percolating microtubule (MT) network, bundles constantly merge (red arrows), extend, buckle (green dashed lines), fracture, and self-heal to produce a robust and highly dynamic steady state. Time interval, 11.5 s; scale bar, 15 µm. **b**) An active MT network viewed on a large scale. Arrows indicate local bundle velocity direction. Scale bar, 80 µm.

1.4.2 The 2D active nematic

Strikingly, when the protein suspension is placed in contact with an oil/water interface decorated with a surfactant, the MT-bundles adsorb onto such interface. The increase in the filaments' density triggers the spontaneous formation of a liquid crystalline phase, where the bundles are locally aligned, with the orientational order only disrupted by half-integer defects, seen as darker regions depleted of MTs Fig. 1.13. Notice that the presence of half-integer defects is a signature of nematic symmetry rather than polar order, where defects with semi-integer defects are geometrically constrained. In polar liquid crystals, one would expect the appearance of asters or vortices.

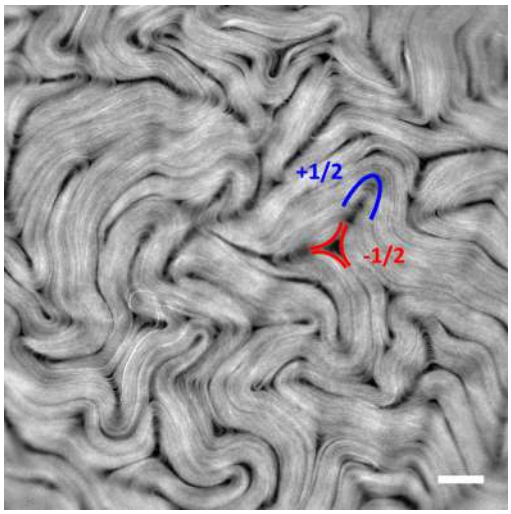

Figure 1.13: Fluorescence micrograph of the MT-based active nematic (AN). One +1/2 and one -1/2 defects are marked in blue and red. Scale bar is 100 µm.

Passive liquid crystals tend to minimize their elastic energy. To do so, they tend to minimize the total number of topological defects. Once the equilibrium liquid crystal finds its state of minimal energy or a metastable state, the defects, if existent, remain essentially static. Conversely, in the presented out-of-equilibrium nematic, defects are constantly being created, unbounded, sheared, and annihilated, reaching a steady state with a statistically constant number of defects. These defect dynamics are fundamentally and drastically different from those of passive liquid crystals.

In this system, the buckling of aligned bundles drives the self-fracture of the material, originating two oppositely-charged half-integer defects placed at each end of the rupture. This disclination line can self-heal, resulting in the

unbinding of the defects, which then move around until their annihilation with oppositely charged defects. The comet-like symmetry of the $+1/2$ singularity renders the defect self-motile. In contrast, the threefold symmetry of $-1/2$ defects counterbalances the flows originating from the activity. As a result, $-1/2$ defects are not self-propelled and can only move stirred by the background flow. [72].

Infobox 1.4: Topological defects

Topological defects are singularities in the orientation field of a phase featuring orientational order, such as a liquid crystal. Within such singularities, domains with different alignment meet, and consequently, the perfect order is lost. Moreover, they cannot be removed by a continuous deformation of the material where they are embedded. This is, indeed, why they are called topological. In 2D materials, one can characterize topological defects based on their topological charge, which provides how much the orientation of the composing molecules or particles varies after a full rotation around the considered defect point.
The most common topological defects are the $\pm 1/2$ defects, where the orientation of the molecules rotates ± 180 degrees, and ± 1 defects, where the molecules rotate an entire loop (± 360 degrees) (see Fig. 1.14).

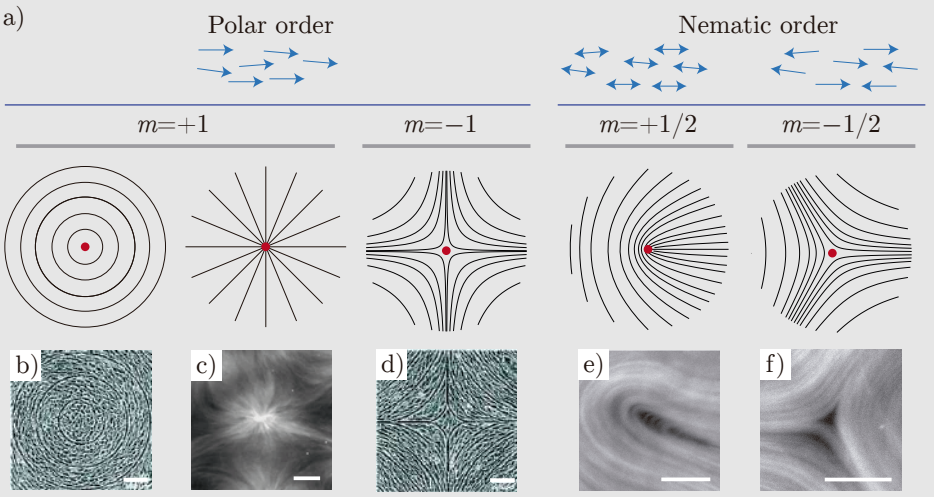

Figure 1.14: Topological defects. **a**) Sketch of topological defects in 2D orderd phases depending on the system symmetry (polar and nematic) and the topological charge (m). **b**–**f**) Experimental micrographs of active systems featuring the topological defects in **a**. **b** and **d** show a monolayer of fibroblasts onto patterns imposing the topological charge. Scale bars: 120 µm. **c**, **e** and **f** are suspensions of microtubules and kinesins. Scale bars: 50 µm. **b** and **d** are adapted from Endresen et al. [73] under Attribution-NonCommercial 3.0 Unported license (CC BY-NC 3.0). **c** is adapted from Nédélec [8] with permission from Springer Nature

Overall, the permanent defects dynamics lead to spatiotemporally chaotic flows with a high visual resemblance to classical turbulence (Fig. 1.16). Due to this similarity, this chaotic state is known as **active** or **mesoscale turbulence**, and it has been the main focus of the here presented thesis. More specifically, the **active turbulence in 2D active nematics**.

1.4.2.1 Modelization of the active nematic

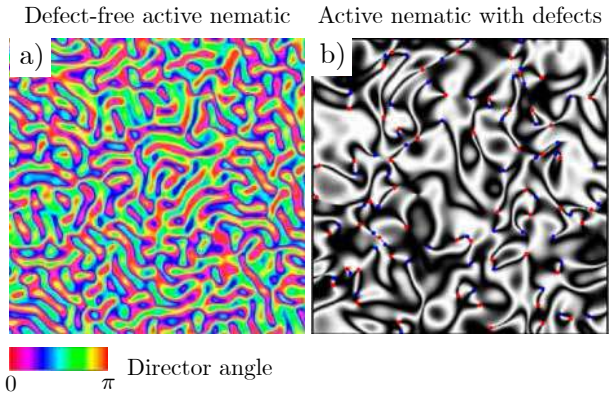

Figure 1.15: Simulations of 2D active nematics. Snapshots of the angle field of a defect-free active nematic (**a**) and of the Schlieren texture constructed from the director field of an active nematic with defects (**b**). The orientational field of the active fluid in **a** has been parameterized with the nematic vector $n = (\cos\theta, \sin\theta)$, whereas the one in **b** has been parameterized with the $\mathbf{Q} = S(\mathbf{nn}^T - \mathbf{I}/2)$ tensor, which allows for defects (marked as red (+1/2 defects) and blue (-1/2 defects) dots). **a** has been adapted from [74] with permission from Springer Nature and **b** has been adapted from [75] under Creative Commons Attribution 3.0 license (CC BY 3.0).

Infobox 1.5: Models of active systems. Dry and wet systems and polar and nematic systems

Active fluids, especially those formed by living units, are of great complexity. Consequently, a very detailed modelization is, nowadays, unattainable. Notwithstanding, many macroscopic properties are shared among some active materials. Therefore, Marchetti et al. [3], in a strive to categorize active materials within a small number of universal groups capturing some essential features, proposed two classifications: one considering the momentum conservation and another considering the broken symmetry of the ordered phase. Regarding momentum conservation, active systems can be classified as *dry* (no momentum conservation) or *wet* (with momentum conservation). As for the average alignment of the constituents, systems with their microscopic objects pointing on average towards the same direction are classified as polar, whereas systems with microscopic objects aligned on average along a preferential axis, but pointing in either direction along this axis, are classified as nematic.

In the case of the MT-based active nematic, it can be regarded as a wet system with nematic symmetry (see Info Box 1.5). Therefore, the modelization of this active system has been mainly based on the generalization of nematohydrodynamics for systems actively driven. Such models coarse-grain the microscopic properties of the material as continuous variables to further predict macroscopic behaviors. In the most simplistic case, one assumes an incompressible one-component phase with constant density. Then, the two regarded variables that enable the description of the active nematic film are the coarse-grained velocity and nematic orientation. For the latter, one can either use a vectorial representation with the $\mathbf{n} = (\cos\theta, \sin\theta)$ director, with θ the local orientation of the molecules (here MTs) restricted within 0 and π and $\mathbf{n} = -\mathbf{n}$, or a tensorial representation with the $\mathbf{Q} = S(\mathbf{nn}^T - \mathbf{I}/2)$ tensor, where S is the scalar order parameter that goes from 0 to 1 and $\mathbf{I}$ is the identity matrix. Notice that the vectorial representation fixes the modulus of each director, and consequently, defects are not taken into account (see Fig. 1.15). The phenomenology of active nematics is then captured by the velocity and orientational field dynamics using partial differential equations. In the case of the velocity dynamics, one can use the Navier-Stokes equation with no inertial terms. For the system here considered, this equation must contain the following ingredients:

- Shear viscosity
- Pressure

- Flow alignment
- The stress due to deformations in the orientational field
- Activity

As for the orientational dynamics, the included ingredients must be:

- Advection by the flow
- Corrotation of the director. This accounts for the response of the elongated MTs to gradients in the flow.
- Rotational viscosity arising from the relaxational dynamics of the orientational field that tends to push the system towards the minimum of free energy.

1.5 Inertial and active turbulence

As explained earlier, active turbulence is a state characterized by chaotic flows constantly mixing and arising from the self-organization of an active system's constituents. Despite the visual likeness of this state with classical (or inertial) turbulence (Fig. 1.16), fundamental differences might lead to the establishment of new classes of turbulence.

Since inertial turbulence is an already well-established concept, we will first introduce its principal properties to later comment on the main similarities and differences between inertial and active turbulence and raise some still open questions.

1.5.1 Inertial turbulence

Inertial turbulence in a fluid emanates from an external forcing at high Re. In general, at the injection scales, there is no dissipation mechanism. Consequently, energy is transferred from these scales to other scales where it can be dissipated and, thus, prevent infinite energy accumulation. In the case of 3D turbulence, kinetic energy uniquely cascades from the largest to the smallest scales, where viscosity can dissipate energy. Richardson proposed that this energy transfer results from hierarchical instabilities, where large eddies break up into smaller ones, which break again into even smaller eddies, and so on, until viscous stresses can dissipate the kinetic energy [77, 78, 79]. Put in his own words:

"Big whirls have little whirls that feed on their velocity,
and little whirls have lesser whirls and so on to viscosity."

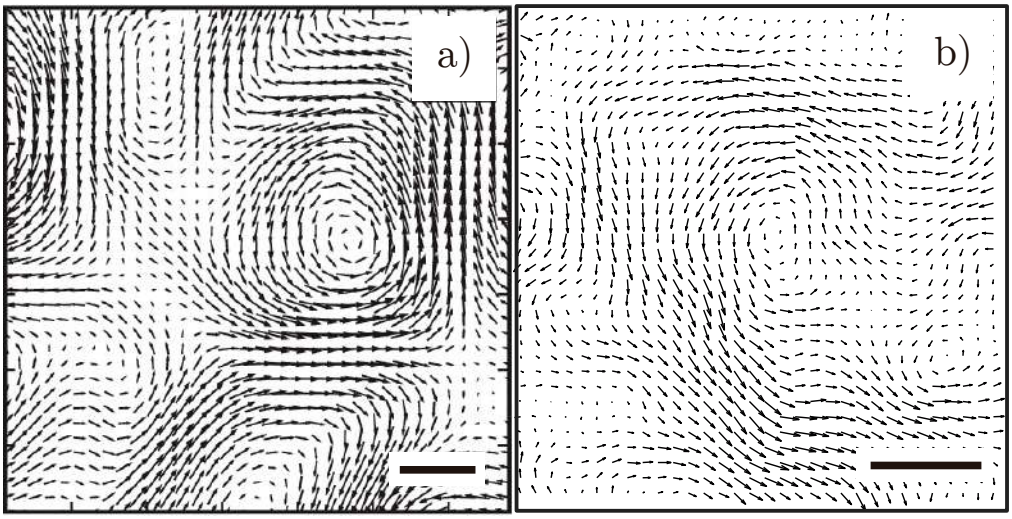

Figure 1.16: Inertial vs active turbulent flows. Experimental flow fields of an inertial turbulent 2D soap film (**a**) and of the 2D MT-based active nematic featuring active turbulence (**b**). **a** has been adapted form Rivera et al. [76] with permission from AIP Publishing. Scale bars: 0.1 cm (**a**) and 50 µm (**b**)

Interestingly, as Kolmogorov postulated in 1941, the energy cascade promotes the loss of any possible anisotropy coming from the injection source. In other words, the information regarding the large eddies' geometry is lost as the energy cascades down to smaller scales. Thus, for well-separated injection and dissipation lengths, fluctuations at intermediate scales are statistically isotropic and do not depend on the forcing mechanism [77]. This gives rise to universal exponents in the kinetic energy spectrum as a function of the wave number q, $E(q) \sim q^{-5/3}$. Here, universal exponents mean that they do not depend on the fluid's nature or the forcing mechanism. The implication of this result is enormous because, even though the hallmark of turbulence is the presence of chaotic flows, the existence of universal exponents stresses that there is something predictable in something seemingly unpredictable (turbulence). Further research in this regard has shown that some deviations from universality are possible and they arise from what is known as intermittency, a phenomenon linked to strong and abrupt fluctuations in the flow [78, 79]. Nevertheless, the effects are minimal. Therefore, the results by Kolmogorov are still of great significance and constitute a paradigm of inertial turbulence [78]. As a curiosity, Kolmogorov's theory has even been applied to analyze the degree of realism of some Van Gogh's paintings, mainly the *Starry Night* [80], which clearly captures

Figure 1.17: Turbulence in Vincent van Gogh's *Starry Night*. This painting from 1889 includes eddies of very different sizes, evoking to real turbulence. Public domain, via Wikimedia Commons

turbulence (see Fig. 1.17).

The cascades in fully developed turbulence are ultimately due to inertial forces. However, the exact mechanism driving the energy cascade is still under debate. Many mechanisms have been proposed [81, 82, 83], yet the most accepted one is vortex stretching. Notice that this mechanism is absent in 2D turbulent flows because vortex stretching entails the third dimension. Indeed, in 2D turbulence, studies claim the existence of two cascades: a direct enstrophy cascade and an inverse energy cascade [79, 84, 85, 86]. This means that energy and enstrophy are injected by external forcing at a given intermediate scale. Then kinetic energy is transferred to larger scales until it is eventually dissipated by friction, while enstrophy is transferred to smaller scales until its dissipation by viscous stresses Fig. 1.18. These two inertial ranges endowed with cascades present universal scaling regimes in their kinetic energy spectrum. Kraichnan, back in 1967, was the first one to predict such scaling laws. By assuming that the energy and enstrophy spectra depend on the energy and enstrophy dissipation rate, respectively, plus the wave number q, he could use dimensional analysis to demonstrate that the energy spectrum scales as $E(q) \sim q^{-5/3}$ in the inertial energy range and $E(q) \sim q^{-3}$ in the enstrophy inertial range [87].

1.5.2 Active turbulence

Once we have introduced the main properties of turbulence at high Reynolds numbers, we are ready to dive inside active turbulence and its essential distinctions from its inertial counterpart.

The first observation of spontaneous chaotic flows in an active system we

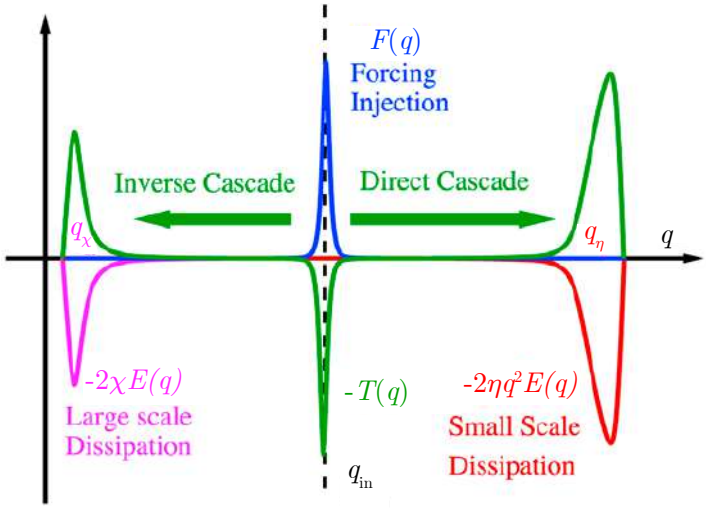

Figure 1.18: Qualitative sketch of the stationary scale-by-scale energy balance of inertial turbulence. In the presence of energy cascades, the energy balance has an injection term, $F(q)$, peaked around the forcing length q_{in}, and two well separated peaks at q_χ and q_η, where energy is dissipated through friction ($-2\chi E(q)$ term) and viscous damping ($-2\eta q^2 E(q)$ term), respectively. Then, energy balance satisfies $T(q) = F(q) - 2\chi E(q) - 2\eta q^2 E(q)$. Here, the three peaks are well separated $q_\chi \ll q_{\text{in}} \ll q_\eta$ and should integrate to 0. Image adapted from Alexakis et al. [79] with permission from Elseiver.

encounter within the literature is the bacterial suspension reported by Dombrowski et al. [88]. These chaotic flows were then termed *bacterial turbulence*. This chaotic state was later demonstrated in many other living and artificial systems, prompting its rename to **active turbulence** [89]. Active turbulence has then been observed in very disparate systems, such as monolayers of epithelial cells [19, 90], suspensions of filamentous proteins and molecular motors [17, 91, 92], and swarming sperm [18] (Fig. 1.19). All these examples are at low Reynolds numbers, where inertia is negligible. This is the first main difference between active and inertial turbulence.

The second distinction between active and inertial turbulence is that, in the former, the scale of energy input is imposed by the external driving mechanism. Conversely, in active turbulence, the energy is injected by the constituents, and the input scale ultimately depends on the self-organization of the active units. In other words, the injection scale is set by the typical distance of correlated motion. Without this self-organization phenomenon, the appearance of spatiotemporal chaos would be precluded by viscous damping: a single swimming bacteria does not trigger turbulent flows but produces laminar flows characterized by the smooth sliding of fluid layers with no mixing [23].

Both types of turbulence occur as multiscale phenomena, with vortices spanning a vast range of length scales. Nevertheless, active turbulent flows, albeit their chaotic behavior, are endowed with a characteristic length, which organizes the flow pattern. Such length is generally much larger than the size of one active unit and is set by the balance between elastic and active forces. In the case of active turbulence in 2D active nematics, the signature of such length appears as an exponential distribution of vortex areas. Such geometrical structure of the flow was first predicted by Giomi's in-silico study [75]. Experiments with cytoskeletal reconstitutions [92, 93] and epithelial cell monolayers [19] later verified this remarkable result. In contrast, in inertial turbulence, the distribution of vortex areas is self-similar and thus follows a power law [94].

There is still an ongoing debate regarding the presence of universal exponents in the kinetic energy spectrum of active turbulence. In fact, before going any further, we should emphasize that, oppositely to inertial turbulent flows, which can be properly described with the Navier-Stokes equation, active turbulence does not hold a unique fundamental equation. For example, equations describing systems with polar symmetry differ from those modeling systems with nematic symmetry. This emphasizes the disparate physics governing active systems. The first experimental study fully dedicated to this matter was done by Wensink et al. [16], who measured the flows of dense bacterial 3D and quasi-2D suspensions (B. subtilis). In particular, they showed that the kinetic energy spectrum of the chaotic flows in the 2D geometry exhibits regimes with power laws: $q^{-8/3}$ (small-q) and $q^{+5/3}$ (large-q) separated by the bacterial injection scale. The authors

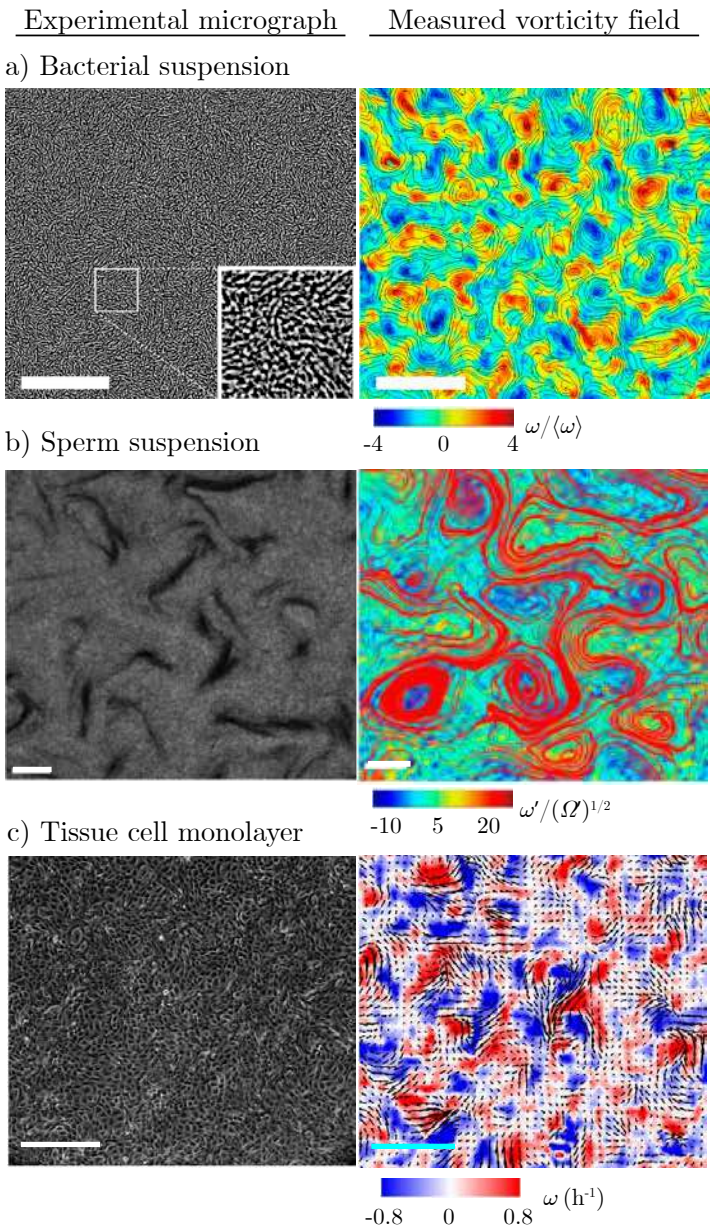

Figure 1.19: Examples of experiments on active turbulence. Each panel shows the experimental image (left) and the measured vorticity field (ω). **a** and **b** are quasi-2D systems and **c** is a 2D system. Scale bars are: 50 µm (**a**), 200 µm (**b**) and 300 µm (**b**). **a** is adapted from [16] through the PNAS open access option. **b** is adapted from [18] with permission from the American Physical Society. **c** is adapted from [90] under Creative Commons Attribution 4.0 International license (CC BY 4.0).

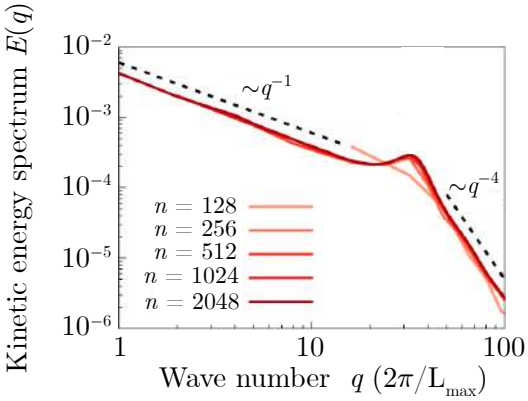

Figure 1.20: Kientic energy spectrum of an active nematic film. Simulations have shown that the kinetic energy spectrum of an isolated 2D active nematic has to scaling regimes with exponents: q^{-1} for small-q (large scales) and q^{-4} for large-q (small scales). Image adapted from Alert et al. [74] with permission from Springer Nature.

also perform particle simulations and formulate a minimal continuum theory that agree with the experimentally measured scaling regimes. Nevertheless, the universality of such exponents is not discussed there.

Some years later, Bratanov et al. [95], inspired by the model of Wensink et al. [16], claimed that the energy spectra of 2D active fluids feature power laws at large scales with non-universal exponents that depend on both finite-size effects and physical parameters. However, the models used in these two studies [16, 95] are extensions of Toner-Tu equations that include the terms admitted by the problem's symmetry. Such models are usually considered as dry. In contrast, some recent theoretical works on active nematics have claimed the existence of scaling laws with universal exponents independent of the active fluid properties [74, 75]. Interestingly, these two studies arrived at identical results using two different approaches (also see Fig. 1.20). For now, we will not get into much detail because we will discuss this issue in Chapter 3. In that chapter, we show the experimental results, already published in [96], regarding the presence of scaling regimes in the kinetic energy of the interfaced MT-based active nematic.

Finally, some studies have addressed the existence of energy cascades in active turbulent flows [74, 97, 98, 99]. In the case of active nematics, the most consensual conclusion, according to simulations, is that there are no energy cascades [74, 97, 98]. However, this result still lacks experimental evidence, which we aim to provide. In Chapter 4, we present preliminary experimental results obtained by means of simultaneous measurements of the velocity and orientational fields of the MT-based active nematic.

1.6 Objectives

As anticipated in the introduction, the main objective of this thesis is to contribute to the current understanding of active turbulence through experiments. More precisely, in this thesis, with this principal aim, we use the MT-based active nematic presented in Section 1.4.2 to cover and try to address the following sub-objectives divided by the different chapters:

Chapter 2

2.1) Observe and characterize the primary bend instability in extensile active nematics that finally leads to active turbulence.

2.2) Ascertain and decipher the dependence of the characteristic time and length scales of the instability with different material parameters.

2.3) Test the suitability of a linear stability analysis of aligned MT-bundles leading to active turbulence.

Chapter 3

3.1) Measure the kinetic energy spectrum and related statistical properties of active nematic turbulence.

3.2) Evaluate the emergence of scaling regimes in the kinetic energy spectrum of active nematic turbulence.

Chapter 4

4.1) Measure the free energy balance of a turbulent active nematic

4.2) Assess the presence of energy cascades between scales in active nematic turbulence.

Chapter 5

5.1) Develop techniques to simultaneously measure the director and the velocity field of the active nematic.

Chapter 2

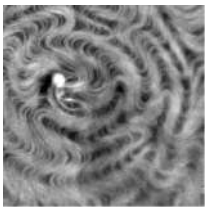

The bend instability: a route to active turbulence

2.1 Introduction

Active turbulence is characterized by chaotic flows visually reminiscent of those observed in inertial turbulence [16, 18, 19, 74, 95]. Nonetheless, these two states present a fundamental difference: unlike inertial turbulence, active turbulence is endowed with a characteristic length, typically referred to as active length. This length is defined as the ratio between the material's elastic constant and the activity coefficient and sets the mean distance between defects within the active fluid. The origin of such length is thought to be re-orientational instabilities continuously evolving in the aligned domains within the active system. This is because homogeneously oriented active nematics with extensile (contractile) stresses are prone to destabilize, leading to bend (splay) long-range distortions [100, 101, 102, 103]. In this chapter, I review our experimental results published in [1], where we show this instability at its onset and demonstrate that the length scale present at the fully developed turbulence is selected at the beginning of the instability. Furthermore, we rationalize the wavelength selection mechanism as a result of the activity amplifying any orientational fluctuation and the elasticity and the hydrodynamic coupling to the adjacent viscous fluids stabilizing short and long wavelength modes, respectively. Here, I should emphasize that such instability, albeit known for years, had never been observed at its early-stage development for an unconfined active nematic. The closest study devoted to characterizing this instability was published by Duclos et al.

[104], who used spindle-shaped cells confined within stripes spontaneously developing shear flows. Nevertheless, these flows depended on the width of the confining; thus, they were not enforced by a genuine wavelength selection mechanism. Therefore, our findings represented the first experimental evidence of such instability from an unconstrained radially aligned active nematic.

Since then, there have been other studies regarding orientational instabilities of active flows. A noteworthy example is a work by Senoussi et al.[13], who showed that a 2D free-standing nematic active sheet spontaneously buckles out of plane, creating a corrugated pattern. Notice that this buckling in the third dimension is possible because the active film is not constrained by the two interfacing oil and water layers as in our system. Indeed, at high activity, the active fluid develops turbulent after the instability, forming a 3D percolating active network. Later, two similar studies, one by Sarfati et al. [105] and another by Najma et al. [106], demonstrated that it is possible to select the type of orientational instability in an initially nematic-aligned 3D active gel by changing the composition of the material. At low activity, the active fluid undergoes an out-of-plane buckling instability like the one in [13], whereas, at higher activity, the instability leading to chaotic flows becomes an in-plane bend instability, similar to the one observed in our experiments [1] and shown below.

2.2 Results

2.2.1 The onset of active turbulence. A Pattern forming instability

As described in [1] and in Methods Section 6.2, we impose a radial alignment of the active nematic layer by placing a capillary right at the oil/water interface. Capillary forces induce an inward flow into the tube that aligns the nematic material with the bundles oriented toward the cylinder. We immediately withdraw the capillary and let the active material evolve freely. This radial disposition (see Fig. 2.1a) is instantly destabilized and broken by the spontaneous buckling of the MT-bundles. Bend fluctuations, reinforced by the active stresses, rapidly grow, forming concentrical equispaced kinks, also known as walls [72, 102], separating nematic domains Fig. 2.1b. Elastic stresses accumulated at the walls, where the bend deformation is the strongest, are then lessened by the nucleation of $\pm 1/2$ defects, which momentously move along the kinks producing dark circular lanes (see Fig. 2.1c). This striated pattern is shortly dismantled by the movement of $+1/2$ defects, which, being strong sources of vorticity [102, 107], can deviate and break the symmetry of the disposition (see Fig. 2.1d). The system finally reaches the characteristic turbulent regime.

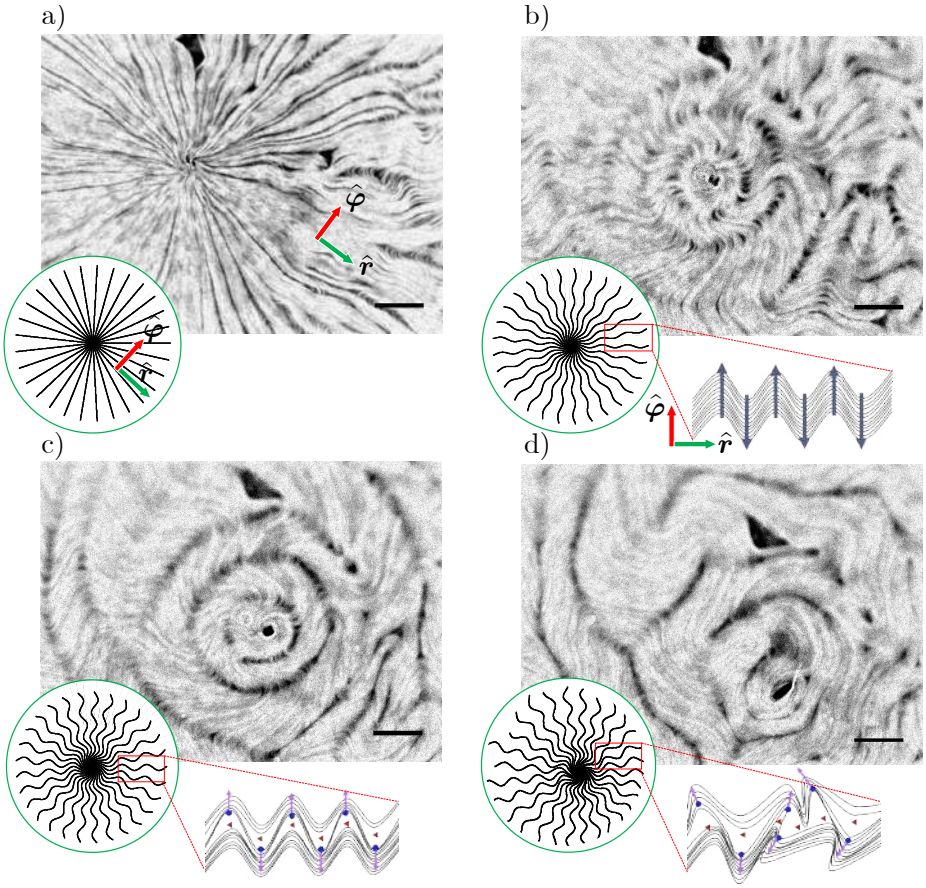

Figure 2.1: The onset of active turbulence. a-d) Fluorescence microscopy images displaying the spontaneous evolution of a radially aligned active nematic towards the turbulent regime. The insets include diagrams illustrating the disposition of the microtubule bundles. Elapsed times from **a** are 13 s (**b**), 26 s (**c**) and 47 s (**d**). **a)** Radially aligned active nematic. This geometry is obtained after the introduction and the subsequent removal of the capillary tube at the oil/water interface. The polar coordinate variables are sketched on the image and in the diagram. **b)** Onset of the bend instability. Blue arrows indicate the active stresses that reinforce the buckling deformation and lead to the formation of kinks. **c)** Nucleation of $\pm 1/2$ defect pairs within the kinks, leading to a degradation of the orientational order. In the diagram, -1/2 defects are shown by red triangles and $+1/2$ by blue circles. Because of their geometry, $+1/2$ defects can self-propel and travel transiently along the walls. Their trajectories are indicated with pink arrows. **d)** Eventually, $+1/2$ defects alter their trajectories and finally break the patterned structure. Scale bars, 100 µm. Experimental conditions are [ATP] = 280 μM, [streptavidin] = 8.2 µg/mL, [MT] = 1.3 mg/mL, [PEG]=1.7 %(wt/wt), and Oil viscosity= $9.6 \cdot 10^{-2}$ Pa·s. See also Video 2.1.

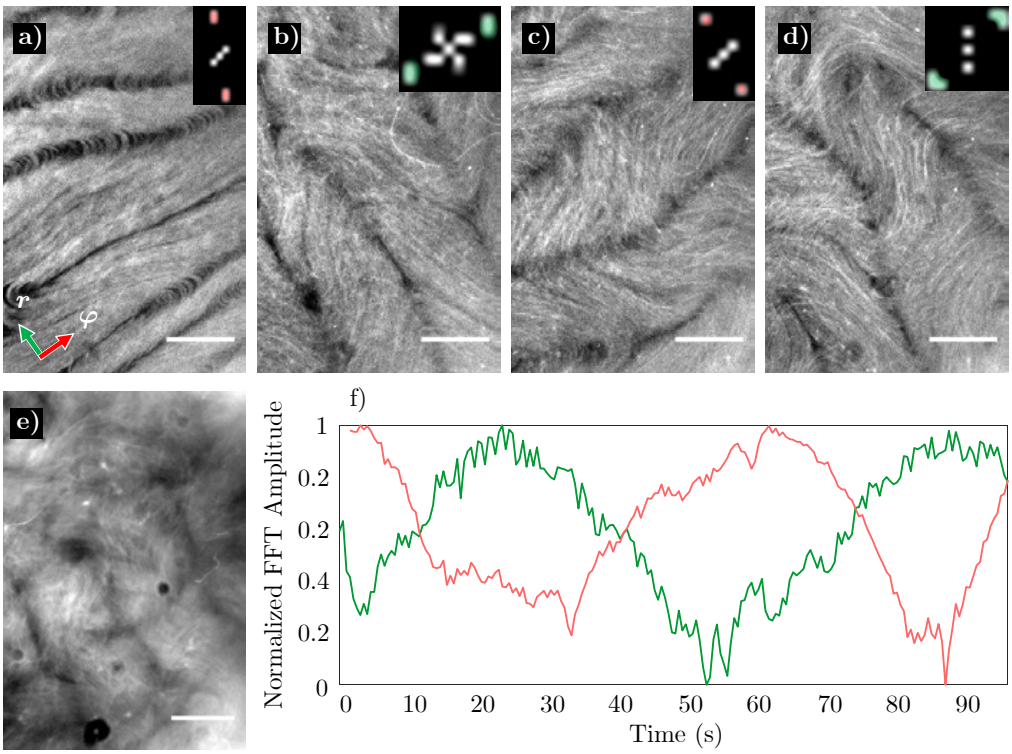

Figure 2.2: Cascade of instabilities. **a-f** Fluorescence micrographs showing the patterns formed after consecutive instabilities happening in orthogonal directions (along the radial, $\hat{\boldsymbol{r}}$, and azimuthal, $\hat{\boldsymbol{\varphi}}$ directions sketched in **a**. Elapsed times from **a** are 22 s (**b**), 63 s (**c**) and 92 s (**d**). The amplitude of the 2D Fast Fourier Transform (FFT) is included as an inset in each image. For clarity, we have highlighted in the FFTs the peaks corresponding to every pattern emerging in the azimuthal and radial directions, in red and green, respectively. **e**) Time average of all the micrographs in **a-d**, evidencing the orthogonal arrangement of the dark lanes in the fluorescence micrographs. **f**) Normalized FFT amplitude in the peaks corresponding to patterns formed along the radial direction (green trace) and along the azimuthal direction (red trace). Scale bars: 100 µm. Experimental conditions are [ATP]=1.5 mM, [streptavidin]=7.5 µg/mL, [MTs]=1.3 mg/mL, [PEG]=1.7 %(wt/wt), and Oil viscosity= $9.6 \cdot 10^{-2}$ Pa·s. Image adapted from [1] with permission from Springer Nature. See also Video 2.2

2.2.2 Instability cascade

The pattern with the dark circular lanes is not stable, as mentioned earlier. In general, this geometry is melted by the +1/2 defect motion, yet, at low activity conditions, a cascade of bend instabilities orthogonal to each other befall (see Figs. 2.2a to 2.2d). The order of the active nematic keeps decreasing after each instability until the material reaches the characteristic turbulent regime. This instability sequence develops as a consequence of the defect motion that aligns the MT fibers tangentially to the lanes. These aligned domains become unstable and the bend instability originates again, but with the bundles buckling in the orthogonal direction. New defects unbundle anew, prompting another instability all over again. The superposition of fluorescence images of subsequent instabilities produces a square grid highlighting the constant instability wavelength (sse Fig. 2.2e). Moreover, we measure the radial, and azimuthal modes of the Fourier transform FFT of the fluorescence images, which evidence the alternation between these two directions (see Fig. 2.2f). This observation stresses that defects originate due to regions with aligned bundles inside the system that become unstable and form walls that will later result in defects. The newly created +1/2 defects will then self-propel and produce new aligned areas prompt to destabilize back again. Aligned regions can as well arise from the annihilation of +1/2 with −1/2 defects. Hence, the persistent creation and annihilation of defects lead to and sustain the active turbulent regime.

2.2.3 Quantitative characterization of the bend instability

We quantitatively describe the instability in terms of the characteristic wave number $q^* = 2\pi/\ell^*$ and growth rate Ω^*, both corresponding to the leading distortion mode. Briefly, we first determine q^* by performing an FFT of the intensity profile along a direction orthogonal to the kinks (see Methods Section 6.4.4.1) and, afterward, track the temporal evolution of the FFT amplitude of the known q^*. At the first stages of the instability, the FFT amplitude follows an exponential trend; thus, we exploit such trend to extract Ω^* (see Fig. 2.3). Remarkably, this exponential growth is consistent with a linear selection mechanism. Here, we should remark that in [1], we use k instead of q to refer to wave numbers. The relation between these two quantities is $q = 2\pi k$. This notation has been chosen for consistency with the other chapters.

Then we study the influence of four control parameters: ATP, motor clusters, MTs, and PEG on the quantitative properties of the AN's orientational instability. First, we analyze how ATP affects the pattern-forming instability. Our results (Fig. 2.4) show that as we increase the ATP concentration, the instability begets and grows faster (Ω^* increases) and q^* gets larger. Moreover, at ATP concentrations lower than ~ 400 µM, q^* saturates due to system size limi-

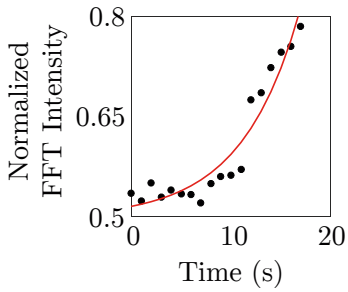

Figure 2.3: Long-range fluctuations grow exponentially at initial times. The time evolution of the FFT amplitude at the wave number q^* grows exponentially at early times, this allows to extract the characteristic growth rate Ω^*. This temporal evolution is extracted as explained in Methods Section 6.4.4.2.

tations. Within this latter regime, the system cannot be considered unbounded and the selection mechanism becomes system-size dependent, similarly to what happens in confined cellular nematics [104].

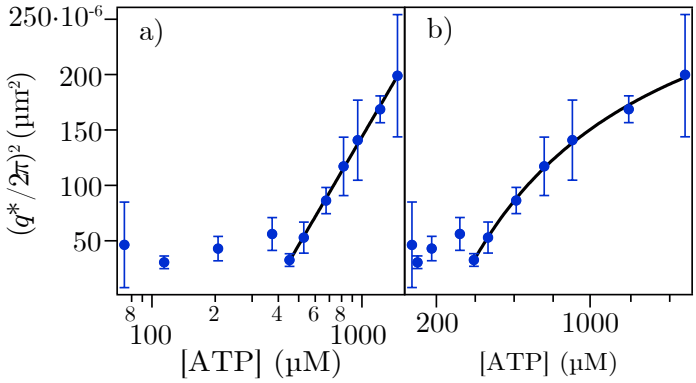

Figure 2.4: Dependence of the characteristic wave number q^* on ATP concentration ([ATP]) The experimental characteristic wave number $q^* = 2\pi/\ell^*$, upon a threshold, grows with the [ATP]. Both assumptions that q^{*2} scales as $q^{*2} \sim \log[\text{ATP}]$ (fitting in **a**), and Michaelis-Menten kinetics (Eq. 2.1) (fitting in **b**) are plausible. The fitting to **b** gives $q^{*2}_{\max} = (3.5 \pm 0.2) \cdot 10^{-4}$ μm^2, $K_M = 959 \pm 11$ μM, and $[\text{ATP}]_{\text{thr}} = 274 \pm 12$ μM.

ATP concentration essentially affects the parameter controlling the active stresses, α. Nevertheless, their relationship is still under debate. Thermodynamic approaches suggest that the magnitude of the active stress scales as the logarithm of ATP concentration: $\alpha \sim \log[\text{ATP}]$. This relation arises from considering that the velocity of a kinesin is proportional to the ATP/ADP hydrol-

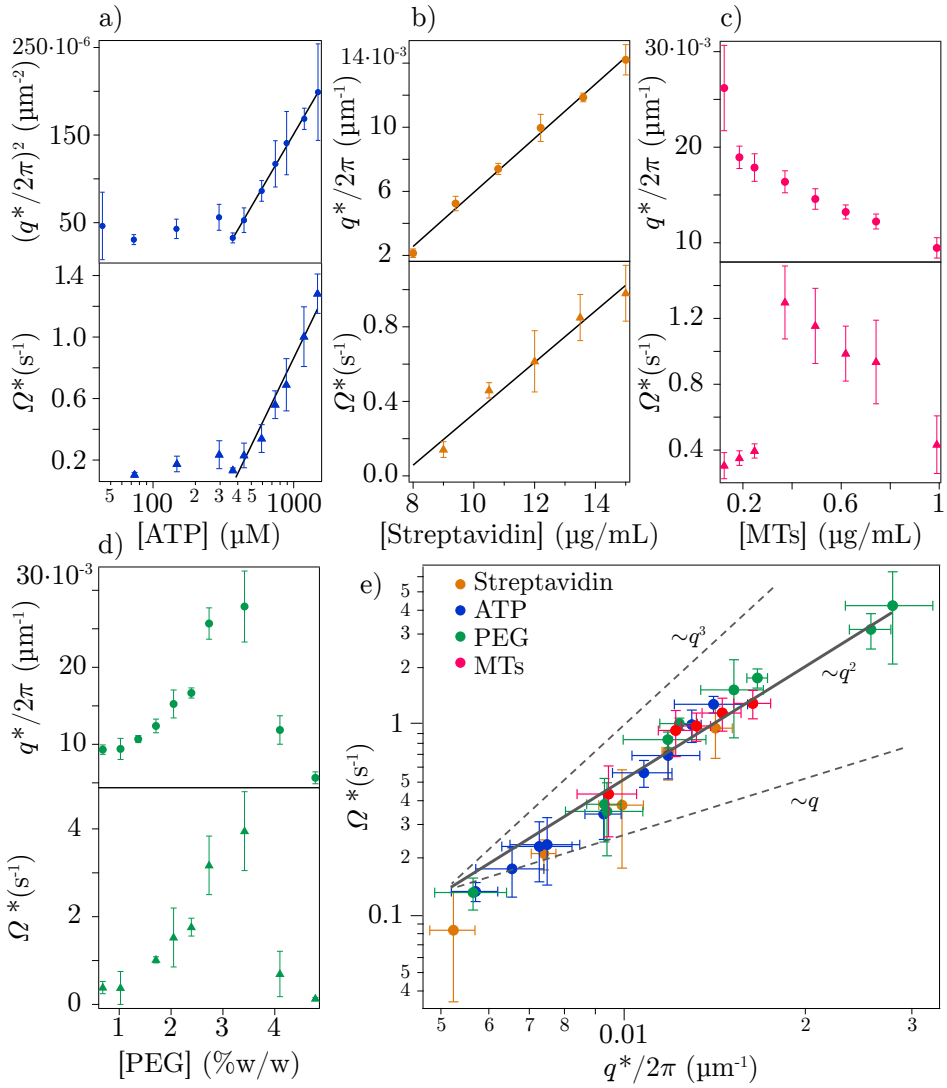

Figure 2.5: Dependence of the characteristic wave number q^* and growth rate Ω^* and scaling $\Omega^*(q^*)$ a-d) Experimental scaling relations of the characteristic wave number $q^* = 2\pi/\ell^*$ and growth rate Ω^* of the instability of aligned active nematics, as a function of the different control concentrations. In **a** and **b**, solid lines are guides for the eye in regions where $q^* \sim \log[ATP]$. **b**) Ω^* versus q^* for all experiments. Data collapse in a single master curve that can be fitted well by $\Omega^* \propto q^{*2}$ (solid line). For comparison, other power-law relations are included as dashed lines. Error bars in q^* represent standard deviation for measurements of different images. Error bars in Ω^* represent uncertainties from data fitting (see Methods Section 6.4.4). Image adapted from [1] with permission from Springer Nature.

ysis rate, which is, in turn, proportional to the difference between ATP and ADP and phosphate (P_i) chemical potentials, $\Delta\mu = \mu_{ATP} - \mu_{ADP} - \mu_{P_i} \approx RT\log([ATP]/[ADP]) \approx RT\log[ATP]$, where R is the ideal-gas constant, and T is the temperature of the system. In fact, within the active gel theory framework, the activity coefficient is proposed to be $\alpha = \zeta\Delta\mu$ [100, 108], with ζ a coefficient characterizing the proportionality between α and $\Delta\mu$. This assumption has been revealed to work well for diverse experiments and simulations in active nematics [91, 92, 109]. In our experiments, we measure q^*, which we expect to scale with the active length ℓ_a as $q^* \sim \ell_a^{-1}$, a quantity that depends on the ratio between the elastic constant, K, and α: $\ell_a \sim \sqrt{K/\alpha}$[1]. Hence, $(q^*)^2 \sim \alpha \sim \log[ATP]$. We observe that, past a threshold [ATP], our data is fully compatible with the prediction that $(q^*)^2$ grows as log[ATP] (see Fig. 2.4a). In contrast, other experiments with single MTs driven by kinesins attached to either a glass slide or silica beads [110] have proven a Michaelis-Menten dependence of the gliding or bead velocity with the ATP concentration. This trend seems to be also applicable to experiments involving highly concentrated MTs systems forming an active nematic [93, 111]. Accordingly, we have also fitted our data to Michaelis-Menten kinetics (see Info Box 2.1, Eq. 2.9, and Fig. 2.4b). We need to add an extra fitting parameter $[ATP]_{thr}$ that accounts for the threshold ATP concentration upon which we see a dependence between q^* and the fuel content:

$$q^{*2} = \frac{q^{*2}_{max}([ATP] - [ATP]_{thr})}{K_M + ([ATP] - [ATP]_{thr})} \tag{2.1}$$

Infobox 2.1: Michaelis-Menten kinetics

Michaelis-Menten relates the velocity of an enzimatic reaction with the concentration of the reacting substrate [50] and is applicable to reactions of the form

$$S + E \underset{k_{-1}}{\overset{k_1}{\rightleftharpoons}} ES \xrightarrow{k_2} P + E,$$

where S is the substrate, E the enzyme, ES the enzyme-substrate complex, and P the product. Note that in the evolution of ES to P, there is a single arrow, indicating that this reaction is assumed to be irreversible. For a reversible reaction, this assumption will work as far as the concentration

[1] α is taken throughout the whole text as positive for extensile systems.

of P is low. In this way, the velocity of product formation is given by:

$$\frac{\mathrm{d}^{\mathrm{P}}}{\mathrm{d}t} = k_2[\mathrm{ES}]. \tag{2.2}$$

Another approximation made to derive the Michaelis-Menten equation is supposing that the system reaches an steady state where the concentration of ES remains constant until nearly all the substrate molecules have reacted. This is as considering that [S]≫[E]. Therefore,

$$\frac{\mathrm{d}^{\mathrm{ES}}}{\mathrm{d}t} = -(k_2 + k_{-1})[\mathrm{ES}] + k_1[\mathrm{S}][\mathrm{E}] = 0. \tag{2.3}$$

Rearranging this last equation

$$\frac{[\mathrm{S}][\mathrm{E}]}{[\mathrm{ES}]} = \frac{k_2 + k_{-1}}{k_1} = K_M, \tag{2.4}$$

we can define the Michaelis constant, K_M. Since the enzyme is not converted during the chemical process, it only catalyzes the reaction, we can write:

$$[\mathrm{E}]_{\mathrm{T}} = [\mathrm{E}]+[\mathrm{ES}], \tag{2.5}$$

where $[\mathrm{E}]_{\mathrm{T}}$ is the total concentration of enzyme. Combining Eq. 2.4 with Eq. 2.5

$$[\mathrm{ES}] = \frac{[\mathrm{E}]_{\mathrm{T}}[\mathrm{S}]}{K_M + [\mathrm{S}]}, \tag{2.6}$$

Introducing this last equation to Eq. 2.2

$$\frac{\mathrm{d}^{\mathrm{P}}}{\mathrm{d}t} = k_2\frac{[\mathrm{E}]_{\mathrm{T}}[\mathrm{S}]}{K_M + [\mathrm{S}]} \tag{2.7}$$

Finally, we can define a maximum velocity

$$V_{\max} = k_2[\mathrm{E}]_{\mathrm{T}} \tag{2.8}$$

that will correspond to a situation where $[S]$ is very high and all the enzymes are in the form of ES. In this way, Eq. 2.7 takes the form of

$$\frac{\mathrm{d}^{\mathrm{P}}}{\mathrm{d}t} = \frac{V_{\max}[\mathrm{S}]}{K_M + [\mathrm{S}]}, \tag{2.9}$$

which is the Michaelis-Menten relation. Notice that the asymptotic value of $V_{\max}$ in Eq. 2.9 is translated as $q^2_{\max}$ in Eq. 2.1.

Next, we scrutinize the impact of the molecular motors concentration on the bend instability (Fig. 2.5b). We find a linear dependence of both q^* and Ω^* with the concentration of motor units. In this respect, we can refer to an earlier study [112] regarding the velocity of the active MT-based material, which suggests that this velocity scales linearly with the motor concentration in the used concentration range. Moreover, a relation $v \propto \alpha^{1/2}$ has been predicted theoretically [75, 108] and confirmed experimentally [13, 91]. Consequently, the increase of q^* and Ω^* with motor concentration (see Fig. 2.5b) is entirely consistent.

As for the content of MTs, we observe a decrease in q^* and Ω^* past a range of minimal MT concentration (Fig. 2.5c). We interpret this behavior by assuming that the densification of the active nematic by increasing the MT concentration stiffens the system (larger K), making q^* and Ω^* decrease.

Finally, the variation of the depleting agent PEG highlights a non-monotonous behavior (Fig. 2.5d). At low concentrations, increasing [PEG] conduces to the destabilization of smaller wavelengths, whereas at higher concentrations, increasing the [PEG] translates into a stiffer material unable to accommodate distortions even with wavelength comparable to the system size. As we understand it, the depleting agent makes the system more efficient at low concentrations by optimizing motor translocation, thus resulting in an enhanced effective α. At high PEG concentrations, our results highlight that, beyond a threshold, PEG has a similar effect to the one observed for the case of increasing MT concentration. The decrease in q^* and Ω^* with PEG concentration can be understood by either considering an increase in K or a decrease in α due to an increase in interfilament friction at high PEG concentration [113].

2.3 Discussion

2.3.1 Selection mechanism. Linear stability analysis

To elucidate the wavelength selection mechanism, we draw on the active gel theory [100, 114, 115] (see also Appendix A.1) and perform a linear stability analysis of a parallelly aligned isolated active nematic (see Appendix A.2). We find that, for such a system with extensile stresses like our AN, longitudinal perturbations grow with a growth rate Ω given by (see Eq. A.22 in Appendix A):

$$\Omega = -\frac{Kq_y^2}{\gamma}\left(1 + \frac{\gamma}{4\eta}(\nu - 1)^2\right) + \frac{\alpha(1-\nu)}{2\eta}, \tag{2.10}$$

where K is the elastic constant in the one constant approximation, γ is the rotational viscosity, η the shear viscosity, ν the flow alignment parameter, and α the activity coefficient. Therefore, fluctuations perpendicular to the direction

of initial alignment are unstable if $\nu < 1$, corresponding to rod-like and flow aligning objects [101], like MTs.

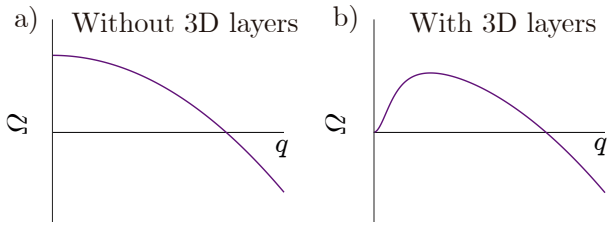

Figure 2.6: Schematics of the dispersion relation with and without the 3D fluid layers. (**a**) is computed with Eq. 2.10 and (**b**) with Eq. 2.11

According to Eq. 2.10, active stresses equally strengthen fluctuations at all scales, whereas the elastic restoring stresses stabilize large wave number fluctuations because of their high elastic cost. As a result, the most unstable wavenumber is $q^* = 0$ (Fig. 2.6a), meaning that the linear regime of the instability does not entail any intrinsic wavelength selection. For a confined system, however, the confinement forces the discretization of the growth rate spectrum, selecting a finite scale that accommodates the adequate boundary conditions. However, a radial alignment would not provide a wavelength selection mechanism in an unconfined system (see Appendix A.3). Therefore, the only left mechanism by which the wavelength can be selected at a linear level is through the viscous coupling of the active fluid layer with the two surrounding passive fluids with shear viscosities η_{oil} and η_{water} (see Appendix A.4). The selection is a result of a viscous damping by the oil and water layers that screen long-range hydrodynamic interactions and thus hampers the long-wavelength fluctuations [116, 117]. Thus, we can consider explicitly the effect of the contacting fluids in the dispersion relation by redoing the linear stability analysis in this latter case. In Appendix A.4, we analytically obtain the following relation dispersion for a parallel alignment (see Eq. A.56):

$$\Omega = -\frac{K}{\gamma} q_y^2 \left(1 + \frac{1}{4}\frac{\gamma(\nu-1)^2 q_y^2}{\Gamma}\right) + \frac{1}{2}\frac{\alpha(1-\nu)q_y^2}{\Gamma}. \tag{2.11}$$

with

$$\Gamma = \eta q_y^2 + \eta_{\text{water}}\, q_y \coth(q_y H_{\text{water}}) + \eta_{\text{oil}}\, q_y \tanh(q_y H_{\text{water}}), \tag{2.12}$$

which does have a maximum at $q \neq 0$ (Fig. 2.6b). We assume this relation to be also valid for the radial case. We later discuss the role of the axial symmetry.

2.3.2 Comparison between theory and experiments

Scrutinizing Eq. 2.11, we can see that the first term is always positive; hence, it damps any perturbation around the ordered state. In contrast, the second term can be either positive or negative depending on the value of ν and, consequently, it controls the stability of small wave number perturbations. Therefore, α enhances any perturbation, whereas K hinder them. To gain insight into the wavelength selection, we compute the dispersion relation $\Omega(q)$ for different values of α. To select the range of values for α, we use the relation $\omega_{\mathrm{v}} \sim \alpha/\nu$, where ω_v is the mean vorticity inside vortices [75]. We use $\eta = 4 \cdot 10^{-6}$ Pa·s·m from [96] and $\omega_v = 0.2$ s^{-1} obtained from the detection of vortices. In this way, $\alpha \approx 9 \cdot 10^{-7}$ Pa·m, corresponding to saturating conditions of ATP and a fixed oil viscosity $\eta_{\mathrm{oil}} = 1 \cdot 10^{-1}$ Pa·s. The final range of investigated α values are chosen according to the range of variation of q^*. Our guess for α is of the same order of magnitude as the one estimated by Ellis et al. [118], who inferred α from the velocity of defects of the AN confined in a torus. Note that, in their article, they give a 3D active coefficient ($\alpha_{3D} \approx 250$ mPa) that we can rescale by the thickness of the AN layer ~ 1 µm and get $\alpha \approx 2.5 \cdot 10^{-7}$ Pa·m. Finally, we neglect flow alignment ($\nu = 0$), set $\gamma \approx \eta$, and get an estimate of $K \approx 1 \cdot 10^{-15}$ N·m from $\ell_a \approx R_* \approx \sqrt{K/\alpha}$ where $R_* = 3 \cdot 10^{-5}$ m, is the mean vortex radius extracted from the exponential distribution of vortex areas [96].

Hence, introducing all the estimated parameters (also listed in Table 2.1) into Eq. 2.11, we calculate the dispersion relations for $\alpha \in [2 - 9] \cdot 10^{-7}$ Pa·m (see Fig. 2.7a) and extract the q of maximal growth, q^*, and the corresponding growth rate Ω^*. Interestingly, Eq. 2.11 predicts a relation $q^{*2} \sim \alpha$ (see Fig. 2.7b). Notice that this relation is the well-known scaling reported in the literature for the active length scale [75]. Then, we proceed analogously, but this time we vary K instead of α, which we fix to $9 \cdot 10^{-7}$ Pa·m. In this case, we only vary K one order of magnitude from the previously obtained value and observe that, as expected, the selected q^* decreases with K (see Fig. 2.7c). Furthermore, the dependence is fully compatible with $q^* \sim 1/K$, and therefore, with the just mentioned scaling for the active length scale.

Next, we plot $\Omega^*(q^*)$ using the obtained data sets when varying α and K (see Fig. 2.7d). In the former case, we find a power-law scaling between Ω^* and q^* with an exponent between 2 and 3, agreeing with the master curve in Fig. 2.5e. However, when changing K, the theory yields a power-law scaling of Ω^* with q^* with an exponent smaller than 2. Moreover, q^* and Ω^* predicted from the theory are ~ 1 and ~ 2 orders of magnitude, respectively, smaller than the ones captured from the experiments. This disparity is presumably due to a lack of knowledge in the material parameters of the AN.

Finally, as the theory predicts that the oil viscosity also modifies the selected wavelength, we perform supplementary experiments varying the oil viscosity.

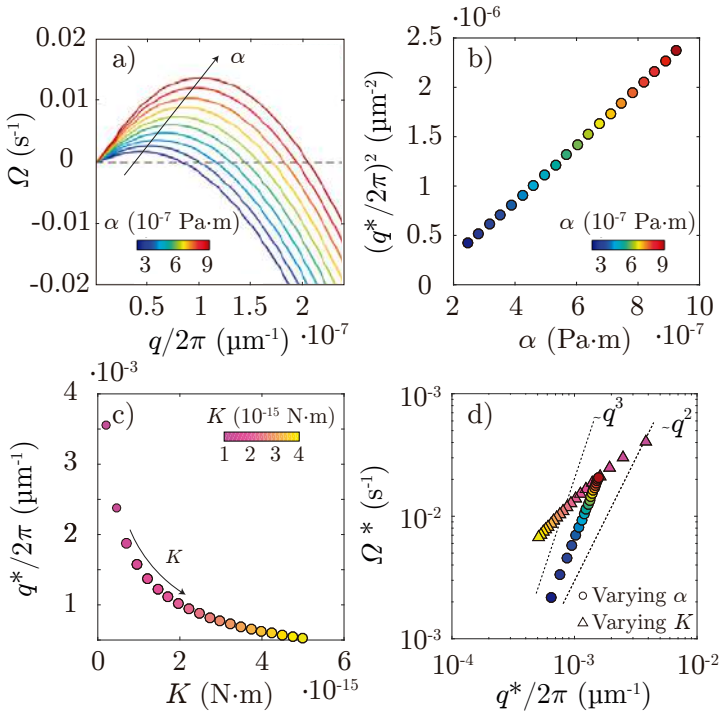

Figure 2.7: Wave length selection of the bend instability according to the theory. **a**) Dispersion relation $\Omega(q)$ (Eq. 2.11) for different values of the activity coefficient α (from $2{\cdot}10^{-7}$ Pa·m to $9{\cdot}10^{-7}$ Pa·m). **b**) $(q^*)^2$ is proportional to α. q^* is extracted from the maxima for each value of α in **a**. Colors of the lines (**a**) and the circles (**b**) correspond to the values of α used to calculate $\Omega(q)$.**c**) q^* decreases with K. Colors of the circles correspond to the values of K used to calculate $\Omega(q)$. **d**) $\Omega^*(q^*)$ for the data when varying α ($\circ$) and K ($\triangle$). Dashed lines indicate q^{*2} and q^{*2} power-laws. The parameters introduced in Eq. 2.11 to obtain the plots are listed in Table 2.1.

Used parameters			
Parameter	Values		
	Varying α	Varying K	Varying η_{oil}
α	$(2-9)\cdot 10^{-7}$ Pa·m	$9\cdot 10^{-7}$ Pa·m	$9\cdot 10^{-7}$ Pa·m
K	$1\cdot 10^{-15}$ N·m	$(0.2-4)\cdot 10^{-15}$ N·m	$1\cdot 10^{-15}$ N
η_{oil}	$1\cdot 10^{-1}$ Pa·s	$1\cdot 10^{-1}$ Pa·s	$(10^{-4}-10^{0})$ Pa·s
η	$4\cdot 10^{-6}$ Pa·s·m		
γ	$4\cdot 10^{-6}$ Pa·s·m		
η_{water}	$1\cdot 10^{-3}$ Pa·s		
H_{oil}	$3\cdot 10^{-3}$ m		
H_{water}	$4\cdot 10^{-5}$ m		
ν	0		

Table 2.1: Values used to compute the dispersion relations $\Omega(q)$ in Fig. 2.7 using Eq. 2.11.

Our results show that as η_{oil} is increased, q^* increases as well. In contrast, the theory yields a non-monotonous behavior of q^* with η_{oil}. In our experiments, we use oil viscosities ranging from $10^{-4}-10^{0}$ Pa·s, and, inspecting Fig. 2.8b, we see that for the input parameters and this range of oil viscosities, we should have uncovered the non-monotonic behavior. This could be interpreted in the sense that the predicted value of α depends on the oil viscosity.

2.4 The role of the axial symmetry

To understand our experimental results, we have leveraged the stability analysis presented in Appendix A.4 for an active nematic surrounded by two fluid layers. This analysis is incomplete because it does not include the axial symmetry of the AN in our experiments. Nonetheless, to try to comprehend the role of such symmetry, we can draw on the stability analysis in Appendix A.3, which corresponds to the problem with axial symmetry but without external layers. According to our analysis, the axial symmetry modifies the structure of the flows and the nematic director. More specifically, at early stages of the instability, the angle perturbations $\delta\theta$ adopt the form of Bessel functions instead of a superposition of Fourier modes, as in the problem with a parallel alignment. We accordingly measure the director field using the method described in [118] and Methods Section 6.4.2 and extract $\delta\psi = \text{asin}(n_\varphi)$ (Fig. 2.9a), the angle

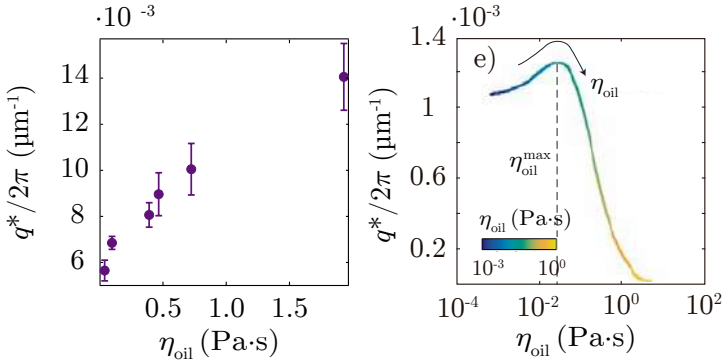

Figure 2.8: Dependence of the characteristic wave number q^* with the oil viscosity $\eta_{\mathbf{oil}}$ a) Experimental characteristic wave number $q^*/2\pi = 1/\ell^*$ as a function with the oil viscosity η_{oil}. q^* is extracted as explained in Methods Section 6.4.4. Error bars correspond to the standard deviation for measurements of different frames. **b**) Dependence of q^* with η_{oil} according to Eq. 2.11. Color of the line corresponds to the oil viscosity. $\eta_{\mathrm{oil}}^{\mathrm{max}}$ corresponds to the oil viscosity with maximal q^* for the parameters used (listed in Table 2.1).

between the radial direction and the local nematic orientation. Averaging $\delta\psi$ over the azimuth direction, we get the relation $\delta\psi(r)$ presented in Fig. 2.9b, compatible with the predicted Bessel functions. We accordingly measure the director field using the method described in [118] and Methods Section 6.4.2 and extract $\delta\psi = \mathrm{asin}(n_\varphi)$ (Fig. 2.9a, the angle between the radial direction and the local nematic orientation. Averaging $\delta\psi$ over the azimuth direction, we get the relation $\delta\psi(r)$ presented in Fig. 2.9b, which is compatible with the predicted Bessel functions.

2.5 Conclusions

To summarize the results of this chapter, we have designed an experimental setup that has permitted us to analyze the onset of the primary bend instability, which leads to active nematic turbulence.

In particular, we have demonstrated that right at the onset of the instability, the generated chaotic flows are endowed with characteristic length and time scales given, respectively, by the inverse of q and Omega. Interestingly, they appear related through a quadratic or quasi-quadratic scaling, i.e., Ω $(q^*)^2$.

As support for our experimental observations, we have resorted to a theoretical description of the instability in terms of a linear stability analysis. The first important conclusion that we can extract from the theory is that once the

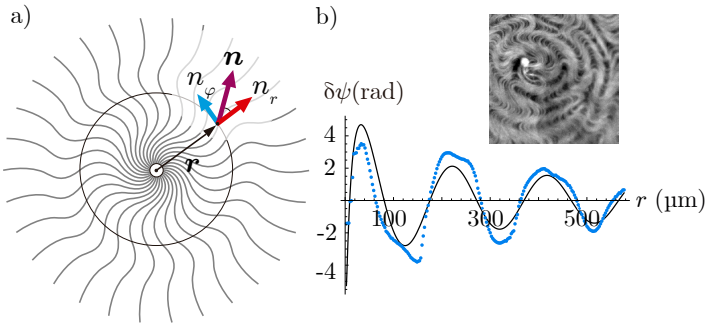

Figure 2.9: Angle perturbations at the threshold of the instability. **a**) Sketch illustrating the disposition of the MT-bundles and the nematic director $\boldsymbol{n}$ at a given point. $\boldsymbol{n}$ can be described in terms of the radial and azimuth components n_r and n_φ, respectively, from which we extract $\delta\varphi = \operatorname{asin} n_\varphi$, the angle between the radial direction and the local orientation of the filaments. **b**) Angle average of the experimentally measured 2D $\delta\psi$. The inset represents the image used to extract $\delta\psi(r)$, with $r = |\boldsymbol{r}|$. The continuous black line represents the fitting to a Bessel function. Scale bars: 100 µm

viscous coupling of the AN with the adjacent layers is considered, the growth of long wavelengths is prevented, and a wave number selection principle is enforced.

Moreover, from this linear stability analysis, we can conclude that $(q^*)^{-1}$ is a proxy for the active length scale ℓ_a, the length scale identified as characteristic of the fully turbulent regime. This conclusion is based on the observation that the scaling of q^* in relation to the activity parameters alpha and elastic parameters (K) is compatible with the predicted scaling $\ell_a \sim \sqrt{K/\alpha}$ (see Figs. 2.7b and 2.7c).

In another respect, the agreement between the predictions of the linear stability analysis and the experimental observations at the onset of active turbulence appears more questionable in quantitative and qualitative terms. In any case, we recognize the difficulty of attempting such a direct comparison, which is largely hampered by the lack of knowledge of most of the AN's material parameters. This is an underlying limitation that reappears in other parts of this thesis, more particularly in Chapter 4.

2.6 Videos

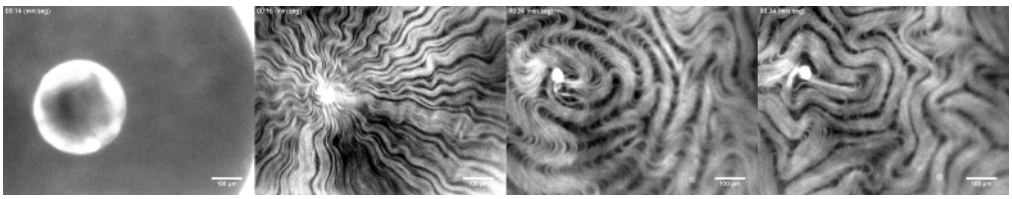

Video 2.1: Route to active turbulence A capillary tube is introduced into the open sample inducing the radial alignment of the material, which rapidly buckles displaying a concentric pattern. Proliferation of $\pm 1/2$ defects prompts the breaking of the structure. Experimental conditions are [ATP]=1.5 mM, [streptavidin]=8.2 µg/mL, [MTs]=1.3 mg/mL, [PEG]=1.7 %(wt/wt), and Oil viscosity= $9.6 \cdot 10^{-2}$ Pa·s. Image adapted from [1] with permission from Springer Nature. To watch the video, click here or scan the QR-code in List of Videos

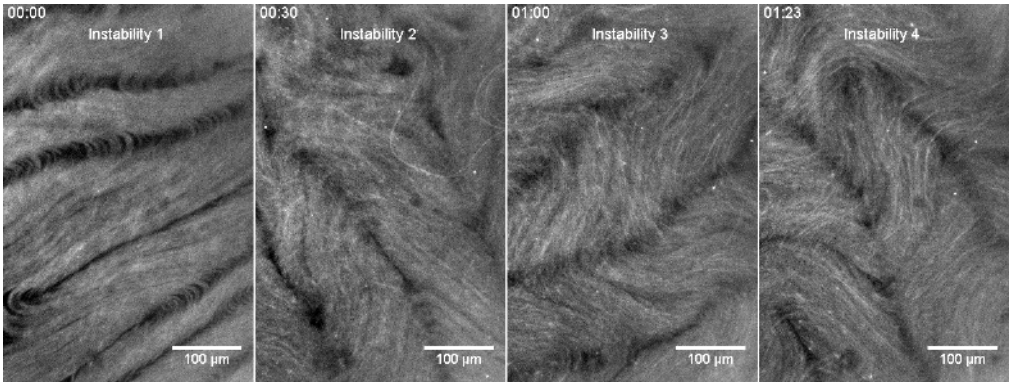

Video 2.2: Sequential instabilities At low concentration of motors (i.e., low concentration of streptavidin), we can observe sequential patterns with orthogonal directions formed because of repeated bend instabilities. Experimental conditions are [ATP]=1.5 mM, [streptavidin]=7.5 µg/mL, [MTs]=1.3 mg/mL, [PEG]=1.7 %(wt/wt), and Oil viscosity= $9.6 \cdot 10^{-2}$ Pa·s. Video adapted from [1] with permission from Springer Nature. To watch the video, click here or scan the QR-code in List of Videos

Chapter 3

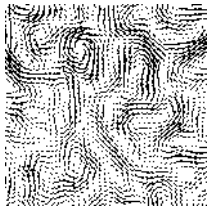

Scaling regimes of active turbulence with external dissipation

3.1 Introduction

Recent studies have exploited the body of knowledge accumulated around inertial turbulence to establish the fundamentals of active turbulence and the main similarities and differences between the two types of turbulence. More specifically, some works have been devoted to the search for the emergence of universal behaviors and scaling laws. An initial work involving bacterial turbulence showed that these fluids display flow spectra with scaling regimes with nonuniversal exponents in the sense that they are parameter-dependent [16, 95]. Note that highly-concentrated bacterial suspensions are traditionally modeled as dry systems, which can be described with models with no momentum conservation. In contrast, the theoretical studies on active nematics by Giomi [75] and Alert et al. [74] predicted spectra with universal exponent, whose values are independent of the active nematic properties. Interestingly, these two studies arrived at the same result following two different approaches. First, Giomi's work is based on a statistical analysis of the vorticity field of a 2D active nematic that allows obtaining the energy and enstrophy spectra and extracting the corresponding scaling regimes at large wavenumbers. Alternatively, Alert et al., building on the active gel theory [114], could predict the same exponents as Giomi's. Unfortunately, experimental corroboration of such universal scalings

remained elusive until very recently [96].

In this chapter, we review the work in [96], where we measure the kinetic energy density spectrum per unit mass[1] of the AN explained in this thesis, spanning a broad range of spatial scales. In this way, we can corroborate previously predicted scaling regimes and find new ones that we rationalize in terms of the coupling of the 2D active layer (1 µm thick) with the two adjacent 3D fluid layers. Since the previous theoretical models consider the active nematic as an isolated system, we propose a new theoretical framework that incorporates the hydrodynamic coupling of the active fluid with the environment and allows us to obtain an explicit expression for the full spectrum of turbulent active flows.

From the obtained expression for the kinetic energy spectrum, we can predict six different scaling regimes, whose crossovers depend on three different lengths: the average vortex size, the height of an external fluid layer, and a viscous length controlling whether dissipation is dominated by either the active or the external fluid. To explore the different scaling regimes, we perform experiments varying the oil viscosity over more than four orders of magnitude. However, we only observe three of the six predicted exponents. The missing scaling regimes might be observed in other systems, such as cell monolayers. Overall, we see that varying the oil viscosity changes the crossovers between the distinct scaling regimes. Thus, our results showcase that external dissipation not only introduces a small-q cutoff to the scaling behavior but also yields a new scaling regime.

The obtained closed expression for the kinetic energy spectrum matches remarkably well to the experimental results with intermediate oil viscosities but fails for extremely low and high viscosities. Therefore, our analysis calls for future work on the theory of active turbulence. Directions for future improvement of our hydrodynamic theory would be incorporating vortex-vortex correlations, flow alignment, and, especially for high oil viscosities, going beyond descriptions based on single phase active fluids.

Finally, we compare the results in Chapter 2 concerning the selected wavelength with the average vortex radius, shown in this Chapter 3, as a function of oil viscosity. In this way, we can show that the linear selection mechanism originated by the viscous damping is insufficient to explain the mean vortex size observed in the turbulent regime. Therefore, our analysis points out that nonlinear effects in the active fluid might contribute to vortex size selection.

[1] Hereafter, we will call the kinetic energy density spectrum per unit mass simply kinetic energy spectrum.

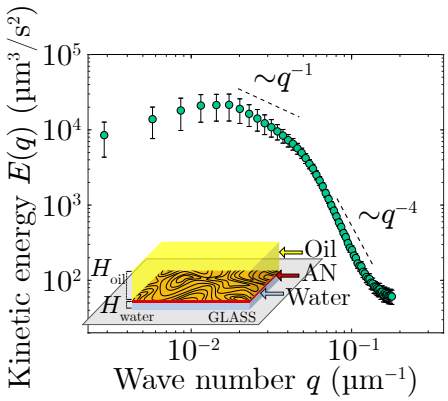

Figure 3.1: Kinetic energy spectrum of active nematic turbulence. The dashed lines indicate the previously predicted scaling regimes by theory and simulations [74, 75]. The plotted data is an average of 500 frames with a standard deviation represented by the error bars. The inset shows a diagram of the experimental setup

3.2 Experimental kinetic energy spectra of active nematic turbulence

To gain insight into how the kinetic energy of an active turbulent flow is structured over different length scales and motivated by the way inertial turbulent (at a high Reynolds number) is studied, we measure the spectrum of the kinetic energy density of the microtubule-based AN (see Methods Section 6.1). This quantity is $\langle E(\boldsymbol{q})\rangle \propto \langle|\tilde{\boldsymbol{v}}(\boldsymbol{q})|^2\rangle$, where $\tilde{\boldsymbol{v}}(\boldsymbol{q})$ is the Fourier decomposition of the 2D velocity field $\boldsymbol{v}(\boldsymbol{r})$ with wave number $\boldsymbol{q} = 2\pi(n_x/L_x, n_y/L_y)$ and $\langle\cdot\rangle$ indicates a temporal average. Finally, as the state of fully developed turbulence is isotropic, we angle average $E(\boldsymbol{q})$ and obtain the one-dimensional kinetic energy spectrum $\langle E(q)\rangle \propto q\langle|\tilde{\boldsymbol{v}}(q)|^2\rangle$ with $q = |\boldsymbol{q}|$ (see Methods Section 6.4.9), which is shown in Fig. 3.1.

The experimental $E(q)$ features two regimes compatible with the scalings predicted by the theory [74, 75]: q^{-1} and q^{-4} at large wave numbers. However, it presents an extra scaling regime with a positive exponent at small wave numbers. We must remark that in these theories, the regarded system is an isolated 2D active nematic layer. In contrast, in our experiments, we have a quasi-twodimensional active layer unavoidably in contact with two 3D passive layers: a thick oil layer ($H_{\text{oil}} \approx 3$ mm) above the AN and a thinner water layer ($H_{\text{water}} \approx 40$ µm) below the AN. Moreover, Guillamat et al. [119], working with the same system, demonstrated that the velocity of defects and, thus, of the

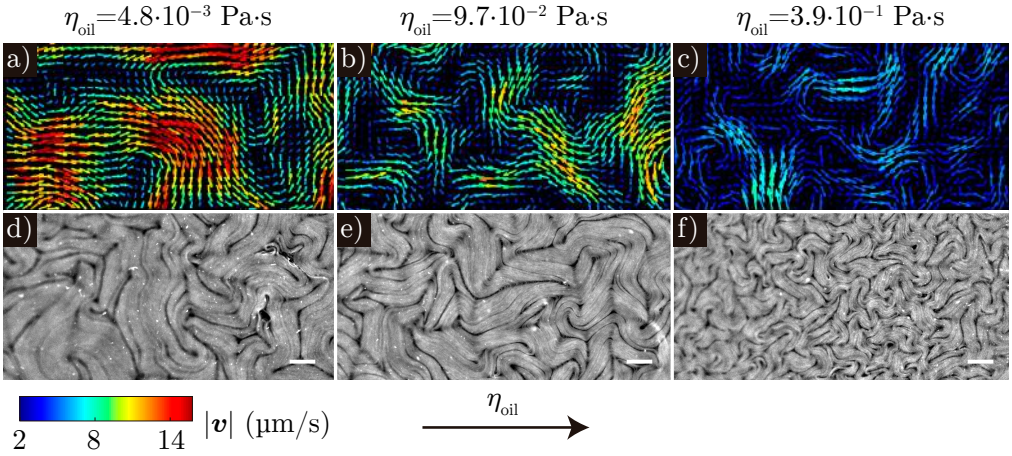

Figure 3.2: Flow filed and epifluorescence images of the AN with different oil viscosities. **a-c**) Measured flow fields of the AN through PIV (see Methods Section 6.1.5) using images as the ones in Video 3.1. The color of the arrows indicate the fluid speed (speed= $|\boldsymbol{v}|$). See also Video 3.2. **d-f**) Epifluorescence micrographs of the AN. Here, all the MTs are fluorescently labeled. See also Video 3.3. The experiments are performed with low (**a** and **d**), intermediate (**b** and **e**) and high (**c** and **f**) oil viscosities. Scale bars: 100 µm.

flow diminishes with increasing oil viscosity, highlighting the oil and water layers' significant role in the experimental system. This point can also be observed in Fig. 3.2, which displays three flow fields and epifluorescence images of experiments with different oil viscosities. We, therefore, hypothesize that the newly observed regime arises from the viscous coupling of the AN with the water and oil layers.

To investigate the effect of the 3D passive fluid layers on $E(q)$, we systematically perform a series of experiments varying the oil viscosity while keeping the rest of the control parameters fixed, namely the motor, ATP, and PEG concentrations and the thicknesses of the oil and water layers. In this way, the active length should be the same in all the experiments. As depicted in Fig. 3.3, the oil viscosity significantly modifies the kinetic energy spectrum. First, upon an increase of the oil viscosity, the whole kinetic energy spectrum decreases, consistently with the decrease in the flow speed [119, 120]. Moreover, at low oil viscosities, we observe a small-q (large-scale) regime where $E(q)$ increases until reaching a peak, an intermediate-q regime, and a crossover to another regime at large wave numbers (small-scales). Nevertheless, as the oil viscosity increases, the peak shifts to larger wave numbers, shrinking the intermediate regime until its disappearance at high oil viscosities. We attribute this effect to a strengthen-

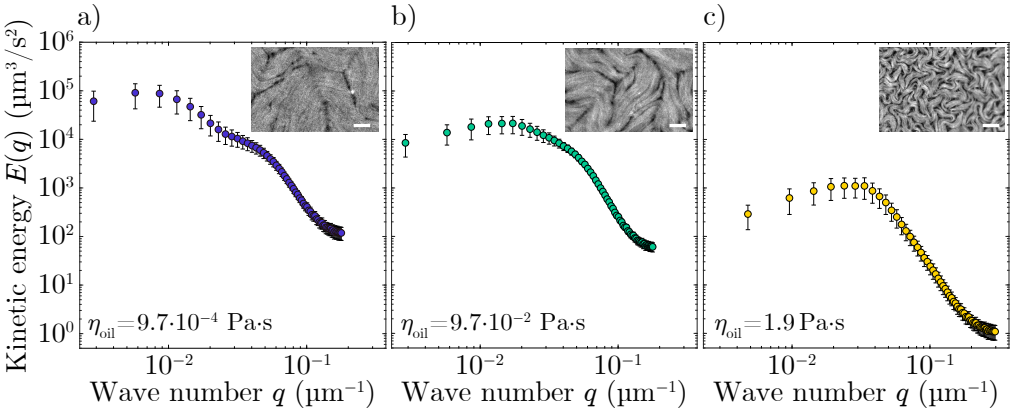

Figure 3.3: Oil viscosity changes the kinetic energy spectrum of active nematic turbulence. **a-c** Kinetic energy spectrum of the flows of an active nematic sandwiched between a water and oil layer of low (Fig. 3.3a), intermediate (Fig. 3.3b) and high (Fig. 3.3c) viscosity. The plotted data is an average of 500 frames with a standard deviation represented by the error bars. The top insets in each panel display a representative fluorescence micrograph. Scale bars: 100 µm. Image adapted from [96] under Creative Commons Attribution 4.0 International license.

ing of the hydrodynamic screening towards large-scale flows as the oil viscosity is increased.

3.3 Theoretical model and predicted scaling regimes

The chaotic flows within the active nematic propagate to the passive layers, which, in turn, influence the active film flows. We derive a theoretical framework that accounts for this hydrodynamic coupling to justify our experimental results (for an in-depth explanation, see Appendix B). Shortly, we begin by including in the active fluid's Navier-Stokes equation the viscous stresses exerted by the oil and water layers of thicknesses H_{oil} and H_{water} and viscosities η_{oil} and η_{water}. Next, following the strategy designed by Lubensky et al. [121], we obtain the corresponding Green's function, which gives the response of a flow field in a 2D fluid film adjacent to two 3D fluid layers of other fluids (see Appendix B.1). Using this Green's function, we arrive at an expression that relates the velocity power spectrum $|\boldsymbol{v}|^2$ with the vorticity power spectrum $|\omega|^2$ of an isolated active nematic film. The latter power spectrum was earlier predicted by Giomi [75], who developed a mean-field theory based on the decomposition of the AN's vorticity field into N uncorrelated vortices. Moreover, based on

simulations, he could assume that the vortices feature a homogeneously distributed and size-independent vorticity ω_v and that the vortex areas follow an exponential distribution with mean area $A_* = \pi R_*^2$, where R_* is the mean vortex radius. We finally obtain the following expression for the $E(q)$ of a system with N vortices, on average, over a total area of $\mathcal{A}$:

$$E(q) = \frac{Bq R_*^4 \, e^{-q^2 R_*^2/2} \left[I_0\left(q^2 R_*^2/2\right) - I_1\left(q^2 R_*^2/2\right) \right]}{\left[q + \eta_{\text{oil}}/\eta_{\text{n}} \tanh(qH_{\text{oil}}) + \eta_{\text{water}}/\eta_{\text{n}} \coth(qH_{\text{water}}) \right]^2}, \tag{3.1}$$

where $B = N\omega_{\text{v}}^2/(32\pi^3\mathcal{A})$, which is a coefficient related to the total enstrophy, and I_0 and I_1 are modified Bessel's functions of the first kind of order 0 and 1. Notice that here we have denoted the active nematic viscosity with a subindex n (η_{n}) to avoid confusion with the external fluids' viscosities.

By inspecting Eq. 3.1, one can appraise that the problem holds five lengths controlling the crossovers between the different regimes. Apart from the mean vortex radius, the two passive fluid layers introduce into the problem four extra lengths: the two layers' thicknesses, plus two viscous lengths set by the ratio $\ell_{\text{water}} = \eta_{\text{n}}/\eta_{\text{water}}$ and $\ell_{\text{oil}} = \eta_{\text{n}}/\eta_{\text{oil}}$. These viscous lengths control whether dissipation is dominated by either the active or the external fluids.

As in Appendix B.3, we consider only one external layer to simplify the discussion regarding the scaling regimes predicted by Eq. 3.1. This simpler scenario is sufficient to elucidate the effects of external fluid layers on the active film. Indeed, as we argue latter, the water layer does not have a notorious effect in $E(q)$ within the length scales of our measurements. Then, the lengths controlling the crossovers between the different scaling regimes are R_*, the thickness of the external layer (H), and the viscous length ℓ_v set by the ratio between the 2D active nematic viscosity, η_{n}, and the 3D viscosity of the external fluid, η_{ext}. As we will demonstrate in the next section, we can assume the thick-layer limit ($qH \gg 1$) for our experimental system, which we now discuss.

To elicit the different scaling regimes predicted by our theoretical model, we dissect the behaviors of Eq. 3.1 at scales smaller and larger than the mean vortex size R_* and the viscous length ℓ_v. For $q\ell_v \gg 1$, the scaling laws are those predicted and numerically corroborated for isolated active nematics [74, 75]. These are q^{-1} for $2\pi/q > R_*$ and q^{-4} for $2\pi/q < R_*$ (top half Fig. 3.4). In contrast, for $q\ell_v \ll 1$, new scaling laws emanate: q^1 and q^{-2} (bottom half Fig. 3.4).

3.4 Comparison with experiments

As conveyed later, we infer the active film viscosity $\eta_{\text{n}} = (4 \pm 2) \cdot 10^{-6}$ Pa·s·m from the fitting of the model (Eq. 3.1) to our experimental measurements. In

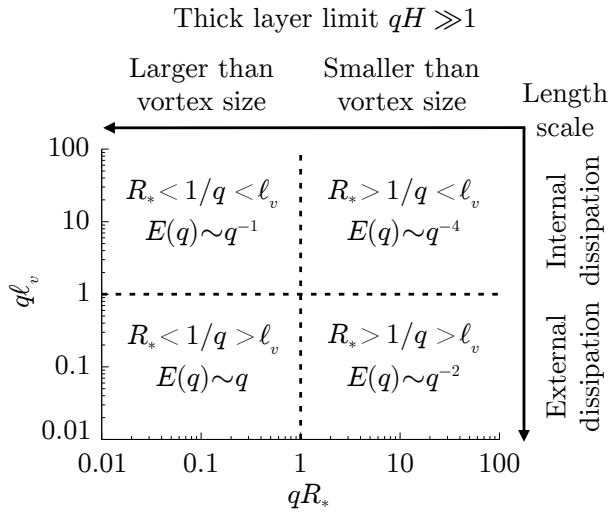

Figure 3.4: Scaling regimes of turbulent flows in an active nematic film in contact with a thick external fluid layer. The different regimes are predicted at length scales $(2\pi/q)$ either larger or smaller than the mean vortex radius R_*, the viscous length $\ell_v = \eta_n/\eta_{ext}$, and the thickness H of the external fluid layer. This figure summarizes the scalings in the thick-layer limit $qH \gg 1$; see Fig. B.2 in Appendix B.3 for the predictions in the thin-layer limit $qH \ll 1$.

this way, by taking $\eta_{\text{water}} = 10^{-3}$ Pa·s and $\eta_{\text{oil}} = (6.4 \cdot 10^{-4} - 12)$ Pa·s for the different oil viscosities, we can extract the two viscous lengths $\ell_{\text{water}} \approx 4$ mm, and $\ell_{\text{oil}} \approx 6$ mm-0.3 µm, depending on the oil viscosity used. Note that ℓ_{water} is larger than our field of view ($L = 2187$ µm, $q_{\text{min}}^{-1} \approx 0.3$ mm). Consequently, the flows in the water do not render any new scaling regimes. On the other hand, several of the oils we use yield ℓ_{oil} that fall within our measurement window. In addition, the oil layer in our experiments has a thickness $H_{\text{oil}} \approx 3$ mm, which is larger than the length scales we probe. We can accordingly assume the thick-layer limit.

3.4.1 Scaling regimes

Congruent with our predictions, the experiments, independently of the oil viscosity, exhibit $E(q) \sim q$ at large scales (small-q) and $E(q) \sim q^{-4}$ at small scales (large-q) (see Figs. 3.5a and 3.5b). Nevertheless, the expected q^{-1} power law only materializes in experiments with intermediate oil viscosities at scales between ℓ_{oil} and R_*. An example can be seen in Fig. 3.5c. At this point, we must remark that the observed scaling regimes do not span a wide enough range of length scales to be conclusive about the scaling laws. However, our experiments verify the theoretical predictions that active nematic turbulence is vested with inherent scaling laws with universal exponents. Here, by universal, we mean that these exponents are independent of the nature of the material, such as the sign of the active stress: these power laws should be observed both in contractile and extensile active systems. The nature of the material essentially changes the crossover between each power law.

The prevailing dynamics at a given length scale dictates the scaling law characterizing the active flows. Therefore, at length scales smaller than the oil viscous length ℓ_{oil}, the effect of the external fluid layer is negligible, and, consequently, dissipation is dominated by the viscosity of the active film. Within this regime, the predicted scaling laws for an isolated active film arise: q^{-1} and q^{-4}. The former exponent emerges from the dynamics of large patches of non-coherent but correlated flows. As explained in [122], this exponent originates from the long-range hydrodynamic interactions that convert short-range angle correlations into long-range correlations of the flow field. Conversely, the latter scaling law occurs from the flow dynamics within vortices, i.e., within coherent and correlated flows (see Figs. 3.6a and 3.10b). Ultimately, at length scales larger than ℓ_{oil}, the external viscosity takes over dissipation, leading to new scaling laws. In the case of our experiments, we uniquely observe the $E(q) \sim q$ power law. The role of the external fluid is to screen the hydrodynamic interactions and, as a consequence, preclude q^{-1} from becoming the asymptotic behavior of $E(q)$. This argument agrees with the fact that these correlated flows, which wrap the vortices and prompt the $E(q)$ q^{-1} scaling, become smaller as the

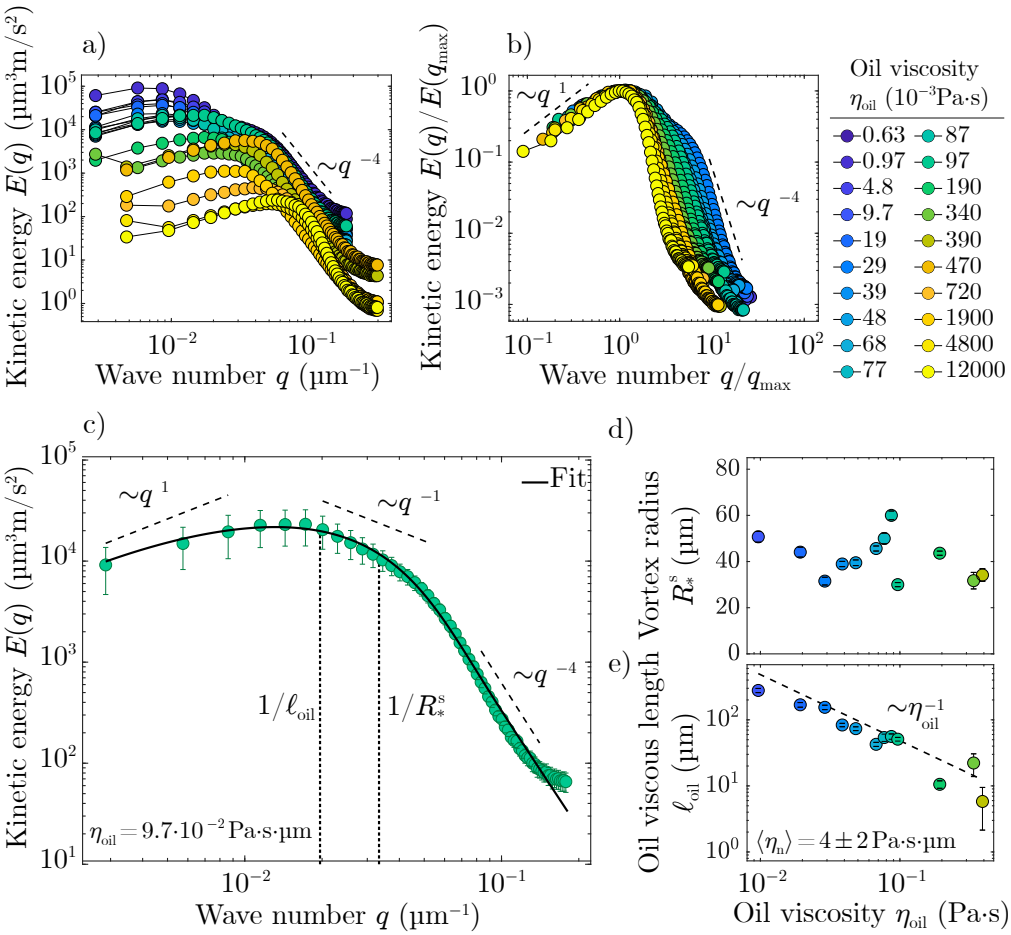

Figure 3.5: Oil viscosity tunes the scaling regimes of active nematic turbulence. **a**) Kinetic energy spectra of turbulent flows in an active nematic film in contact with a layer of oil, for 20 different oil viscosities. The data are averaged over 500 frames. **b**) Rescaling each spectrum by its maximum and its corresponding wave number clearly showcases the large-scale scaling regime. **c**) Fit of Eq. 3.1 to a representative spectrum at intermediate oil viscosity (see fits for all oil viscosities in Fig. 3.9). As predicted by our theory (see Fig. 3.4), the spectrum features signatures of three scaling regimes, separated by two crossover lengths: the mean vortex size R^s_* and the viscous length $\ell_{oil} = \eta_n/\eta_{oil}$ (vertical dashed lines). The superindex s in R^s_* means that it is extracted from the fitting of the spectral data. Averages are over 500 frames **e**) Error bars are standard deviations. **d-e**) Mean vortex radius (**d**) and oil viscous length (**e**). The mean nematic viscosity obtained from these fits is indicated in (**e**) as an inset (see also Fig. 3.11).

oil viscosity increases (see Figs. 3.10c to 3.10e). This hydrodynamic screening at large scales is also responsible for the wavelength selection in Chapter 2. As a result, as we change the oil viscosity, the range of the different regimes consistently varies while retaining the scaling laws.

3.4.2 Fitting of the model to the experimental data

Now, we fit the experimental energy spectra to Eq. 3.1 for the different oil viscosities. Since η_{water}, η_{oil}, H_{water}, and H_{oil} are known, we only use B, η_{n}, and R_* as fitting parameters. We find that our theory is remarkably well suited for a wide range of oil viscosities ($2.9 \cdot 10^{-2} < \eta_{\text{oil}} < 0.39$ Pa·s; see Fig. 3.9). An example of such notable agreement is presented in Fig. 3.5c.

In the remaining panels of Fig. 3.5, we plot the estimations for the mean vortex radius, R_*^{s}, and the oil viscous length, ℓ_{oil}, extracted from the fits within our theory's range of validity. We have added the superindex s to refer to R_* values obtained from the spectra and to avoid confusion with the average vortex radius inferred from the exponential distribution of vortex areas [75]. As illustrated in Fig. 3.5d, R_*^{s} does not change with oil viscosity in the shown range. Finally, concerning ℓ_{oil}, we observe that this length scale decreases with oil viscosity as $1/\eta_{\text{oil}}$, revealing that η_{n} is independent of oil viscosity in the range of validity of the model. Hence, we infer a mean active nematic 2D viscosity $\langle \eta_{\text{n}} \rangle = 4 \pm 2$ Pa·s·µm, which is two orders of magnitude smaller than that obtained by Guillamat et al. from the speed of topological defects [119]. Such discrepancy is plausibly due to an overestimation of the flow screening length in their model, leading to an underestimation of the nematic viscosity.

To assess the consistency of the prediction by our model that the mean vortex radius gets unmodified by the oil viscosity, we infer the mean vortex radius through the vortex area distribution $n(a)$, as reported in [75]. Interestingly, we find exponential distribution of vortex areas for all oil viscosities (see Fig. 3.6a), in agreement with the theoretical assumption and previous experimental studies [19, 92, 93]. Therefore, we can obtain the mean vortex radius from fitting such tails to $n(a) \propto \exp(a/a^*)$, with $a^* = \pi(R_*^{\text{v}})^2$. Using this method, we observe that the mean vortex radius follows a monotonous decrease with the oil viscosity, albeit with a weak dependence considering the significant variation in the oil viscosity (see Fig. 3.6b). This result is consistent with our experiments when we restrict the measurements to the oil viscosities within the range of validity of our model. Indeed, if we compare R_*^{v} and R_*^{s}, in this case, we find that both methods yield similar vortex radius values (see Fig. 3.12), roughly independent of oil viscosity.

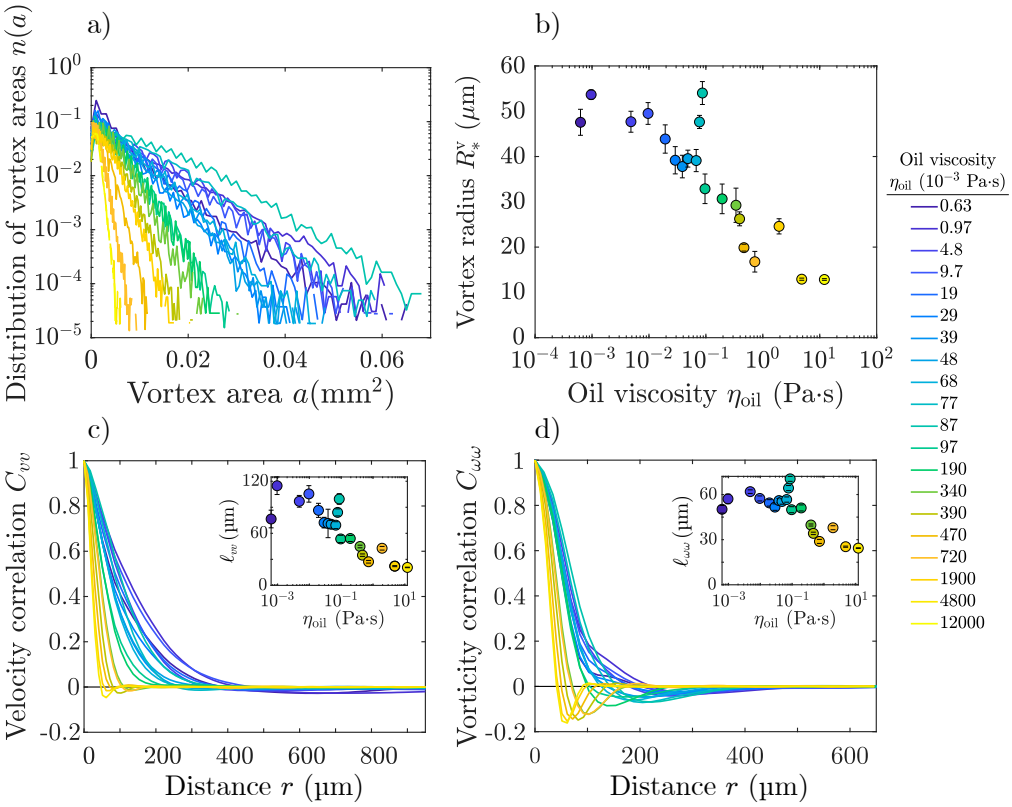

Figure 3.6: Vortex size and correlation functions in active nematic turbulence. **a**) Vortex area distributions in the active turbulence regime for 20 different oil viscosities. The distributions are obtained by measuring vortices in 500 frames. **b**) Mean vortex radius obtained from the exponential tails of the vortex area distributions in panel **a** (see Methods Section 6.4.5). Error bars are standard errors of the mean. **c**,**d**) Spatial autocorrelation functions of the velocity (**c**) and vorticity (**d**) fields, for all 20 oil viscosities. The data are averaged over 500 frames. The insets show the corresponding correlation lengths (ℓ_{vv} and $\ell_{\omega\omega}$), defined by the conditions $C_{vv}(\ell_{vv}) = 0.5$ and $C_{\omega\omega}(\ell_{\omega\omega}) = 0.5$, respectively. Error bars are standard errors of the mean.

3.4.3 Assumptions in the model

Next, to understand why the theory fails at low and high oil viscosities, we evaluate the validity of the assumptions made to build the model. For the sake of clarity, we list all the assumptions one by one and discuss its adequacy:

1. The model assumes that the vortex areas are exponentially distributed; this does not need to be true for all oil viscosities. However, as mentioned above, all our experiments present respective exponential tails in the vortex area distribution.

2. Another premise in the model is the uncorrelation between neighbouring vortices. We accordingly measure the correlation functions for velocity and vorticity (Figs. 3.6c and 3.6d), and, especially in the latter, we find negative correlations at distances comparable to, and even larger than, the vortex size for intermediate and high oil viscosities. We can understand this because vortices are surrounded mainly by other vortices with opposite vorticity. Thus, the absence of this feature in the mean-field framework might explain why the theory breaks down for experiments at high oil viscosities.

3. The model also assumes that there is only one length related to the activity. To validate this assumption, we retrieve the correlation lengths from the velocity and vorticity correlation functions (Figs. 3.6c and 3.6d). Both lengths show dependencies on the oil viscosity akin to that of the vortex size, suggesting that all lengths are proportional to one another. Thus, such observation validates our theoretical assumption.

4. Also, we believe that the modelization of the active fluid as a two-phase fluid might help to understand our results, especially at high oil viscosities, when regions depleted of MTs are very prominent.

To bolster further this last point, we perform new and independent experiments and measure the elastic energy spectrum of the active layer $F_n \propto q\langle|\widetilde{\boldsymbol{\nabla}\theta}|^2\rangle$, where $\widetilde{\boldsymbol{\nabla}\theta}$ is the Fourier decomposition of the gradient of the nematic angle $\theta \in [0, \pi)$, obtained as explained in Methods Section 6.4.2 (see also Methods Section 6.4.10). A representative example of $F_n(q)$ is displayed in Fig. 3.7a. By measuring such spectrum for different oil viscosities, we can extract the dependence of an elastic length ℓ_{el}, set by the maximum in the spectrum, with the oil viscosity (see Fig. 3.7b). If we neglect flow alignment, the only characteristic length appearing in the elastic energy spectrum should be equal or proportional to the active length, $\ell_{\mathrm{el}} \sim \ell_a$. The observed behavior of ℓ_{el} with the oil viscosity is similar to that of R_*^{v}, ℓ_{vv}, and $\ell_{\omega\omega}$: at low oil viscosities, all lengths decrease slowly, yet, as the viscosity increases, such decrease accelerates (see Fig. 3.13).

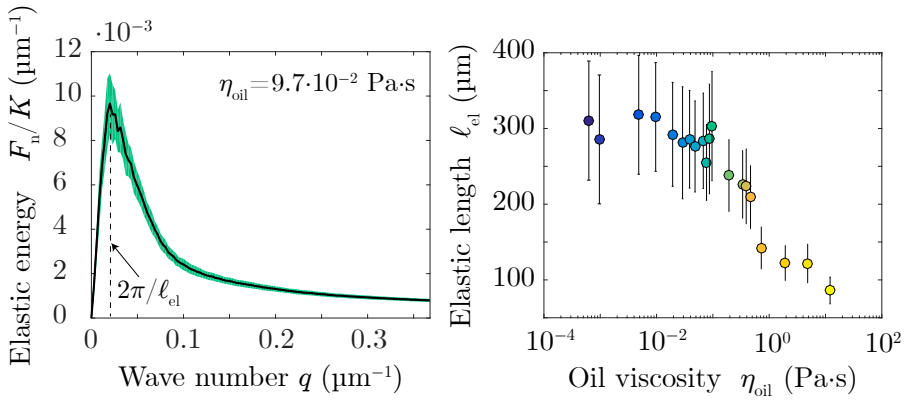

Figure 3.7: The elastic energy spectrum of an active nematic is also modified by the oil viscosity. **a**) elastic energy spectrum of the AN prepared in contact with an oil with viscosity $\eta_{oil} = 9.7 \cdot 10^{-2}$ Pa·s. The maximum sets an elastic length ℓ_{el} (vertical dashed line). **b**) Dependence of ℓ_{el} with the oil viscosity η_{oil}.

3.5 Vortex size selection

In Chapter 2, we demonstrated that the oil damping begets the selection of a length scale $2\pi/q^*$ right at the threshold of the bend in a radially-aligned AN when linear effects dominate. Such length is imprinted at the orientation field of the active nematic as the typical distance between well-aligned regions of the pattern formed after the orientational instability [1]. Now, the question is: how does this length relate to the characteristic length in the flow field, i.e., the mean vortex radius R_* in fully developed turbulence? Is also R_* the result of a linear selection mechanism? To address such questions, we begin by comparing in Fig. 3.8 both lengths as a function of the oil viscosity. This figure shows that the oil viscosity weakly modifies the mean vortex radius compared to the variation observed for the selected wavelength. Thus, q^* does not seem to determine the mean vortex radius directly. Such difference might be attributed to nonlinear effects that can modify the firstly selected length by the linear dynamics upon the instability. For instance, a recent computational study [74] showed that the vortex size in stationary and fully developed turbulence is set by nonlinear dynamics of the active nematic and given by the critical wavelength of the instability.

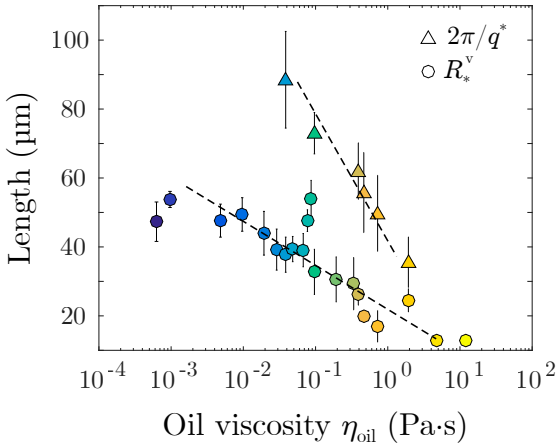

Figure 3.8: Comparison of the selected wavelength upon the primary bend instability with the average vortex radius in the turbulent regime. The characteristic wavelength emerging at the threshold of the bend instability of a radially-aligned nematic ($q^*/2\pi$, △) and the mean vortex radius (R_*^s, ○) at fully developp turbulence as a function of the oil viscosity. Values of q^* correspond to the data in Fig. 2.8 and values of R_*^v to data in Fig. 3.6b. Dashed lines indicate the logarithmic fitting of each set of data.

3.6 Conclusions

In conclusion, we have experimentally measured and theoretically justified the kinetic energy spectrum of active nematic turbulence. More precisely, we have experimentally verified the presence of previously predicted scaling regimes with universal exponents intrinsic to an active nematic film. In addition, we have discovered other regimes stemming from the coupling to an external field. To rationalize our experimental results, we have developed a theoretical model that predicts the entire spectrum as a function of diverse system parameters. Remarkably, the fitting of the data to our model in the intermediate range of oil viscosities, where the theory appears to be valid, enables us to extract the nematic viscosity and its dependence on the oil viscosity, which seems to be constant. Overall, our study fosters the resolution of other open questions, from vortex size selection to the role of vortex-vortex correlations, aiming to better understand the fundamental similitudes and distinctions between inertial and active turbulence.

3.7 Supplemental images

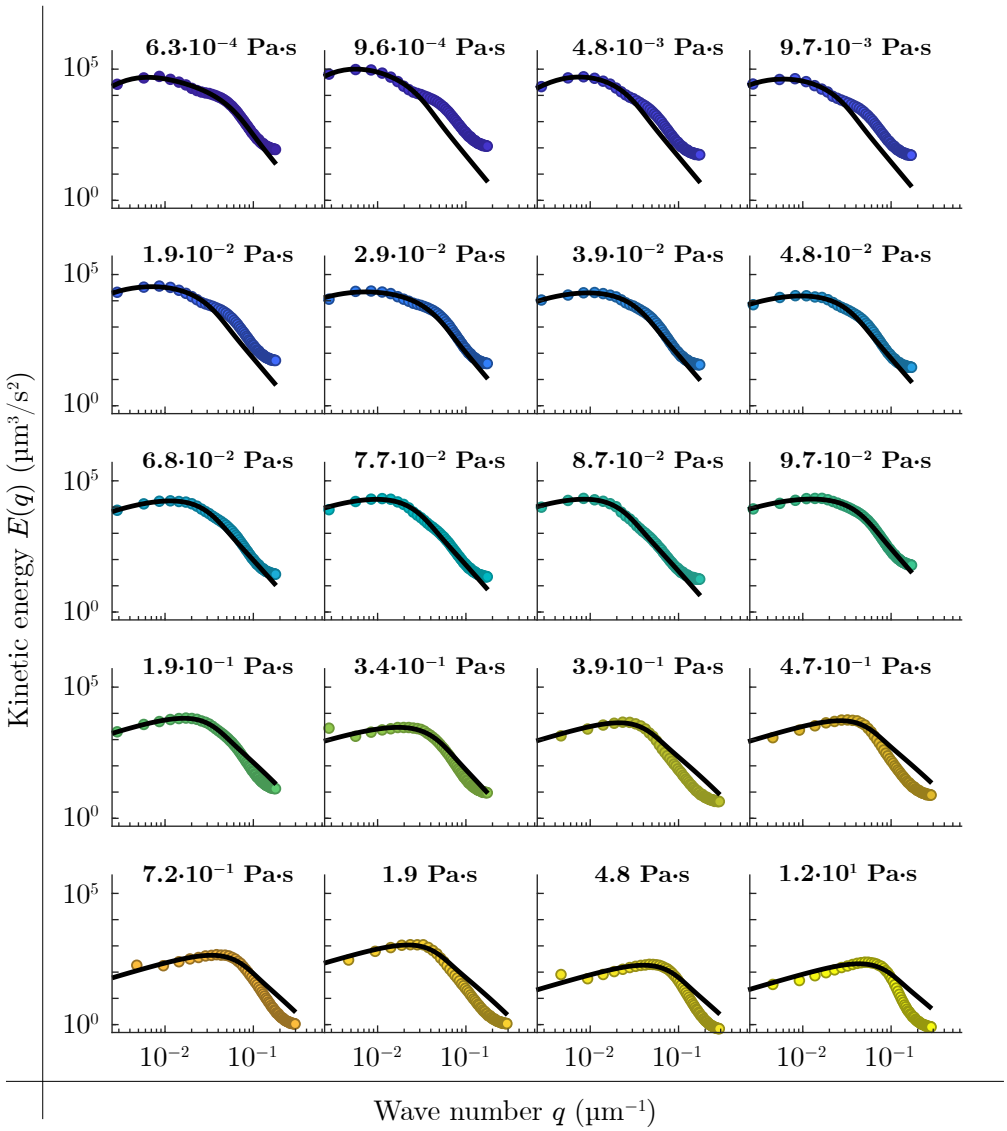

Figure 3.9: Fits of the spectra for all oil viscosities. The theory (Eq. 3.1) adjusts well to data for an intermediate range of oil viscosities ($9.7 \cdot 10^{-3} < \eta_{\text{oil}} <$ 0.39 Pa·s), as illustrated in Fig. 3.5c, with deviations for very low and very high oil viscosities.

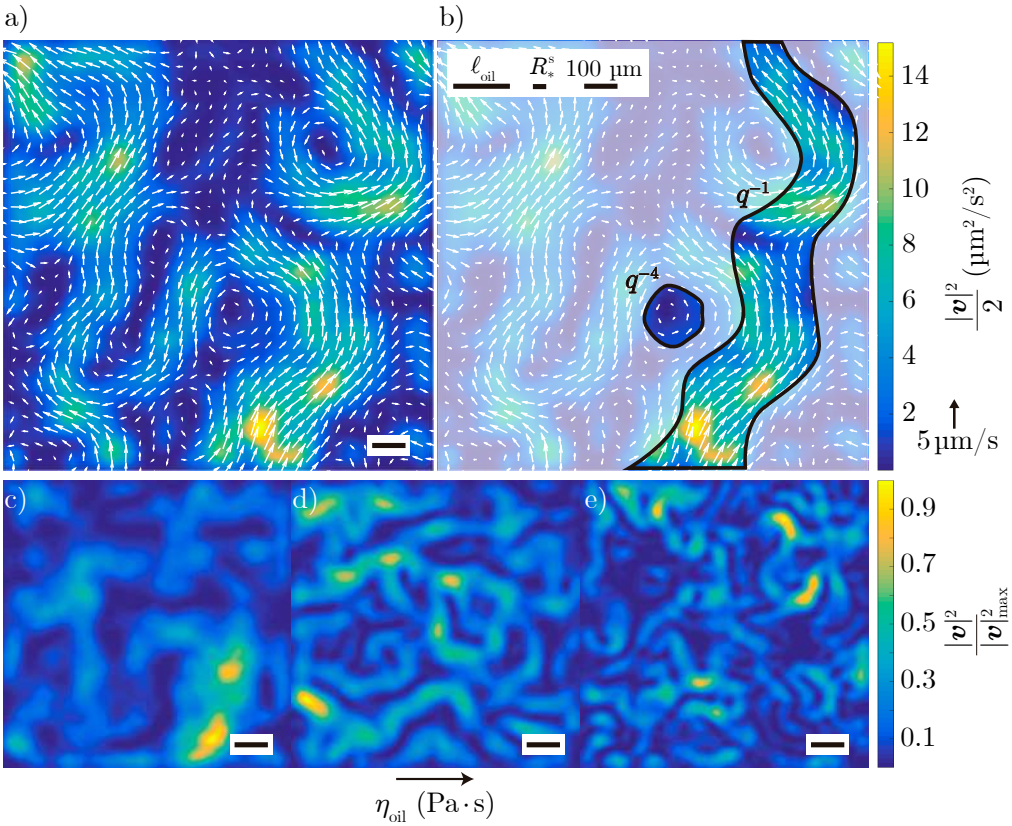

Figure 3.10: The flows that induce the q^{-1} and q^{-4} power laws. **a**) Local kinetic energy ($|\boldsymbol{v}|^2/2$) of an active nematic film with an oil viscosity $\eta_{oil} = 1.9 \cdot 10^{-2}$ Pa·s. Lighter regions (more yellowish-greenish) correspond to areas with large patches of correlated flow, where kinetic energy is mainly accumulated and responsible for the $E(q) \sim q^{-1}$ power law. The typical thickness of such domains is $\sim \ell_{oil}$. Conversely, darker (more blueish) areas correspond to vortices, coherent regions in the flow with a mean radius R_*, related to the $E(q) \sim q^{-4}$ scaling. Respective examples of such flows are marked in **b**, along with the corresponding power laws. For comparison, R_*^s and ℓ_{oil} extracted from the fits are shown in the top inset in **b**. White arrows in **a** and **b** indicate the local flow velocity extracted from PIV. Velocity vectors are rescaled to the black arrow in panel **b**. **c**-**e**) Local normalized kinetic energy ($|\boldsymbol{v}|^2/|\boldsymbol{v}|^2_{max}$) for different experiments with oil viscosities η_{oil}: $1.9 \cdot 10^{-2}$ (**c**), $9.7 \cdot 10^{-2}$ (**d**), and $3.9 \cdot 10^{-1}$ (**e**). As η_{oil} is increased, the lighter regions get smaller. The black arrow indicates the direction of η_{oil} increase.

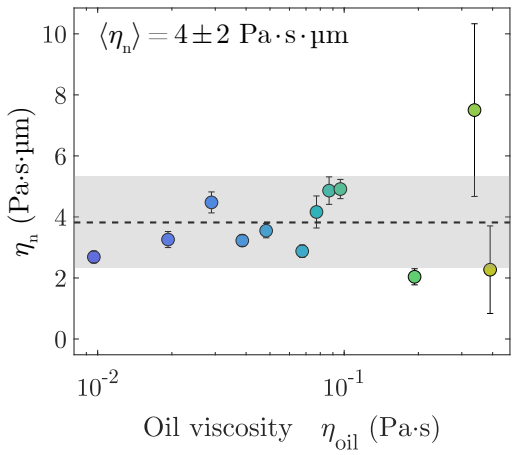

Figure 3.11: Active nematic viscosity. Effective viscosity of the active nematic layer, η_n, in contact with oils of different viscosities. We obtained η_n from the fits of Eq. 3.1 to the experimental data, as in Fig. 3.5c. The dashed line and the shaded gray area indicate the mean and the s.d of the nematic viscosity (η_n). Adapted from [96] under Creative Commons Attribution 4.0 International license.

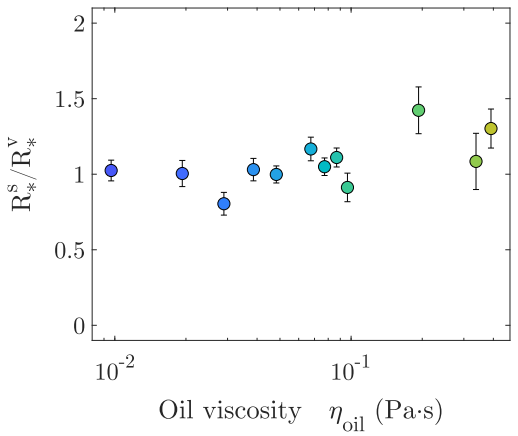

Figure 3.12: Comparing vortex sizes. Ratio of the mean vortex radii obtained from the spectral fits (R_*^s, Fig. 3.5d) and from the vortex area distribution fits (R_*^v, Fig. 3.6b). In the range of oil viscosities in which the theory fits the data well, both estimates of R_* exhibit similar trends with oil viscosity. Hence, their ratio is rather independent of oil viscosity. Adapted from [96] under Creative Commons Attribution 4.0 International license.

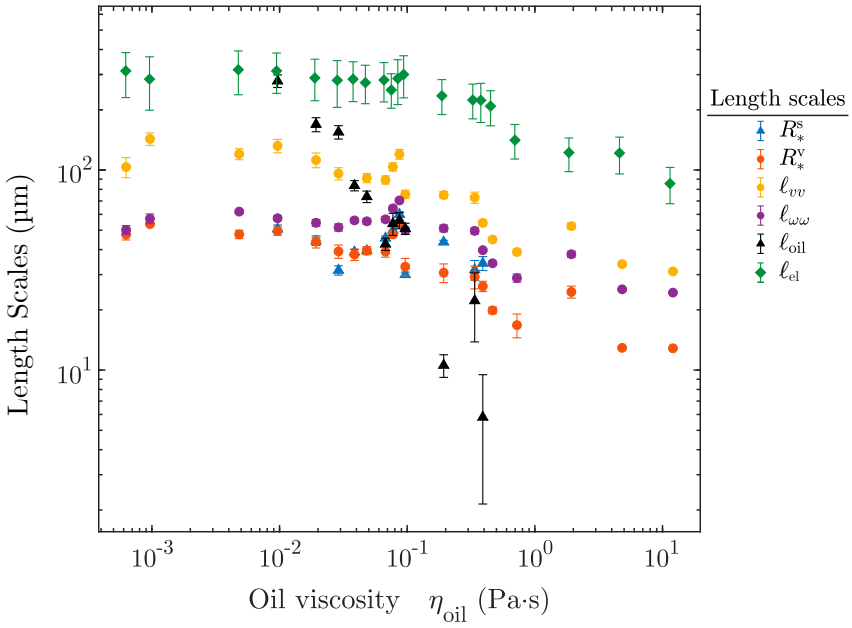

Figure 3.13: Comparison of characteristic length scales of active nematic turbulence. The different length scales are defined as follows: R_*^s is the mean vortex radius obtained by fitting the kinetic energy spectra (Figs. 3.5c and 3.5d); R_*^v is the mean vortex radius obtained by fitting the exponential tail of the vortex area distribution (Figs. 3.6a and 3.6b); ℓ_{vv} is the distance at which the velocity autocorrelation is 0.5 (Fig. 3.6c); $\ell_{\omega\omega}$ is the distance at which the vorticity autocorrelation is 0.5 (Fig. 3.6d); $\ell_{oil} = \eta_n/\eta_{oil}$ is the oil viscous length obtained from the fits of the kinetic energy spectra (Fig. 3.5c); $\ell_e xtel$ is the length corresponding to the maximum in the elastic energy spectrum. Except for ℓ_{oil}, all other length scales have similar behaviours with oil viscosity, consistent with them being proportional to one another. Adapted from [96] under Creative Commons Attribution 4.0 International license.

3.8 Videos

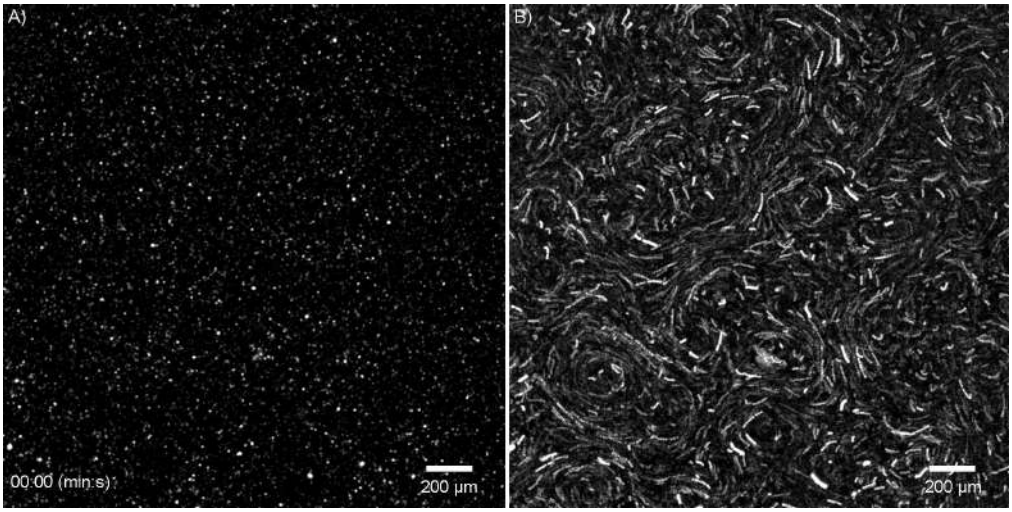

Video 3.1: Fluorescence micrographs used to measure the flow field of the active nematic. **a**) Active nematic with 0.8% of the MTs labeled with a fluorophore forming a speckle pattern, from which we measure the velocity field by PIV. To filter out the noise from the images, a mean filter with a width of 2 px is applied. **b**) Maximum-intensity projection of each frame in **a** and its 10 subsequent frames, visually revealing vortical flows. Time interval between frames is 0.5 s. The movie is sped up x5. Oil viscosity: $4.8 \cdot 10^{-3}$ Pa·s. To watch the video, click here or scan the QR-code in List of Videos

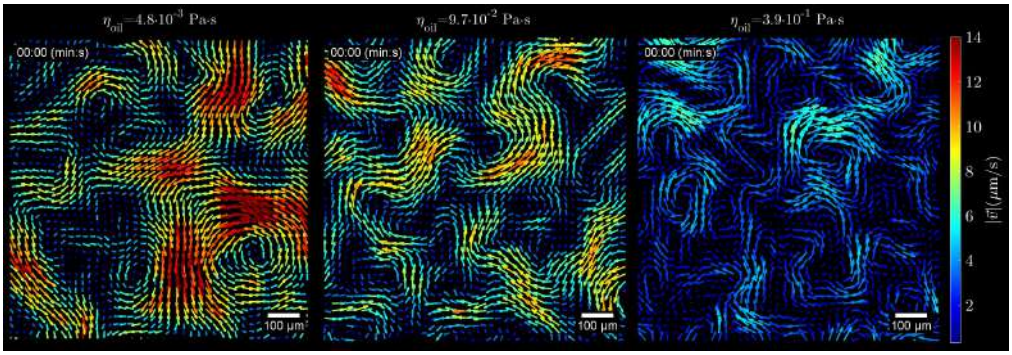

Video 3.2: Flow field of the active nematic with different oil viscosities. The flows within the active nematic layer become slower and the characteristic vortex size decreases as η_{oil} is increased (from left to right). Colors of the vectors indicate their magnitude. For the sake of a better visualization, we show a field of view smaller than the one used to compute the kinetic energy spectra, and we plot one vector every three. The video is sped up x5. The oil viscosities are indicated in each panel. To watch the video, click here or scan the QR-code in List of Videos

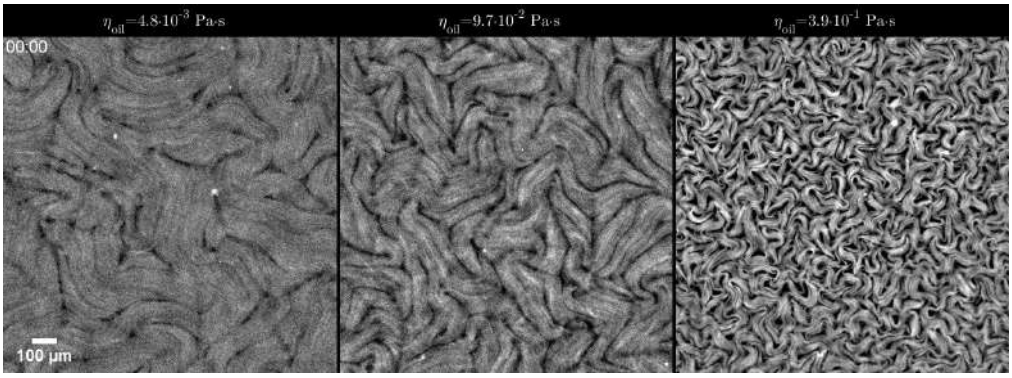

Video 3.3: Epifluorescence images of the active nematic with different oil viscosities The distance between defects becomes smaller as η_{oil} is increased. The video is sped up x5. The oil viscosities are indicated in each panel. To watch the video, click here or scan the QR-code in List of Videos

Chapter 4

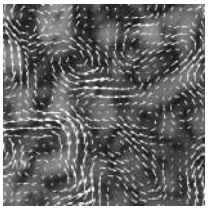

Energy cascades in active nematic turbulence

4.1 Introduction

Considering what was explained in the introductory section Section 1.5.1, it is evident that when one thinks about turbulence, one also thinks about energy (or enstrophy) cascades. Therefore, it is natural to ask whether active turbulence also features this phenomenon. In fact, some authors have suggested an abusive use of the word turbulence in the sense that a fluid assumed as turbulent should not only be chaotic but also feature energy transfer [79, 97, 98].

As conveyed in the introduction, an essential difference between the classical and active turbulence is that the former stems from external forcing at high Re. Conversely, active flows are self-sustained, meaning that the energy is injected by the very same microscopic constituents of the flow, be they bacteria or cytoskeletal proteins, which are at vanishing Re. Then, the energy injection scale is ultimately set by the characteristic scale of the flows originating from the particles' collective behavior. Consequently, a priori, there is no need for cascades, unlike in inertial turbulence. Moreover, the inertial effect that triggers the cascades at high Reynolds numbers, which is the nonlinear advection, is negligible at low Reynolds numbers. Notwithstanding, other nonlinear effects, such as elastic stresses or flow alignment, could contribute to an energy cascade in active turbulence, but energy transfer involving an extensive range of length scales is not expected [122].

Here, starting from the nematohydrodynamic[1] theory, we derive the free energy balance of an AN. Also, as the active fluid layer in our experiments is unavoidably coupled to two 3D fluid layers (see Methods Section 6.1), we include in the theory the corresponding terms accounting for the dissipation emanating from such coupling. Next, exploiting the derived expressions, we experimentally assess the different contributions to the energy balance. Our findings show that the energy transfer terms are negligible and that we cannot conclude that there is an energy cascade. Notice that these results are still in the preliminary stages; therefore, further investigation is required.

4.2 Free energy balance of an active nematic in contact with two fluid layers

As stated elsewhere [3, 114, 123], it is possible to describe the dynamics of an active fluid using irreversible thermodynamics. All these studies generalize the hydrodynamic theory of liquid crystals [124] to systems self-maintained out of equilibrium. Within this framework, one considers local thermodynamic equilibrium while the whole system is still away from equilibrium. In this regard, the contributions to the total free energy are the kinetic and elastic energies (E and F_n, respectively). Thus,

$$\dot{F} = \frac{\mathrm{d}}{\mathrm{d}t}\int (E + F_n)\,\mathrm{d}\mathbf{r} \tag{4.1}$$

In the above-listed studies, the kinetic and elastic energy change rates are derived using a vectorial parametrization of the nematic orientation based on the Leslie-Ericksen nematohydrodynamic theory. Such parametrization is an idealization because it does not include defects, which are undoubtedly present in our experiments with the MT-based AN. A way to incorporate defects in the theory is to use the nematic $\mathbf{Q}$ tensor description based on the generalization of the Beris-Edwards approach for active nematics [3]. We, therefore, combine nonequilibrium thermodynamics with this last framework to obtain the different contributions to the energy balance. In Section 1.4.2.1, we saw that continuum models for active nematics included terms accounting for the relaxation dynamics of the nematic phase towards a free-energy minimum. Models based on the Beris-Edwards scheme usually invoke the Landau-de-Gennes free energy for nematic liquid crystals [5, 124, 125, 126], which, for 2D systems and assuming a single elastic constant reads:

$$F_{\mathrm{LdG}} = \int \left[\frac{A}{2}(\partial_\alpha Q_{\beta\gamma})(\partial_\alpha Q_{\beta\gamma}) + \frac{B}{2}Q_{\alpha\beta}Q_{\alpha\beta} + \frac{C}{4}(Q_{\alpha\beta}Q_{\alpha\beta})^2\right] \mathrm{d}^2\mathbf{r}, \tag{4.2}$$

[1] Hydrodynamic theory applied to liquid crystals with nematic order

where we have used the Einstein summation convention (see Info Box A.1). B and C are material parameters, and A is an elastic constant. Here, we have used A instead of K to avoid confusion with the elastic constant in the Frank elastic free energy. Indeed, $A = K/2$. Then, the first term in Eq. 4.2 accounts for the free energy cost of spatial deformations of the order parameter field, whereas the two last terms include the free energy related to the nematic/isotropic transition. For simplicity, we overlook these last two terms. This approximation should be adequate as far as the active nematic is far from the nematic/isotropic transition [124]. Thus, we write Eq. 4.1 as:

$$\dot{F} = \frac{\mathrm{d}}{\mathrm{d}t} \int \left[E + \frac{A}{2} (\partial_\alpha Q_{\beta\gamma}) \right] \mathrm{d}\mathbf{r} \tag{4.3}$$

Moreover, by exploiting the hydrodynamic model presented in [96], we can also include the dissipation due to the two external adjacent layers present in our experiments (see Methods Section 6.1.4). Overall, introducing the Navier-Stokes equation and the dynamics of the orientation field inside Eq. 4.3 (see Appendix C), we find the following energy balance expressed in the Fourier space:

$$\dot{F}(q) = -D_s(q) - D_r(q) - D_{\mathrm{water}}(q) - D_{\mathrm{oil}}(q) + T_{FA}(q) + I(q) + T_{\mathrm{el}}(q) \tag{4.4}$$

where q is the modulus of the wave number $\mathbf{q} = 2\pi(n_x, n_y)/L$; D_s and D_r are the shear and rotational viscous dissipations, respectively; D_{water} and D_{oil} are the viscous dissipations due to the water and oil layers; I is the energy injected by the active stresses; and T_{el} and T_{FA} are the terms including the energy transfer across scales originating from elastic stresses and flow alignment, respectively. This energy balance should vanish in a steady state. The full expressions for all these terms can be found in Methods Section 6.4.11.

4.3 Experimental measurements of the free energy change rate

To experimentally infer the terms in the right-hand side of Eq. 4.4, we must simultaneously measure the velocity field $\boldsymbol{v}(\mathbf{r})$ and the $\mathbf{Q} = S(\mathbf{n}\mathbf{n}^T - \mathbf{I})$ tensor, with $\mathbf{n}$ the local nematic column vector and $\mathbf{I}$ the identity matrix. To this aim, we use the modular microscope presented in the next Chapter 5 that couples fluorescence with birefringence imaging with negligible temporal offsets between both techniques. In this way, we can exploit fluorescence images to obtain the velocity field, whereas, with the birefringence measurements, we can attain the $\mathbf{Q}$ tensor.

In the experiments presented throughout this thesis, we have mainly used the open sample set-up (see Methods Section 6.1.4). However, to perform these measurements, we have found it is better to use the flow cell setup, which ensures that the oil/water interface is flat. In the open cell configuration, the aqueous phase containing all the proteins is deposited onto a glass substrate and surrounded by the oil fluid layer. Consequently, minimization of the surface tension induces the spontaneous curvature of the oil/water interface. Since the light paths from the fluorescence and the birefringence imaging are not the same, a curved interface, which is, in fact, highly dependent on the sample's preparation, introduces uncontrollable spatial offsets.

The analysis we are performing here requires accurate knowledge of many material parameters, namely the elastic constant A, the rotational γ and shear viscosities η, the flow alignment parameter ν, and the activity coefficient α. Even though some of them have been previously forecasted in the literature [118, 119, 127], small changes in the AN preparation can entail significant variations in the material parameters. To begin with, we leverage some relations that we have already used previously in Chapter 2. First, we estimate the activity coefficient α with $\alpha \approx \omega_v \eta$ [75], where ω_v is the mean vortex vorticity. We retrieve ω_v from the location of vortices as explained in [75, 93] and Methods Section 6.4.5, and then infer η from the fitting of the kinetic energy spectrum to Eq. 3.1 as in [96] (also see Methods Section 6.4.9). Afterwards, we extract A from the relation $A \approx R_*^2 \alpha$ [75], where R_* is the mean vortex radius, which we extract from the exponential fitting of the distribution of vortex areas [75, 93] (also see Methods Section 6.4.5).

To estimate the order of the rotational viscosity, we refer to previous studies [128, 129] where the anisotropy in the three Miesowicz shear viscosities and rotational viscosity (see Info Box 4.1) of lyotropic liquid crystals[1] based on polymers are measured. More specifically, liquid crystals composed of a suspension of the tobacco mosaic virus (TMV) [128], which can be thought of as an ideal model for a rigid rod polymer, and poly-γ-benzyl-glutamate (PBG) [129]. The inferred viscous anisotropies in these two analysis are listed in Table 4.1. Notice that, for the 2D geometry of our problem, orientations outside the formation plane are constrained. We can accordingly neglect η^a. The theory we have relied on uniquely considers one shear viscosity, which corresponds to a situation with isotropic viscous properties. In practice, as the results by Hurd et al. [128] and by Taratura et al. [129] demonstrate, this is not the case for long molecules organized in a liquid crystalline phase. This point has been reinforced by later experimental [130, 131] and in silico [131, 132, 133] studies.

[1] A lyotropic liquid crystal is a liquid crystal formed by the dissolution of a molecule, usually an amphiphilic molecule, within a solvent. Such mixture, at a given temperature and concentration forms an ordered phase featuring liquid crystalline order.

Therefore, the viscosity extracted in [96] is indeed an effective quantity, which we expect to be the result of a particular combination of η^b and η^c. Assuming that such combination is linear, we draw on our experimental measurements to infer the contribution of each shear viscosity. Briefly, we locally contract the $\mathbf{n} = (\cos\theta, \sin\theta)$ director with the symmetric part of the shear stress tensor $v_{\alpha\beta} = 1/2(\partial_\alpha v_\beta + \partial_\beta v_\alpha)$: $n_\alpha v_{\alpha\beta}$. This operation yields a vector whose x, and y components respectively give the contributions of η^c and η^b to η in our experiments. We find that $\eta = 0.53\eta^b + 0.47\eta^c$. Using the relations in Table 4.1, one obtains $\gamma \approx 2\eta$ regardless of the polymer (TMV or PBG) and even with the generalized theory for hard rods.

Ratio	Experiments		Theory
	TMV[†]	PBG[‡]	Hard-rod theory[§]
η^b/η^c	0.015	0.0046	0.054–0.017*
γ/η^c	0.95	1.0	1.13–1.06*

Table 4.1: Viscous anisotropy of lyotropic polymer liquid crystals. Typical viscous anisotropies for the Tobacco mosaic virus (TMV), poly-γ-benzyl-glutamate (PBG), and for hard-rods (theory). [†] Reference [128], [‡] Reference [129], [§] Reference [131]. * The anisotropies vary depending on the order parameter S input in the theory, here $S \in [0.7, 1]$ [131].

Finally, as the MTs are rod-like and have a flow-aligning behavior, we expect $\nu \approx -1$, similar to the case of PGB [130][1]. To summarize, we include a table with all the parameters utilized to compute the terms of the energy balance.

Infobox 4.1: The Miesowicz shear viscosities

The symmetry of liquid crystals confers them with viscous anisotropy. This means that such rheological property varies depending on the measurement direction. Experimentally, the anisotropy of viscosity can be assessed by measuring effective viscosities at different director orientations with respect to the flow direction. In this regard, one can define three different shear viscosities, η^a, η^b, or η^c, when the director lies along the z, y, or x axis, respectively (see Fig. 4.1). These viscosities correspond

[1] In this article the flow alignment parameter is not explicitly computed, but one can retrieve it from the specified values of the different viscosities. In [134] the Leslie viscosity coefficients obtained from [130] are already listed. Interestingly, one can readily obtain the flow alignment parameter from such coefficients. using Eq. 4.6

to the so-called Miesowicz viscosity coefficients [134].

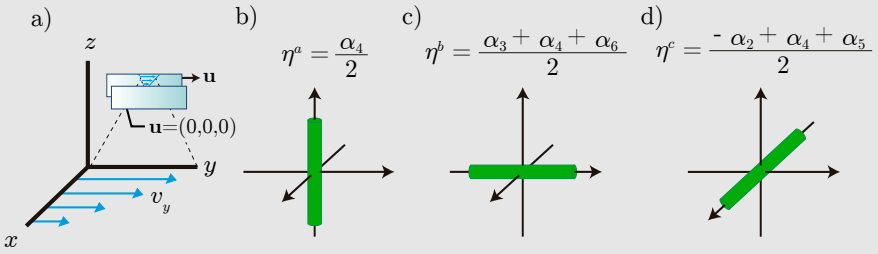

Figure 4.1: The Miesowicz geometry. **a**) Diagram of a plane Couette flow. A Couette flow can be created by moving one plate and fixing the opposite one (Inset in **a**). The LC director can be fixed with a magnetic field while the flow is imposed by the moving plate. The measured shear viscosities give the Miesowicz coefficient viscosities when **n** is: parallel to the vorticity field (**b**), parallel to the flow (**c**), and parallel to the velocity gradient (**c**). η^a, η^b, and η^c are the Miesowicz viscosity coefficients and are functions of the Leslie coefficients α_i, which appear in the Ericksen–Leslie Model. [124, 134].

The rotational viscosity γ (γ_1 in [134]) can be computed as

$$\gamma = \alpha_3 - \alpha_2, \tag{4.5}$$

and the flow alignment parameter, ν:

$$\nu = \frac{\alpha_2 + \alpha_3}{\alpha_2 - \alpha_3} \tag{4.6}$$

Then, using the parameters in Table 4.2 and the measured **Q** tensor and flow field, we obtain the different terms contributing to the AN's free energy balance. As Fig. 4.2a illustrates, the dissipation is not compensated by the injection, presumably due to material parameter mispredictions. In fact, scrutinizing Fig. 4.2a, it is possible to appraise that the shear dissipation, D_s, is practically counterbalanced by the active injection I. To fetch the parameters necessary to compute the free energy terms, we have leveraged several relations, which we have assumed to be exact. Yet, such relations can hold prefactors different from 1, significantly modifying the estimations for the material parameters. To assess the extent of such variation, we appeal to simulations of isolated 2D ANs[1], whose material parameters are known, and measure the mean vortex radius. In

[1]The simulations have been carried out by Daniel Pearce.

Parameter	Value	Obtained from
Shear viscosity, η	$4 \cdot 10^{-6}$ Pa·s·m	Fitting $E(q)$ to theory in [96]
Rotational viscosity, γ	$8 \cdot 10^{-6}$ Pa·s·m	$\gamma \approx 2\eta$
Activity coefficient, α	$1{\cdot}10^{-6}$ Pa·m	$\alpha \approx \omega_{\mathrm{v}}\eta$
Elastic constant, A	$3 \cdot 10^{-15}$ N·m	$A \approx R_*^2\alpha$
Renormalized elastic constant, A	$3 \cdot 10^{-16}$ N·m	$A \approx R_*^2\alpha/a^2$
Flow alignment, ν	-1	From [130]

Table 4.2: Values used to compute the terms of the energy balance. These parameters are for an experiment performed in a flow cell geometry (see Methods Section 6.1.4) and with compound concentrations listed in Table 6.3. The mean vortex vorticity, ω_{v} and mean vortex radius R_* for these experiments they are: $\omega_{\mathrm{v}} = 0.25$ s^{-1} and $R_* = 52$ µm.

this way, we can obtain the prefactor a relating the mean vortex radius with the elastic constant and activity coefficient: $R_* = a\sqrt{A/\alpha}$. According to the simulations, $a = 3$. Moreover, trying to draw parallels to the viscous damping in experiments, we include a friction term in the simulations. Interestingly, the prefactor remains essentially the same, with only a deviation of 0.1. Including this prefactor to retrieve the experimental elastic constant (the renormalized elastic constant in Table 4.2), we find $A = 3{\cdot}10^{-16}$ N·m. With this value for the elastic constant, the rotational dissipation decreases, becoming almost negligible (Fig. 4.2b). Additionally, we observe that apart from the shear dissipation and the injection, the rest of the terms, namely the oil and water dissipations and the transfer terms, do not play a role in the free energy balance. It is worth mentioning that even though the 3D oil layer significantly modifies the kinetic energy spectrum, here, according to these preliminary results, we see that the oil dissipation is insignificant. Moreover, we only observe one characteristic scale, which corresponds to the maximum in the power spectra.

Overall, the energy balance is not 0 for all the values of q. This could be consistent with an energy transfer, albeit small, between scales, especially because this term seems to integrate to 0. In the present case, the total energy balance would indicate an energy transfer from large to small scales (from small-q to large-q). Nevertheless, the terms included in Eq. 4.4 would not capture the resultant energy transfer we observe. Another hypothesis for the non-zero energy balance could be experimental error derived from noise leading to spurious results. To further evaluate this point, we compute the power spectrum of the free energy balance of a simulated isolated AN.

Given that all the ingredients included in the simulations, except noise, ap-

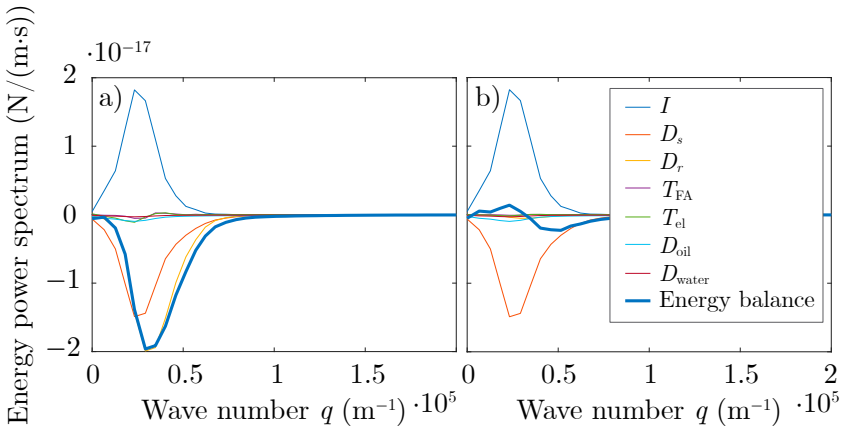

Figure 4.2: Experimental free energy balance of the AN

pear in Eq. 4.4, one would expect to find an energy balance that vanishes for all q values. However, as depicted in Fig. 4.3, the injection does not wholly balance with the dissipative and transfer terms. Indeed, to obtain the terms shown in Fig. 4.3, we first need to filter out the noise from the velocity and $\mathbf{Q}$ tensor fields. To do so, we respectively apply a Gaussian filter of size σ_v and σ_θ. One should be careful when applying these filters because too large σ_v and σ_θ values can wash out the data, leading to erroneous results (see Fig. 4.4).

Therefore, simulations indicate that a correct data treatment is essential to obtain the energy balance. Nonetheless, despite the data pre-processing, noise can still lead to a non-vanishing energy balance for some q-values. Therefore, since there is not an energy transfer term that explains the experimental energy balance, plus, simulations have revealed that noise and data treatment significantly modify the power spectra, we cannot conclude that there are energy cascades in our experiments.

4.4 Conclusions

In a nutshell, we have experimentally obtained the power spectra of the energy terms contributing to the free energy balance of an AN. To do so, we have first theoretically derived the free energy balance of an AN in contact with two fluid 3D layers encoding the orientational field of the active fluid layer using the $\mathbf{Q}$ tensor description rather than the $\mathbf{n}$ vectorial one, as in [74]. Combining the theory with the experimental measurements obtained through the modular microscope shown in the next Chapter 5, we have been able to measure all the terms in the energy balance. Nevertheless, these results are still preliminary,

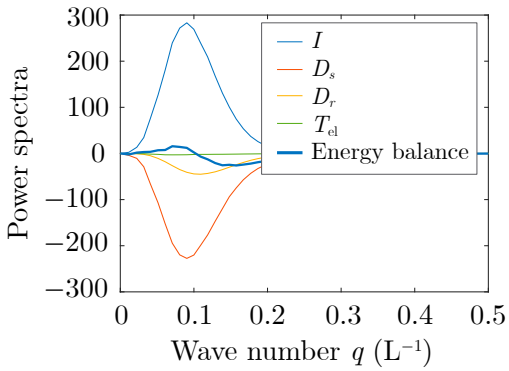

Figure 4.3: Free energy balance of the AN as obtained from simulations. The simulations are of an isolated AN. Here, the friction and flow alignment terms are 0.

and a more accurate obtaining of the material parameters is required. With the now accessible parameters, we have retrieved an energy balance different from 0 for some q-values that we cannot explain with the theory. Exploiting simulations, we have seen that a non-vanishing energy balance at some length scales is expected. Therefore, with the tools we have nowadays, we are not in a position to ensure the presence of energy cascades in active turbulence.

4.5 Supplemental images

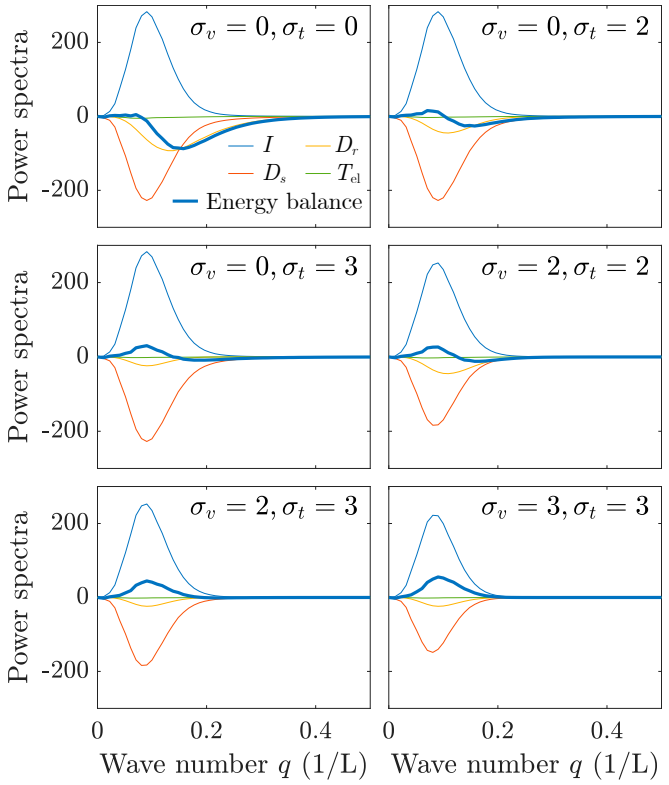

Figure 4.4: Data-filtering modifies the power spectra of the contributions to the energy balance. These results are obtained changing the size of the filters applied to the velocity and **Q** tensor fields (σ_v and σ_θ, indicated in each panel). In these simulations, the flow alignment and the friction terms have been set to 0.

Chapter 5

Imaging the active nematic with polarimetry techniques

5.1 Introduction

The elongated geometry of MTs confers them with birefringence. This means that light does not travel at the same speed along the long axis of a MT as it does along the transverse direction. The ray crossing the fastest oscillates along the so-called fast axis, whereas the slowest beam oscillates along the slow axis. Therefore, when linearly polarized (see Appendix E.1 light crosses a MT, it is split into two wave components perpendicular to and not perpendicular to the optic axis[1] (the ordinary and the extraordinary rays, respectively). When these two rays come out from the anisotropic sample, they are out of phase with a phase (or retardance) that depends on the birefringence. The combination of the two exiting waves produces an elliptic wave. (see Appendix E.1). This phenomenon accentuates when MTs self-organize into bundles or as an active nematic due to an enhanced birefringence.

The microscope most widely employed to image birefringent materials is the polarized optical microscope (POM) [135]. This device is a conventional optical microscope incorporating two linear polarizers in the light path between the

[1]The optic axis is a direction in a birefringent material along which light polarization is preserved. Thus, light propagating along this axis in a birefringent material behaves as if there were no birefringence, i.e., as if the material were optically isotropic. Waves traveling along the optic axis are called ordinary rays and follow Snell's law, whereas waves travelling perpendicularly to this axis are the extraordinary rays, which do not follow Snell's law.

sample to enhance the contrast of images of anisotropic materials. These two elements are traditionally called the polarizer and the analyzer (see Fig. 5.1a). The former is placed after the light source, whereas the latter is before the detector. Furthermore, these two optical elements are generally oriented at a right angle to each other to maximize the image contrast of the anisotropic sample. The role of the polarizers is to select only one light polarization: the one parallel to their polarizing axis. Thus, unpolarized light coming from the light source becomes linearly polarized when it crosses the first polarizer. Then, as aforementioned, when this polarized light passes through the sample, it becomes elliptically polarized. Finally, this beam is recombined in the analyzer into a linearly polarized wave. Moreover, depending on the birefringent material's orientation, which does not need to be equal throughout the sample, light intensity arriving at the director changes (see Fig. 5.1b). The minimum in intensity is reached when the birefringent specimen's optical axis is parallel or perpendicular to the polarizer as it does not produce a light splitting, i.e., the polarization does not change; hence, the analyzer blocks out the light coming from the sample.

More interestingly, POMs incorporating one or more retarder[1] (or compensators) can unambiguously measure the local optical axis and birefringence of anisotropic materials, which enables to unveil, in a non-invasive manner, the ordering at the microscale. Such analysis, however, requires the numerical combination of several images, acquired for different configurations of the optical elements, that must be acquired without spatial offsets between them. In the late 1990s, the use of liquid crystal retarders (LCRs) was demonstrated to significantly increase the versatility of such protocols. LCRs are aligned liquid crystal slabs whose retardance can be quickly and reversibly changed with a low-voltage electric field without altering the orientation of the slow axis. A celebrated implementation of such devices is an instrument called LC-Polscope [136, 137, 138], which combines two LCRs along with several passive polarizing elements. Although this instrument can be easily coupled to a standard polarizing optical microscope, it is a costly solution whose temporal resolution is well above one second, thus hampering its use as a real-time imaging technique to monitor dynamic events.

In our lab, we have assembled two alternative implementations to perform live birefringence imaging. The first one is based on a computer-controlled commercial variable LCR. By measuring the light intensity for at least, three different configurations of the LCR, we can unequivocally obtain the local orientation of the birefringent specimen's molecules. Conversely, the second arrangement includes a polarization camera, which simultaneously measures the light intensity

[1] Retarders are birefringent optical devices that introduce a phase shift between two orthogonally polarized beams

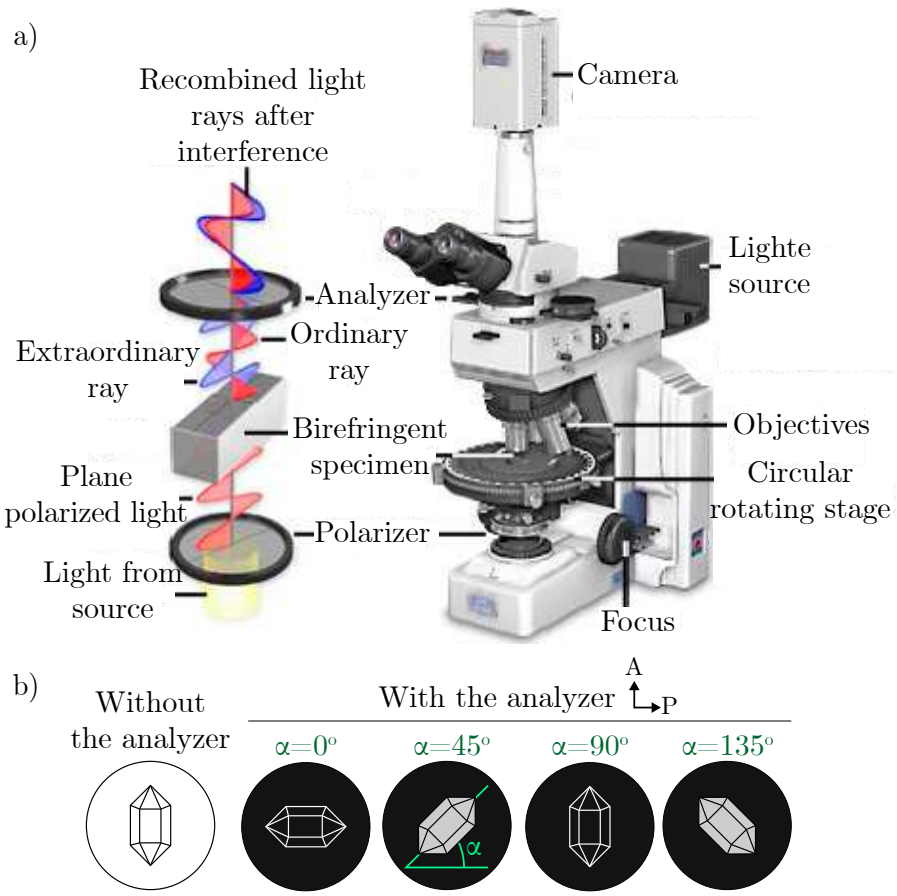

Figure 5.1: Polarized optical microscope - a) In POMs, a birefringent sample is stacked between two polarizers: the polarizer and the analyzer. Unpolarized light emerging from the light source suffers different polarizations as it crosses the different optical elements (the polarizer, the sample, and the analyzer). With this disposition, the contrast is enhanced over optical microscopy (Adapted from [135]). **b)** Light intensity varies cyclically with the orientation of the birefringent specimen, having maximum light extinction (minimum intensity) when α=0°or 90°and minimum light extinction when α=45°and 135°(α is the angle between the ordinary axis of the sample and the polarizer). Regions deprived of birefringent material will appear as dark, independently of the sample's orientation.

for four different light polarizations. By combining the four intensity measurements, we can extract the local orientation of the sample. Remarkably, with this imaging technique, we can measure the birefringence with extreme accuracy, allowing us to produce images of the MT-based AN with a quality similar to those obtained through epi-fluorescence imaging (see Methods Section 6.3). Moreover, both setups, being custom-made, are very versatile. Thus, they can incorporate extra modules, such as a module for epi-fluorescence that can be synchronized in space and time and allow for simultaneous measurements of different variables. In fact, this is the arrangement we use to simultaneously obtain the director field with the polarimetry measurements and the velocimetry with the fluorescence images and further PIV analysis (see Methods Section 6.4.1). Finally, the two setups attain better temporal resolutions and are more low-priced than the commercial LC-Polscope.

In this chapter, I present these two techniques for birefringence measurements. First, I start with the LCR-based setup and follow with the polarization camera-based setup. The former arrangement has been developed in our lab in collaboration with the specialist in optics, Dr. Oriol Arteaga. Hence, we intend to publish an article illustrating its assemblage and functionalities. In the case of the latter instrument, we have mounted it following the work by Gottlieb et al. [139].

5.2 Fast adaptive polarimetry based on liquid crystal compensators for birefringence measurements

5.2.1 Instrument description

The first setup for birefringence imaging is comprised of a variable LCR (LCC1411-A (half-wave retarder), Thorlabs) along with two linear polarizers (LPVISE100-A, Thorlabs), two quarter waveplates (QWPs) (WPQ10ME-633, Thorlabs) and a camera (QImaging EXi Blue CCD camera or Blackfly S GigE camera with an ethernet network interface card) (see Fig. 5.2a). All these elements are mounted and stacked using Thorlabs optomechanical components on an optical table. Then, the LCR is connected to a liquid crystal controller (LCC25, Thorlabs), which modulates the retardance of the variable LCR by applying a voltage [140]. The applied voltage can be set with the corresponding knob of the LC controller or with the software provided by the manufacturer [141]. Alternatively, the installation of such software includes the appropriate drivers to command the LC controller with the off-the-shelf software LabVIEW [142]. Our chosen way of control is this latter because it enables the acquisition of images right after each voltage application with a custom-made LabVIEW program. Note that there are cameras that might not be controllable with LabVIEW. As for our cam-

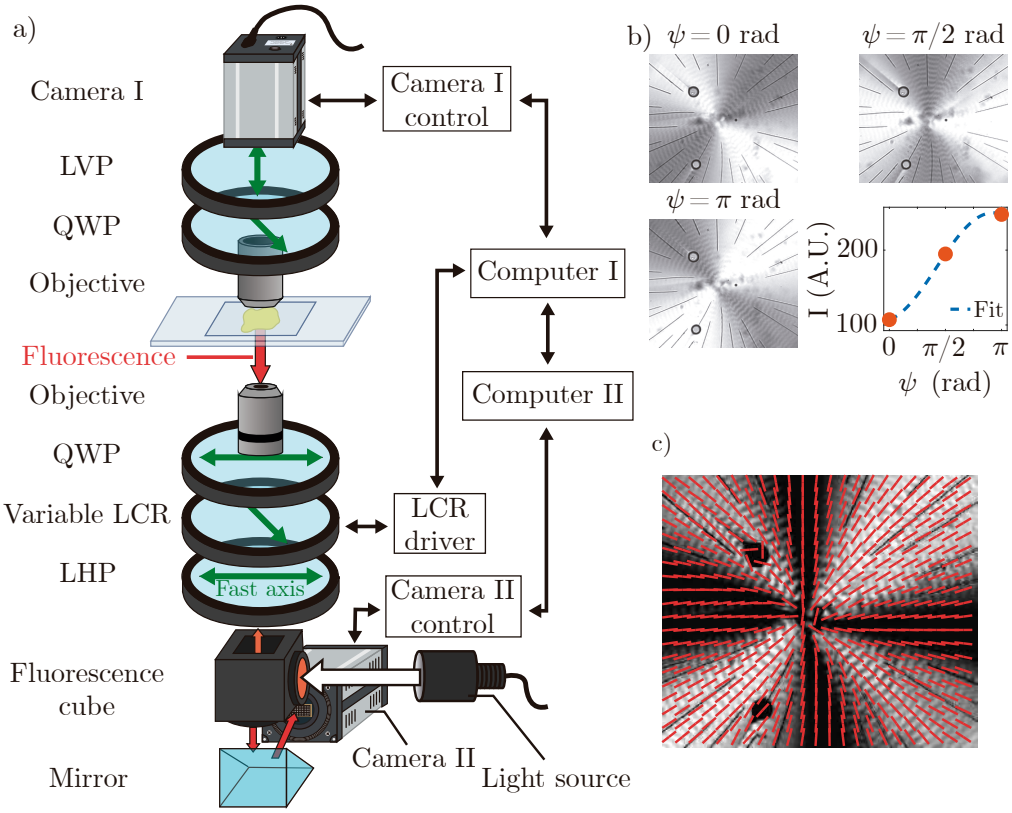

Figure 5.2: Fast adaptive polarimeter. **a)** Sketch of the fast adaptive polarimeter we have assembled in the lab. Green arrows indicate the orientation of the fast axis (0, $\pi/4$ or $\pi/2$ rad) of the respective optical elements. Camera I acquires polarimetric images whereas Camera II fluorescence images. The variable LCR and Camera I are connected and synchronized through *Computer I*, which sends a signal to *Computer II* to acquire fluorescence micrographs once Camera I has collected images at different dispositions of the LCR, like the ones in **b**. Due to space limitations, we include an elliptical mirror between the linear vertical polarizer (LVP) and Camera I. However, for the sake of simplicity, we do not illustrate it here (see Fig. 5.15 and Video 5.1 for the full assembly). **b**) Micrographs at different retardance values (ψ) of the variable LCR and the fitting of the light intensity to Eq. 5.2 for a given (x, y) point. **c**) Result of the polarimetry after fitting every pixel of images in **b** to Eq. 5.2.

eras, they both require the installation of the corresponding drivers. However, the QImaging EXi Blue CCD camera is commanded using specific LabVIEW SubVIs [143], whereas the Blackfly S GigE camera can be controlled with LabVIEW's NI-DAQmx package [144].

As we demonstrate later, the QWPs and the variable LCR stacked between the crossed polarizers break the degeneracy present in a conventional POM between supplementary angles. Hence, by imaging the birefringent sample at different dispositions of the LCR, we can unequivocally map the optical axis at a pixel-level resolution of anisotropic materials, such as the AN or a D-Mannitol sample featuring spherulites (see Figs. 5.2b and 5.2c). Besides, the time resolution is only limited by the temporal response of the variable LCR. To speed up as much as possible the image acquisition, we vary the voltage as a sawtooth wave instead of a triangle wave. In this way, we strike frame rates higher than 2 Hz, significantly higher than those achieved with LC-PolScope.

To enable simultaneous observation of the AN through fluorescence imaging, we couple the setup with a fluorescence microscopy module composed of a Cy5 filter set (67-010, Edmund Optics) assembled with a fluorescence cube (DFM1/M, Thorlabs), a mirror (BB2-E02, Thorlabs), and a camera (Zyla 4.2 PLUS sCMOS camera, Andor) controlled with another computer through LabVIEW (*Computer II* in Fig. 5.2a). The fluorescence cube also serves as a wavelength filter for the polarimetry since we require monochromatic light. More precisely, we need red light ($\sim$ 630 nm) because it is at this wavelength that our optical devices introduce the retardance specified by the manufacturer. For instance, according to the manufacturer's specifications, the variable LCR was calibrated at $\lambda = 635$ nm. For our device, we use the 660 nm LED from Thorlabs (M660L4), which yields enough light intensity for both imaging techniques, even with the filter set blocking out all the wavelengths not laying within 604 and 644 nm. Finally, we must remark that the fluorescence cube must be placed before the first linear polarizer since otherwise, it might unpolarize the light beam and alter our measurements. A diagram showing the full assembly can be seen in Fig. 5.15 and Video 5.1. Furthermore, the budget of the full assembly can be found in Appendix F in Appendix F.

5.2.2 Fluorescence and polarimetry synchronization

The synchronization of both computers and, in turn, of both cameras and the variable LCR is attained with DataSocket within LabVIEW [145], which enables the interchange of two boolean variables (true/false variables, `Start` and `Ready`) between the two computers. When the user starts the measurement process, both boolean variables are set to true, *Computer I* sends the `Start` (true) variable to *Computer II*, and *Computer II* sends `Ready` (true) to *Computer I*, and the measurement process begins. *Computer I*, once it reads a true

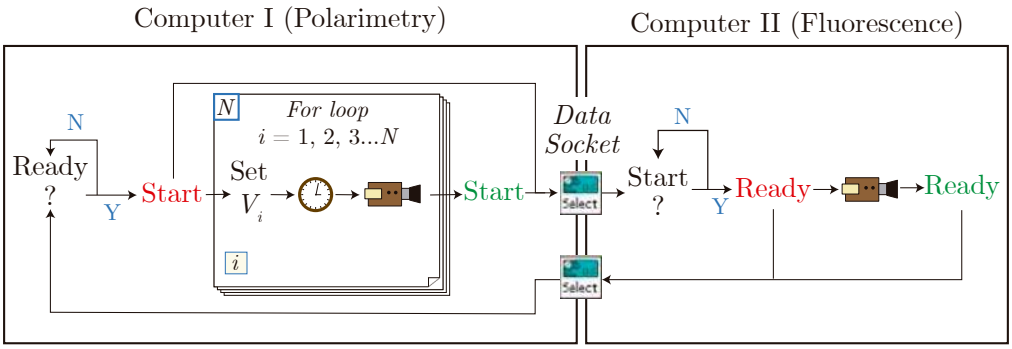

Figure 5.3: Temporal synchronization of polarimetry and fluorescence. Schematic representation of the way we shynchronize

value of `Ready`, sets `Start` to false and enters the For loop. For each For cycle, a different voltage is applied to the variable LCR, then the system waits for at least 120 ms (the optimal settling time, see Section 5.2.4.3) and acquires an image. Once the system exits the for loop, it sets the `Start` boolean to true, which is sent to *Computer II*. *Computer II*, which has been awaiting until it receives a true value of the `Ready` variable, changes the `Ready` variable to false, acquires a fluorescence image, and changes `Ready` back to true. In this way, `Ready` and `Start` are continuously exchanged between both computers and control the acquisition time. This process is depicted in Fig. 5.3 and is repeated until the user stops the acquisition. Note that this synchronization procedure can also be performed using only one computer. We have used two due to computer performance limitations.

To ensure maximum synchronization, we also store the acquisition time of each frame for both imaging techniques and then compare both times. Fluorescence/polarimetry frames with a time difference with polarimetry/fluorescence frames surpassing a threshold (usually 300 ms) are discarded.

Spatial synchronization is also a critical process. To determine the x and y offsets between the fluorescence and polarimetry images, we use a microscope stage calibration slide containing a 1 mm ruler divided into 10 µm sections. By imaging the ruler simultaneously with both imaging techniques and measuring the position of several points in the ruler relative to each field of view, we can finally obtain the spatial offsets.

We must remark that all the optical and optomechanical elements must be correctly assembled, avoiding any inclination. Otherwise, when the sample or an objective is translated along the z direction (perpendicular to the ground) to focus both polarization and fluorescence images, the objectives' focal points will change not only in the z-axis but also in the xy plane. A shift of the

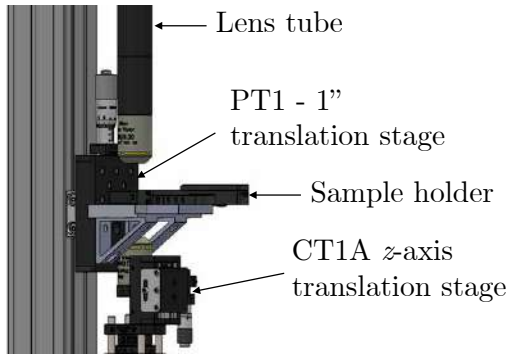

Figure 5.4: Diagram displaying the optomechanical elements used to focus the sample. To assure constant x and y offsets between polarization and fluorescence images, we fix the objective for birefringence imaging (upper objective) with a lens tube. Polarization images are focused by translating the sample with the PT1-1” translation stage from Thorlabs. Fluorescence images are focused by moving the objective (bottom objective) with CT1A z-axis translation stage, also from Thorlabs.

focal point of any of the two objectives in the xy plane also causes a shift in the x and y offsets between both fluorescence and polarimetry image fields. If there is no way to know these two offsets, the images cannot be correlated. In addition, we have also observed that some z moving stages also introduce a shift in the xy plane. Thus, selecting a stage that finely translates either the sample or the objective is essential. For instance, we have found that zoom housings coiled to optical tubes might introduce not desired x and y offsets during their translation along z. In our case, the elements that have worked the best for us are the PT1 - 1” translation Stage from Thorlabs, which holds and moves the sample, and the CT1A z-axis Translation Stage, also from Thorlabs, for one of the two objectives, while the other objective is fixed (see Fig. 5.4).

5.2.3 Theoretical description of light polarization

We use the Mueller calculus to predict light polarization with our setup and thus determine the fast optical axis of anisotropic materials. With this formalism, light polarization is described with a four-element vector (the Stokes vector, see Appendix E.2) and optical elements with 4×4 matrices (Mueller matrices) [146, 147]. The product of the Mueller matrix ($\mathbf{M}$) associated with an optical device by the Stokes vector of the incident light ($\mathbf{S}_{\text{in}}$) gives the polarization of this beam after crossing the optical device ($\mathbf{S}_{\text{out}}$), i.e. $\mathbf{S}_{\text{out}} = \mathbf{M}\mathbf{S}_{\text{in}}$. Hence, for our setup:

$$\mathbf{S}_{\text{out}} = \mathbf{M}^{90}_{\text{LP}} \cdot \mathbf{M}^{45}_{\text{QWP}} \cdot \mathbf{M}^{\alpha}_{\text{sample}} \cdot \mathbf{M}^{0}_{\text{QWP}} \cdot \mathbf{M}^{45}_{\text{LCR}} \cdot \mathbf{M}^{0}_{\text{LP}} \cdot \mathbf{S}_{\text{in}}. \tag{5.1}$$

A thorough explanation of Mueller calculus and the full equation describing light polarization with our setup can be found in Appendix E: Mueller Calculus. According to our calculus, the intensity of the emergent light depends on the retardance of the LCR (ψ) and the sample's fast axis orientation and retardance (α and δ, respectively) as follows:

$$I(\psi) = a + b\cos\psi + c\sin\psi, \tag{5.2}$$

with

$$a = I_0, \qquad b = I_0 \sin 2\alpha \sin\delta, \qquad c = -I_0 \cos 2\alpha \sin\delta. \tag{5.3}$$

Therefore, acquiring images at different values of ψ, and fitting the data to Eq. 5.2 for each pixel (see Fig. 5.2b), we can extract both α and δ of the birefringent specimen.

Given that, in practice, there is always background noise, and our measurements are very sensitive, we always perform a blank right before initiating the sample's birefringence imaging. To do so, we remove or replace the sample with a transparent isotropic thin material, such as a clean glass slide, and retrieve the a_{blank}, b_{blank}, and c_{blank}. These parameters are later subtracted from the sample's b, and c parameters pixel by pixel as:

$$b' = \frac{b}{a} - \frac{b_{\text{blank}}}{a_{\text{blank}}} \qquad , \qquad c' = \frac{c}{a} - \frac{c_{\text{blank}}}{a_{\text{blank}}}. \tag{5.4}$$

Then, we can infer α and δ as:

$$\alpha = \frac{1}{2}\,\text{atan}\,2\left(\frac{b'}{-c'}\right), \tag{5.5a}$$

$$\delta = \text{asin}\left(\sqrt{b'^{\,2} + c'^{\,2}}\right), \tag{5.5b}$$

(see Fig. 5.2c). Here, atan 2 is the four-quadrant inverse tangent. Since δ is obtained from the inverse sine, the maximum retardance for unambiguous measurement is $\delta = \pi/2$, which corresponds to $\Delta n d = \lambda/4$, where $\Delta n = n_{\text{e}} - n_{\text{o}}$ is the birefringence, with n_{e} and n_{o} the refractive indexes of the extraordinary and ordinary ray, respectively, d is the thickness of the anisotropic specimen and λ stands for the wavelength of the propagating length.

Finally, the local molecular orientation θ not only depends on α, but also on the sign of Δn: if the birefringence is positive, the molecules lie perpendicular to

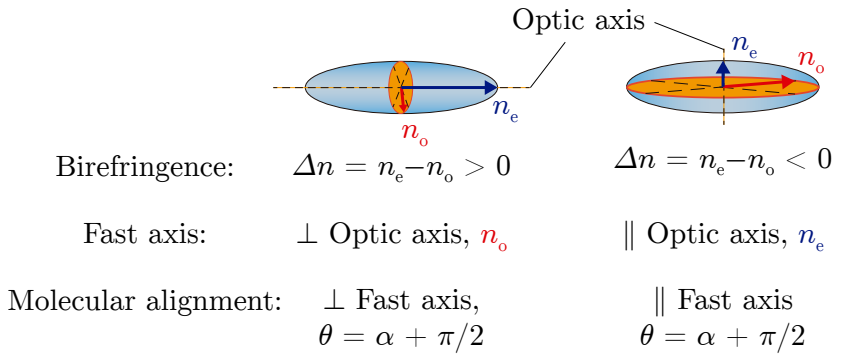

Figure 5.5: The fast axis vs the molecular axis of an elongated molecule

the fast axis, whereas if the birefringence is negative, the molecules are oriented along the fast axis (see Fig. 5.5). Accordingly, we elicit θ as

$$\begin{cases} \theta = \alpha & \text{if } \Delta n < 0 \\ \theta = \alpha + \pi/2 & \text{if } \Delta n > 0. \end{cases} \tag{5.6}$$

Note that, as we assume nematic symmetry, i.e., head-to-tail symmetry, we restrict θ within $[0, \pi)$.

5.2.4 Assembly and calibration of the polarimeter

In this section, I explain the calibration of the optical devices and the polarimeter. The fluorescence module does not require any special calibration further than retrieving the image field of view.

5.2.4.1 Calibration of the optical devices

In order to avoid aberrations when obtaining the local order of a birefringent sample with the instrument described here, it is imperative to calibrate the orientations of all the optical elements, especially when imaging low-birefringent samples, as the AN. Even though the manufacturer specifies the fast axis of the device, it is best to measure them again. For example, we have found misalignments of up to 20° in some of our purchased compensators. Then, to determine the fast axes, we use a power meter (Thorlabs, PM100USB with an S120VC sensor) controlled with the Optical Power Meter Utility from Thorlabs [148] along with a monochromatic laser diode (Monocrom, M- Series VIS 6335 laser diode and PSLDM5-PWR-M power supply). Moreover, right after the LED, we add a polarizing beam splitting prism (Thorlabs, PBS253) mounted

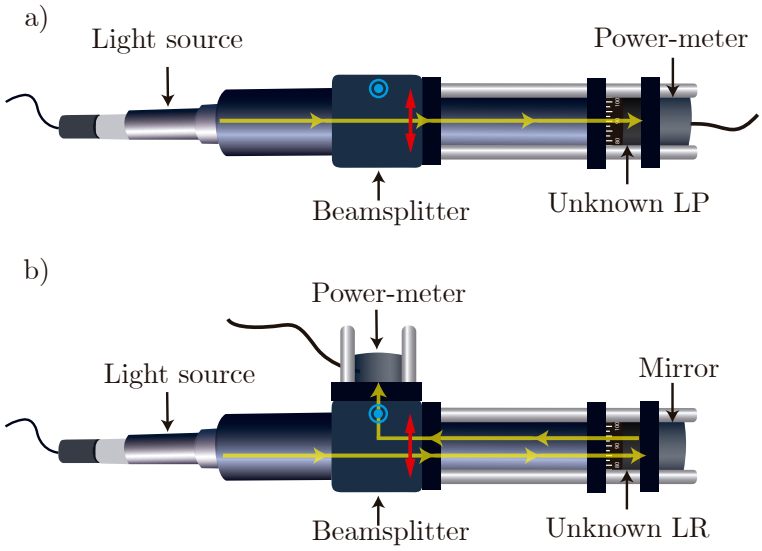

Figure 5.6: Calibration of the optical devices. Sketches that represent the setup used to determine the polarization direction of a linear polarizer (LP) (**a**) and the fast axis of a linear retarder (LR) (**b**). Red (vertical) and blue (perpendicular to the paper) arrows indicate light polarization. The yellow arrow represents the light path.

in a cage cube (Thorlabs, CCM1-4ER/M) to polarize the light emitted by the light source. This prism separates the p- and s-polarized waves by allowing the former to pass while reflecting the latter with the dielectric beamsplitter surface [149]. P-polarized (from the German *parallel*) light has an electric field polarized parallel to the plane of incidence, while s-polarized (from the German *senkrecht*) light is perpendicular to this plane. Ultimately, to calibrate linear retarders, e.g., QWPs, we also use a mirror, which we assume to be an ideal mirror. In the following, we list the setups we use to calibrate each device.

1. Linear polarizers → The polarization axis of a linear polarizer is readily obtained by placing it right after the polarizing beamsplitter and before the power-meter and by looking for the orientation of minimum transmission, i.e., the orientation with the lowest light intensity reaching the detector (see Fig. 5.6a). At this disposition, the linear polarizer is at a right angle (90°) from the beamsplitter's incidence plane. The orientation with minimum light intensity is 90° because the light intensity between linear polarizers follows Malus's law ($I(\alpha) = I_0 \cos^2 \alpha$, where I_0 is the light intensity coming out from the light source and α is the angle between the unknown polarizer and the beamsplitter).

2. Linear retarders (QWP and LCR) → We calibrate all the linear

retarders (LRs) (or compensators), like a QWP or a LCR, using the setup illustrated in Fig. 5.6b. With this assembly, the light is emitted by the LED, which is immediately linearly polarized by the beamsplitter. Then, the beam crosses the LR, collides with the mirror, travels back to the LR, and reaches the beamsplitter again, which polarizes the light vertically and changes the beam propagation direction by 90°, so the ray arrives at the detector. As it is shown in Appendix E.4.1, the minimum and maximum intensities are respectively attained at $\alpha^{\min} = 0°, 90°$, and $\alpha^{\max} = 45°, 135°$. Therefore, to calibrate the device, we need to take as a reference the fast axis provided by the manufacturer and from there, look for the minimum or maximum light intensity, depending on whether we want to orient the LR at 0° or 45°, respectively. In the case of the variable LCR, we modulate the applied voltage so that the retardance is $\psi = \pi/2$. With this configuration, the contrast is enhanced. In fact, the described calibration methodology does not work for linear retarders with a retardance equal to π as a half-wave plate because the contrast is lost. In other words, the detected light intensity is always minimum.

5

5.2.4.2 Assembly and correction of misalignments

Once the fast axes of the optical devices are known, the setup is assembled. To minimize as much as possible the error, we mount the instrument device by device, starting with the two crossed polarizes (one at 0° and the other at 90°) and checking that the light intensity reaching the detector is minimal at such disposition. Then, we incorporate the variable LCR to the setup with an orientation of 45° to the lab reference frame. With this configuration, the intensity must be maximal. Next, we assemble the QWP at 0°, ensuring that the intensity is minimal in this case. We finally add the last QWP at 45° right before the LVP and after the sample. In this disposition, the intensity arriving at the detector must be maximal.

After the assembly of the instrument, we check and correct the presence of offsets between the optical devices. For the sake of simplicity, we neglect errors coming from the orientation of the two linear polarizer (LP) and the retardance of the compensators, which are usually fairly well characterized. Thus, to assess the misalignments, we measure the light intensity when the retardance of the variable LCR is set at 0, $\pi/2$, π, and $3\pi/2$ without a sample. Afterward, we extract the deviations from the theoretical orientations of the variable LCR (Δ_0) and the first and second QWPs (Δ_1 and Δ_2, respectively) with the following relations:

$$\Delta_2 = \frac{1}{2}\frac{I(\pi/2) - I(3\pi/2)}{I(\pi/2) + I(3\pi/2)}, \tag{5.7}$$

$$(\Delta_1 - \Delta_0) = \frac{1}{2}\frac{I(0) - I(\pi)}{I(0) + I(\pi)} \tag{5.8}$$

The two deviations Δ_0 and Δ_1 cannot be isolated from each other. As a consequence, we must correct them by trial and error. We derive these two expressions using Mueller calculus (see Appendix E.4.1).

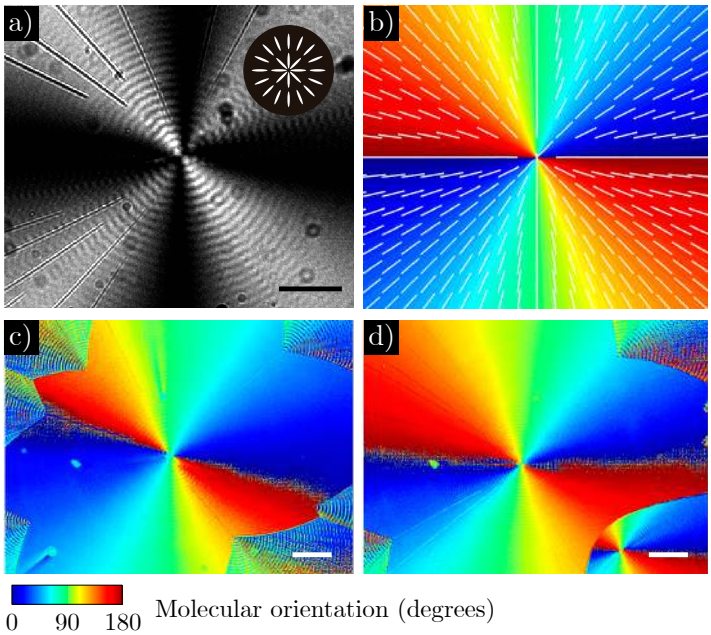

Figure 5.7: Measurements of D-mannitol spherulites. **a**) The alignment of mannitol molecules forms spherulites, which appear as a Maltese cross under an optical microscope with crossed polarizers. The top inset represents the local alignment of a spherulite. **b**) Theoretical colormap indicating the orientation of an ideal spherulite. **c-d**) Colormaps representing the measured orientation of a spherulite using a LCR-based polarimeter with (**c**) and without (**d**) misalignments between the optical elements.

To ascertain the correct assembly of the instrument, we measure the local fast axes of a thin polycrystalline sample of twisted D-mannitol lamellae displaying birefringent spherulites. Samples containing these structures are very convenient for calibrating birefringence imaging techniques because the molecules are organized in a radial pattern, displaying a Maltese cross under a microscope (see Fig. 5.7a). A detailed explanation of how to prepare samples with this spherulitic material can be found in [150]. An ideal spherulite features local orientations as the ones shown in Fig. 5.7b. However, if the optical elements

in the birefringent imaging technique are not accurately aligned, the measured fast axes diverge from this ideal disposition, and, therefore, a more accurate correction of the offsets is required (see Figs. 5.7c and 5.7d.

5.2.4.3 Determination of the optimal settling time

Upon application of a voltage to the variable LCR, as depicted in Fig. 5.8a, the device needs a given time around ∼100–200 ms to relax and stabilize. Actually, if the voltage is changed within a period shorter than the optimal settling time, the error in the sample's fast axis is very significant. To determine the optimal settling time, we use a commercial liquid crystal cell that ensures the perfect tangential alignment of the LC's molecules along the cell's rubbing direction. Then, we repeatedly measure the orientation of the LC's fast axis using images at three different configurations of the LCR ($\psi = 0$, $\psi = \pi/2$, and $\psi = \pi$) but varying the waiting time between the voltage application and the image acquisition for each measurement. As shown in Fig. 5.8b, measurements with a waiting time <120 ms yield an erroneous orientation with considerable uncertainty. We, therefore, establish 120 ms as the optimal settling time between subsequent voltages.

5.2.4.4 Determination of the optimal number of fitting points

Since we leverage Eq. 5.2 to retrieve an anisotropic material's orientation pixel by pixel, we require at least three images recorded at three different configurations of the LCR. Adjustments with a higher number of points yield less-noisy results. Nonetheless, these improved results are at the expense of a poorer temporal resolution. In other words, using more points to fit Eq. 5.2 demands a higher sampling, and considering that the settling time for the stabilization of the LCR, plus the acquisition time calls for up to $\sim$ 200 ms per fitting point, the amount of time needed to resolve one orientation significantly increases. For static samples, this is not a problem. Conversely, samples dynamically changing need high temporal resolution to obtain sharp results. Thus, using the minimum number of fitting points possible for dynamic samples is better.

To evaluate whether results using few fitting points are satisfactory, we measure the fast axis of a homogenous birefringent sample using either 3, 5, or 10 images acquired at different ψ values. As shown in the top panel in Fig. 5.9, the noise, here parameterized by the standard deviation, is almost negligible, indistinctively of the number of fitting points. Lowering the birefringence of the sample increases the noise, but it is still minimal for all measurements (see bottom panel in Fig. 5.9). Overall, employing only 3 fitting points to obtain the fast axis orientation of a birefringent sample already yields good results. If the

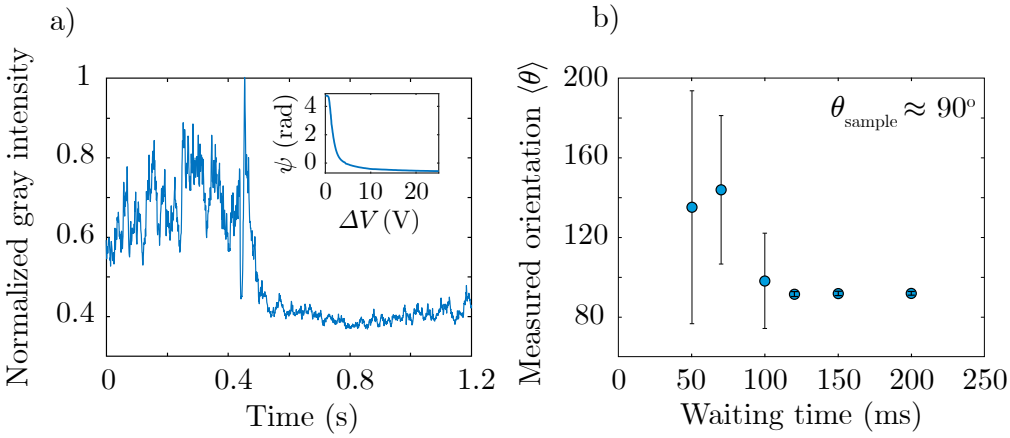

Figure 5.8: Optimal settling time. **a**) Normalized gray intensity of micrographs acquired with the polarimeter without a sample while changing the applied voltage to the LCR. In the beginning, $\Delta V = 0$. Then, around ~ 0.45 s, we apply a voltage $\Delta V = 4.4$ V. The LCR requires around $\sim 100 - 200$ ms to stabilize its retardance. The inset displays the dependence of the variable LCR's retardance ψ with the applied voltage ΔV. At $\Delta V = 0$, the gray intensity fluctuates more than at $\Delta V = 4.4$ V because $\partial\psi/\partial\Delta V|_{\Delta V=0} > \partial\psi/\partial\Delta V|_{\Delta V=4.4\text{ V}}$. **b**) Measurements of an homogeneous LC (CCN-37) cell with different waiting times (time between the voltage application and the image acquisition). All the measurements are carried out from the linear combination of frames taken at three different configurations of the variable LCR ($\psi = 0$, $\psi = \pi/2$, $\psi = \pi$). The LC cell is oriented with its fast axis lying at 90°. The plotted data are means of 10 different measurements. Error bars indicate standard deviations.

noise in measurements of dynamics samples needs to be lowered, it is better to perform spatial averages.

5.2.5 Live birefringence and fluorescence imaging

To prove the potential of this instrument for birefringence measurements, we systematically image dynamic samples of different natures. First, we follow the so-called Frederiks transition of a nematic liquid crystal. This phenomenon happens when an external field, such as an electric or magnetic field, triggers the reorientation of the mesogen molecules [134]. Consequently, topological defects originate and start moving, driven by elastic energy, until their annihilation between two oppositely-charged defects. Next, we measure the orientation of a nematic LC stirred by the AN. This stirring promotes the continuous reorientation of the passive LC, which we can track with our imaging technique. Finally, we measure the nematic director of the MT-based AN. Given that the

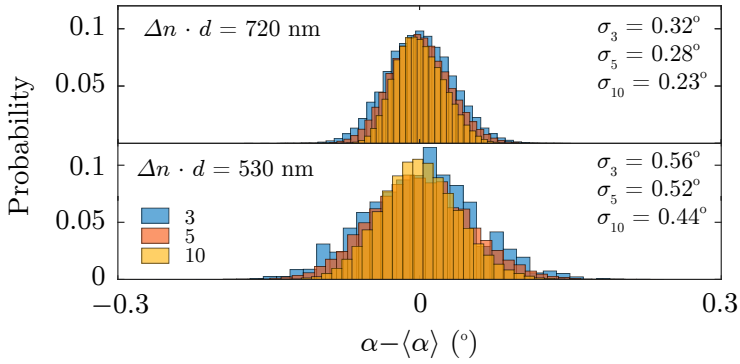

Figure 5.9: Measurements using different number of fitting points. Histograms showing the probability to measure a fast axis orientation α using homogeneous samples with $\Delta n \cdot d = 720$ nm (top) and 530 nm (bottom). We measure the fast axis using either 3, 5, or 10 images acquired at different configurations of the variable LCR (different ψ values). The standard deviations of each histogram is indicated as insets in both panels. The samples are wave plates adapted to be inserted inside a Nikon 50i Pol microscope.

MTs are fluorescently labeled, we can also image the active film through the epi-fluorescence module and demonstrate the possibility of coupling both imaging techniques.

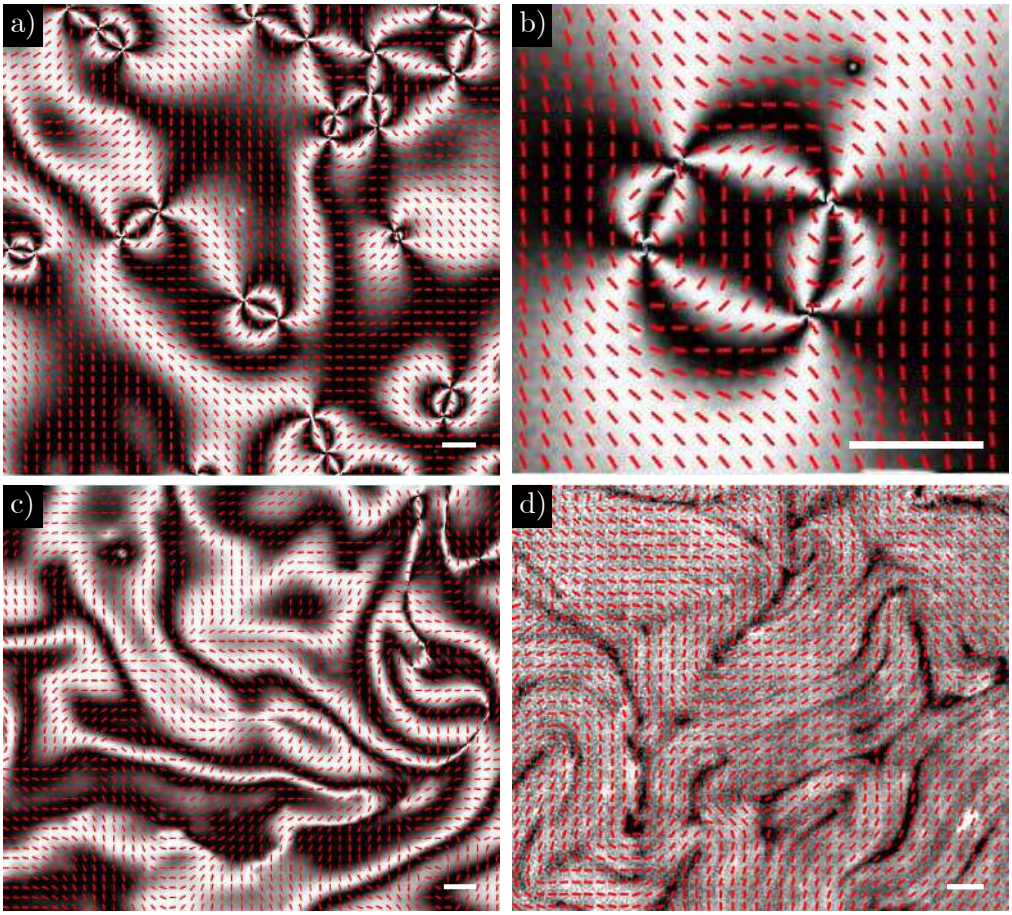

Figure 5.10: Birefringence measurements with the LCR-based polarimeter and simultaneous fluorescence imaging. **a**) Polarization image of a Schlieren texture in a MLC 7029 liquid crystal cell formed after a Friederik transition actuated by an external electric field (also see Video 5.2). **b**) Close-up of four integer defects of the sample in **a** (also see Video 5.3). **c**) 5CB liquid crystal on top of the AN as seen with a POM (also see Video 5.4). Here, the isotropic oil used to prepare our samples (see Methods Section 6.1.4) has been replaced by the LC. All POM images from **a**–**c** are obtained from the measured local director and using the relation $I(\theta) \propto \sin^2 2\theta$. **d**) Fluorescence image acquired simultaneously with the birefringence image (also see Video 5.5). The measured local director θ is represented with red lines in all panels. We have applied a mean filter of size (5×5) px^2 to the director (see Methods Section 6.4.12). Scale bars: 50 µm

.

5.3 Fast birefringence imaging with a polarization camera

The alternative arrangement for birefringence imaging we exploit in our lab is based on the polarimeter described by Gottlieb et al. [139], who propose polarization cameras (see Fig. 5.11) as a way to simplify polarimeters incorporating several compensators. Polarization cameras For instance, for a setup with the same functionalities as the polarimeter described above, we uniquely need the polarization camera, a QWP, and a linear polarizer. Remarkably, this minimalistic arrangement helps reduce the possibility of misalignment errors and also facilitates the whole assembly.

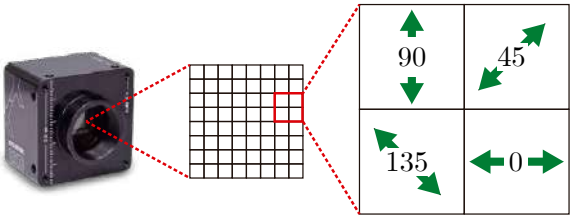

Figure 5.11: Working principle of a polarization camera. The chips of polarization camera incorporate pixels divided into four subpixels, each containing one linear polarizer (LP) with polarization orientation: 0°, 45°, 90°, and 135°. Green arrows indicate the corresponding polarizing axis.

5.3.1 Instrument description

In this case, the setup includes a linear horizontal polarizer (LHP) (LPVISE100-A, Thorlabs) placed after the fluorescence cube, a QWP (WPQ10ME-633, Thorlabs) with the fast axis at 45° right before the sample, and the polarization camera (Exo253ZU3, SVS-Vistek). Furthermore, as we did with the LCR-based polarimeter, we also include a module for epi-fluorescence imaging. In Fig. 5.12, it is depicted a schematic representation of the setup's main components (also see Fig. 5.16 and Video 5.6 for the full assembly). The budget of the full assembly can be found in Appendix F in Appendix F.

Interestingly, as we convey next, we only need one image to unequivocally discern the fast axis and the birefringence of the anisotropic sample. Therefore, the temporal resolution only depends on the maximum frame rate delivered by the camera (up to ∼75 fps for our camera). Moreover, since no other devices need to be commanded apart from the two cameras through LabView [142], temporal synchronization is significantly simplified. As with the other setup, the synchronization is controlled with two boolean variables (`Start` and `Ready`),

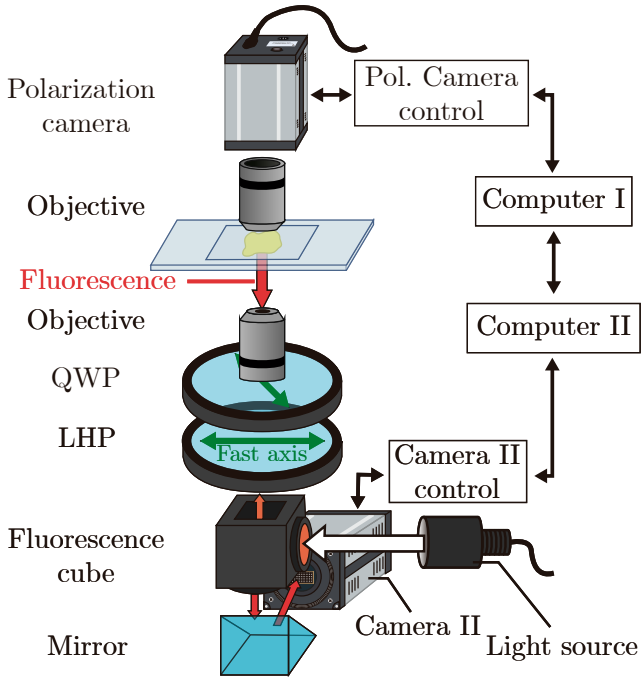

Figure 5.12: Fast adaptive polarimeter with a polarization camera. Sketch of the alternative polarimeter we have assembled in the lab. Green arrows indicate the orientation of the fast axis (0 or $\pi/4$ rad) of the respective optical elements. The polarization camera acquires polarimetric images whereas Camera II fluorescence images. The polarization camera and Camera II are respectively controlled with *Computer I* and *Computer II*. The two computers are interchange boolean variables to synchronize the fluorescence and polarimetry. See Fig. 5.16 and Video 5.6 for the full assembly.

which are continuously interchanged between the two computers. In this way, when *Computer I* receives a true value for `Ready` from *Computer II*, it starts the acquisition process. Analogously, *Computer II* starts the acquisition when `Start` is set to true by *Computer I*.

Spatial synchronization is attained as already presented in Section 5.2.2, and using the same optomechanical elements shown in Fig. 5.4.

5.3.2 Working principle

Polarization cameras contain a sensor whose pixels are divided into four blocks, each incorporating a linear polarizer with polarization direction: 0°, 45°, 90°, and 135°. Thus, to predict light polarization of the arrangement including a

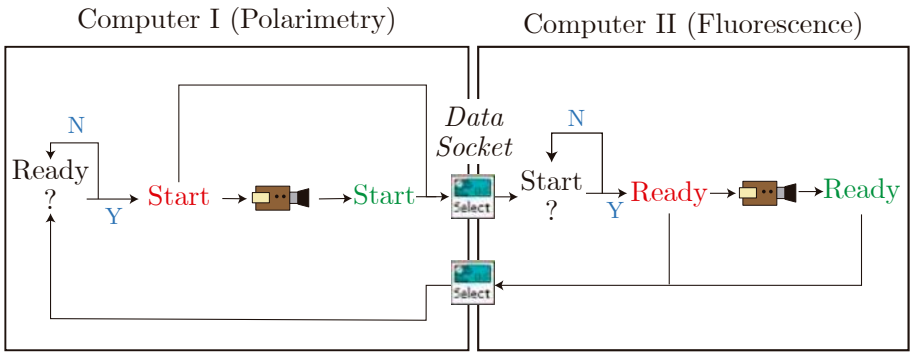

Figure 5.13: Temporal synchronization of the polarization camera and the fluorescence camera. Schematic representation of the way we synchronize the polarimetry performed with the polarization camera and the fluorescence.

sample with fast axis α and retardance δ, we compute four different Mueller calculus, one for each subpixel's polarization (indicated as a superindex):

$$I^{0}(\alpha,\delta) = \frac{I_0}{2}(1+\sin 2\alpha \sin\delta), \tag{5.9}$$

$$I^{45}(\alpha,\delta) = \frac{I_0}{2}(1+\cos 2\alpha \sin\delta), \tag{5.10}$$

$$I^{90}(\alpha,\delta) = \frac{I_0}{2}(1-\sin 2\alpha \sin\delta), \tag{5.11}$$

$$I^{135}(\alpha,\delta) = \frac{I_0}{2}(1-\cos 2\alpha \sin\delta). \tag{5.12}$$

See Appendix E.5 for the full explanation of the Mueller calculi. Notice that the combination of Eqs. 5.9 to 5.12 yieldas the a, b, and c parameters in Eq. 5.3:

$$a = \frac{I^0 + I^{45} + I^{90} + I^{135}}{2}, \tag{5.13a}$$

$$b = I^0 - I^{90}, \tag{5.13b}$$

$$c = I^{135} - I^{45}. \tag{5.13c}$$

Also, as we did before, we subtract the signal of a blank measurement:

$$\begin{aligned} I^{0'} &= I^0 - I^0_{\text{blank}} \quad , \quad I^{45'} = I^{45} - I^{45}_{\text{blank}} \\ I^{135'} &= I^{135} - I^{135}_{\text{blank}} \quad , \quad I^{135'} = I^{135} - I^{135}_{\text{blank}} \end{aligned} \tag{5.14}$$

Proper combination of these last equations allows us to extract α and δ:

$$\alpha = \frac{1}{2}\operatorname{atan}2\left(\frac{I^{0'} - I^{90'}}{I^{45'} - I^{135'}}\right), \tag{5.15}$$

$$\delta = \operatorname{asin}\left(\frac{2\sqrt{(I^{0'} - I^{90'})^2 + (I^{45'} - I^{135'})^2}}{I^{0'} + I^{90'} + I^{45'} + I^{135'}}\right). \tag{5.16}$$

Thanks to the high frame rates reached by the polarization camera, the data can be denoised by acquiring different subsequent images and performing a temporal average while still attaining reasonable measurement rates. Afterward, the director and the retardance are obtained using Eqs. 5.15 and 5.16.

5.3.3 Calibration of the polarimeter

To calibrate the setup, we proceed as previously by first calibrating the optical devices as described in Section 5.2.4.1. After that, the setup is assembled, and misalignments are corrected by minimizing the following metric:

$$\Delta_1 - \Delta_2 = \frac{I^{45}(\Delta_1, \Delta_2) - I^{135}(\Delta_1, \Delta_2)}{I^{45}(\Delta_1, \Delta_2) + I^{135}(\Delta_1, \Delta_2) + I^{0}(\Delta_1, \Delta_2) + I^{90}(\Delta_1, \Delta_2)}, \tag{5.17}$$

where Δ_1 and Δ_2 are the errors in the alignments of the LR and the QWP. To minimize such metric, we just need to rotate the LR and the QWP while there is no sample.

With this setup, no further calibration is required.

5.3.4 Live birefringence

We evaluate the suitability of this setup by measuring the birefringence and the director of the AN. Strikingly, the quality of the retardance map (Fig. 5.14a and Video 5.7), despite the low birefringence of the AN, is comparable to that obtained through epi-fluorescence imaging (Fig. 5.14b and Video 5.8). Also, the director is exceptionally well-determined. Indeed, to perform the experiments in Chapter 4, we have employed this setup rather than the LCR-based polarimeter because of the fine measurement accuracy and the good temporal performance. Finally, in Video 5.9, it is possible to appraise how good the two measurements (birefringence and fluorescence) can be synchronized.

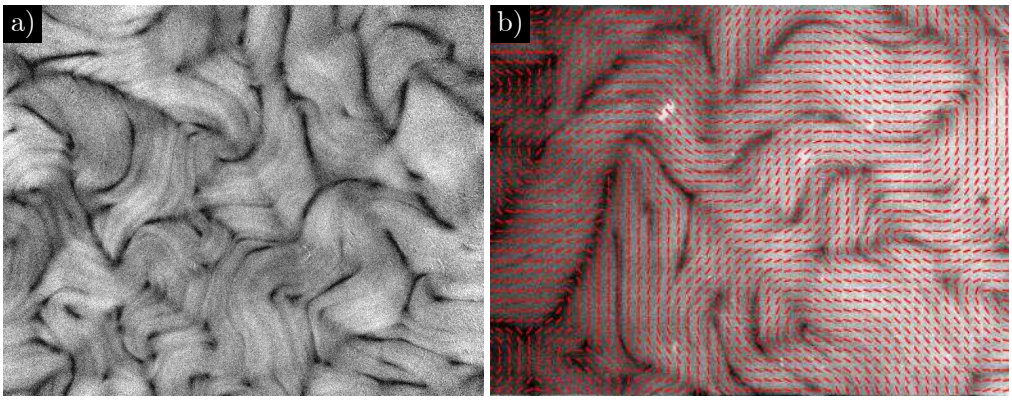

Figure 5.14: Live birefringence measurements with the polarization camera setup coupled to fluorescence measurements. **a**) Retardance map of the AN. The mean retardance is $\langle\delta\rangle = 1.8$ nm. Fig. 5.14b) Fluorescence image of the AN with the nematic director, obtained with the polarimetry, overlaid.

5.4 Supplemental images

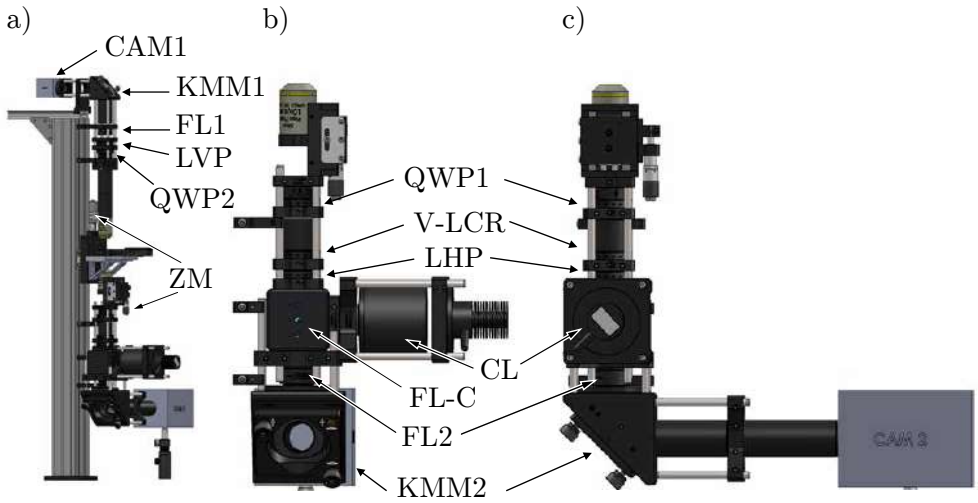

Figure 5.15: Optomechanical assembly of the fast adaptive polarimeter based on LC. These diagrams have been constructed by combining the CAD files for the different parts, as provided by Thorlabs, and are reproduced here with permission. **a**) Global view of the instrument. Labeled items in the upper module are zoom optics (ZM), quarter-wave plate (QWP2), linear vertical polarizer (LVP), field lens (FL1), 90° kinematic mirror mount (KMM1), and camera (CAM1). **b**, **c**) Two magnified orthogonal views of the bottom module. Labeled items are quarter-wave plate (QWP1), variable liquid crystal retarder (V-LCR), linear horizontal polarizer (LHP), LED light source (LED), collimating condenser lens (CL), fluorescence cube assembly (FL-C), field lens (FL2), kinematic mirror mount (KMM2), and fluorescence camera (CAM2). See Video 5.1 for a 360 degree rotation of the full assembly.

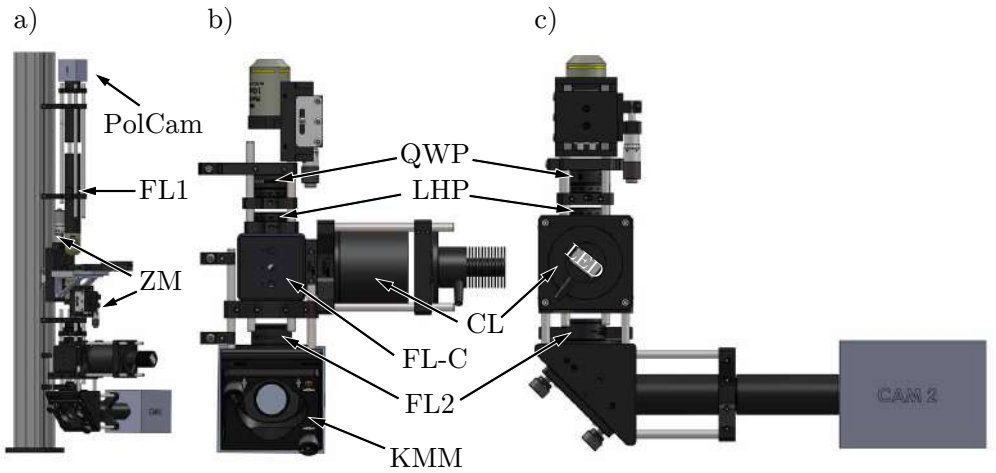

Figure 5.16: Optomechanical assembly of the setup for fast birefringence imaging with a polarization camera. These diagrams have been constructed by combining the CAD files for the different parts, as provided by Thorlabs, and are reproduced here with permission. **a**) Global view of the instrument. Labeled items in the upper module are zoom optics (ZM), field lens (FL1), and polarization camera (PolCam). **b**, **c**) Two magnified orthogonal views of the bottom module. Labeled items are quarter-wave plate (QWP), linear horizontal polarizer (LHP), LED light source (LED), collimating condenser lens (CL), fluorescence cube assembly (FL-C), field lens (FL2), kinematic mirror mount (KMM), and fluorescence camera (CAM2).

5.5 Videos

Video 5.1: 360 degree rotation displaying the full assembly of the LCR-based polarimeter with the fluorescence module. The diagram has been constructed by combining the CAD files for the different parts, as provided by Thorlabs, and are reproduced here with permission. To watch the video, click here or scan the QR-code in List of Videos

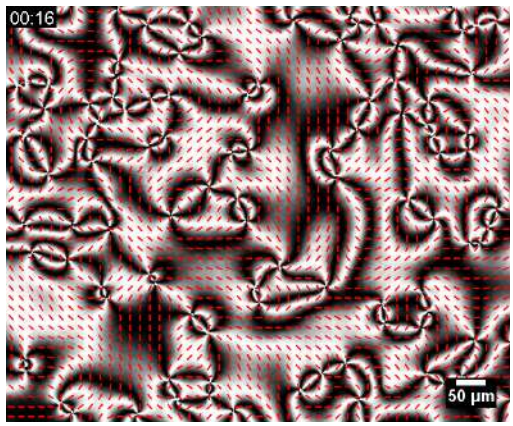

Video 5.2: POM micrographs obtained with the LCR-based polarimeter displaying an LC during the Friederik transition. With the polarimeter, we retrieve the LC's director θ and then we compute the POM micrograph as $I(\theta) \propto \sin^2 2\theta$. Red lines indicate the local director $\mathbf{n} = (\cos\theta, \sin\theta)$. The video is sped up x7.5. The LC used is the MLC 7029. To watch the video, click here or scan the QR-code in List of Videos

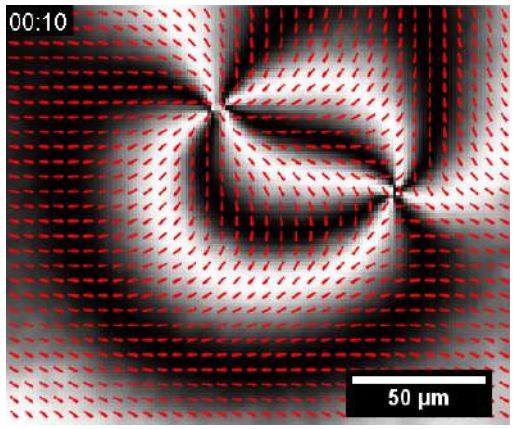

Video 5.3: Close-up POM images obtained with the LCR-based polarimeter displaying four topological defects annihilating. With the polarimeter, we retrieve the LC's director θ and then we compute the POM micrograph as $I(\theta) \propto \sin^2 2\theta$. Red lines indicate the local director $\mathbf{n} = (\cos\theta, \sin\theta)$. The video is sped up x7.5. The LC used is the MLC 7029. To watch the video, click here or scan the QR-code in List of Videos

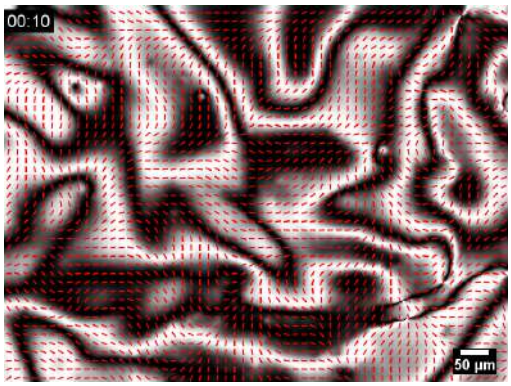

Video 5.4: POM images obtained with the LCR-based polarimeter displaying a passive LC dragged by the MT-based AN. With the polarimeter, we retrieve the LC's director θ and then we compute the POM micrograph as $I(\theta) \propto \sin^2 2\theta$. Red lines indicate the local director $\mathbf{n} = (\cos\theta, \sin\theta)$. The video is sped up x5. To watch the video, click here or scan the QR-code in List of Videos

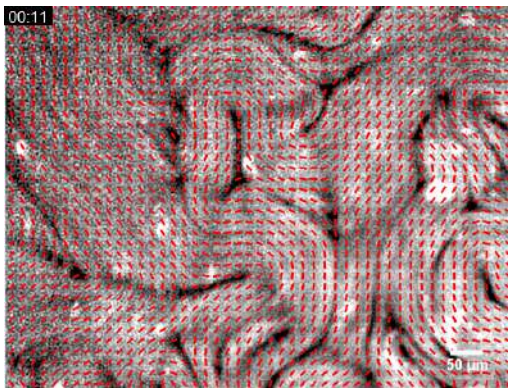

Video 5.5: Epi-fluorescence micrographs of the MT-based AN with the nematic director retrieved with the LCR-based polarimeter. Red lines indicate the local director $\mathbf{n} = (\cos\theta, \sin\theta)$. The video is sped up x10. To watch the video, click here or scan the QR-code in List of Videos

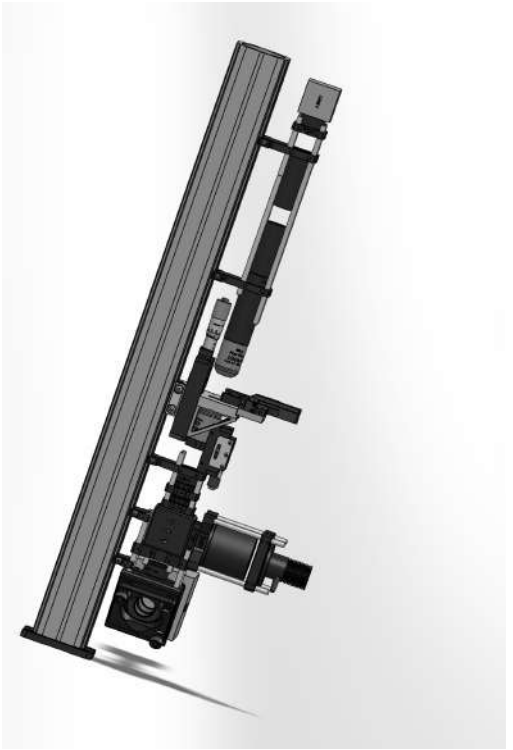

Video 5.6: 360 degree rotation displaying the full assembly of the polarization camera setup with the fluorescence module. The diagram has been constructed by combining the CAD files for the different parts, as provided by Thorlabs, and are reproduced here with permission. To watch the video, click here or scan the QR-code in List of Videos

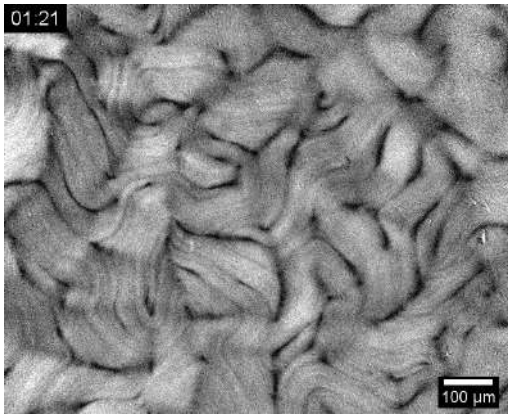

Video 5.7: Retardance map of the AN obtained with the polarization camera setup. Both images are overlaid to show the synchronization of both measurements. The fluorescence image is the one above. The video is sped up x9. To watch the video, click here or scan the QR-code in List of Videos

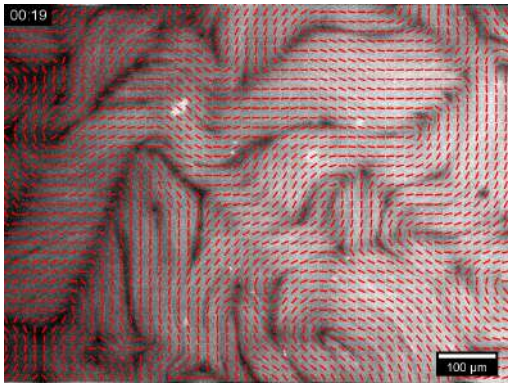

Video 5.8: Epi-fluorescence micrographs of the MT-based AN with the nematic director retrieved with the polarization camera setup. Red lines indicate the local director $\mathbf{n} = (\cos\theta, \sin\theta)$. The video is sped up x10. To watch the video, click here or scan the QR-code in List of Videos

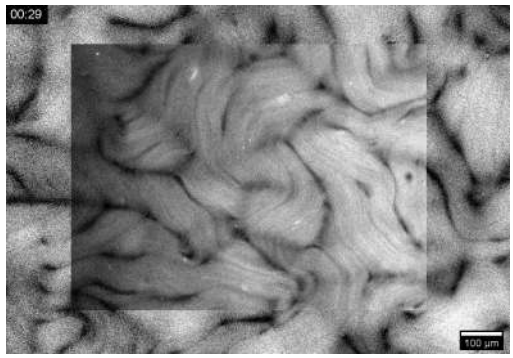

Video 5.9: Overlay of the retardance map, measured with the polarization camera setup, and the simultaneous fluorescence image of the AN. Both images are overlaid to show the synchronization of both measurements. The fluorescence image is the one above. The video is sped up x9. To watch the video, click here or scan the QR-code in List of Videos

Chapter 6

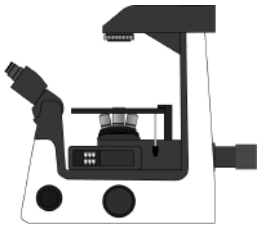

Materials and methods

6.1 Active nematic preparation

6.1.1 Kinesin expression

The kinesin we use in our experiments is the K401-BIO-H6, which is a dimeric kinesin containing the first 401 residues of kinesin-1 heavy chain (see Fig. 6.1a) of *Drosophila Melanogaster* and fused to a region of *Escherichia Coli* biotin carboxyl carrier protein (BCCP) and six histidines to enable protein purification [151]. The BCCP domain allows the formation of kinesin clusters because it can attach to a biotin molecule, which can in turn link to streptavidin molecules. Each streptavidin, as a tetrameric protein [152] with a molecular weight ∼52 kDa, can bind to up to four biotins (see Fig. 6.1b).

K401-BIO-H6 protein is expressed with *Escherichia Coli* (BL21(DE3)pLysS cells, resistant to chloramphenicol) transformed with the pWC2 plasmid (Addgene 15960) from Gelles Laboratory (Brandeis University) that contains the gene of the protein of interest and confers resistance against ampicillin [151].

Briefly, we harvest the E. Coli in LB broth (Sigma, L3022) with 2.5 µg/mL of chloramphenicol, 50 µg/mL of ampicillin, and 24.4 µg/mL of biotin at 37°C and 120 rpm until reaching OD_{600}=0.6, when 1mM of IPTG is added to induce protein overexpression. Cells are left overnight at 22°C and 140 rpm. The next day, the culture is centrifuged at 4,000 rpm and 4°C for 30 min. Pellets are re-suspended with HEPES buffer (50 mM HEPES, 4 mM $MgCl_2$, 10 mM β-mercaptoethanol and 50 µM of ATP at pH 7.2) supplemented with PIC and PMSF. The suspension is left at -80°C for 30 min and then, after adding 1

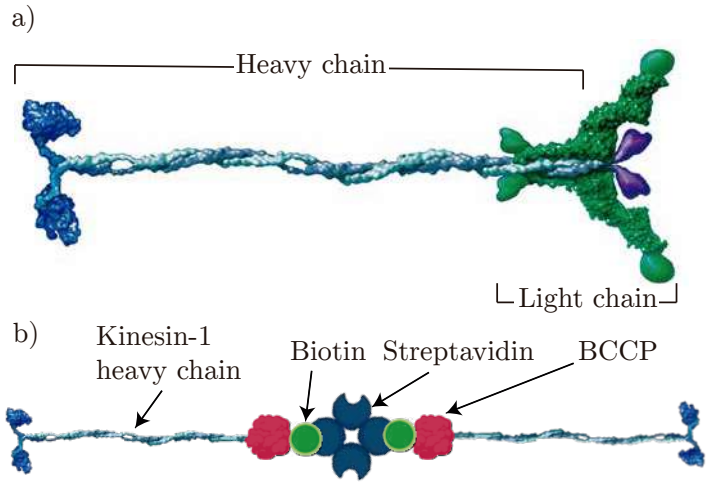

Figure 6.1: Kinesin-1 and K401-BIO-H6 - **a)** Sketch of kinesin-1 where the two chains of the molecular motor are indicated. The heavy chain allows the protein to move and the light chain can attach to cargos to actively transport them inside the cell (Adapted from [153]). **b)** Cluster of two kinesins. The genetically-engineered kinesin is formed by the heavy chain of kinesin-1 (kinesin-1 truncated at the residue 401) and the biotin carboxyl carrier protein (BCCP) which binds to one biotin. A streptavidin molecule then links two kinesins through the biotins. (The BCCP-biotin-streptavidin complex was created with BioRender.com)

mg/mL of lysozyme, it is sonicated with a probe-type sonicator to promote cell lysis. Solid residues are removed via ultra-centrifugation at 20,000 rpm for 20 min at 4°C. The protein is then loaded into a 1 mL nickel column (1 mL HiFliQ Ni-NTA FPLC column), washed with 20 mM imidazole in HEPES buffer, and eluted with 500 mM imidazole in HEPES buffer. A PD10 desalting column (GE Healthcare, GE17-0851-01) is used to exchange the buffer and thus remove the imidazole. We measure the resulting protein concentration by means of UV-Vis spectrophotometry (A_{280}, ε=30370 $^{-1}$cm^{-1}). The kinesin is finally stored with 40 %(w/w) of sucrose at -80°C after flash freezing with liquid nitrogen. In Appendix G, a more detailed protocol of the expression of K401-BIO-H6 can be found.

6.1.2 Microtubules polymerization

MTs are polymerized at 37°C for 30 min in M2B buffer (80 mM PIPES, 1 mM EGTA, 2 mM $MgCl_2$)(Sigma, P1851, E3889 and M4880, respectively) with α and β tubulin from bovine brain (a gift from Z. Dogic's group at Brandeis University (Waltham, MA)) and Guanosine-5'-[(α,β)-methyleno]triphosphate (GM-

PCPP) (Jena Biosciences, NU-405), a non-hydrolyzable analogue of GTP. GMPCPP catalyzes the polymerization of MTs at a similar rate to the one of GTP. Nevertheless, the depolymerization rate of the former is much smaller than the one of the latter. Hence, with GMPCPP it is possible to obtain stable MTs with a fixed length [154]. By controlling the concentration of GMPCPP, we could obtain MTs with a mean length of ∼1.5 µm. To enable the imaging of the active gel through fluorescence microscopy, part of the tubulin is labeled with Alexa-647 (Sigma, A20006). MTs are stored in small aliquots (∼2µL) at -80°C.

6.1.3 Active gel preparation

To assemble the active gel, we use different stock solutions (listed in Table 6.2), that we can store for several months under the appropriate conditions (also included in Table 6.2) upon use. The stock solutions that need to be stored at -20°C or -80°C, are split into smaller aliquotes with a volume ∼10% larger than the volume used to prepare the KSV, the PS, and the final active suspension. All the stocks are prepared either in M2B buffer, or phosphate buffer, or are kept in the aqueous solution as purchased. The pH of all the stock solutions is adjusted with either 1 M HCl (if it is too basic, pH > desired pH) or with 1 M KOH (if it is too acid, pH < desired pH). For small volumes of stock solutions, it is difficult to use a pH meter. Thus, we use pH indicator strips with a pH range between 6 and 8. It is important to use such a small range of pH to have enough sensitivity to adjust properly the pH at ∼6.8 because small changes in the pH can significantly impact the function of the proteins.

We prepare the active gel in four main steps that I explain here in detail. The diagram in Fig. 6.4 shows schematically the protocol we follow to prepare the active gel.

1- Preparation of KSV

K401-BIO-H6 motors (kinesins) are mixed at a 2:1 stoichiometric ratio with tetrameric streptavidin (Invitrogen, 43-4301) and incubated at 4°C for 30 min. This makes the KSV suspension. Here, we must remark that the expression of kinesin as described in Methods Section 6.1.1 can produce not active proteins. As a consequence, the activity of the active gel can be lower than the one expected for the concentration obtained through UV-Vis spectroscopy. One could try to do activity assays to extract the real activity of the protein suspension. Nevertheless, we do it empirically. Starting from the theoretical concentration of kinesin, we follow the protocol here described to prepare the active gel and screen different concentrations of molecular motors keeping the other compound concentrations constant until we obtain a high activity active gel without seeing crosslinking. At low concentrations of kinesins, streptavidin proteins are only bound to one molecular motor, giving a low activity active gel. As the concentration is increased, the activity rises until a point where streptavidins

Stock solutions			
Compound	**Concentration**	**Buffer**	**Storing conditions**
ATP	50 mM	M2B (pH 6.8)	-20°C
Catalase	3.5 mg/mL	20 mM K_2HPO_4 (pH 7.5)	-20°C
DTT	500 mM	M2B (pH 6.8)	-20°C
Glucose	300 mg/mL	20 mM K_2HPO_4 + 70mM KCl (pH 7.2)	-20°C
Glucose oxidase	20 mg/mL	20 mM K_2HPO_4 (pH 7.4)	-20°C
GMPCPP	10 mM	Aqueous solution, as provided by the manufacturer	-20°C
$MgCl_2$	67 mM	M2B (pH 6.8)	4°C
MTs	8mg/mL	M2B (pH 6.8)	-80°C
PEG, 20 kDa	12 % (w/w)	M2B (pH 6.8)	-20°C
PEP	200 mM	M2B (pH 6.8)	-20°C
PKLDH	917 units/mL PK	Aqueous buffered glycerol solution, as provided by the manufacturer	-20°C
Pluronic	17 % (w/w)	M2B (pH 6.8)	4°C
Streptavidin	0.352 mg/mL	M2B (pH 6.8)	-20°C
Trolox	20 mM	20 mM Phosphate (pH 7.48)	-20°C

Table 6.2: Stock solutions for the preparation of the active gel List of the different solutions used to prepare the active solution.

start being bound to more than two kinesins. Consequently, activity starts dropping, and crosslinking can be observed. Maximum activity is reached at a kinesin/streptavidin ratio of ∼1:2 [112].

In our case, we find a good preparation to be: 5 µL stock Kinesin + 1 µL stock streptavidin solution (0.352 mg/mL) + 0.5 µL stock dithiothreitol (DTT)

diluted by 100 (5 mM).

2- Preparation of PS

To prepare the PS suspension, we mix the non-adsorbing polymer PEG (20kDa) (Sigma, 95172) to promote the aggregation of the MTs into bundles through depletion forces, ATP to fuel the kinesins (Fig. 6.2) and an ATP-regenerating system (PK/LDH and phosphoenol-pyruvate) (Fig. 6.3) to maintain the ATP concentration constant. The presence of this regenerating system does not limit the rate of ATP hydrolysis by kinesins [155]. In addition to such compounds, we also add $MgCl_2$ to reach an adequate ionic force and anti-oxidants (Trolox, glucose, glucose oxidase, catalase, and DTT (Sigma, 238813, G8270, G2133, C1345, 43815, respectively)) to ensure the correct functionality of the proteins by preventing photo-bleaching, the formation of sulfur bonds and the oxidation of the proteins by oxygen species. Finally, in the cases when we want to prepare an active nematic that forms at an oil/water interface, we supplement the MTs aqueous suspension with the PEGylated surfactant pluronic (Sigma P2443). This compound assures the bio-compatibility of the proteins with the interface. The volumes of stock solutions we mix are: 8 µL 12 % (w/w) PEG + 8 µL 200 mM PEP + 6 µL 20 mM Trolox + 2.9 µL 67 mM $MgCl_2$ + 1.7 µL 50 mM ATP + 1.7 µL 917 unit/mL PKLDH + 1.5 µL 17 % (w/w) Pluronic + 0.66 µL 3.5 mg/mL Catalase + 0.66 µL 300 mg/mL Glucose + 0.66 µL 500 mM DTT + 0.66 µL 200 mg/mL Glucose Oxidase.

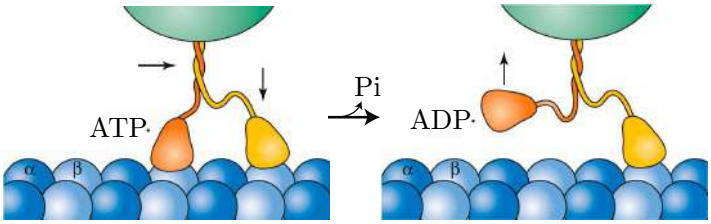

Figure 6.2: Kinesins obtain energy from ATP and release ADP and phosphoric acid - Chemical energy stored in the phosphate-phosphate bond fuels kinesins, which take the ATP, make one step forward, and release adenosine 5′-diphosphate (ADP) and phosphoric acid (P_i). (Adapted from [50]))

3- Mix of KSV+PS+M2B

Once we have waited for 30 minutes to ensure the formation of the kinesin clusters, we can mix the KSV with the PS. We supplement this mixture with M2B to attain suitable concentrations. For the kinesin we have expressed, we

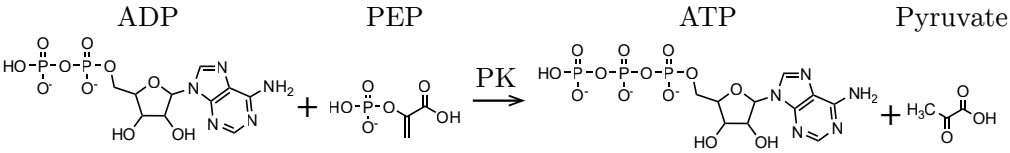

Figure 6.3: ATP regenerating system - ADP is converted back to ATP thanks to pyruvate kinase (PK) that catalyzes the reaction of ADP with phosphoenolpyruvate (PEP).

mix 10 µL PS + 2.75 µL KSV + 2.25 µL M2B. These ratios should be changed depending on the activity of the kinesin.

6

4- Preparation of the active solution or active gel
Finally, we mix a small volume of the motors and ATP solution with the MTs at a ratio of 1:5. Depending on the sample we want to prepare (see Methods Section 6.1.4), we make up a volume of 2 µL or 8 µL. With this mixture, the MTs self-assemble into a percolating active network. The experiments in this thesis have been performed in the presence of such interface.

Final concentrations of all compounds are listed in Table 6.3

Active nematic composition			
Compound	**Concentration**	**Compound**	**Concentration**
Streptavidin	0.16 µM	PK/LDH	27 IU/mL
Kinesin	0.32 µM	Pluronic	0.44 % (w/w)
DTT	5.8 mM	Glucose	3.4 mg/mL
PEG (20 kDa)	1.6 % w/w	Catalase	0.040 mg/mL
PEP	27 mM	Glucose oxidase	0.23 mg/mL
Trolox	2.1 mM	MTs	1.3 mg/mL
$MgCl_2$	3.3 mM	GMPCPP	0.1 mM
ATP	1.5 mM		

Table 6.3: Typical composition of the active nematic

6.1.4 Assembly of the 2D active nematic. Experimental setup

In the presence of an oil/water interface, the network of active filaments bewitchingly forms a 2D active layer with nematic order. This is thanks to depletion

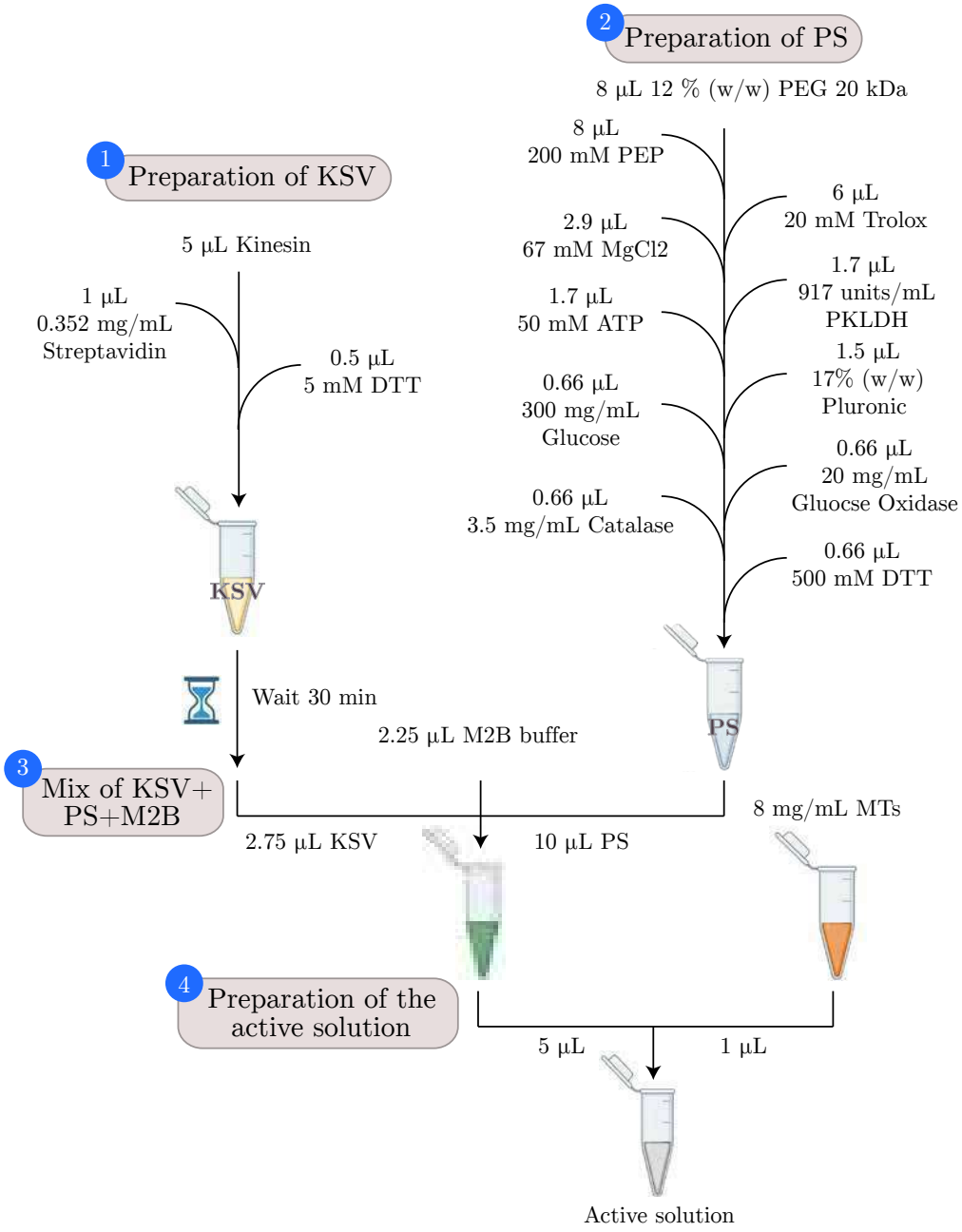

Figure 6.4: Protocol diagram of the preparation of the active gel - All the volumes are of the stock solutions

forces due to the PEG that promote the adsorption of the MT bundles onto the fluid interface. To obtain such interface, we use two different approaches depending on the experimental requirements.

The first one consists of a chamber built between two glass slides with two sheets of double-sided tape (thicknesses from 25 to 100 μm, 3M) as spacers. One of the slides is functionalized with a polyacrylamide brush (see Methods Section 6.1.6.1) to hydrophylize the substrate and prevent the proteins from sticking to the glass and denaturalizing. The other slide is functionalized with aquapel (see Methods Section 6.1.6.2), obtaining in this way a very hydrophobic surface (see Figs. 6.5a and 6.5b). A fluorinated oil (HFE 7500, 3M Novec 7500 Engineered Fluid) with 2% fluorosurfactant (008-FluoroSurfactant, RAN Biotechnology) is then flowed into the chamber (Fig. 6.5c), followed by the MTs aqueous suspension, that displaces the oil (Fig. 6.5d). However, due to the difference in the hydrophobicity of the two slides, a stable thin oil layer remains (Fig. 6.5e).

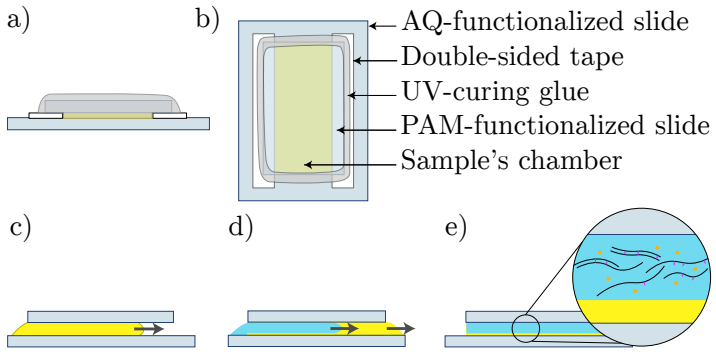

Figure 6.5: Flow-cell experimental setup - Front (**a**) and top view (**b**) of a sketched flow cell. **c**)-**e**) Filling of the cell. The oil is first flowed through the chamber (**c**) and then replaced by the aqueous suspension of proteins (**d**) a thin oil layer remains wetting the hydrophobic slide (coated with Aquapel, AQ) (**e**).

The other approach consists of the assembly of an open cell with the sample contained inside a polydimethylsiloxane (PDMS) block with a well in the center. To prepare the block, we cure PDMS at 70°C for at least 4 hours inside a 3D-printed poly-lactic acid(PLA) mold (Fig. 6.6). Afterward, we glue the block onto a hydrophilic and bioinert polyacrylamide (PAM) coated glass with a UV-curing adhesive (Norland, NOA81). We finally introduced in the pool 1.5 μL of the aqueous suspension and 300 μL of silicon oil (Rhodorsil Oils 47 from Bluestar Silicones) on top of it. Since the active nematic needs to be protected from the air, we use an oil less dense than water, thus gravity forces drag the aqueous suspension to the bottom leaving the oil layer covering it. After ∼20 min the

active nematic spontaneously forms.

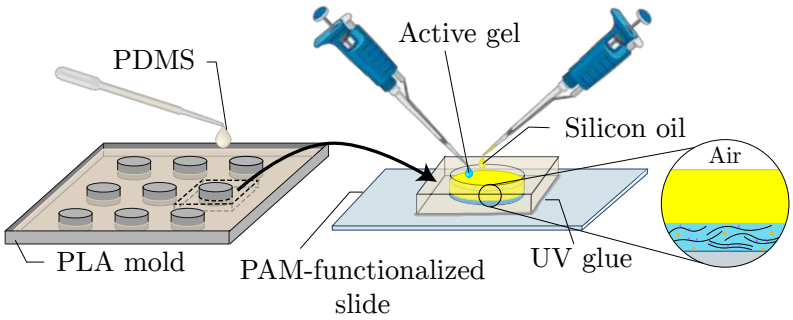

Figure 6.6: Open cell experimental setup - PDMS is polymerized within a PLA mold to create pools. A block containing a well is then cut and glued onto a PAM-functionalized glass slide using UV-curing adhesive. The MT-aqueous suspension (active gel) is injected within the pool and followed by the silicon oil that is in contact with the air and with the active gel droplet. The latter interface is where the MTs condenses and forms the AN.

6.1.5 AN for Particle Image Velocimetry

To extract the flow field of the AN through PIV (Methods Section 6.4.1), we use unlabeled MTs and dope them with fluorescent MTs (200:1) to obtain a speckled pattern. Both types of MTs are prepared as explained in Methods Section 6.1.2, but using either non-fluorescent or highly-fluorescent tubulin (∼75% labeled tubulin), respectively. We remark that multiple freezing and unfreezing cycles of the MTs induces their aggregation Fig. 6.7. This clustering can be useful when working at small magnifications, when more light intensity is required, although, it compromises up to some degree the resolution.

6.1.6 Glass-slides functionalization

Proteins tend to stick onto glass. Hence, it is imperative to functionalize glass slides and make them bio-compatible. Depending on the desired hydrophobicity, we follow the following two protocols.

6.1.6.1 Hydrophilic glass slides. Polyacrylamide brush

One of the most common surface treatments for biological samples is the attachment of a polyacrylamide brush onto the substrate to avoid the adsorption of proteins thanks to steric repulsion. The coating of the slides is pre-

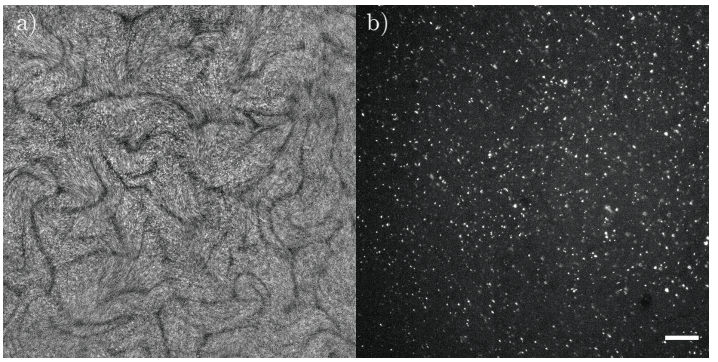

Figure 6.7: Fluorescent MTs tend to aggregate during freezing/unfreezing cycles - Fluorescence micrographs of the AN using highly fluorescent MTs that have been frozen one (**a**) and two (**b**) times. Scale bar, 100 µm.

pared by first cleaning and activating the glasses with an alkaline solution (0.1 M NaOH). Then we silanize the glasses with an acid ethanolic solution of 3-(trimethoxysilyl)propyl methacrylate (Sigma, 440159) to create polymerization seeds. The slides are subsequently rinsed with ethanol followed with Mili-Q water and then immersed in a degassed 2% (v/v) acrylamide solution with the initiator ammonium persulfate (APS, Sigma, A3678) and the catalyst N,N,N',N'-Tetramethylethylenediamine (TEMED, Sigma, T9281) for at least 2 hours. The substrates are stored until their usage in the acrylamide solution.

6.1.6.2 Hydrophobic glass slides

Hydrophobic glass slides are obtained with aquapel functionalization. We place a clean glass slide to be functionalized on top of a glass slide with a small volume (∼20 µL) droplet of Aquapel. We let it sit for 30 seconds and then rinse the glass slide.

6.1.7 Prepration of oil mixtures

To attain oils of many different viscosities, we prepare oil mixtures. Next, we estimate the final viscosity, η_{12}, using the Arrhenius mixing rule $\log \eta_{12} = \chi \log \eta_1 + (1-\chi_1) \log \eta_2$, with η_1 and η_2 the oil viscosities of the mixed compounds 1 and 2, respectively, and χ_1 is the molar fraction of oil 1.

6.2 Radial alignment of the AN layer

To align radially the AN, we hold a capillary tube (outer and inner diameters: 1.2 mm and 0.3 mm) with a linear motion stage (KDC101, Thorlabs) right above the oil layer with the AN already formed at the interface in the open cell experimental set up (see Methods Section 6.1.4 and Fig. 6.8). The tube is then slowly introduced into the fluid until it touches the oil-water interface, creating an inwards flow that aligns the AN. The capillary is removed after a few seconds letting the AN evolve freely from the radial alignment towards the turbulent regime.

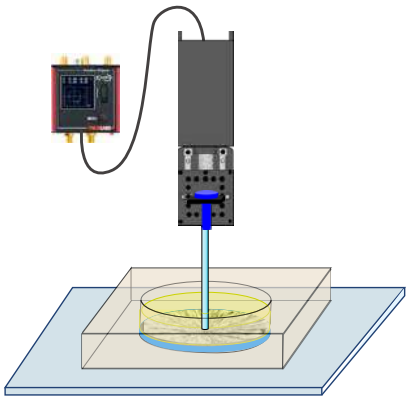

Figure 6.8: Radial alignemnt of the AN. We introduce a glass capillary tube (1.2 mm outer diameter, 0.3 mm inner diameter) into the pool until it touches the oil/water interface to produce inwards flows that organize the active material in a radial geometry. The capillary is removed after few seconds, which allows the radially aligned active nematic to evolve freely. Imaging is only performed after the capillary has been removed, monitoring this way the onset of the bend instability. To enable the introduction of the capillary, this experiment is performed using the open cell setup (see Fig. 6.6).

6.3 Fluorescence microscopy

One of the techniques we use to image the active nematic is fluorescence microscopy. In this type of microscopy, a beam of light with a given wavelength is shined toward the fluorescent sample (the exciting beam). After a few nanoseconds, the fluorophore[1] emit a light beam (the emitting beam) with a wavelength

[1]Fluorophores are fluorescence-emitting molecules generally used to label molecules to be imaged. Fluorophores tend to present conjugated double bonds and aromatic groups (ring

typically larger than the incident one. The exciting light is filtered out, letting only the emitted beam reach the detector. Therefore, only the molecules that fluoresce are seen, whereas the background remains dark [156]. In practice, biological samples do not fluoresce by themselves, thus, they must be attached to a fluorophore. In our case, we tag our tubulin with the far-red-fluorescent dye Alexa-647 (Invitrogen, A2006). This molecule allows us to correctly resolve the image because the exciting and the emission spectra are well separated, and it has a high quantum yield. This quantity gives the ratio between the number of emitted to absorbed photons, and it must be taken into account when choosing the fluorophore to use. A fluorophore with a low quantum yield does not only mean less fluorescence intensity, but also a higher probability of having not desired photochemical processes like bleaching and free radical formation that can significantly affect the sample [156].

For our experiments, we use the so-called epi-illumination fluorescence microscope (Fig. 6.9), in which both the excitation and emission beams cross the objective. Since these two beams overlap in the light path, a beam splitter is needed. This is the dichroic mirror, which reflects shorter wavelengths coming from the light source and transmits longer wavelengths emitted by the sample. Dichroic mirrors should be changed depending on the fluorophore of the sample. Usually, they are integrated into a filter cube set, which also includes two filters: the excitation and the emission filters that block out the wavelengths not contributing to the fluorescence. In our lab, we have two different set-ups for fluorescence microscopy. First, we have a Nikon Eclipse Ti2-U inverted microscope equipped with a Cy5 filter (#67-010-OLY, Edmund), compatible with Alexa-647 dye, and an Andor Zyla 4.2 Plus camera controlled with either the open-source software ImageJ Micro-Manager [157]. This setup is optimal for obtaining high-quality images. Nevertheless, it is not very customizable. In contrast, we have a highly-versatile custom-made microscope assembled with Thorlabs parts. With this setup, we can add almost any module we want to perform different experiments. For instance, we use this fluorescence microscope to attach a z-position motion stage and align our active nematic (see Methods Section 6.2) or to integrate it with the polarimeter explained in Section 5.1.

6.4 Image and data analysis

6.4.1 Particle image velocimetry

PIV is a non-invasive technique used to quantitatively determine the velocity field of a fluid [158, 159, 160, 161]. The idea of this technique is to seed the

structures), like benzenes. This is because a higher degree of conjugation results in a lower exciting energy requirement and a higher fluorescence intensity relative to the exciting intensity.

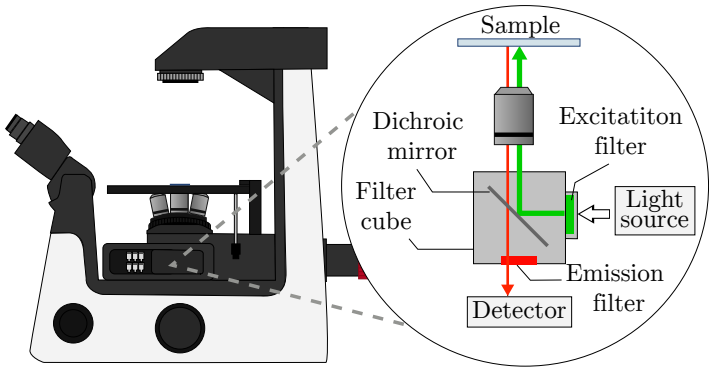

Figure 6.9: Epi-illumination fluorescence microscope - Sketch of an inverted fluorescence microscope with epi-illumination. In this kind of setups, the light source sends a wide range of wavelengths, but only the ones that can excite the fluorophore of interest can go through the excitation filter of the filter cube and arrive at the sample. Fluorophores emit light in all directions and a portion of such light crosses the objective and the emission filter to finally reach the detector. In the detector, the signal is usually amplified since the fluorescence intensity is low. The dichroic mirror separates the excitation from the emitted beam.

fluid with particles to create a speckled pattern in an otherwise homogeneous media. The particles are then tracked to extract the flows within the fluid. These tracers must be small enough and have a similar density to the fluid to assure they follow the streams at the same velocity as the fluid. In our experiments, we use fluorescent-labeled MTs (see Methods Section 6.1.5) that we follow through fluorescence microscopy (see Methods Section 6.3). Afterwards, to extract the flows, the images are divided into sub-areas called interrogation windows (IWs) and the most probable displacement of the particles within an IW is then determined by cross-correlating a pair of subsequent IW A and B with sizes $I \times J$ and $M \times N$, respectively:

$$C(m,n) = \sum_{i=1}^{I} \sum_{j=1}^{J} A(i,j)B(i-m, j-n) \tag{6.1}$$

with $-(M-1) \leq m \leq I-1$ and $-(N-1) \leq n \leq J-1$. Cross-correlation gives the degree of matching between two matrices (in this case two IWs) with a shift. Therefore, the position of the peak in $C(m,n)$ corresponds to the most probable displacement of the particles from A to B. Note that the result of the PIV is highly sensitive to the IW size.

In practice, the computation of cross-correlation in the real space using Eq. 6.1 is highly expensive computationally speaking. Hence, $C(m,n)$ is usually obtained in the Fourier space by applying the cross-correlation theorem [162].

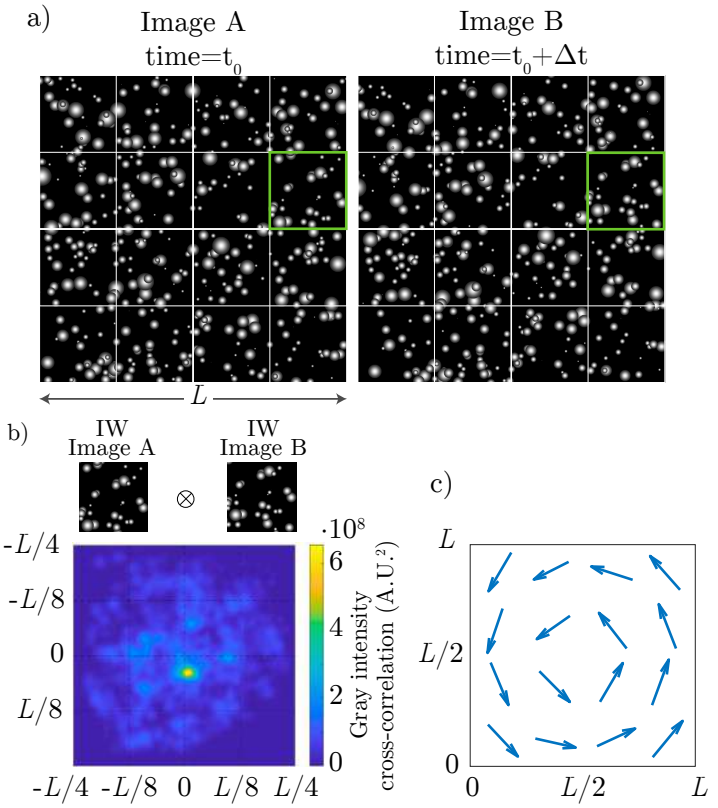

Figure 6.10: The PIV algorithm - **a**) Synthetic image divided into 16 IWs. **b**) Cross-correlation calculation of the IWs framed in green in (**a**). **c**) Resultan flow field of the image in (**a**).

For our analysis, we use the off-the-shelf software PIVlab implemented in Matlab [159, 160]. Post-processing of the PIV results is also carried out with such program, which can filter out the outlying data and smooth the flow field.

Depending on the fluorescence images, the outcome from the PIV analysis can be very noisy. To asses whether the obtained velocity field is not the result of the background noise, but the signal of the fluorescent MTs, we calculate the temporal autocorrelation of the computed velocity field (see Methods Section 6.4.7). If the correlation drastically drops from one frame to the next one, this means that the resulting velocity field is too noisy and further filtering of the fluorescence images should be performed.

6.4.2 AN Director determination through coherence enhanced diffusion

Apart from the previously explained method based on polarizing microscopy (see Section 5.1), we also use an alternative method to obtain the AN director, $\mathbf{n}$, described [118, 163] from fluorescence-microscopy images. In this case, the director is obtained using coherent-enhanced diffusion filtering (CEDF) [164], a technique employed to complete and enhance interrupted lines or flow-like structures, like the ones in fingerprints or the ones formed by the fluorescent MTs in the AN. To this aim, CEDF infers the direction with the weakest spatial intensity fluctuations at a pixel level, which for the AN corresponds to the local alignment of the MTs.

First of all, a gaussian blur filter of standard deviation σ and side length $6\sigma - 1$ is applied to a raw image I to get the blurry image I_σ. Then, we obtain the tensor product of ∇I_σ:

$$(\nabla I_\sigma)(\nabla I_\sigma)^T = \begin{bmatrix} (\nabla_x I_\sigma)(\nabla_x I_\sigma) & (\nabla_x I_\sigma)(\nabla_y I_\sigma) \\ (\nabla_y I_\sigma)(\nabla_x I_\sigma) & (\nabla_y I_\sigma)(\nabla_y I_\sigma) \end{bmatrix} \tag{6.2}$$

We need to work with this tensor instead of the gradient vector, ∇I_σ, itself to preserve the head-to-tail symmetry of MTs. Another Gaussian blur filter of standard deviation ρ is applied to the gradient tensor to get rid of the small-scale fluctuations in the coherence direction. ρ must be of the order of the size of the coherent domains in the images. The eigenvector of the resultant tensor with the smallest eigenvalue, $\mathbf{u}$, gives the orientation where the intensity fluctuates the least. Due to the nematic symmetry of the problem, the angle associated to $\mathbf{u}$ must be within the interval $[0^o, 180^o)$. From $\mathbf{u}$, we can find the 2D tensor nematic parameter, $\mathbf{Q}$:

$$\mathbf{Q} = \left\langle \mathbf{u}\mathbf{u}^{\mathrm{T}} - \frac{1}{2}\mathbf{I} \right\rangle \tag{6.3}$$

where $\langle \cdot \rangle$ indicates an average over a disk of size β and $\mathbf{I}$ the identity matrix. Finally, we have to diagonalize $\mathbf{Q}$ to fetch for each pixel (see Info Box 6.1):

$$\mathbf{Q} = S\left(\mathbf{n}\mathbf{n}^{\mathrm{T}} - \frac{1}{2}\mathbf{I}\right) \tag{6.4}$$

where $S \in [0, 1]$ is the scalar order parameter, which provides information about the degree of alignment of $\mathbf{u}$ (local molecular orientation) relative to $\mathbf{n}$ (mean molecular orientation inside a disk of radius β). Note that this last step is only an average process. Actually, if β was set to 0, we would obtain $S = 1$ and $\mathbf{n} = \mathbf{u}$. We need to perform this average because S is a mean value.

The choice of parameters σ, ρ, and β depends on each experiment because the formulation of the AN, the magnification, and the microscope significantly affect the size of the relevant features in the experiment.

Infobox 6.1: The eigenvectors and the eigenvalues of the Q tensor

We start by expressing the $\mathbf{Q}$ tensor as

$$\mathbf{Q} = S(\boldsymbol{nn}^T - \mathbf{I}/2) = S \begin{pmatrix} \cos(2\theta)/2 & \sin(2\theta)/2 \\ \sin(2\theta)/2 & -\cos(2\theta)/2 \end{pmatrix}, \tag{6.5}$$

where $\mathbf{I}$ is the identity matrix. Now, to look for the eigenvalues λ, we compute the characteristic polynomial

$$\det(\mathbf{Q} - \lambda\mathbf{I}) = \lambda^2 - \frac{\mathrm{S}^2}{4}(\cos^2 2\theta + \sin^2 2\theta) = \lambda^2 - \frac{\mathrm{S}^2}{4}. \tag{6.6}$$

Thus, $\lambda_\pm = \pm S/2$
If we only take the positive eigenvalue, $\lambda = S/2$, we can compute the corresponding eigenvector $\mathbf{v} = \begin{pmatrix} a \\ b \end{pmatrix}$ applying $(\mathbf{Q} - \lambda\mathbf{I})\mathbf{v} = \mathbf{0}$ and find the following relation:

$$b = a\,\frac{1 - \cos 2\theta}{\sin 2\theta} \tag{6.7}$$

Choosing $a = \sin 2\theta$:

$$\mathbf{v} = \begin{pmatrix} a \\ b \end{pmatrix} = \begin{pmatrix} \sin 2\theta \\ 1 - \cos 2\theta \end{pmatrix} \tag{6.8}$$

Now, we can readily see that the orientation of the eigenvector gives the orientation of the nematic field:

$$\theta = \operatorname{atan}\left(\frac{b}{a}\right) = \operatorname{atan}\left(\frac{1 - \cos 2\theta}{\sin 2\theta}\right) = \operatorname{atan}\left(\frac{\sin\theta}{\cos\theta}\right) \tag{6.9}$$

Therefore, if we have $\mathbf{Q}$, we can extract S and $\boldsymbol{n}$ (or θ) from the diagonalization of $\mathbf{Q}$.

6.4.3 Defect location and classification. Winding number

Regions with a low value of S are good candidates to feature topological defects. Hence, using a custom-made MatLab code, we look for areas with S below a threshold value, typically 0.1, and compute the winding number w along a closed-loop centered on the point of minimum S. We numerically obtain w as $w = 1/2\pi \oint(\partial\theta/\partial u)du$, where θ is the angle of $\mathbf{n}$ and u is the arc length along the loop (the script used to compute w, winding.m, can be found in here. You can also scan the QR in List of Codes). Regions of interest with $w \in \pm[0.49, 0.51]$ are identified as $\pm 1/2$ defects. Note that, because of the nematic symmetry of the director field, we need to include in the code that only jumps in the director smaller than $\pi/2$ between subsequent pixels are allowed.

6.4.4 Characterization of the bend instability

6.4.4.1 Determination of the characteristic wave number

After the radial alignment of the AN, the material develops an instability triggering the formation of a concentric pattern with a characteristic spacing between dark lanes (Fig. 6.11a). To characterize such spacing, we time-average subsequent frames and measure light intensity along a direction orthogonal to the kinks (Fig. 6.11b). We finally extract the characteristic wavenumber q^* (in [1] it appears as k^*) performing an FFT with Matlab (Fig. 6.11c). Error bars are calculated as the standard deviation of the mean of 10 measurements along different radial directions in a given experiment.

6.4.4.2 Determination of the characteristic growth rate

Next, we characterize the time evolution of the instability by monitoring the FFT image over time with ImageJ (Figs. 6.12a and 6.12b). To do so, we follow the here listed steps. Unless specified otherwise, all these steps are performed with ImageJ.

1. Cut the image taking a region where the pattern is well observed.

2. Apply a Hann window to diminish the FFT noise. We create a MatLab script to compute a 2D Hann window using the equation $W = 1/2(1 - \cos(2\pi n_x/N_x)) + 1/2(1 - \cos(2\pi n_y/N_y))$. The resulting filter is saved in a file, which is later read with ImageJ as an image and multiplied by the images to be analyzed.

3. Compute the 2D-FFT.

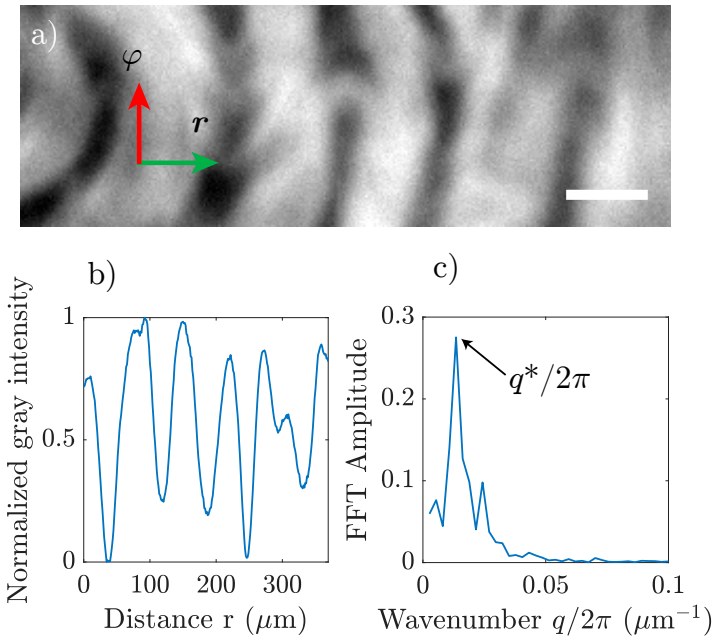

Figure 6.11: Determination of the predominant instability wavenumber. **a**) Striped pattern formed by the active material after it has been radially aligned and it has developed the instability in the azimuthal direction (φ, vector in red). Experimental conditions: [ATP]=1.5 mM, [Streptavidin]=8.2 µg/mL, [MTs]=1.3 mg/mL and [PEG]=1.7 %. Scale bar: 100 µm **b**) Intensity profile in (**a**) along the radial direction ($\boldsymbol{r}$, vector in green) at the center of the image. **c**) Power spectrum of (**b**), with $q = 2\pi/l^*$, showing the predominance of a peak, which defines q^*. Figure adapted from [1]

4. Measure and later average the grey intensity at different radii of the FFT-image along the normal direction to the pattern in the real. We retrieve in this way the average gray intensity for the different modulus of the wave numbers.

These steps are repeated for each frame and finally saved as a 2D matrix. These data is later opened with MatLab. We see that, at short times, the FFT intensity of the characteristic length grows exponentially. Hence, we can fit our data to an exponential trend and extract a characteristic growth rate Ω^* (Figs. 6.12c to 6.12e). Error bars are calculated as the uncertainty in the fitted parameter.

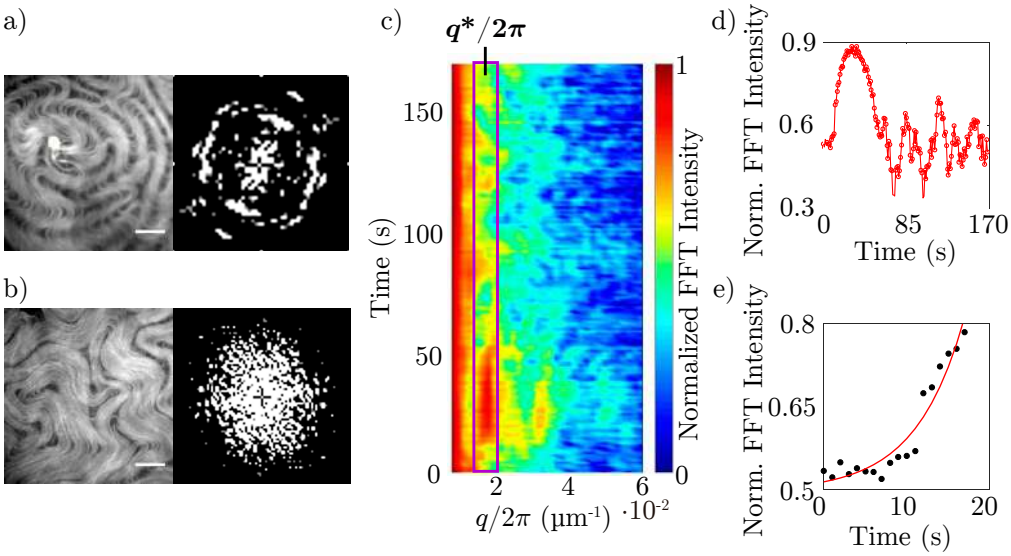

Figure 6.12: Determination of the characteristic time-scale. **a**) Fluorescence micrograph of a pattern displayed by the material after its induced-alignment (left) and FFT image of the micrograph (right). **b**) Fluorescence micrograph of the material once it arrived at the active turbulent state (left) and the corresponding FFT-image (right). Contrary to the images in **a**, there is no predominant wavenumber. Scale bar: 100 μm Experimental conditions of (**a**) and (**b**) are: [ATP]=1.5 mM, [Streptavidin]=8.2 μg/mL, [MTs]=1.3 mg/mL and [PEG]=1.7%. **c**) Kymograph of the normalized FFT amplitude of a growing pattern as a function of the wave number magnitude, $q = 2\pi/l$. For each q, the radial-averaged amplitude is recorded. Near $q/2\pi = 2 \cdot 10^{-2}$ μm^{-1} (region inside the purple rectangle) there is a hotspot region that corresponds to the time when the active material features a periodic pattern like the one shown in **a**. This defines q^*. **d**) Time evolution of the FFT amplitude at the wavenumber q^*. **e**) At early times, this amplitude grows exponentially, allowing to extract the intrinsic growth rate, Ω^*. The red line corresponds to the exponential fitting.

6.4.4.3 Measurement of angle perturbations

Moreover, in Appendix A.3, we show that the axial symmetry of the aster configuration triggers the growth of angle perturbations $\delta\psi(r)$ following Bessel functions of the first kind with imaginary order n. Here $\delta\psi$ is the deviation of the director from the perfect aster disposition. Therefore, we first determine the $\boldsymbol{n} = (n_x, n_y) = (\cos\theta, \sin\theta)$ director field as explained in Methods Section 6.4.2. Now, given the axial symmetry, we must change the coordinate system to polar. However, if we want to angle average $\delta\psi$, we need to polarize the nematic director field towards the center of the pattern. Otherwise $\delta\psi(r)$ will vanish. Then, we write the $\boldsymbol{n}$ director in terms of the polar coordinates $(n_r, n_\varphi) = (\cos\theta\cos\varphi - \sin\theta\sin\varphi, \cos\theta\sin\varphi + \sin\theta\cos\varphi)$ with origin at the center of the aster, which we place manually. We finally extract $\delta\psi$ as:

$$\delta\psi = \operatorname{atan}\left(\frac{n_\varphi}{n_r}\right) \tag{6.10}$$

and perform an angle average.

6.4.5 Detection of vortices

Vortices in the AN are detected using the Okubo-Weiss (OW) criterion [75, 94]. This criterion parametrizes the stability of two initially close particles immersed in a 2D velocity field at a given time $\vec{v}(x, y, t)$ by analyzing the evolution of a small perturbation of the flow field $\delta\vec{v}$. We start by writing the evolution of this small perturbation in terms of the Jacobian of $\vec{v}$ as:

$$\begin{pmatrix}\delta v_x\\ \delta v_y\end{pmatrix} = \begin{pmatrix}\partial_x v_x & \partial_y v_x\\ \partial_x v_y & \partial_y v_y\end{pmatrix}\begin{pmatrix}\delta x\\ \delta y\end{pmatrix} \tag{6.11}$$

Now, we assess the stability of the velocity field by looking for the eigenvalues $\lambda_\pm$ of the Jacobian matrix given by:

$$\lambda_\pm = \frac{-(\partial_y v_y + \partial_x v_x) \pm \sqrt{(\partial_y v_y + \partial_x v_x)^2 - 4(\partial_x v_x \partial_y v_y - \partial_y v_x \partial_x v_y)}}{2} \tag{6.12}$$

If we consider the fluid to be incompressible, $\partial_x v_x + \partial_y v_y = 0$, we can simplify Eq. 6.12 to:

$$\lambda_\pm = \frac{\pm\sqrt{-4(-(\partial_x v_x)^2 - \partial_y v_x \partial_x v_y)}}{2} = \sqrt{(\partial_x v_x)^2 + \partial_y v_x \partial_x v_y} \tag{6.13}$$

The term inside the square root is the OW parameter ($\mathrm{OW} = (\partial_x v_x)^2 + \partial_y v_x \partial_x v_y$). In the regions of the fluid with $\mathrm{OW} < 0$, the distance between the two particles

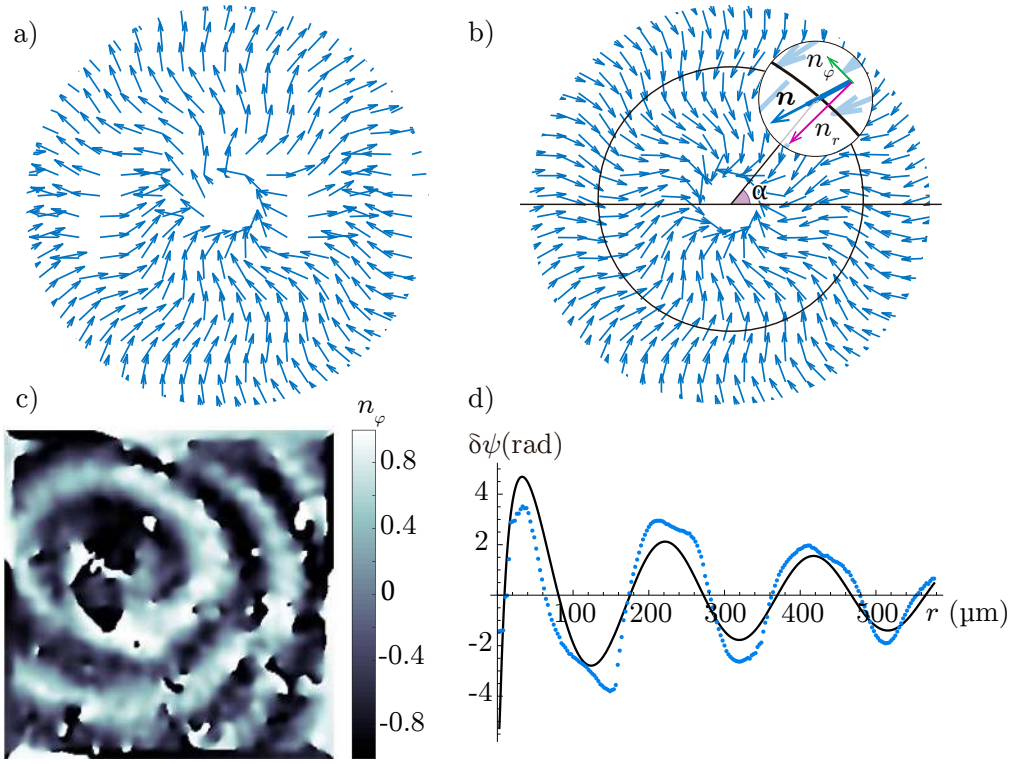

Figure 6.13: Determination of the angle perturbations from the radial aligned state. **a**) Simulated director field of a concentric pattern as the ones seen in the experiments. **b**) Polarized director field in **a** toward the center of the aster. **c**) Azimuth component of $\boldsymbol{n}$, n_φ, of an experiment. **d**) Resultant $\delta\psi = \text{atan}(n_\varphi/n_r)$, with n_φ represented in **c**, after the angular average.

embedded in the fluid will not diverge exponentially with time, whereas in the regions with OW > 0, it will diverge. Hence, coherent vortices are expected to be at simply connected regions with OW < 0 (see Fig. 6.14a). Notice here the term coherent. Not all regions with OW < 0 feature vortices. Thus, to classify a simply connected region as a vortex, we must check if it contains a singularity with a winding number of $+1$ (see Section 6.4.3 and Fig. 6.14b).

As the velocity fields of our experiments are discrete, we use the five-point method to compute the spatial derivatives of the velocity. Hence, for a function $f(x, y)$ and for the derivative with respect to x with a spacing between points

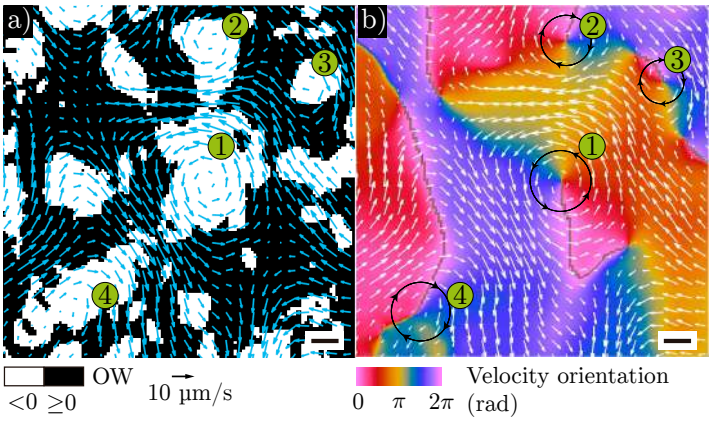

Figure 6.14: Detection of vortices. **a**) OW parameter computed using the experimental velocity field depicted in blue arrows. **b**) Orientation of the local velocity. The vortices are regions with OW< 0 (areas in white) and with a rotation of the velocity field of 2π within a closed loop (black lines in **b**. The direction of the arrows indicate the direction of circulation of the flow). White arrows indicate the local flow velocity (same as in **a**. The located vortices are enumerated in both panels (green circles). The velocity field, obtained from PIV (see Fig. 6.10) has been filtered with a mean filter of size 7 px. For the sake of a better visualization, we plot one vector every four. The velocity vectors are scaled with respect of the bottom black arrow in panel **a**. Scale bars: 100 µm

in the grid of Δx, $\frac{\partial f(x,y)}{\partial x}$ is given by:

$$\frac{\partial f(x,y)}{\partial x} \approx \frac{-f(x+2\Delta x,y)+8f(x+\Delta x,y)-8f(x-\Delta x,y)+f(x-2\Delta x,y)}{12\Delta x} \tag{6.14}$$

Finally, once we have detected the vortices, we count the number of vortices with an area within a_i and $a_i + \mathrm{d}a$. To find the total area we look for neighbour pixels with $OW < 0$. In this way we can obtain the distribution of vortex areas (Fig. 6.15), which features an exponential tail. From the exponential fitting $N \propto e^{a/a_*}$, we can extract the characteristic (or mean) vortex area, a_*, and therefore, the mean vortex radius, $R_* = \sqrt{a_*/\pi}$. We also extract the mean vorticity inside each vortex (inset in Fig. 6.15). The mean of this average vorticities gives the mean vorticity of vortices, ω_v.

6.4.6 Spatial autocorrelation functions

2D spatial autocorrelation of a discrete function $f(x_i, y_j)$, C_{ff}, is defined as:

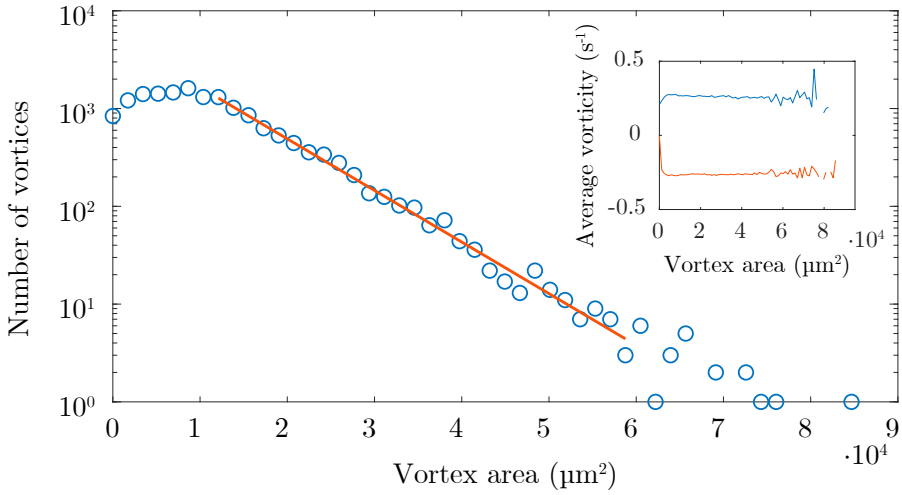

Figure 6.15: Determination of the mean vortex radius and mean vortex radius. The distribution of vortex areas shows an exponential tail ($N \propto e^{a/a_*}$), from which we can retrieve a mean vortex area $a_* = \pi R_*^2$, with R_*^2 the average vortex radius. Inset: The mean vorticity of each vortex seems not to depend on the vortex area. We can therefore extract a mean vorticity of vortices ω_v.

$$C_{ff}(\Delta x, \Delta y) = \left\langle \frac{\sum_{i=0}^{N_x-1} \sum_{j=0}^{N_y-1} f(x_i, y_j) f(x_i + \Delta x, y_j + \Delta y)}{\sum_{i=0}^{N_x-1} \sum_{j=0}^{N_y-1} |f(x_i, y_j)|^2} \right\rangle, \tag{6.15}$$

where $\langle \cdot \rangle$ indicates a temporal average.

In practice, the functions we can extract from our experiments are discrete, hence, to compute C_{ff}, we have to multiply f point by point. As a consequence, the calculation of C_{ff} can be very expensive computationally speaking, especially when the system size is large. Therefore, we apply the Wiener-Khinchin theorem (see Eq. D.15 in Appendix D), which relates the Fourier transform of f, $\tilde{f}(\vec{q})$, with the correlation function as:

$$C_{ff}(\vec{r}) = \left\langle \frac{\mathcal{F}^{-1}\left[\tilde{f}(\vec{q})\, \tilde{f}(\vec{q})^*\right]}{\mathcal{F}^{-1}\left[\tilde{f}(\vec{q}=0)\, \tilde{f}(\vec{q}=0)^*\right]} \right\rangle, \tag{6.16}$$

where $*$ indicates the complex conjugate and $\mathcal{F}^{-1}$ the inverse Fourier transform, that we compute with the built-in function `ifft2()` in Matlab. Also, we shift the output with `ifftshift()` in such a way that $r = 0$ is at the center of the output matrix.

If the 2D autocorrelation function is isotropic, we angle average $C_{ff}(\vec{r})$ as:

$$C_{ff}(r) = \frac{1}{2\pi} \sum_{\varphi} C_{ff}(r, \varphi) \Delta\varphi. \tag{6.17}$$

The code used to compute spatial auto-correlations, autocorrfun.m, can be found in here, you will also need the function AngAverage.m, available here. You can also scan the QR in List of Codes

6.4.7 Time autocorrelation function

We compute the time autocorrelation, C_{tt} as follows:

$$C_{tt}(x, y, \tau) = \frac{\sum_{i=0}^{N-1} f[x, y, t_i] \cdot f[x, y, t_i + \tau]}{\sum_{i=0}^{N-1} |f[x, y, t_i]|^2}. \tag{6.18}$$

Furthermore, we also average $C_{tt}(x, y, \tau)$ over the space:

$$C_{tt}(\tau) = \frac{1}{N_x N_y} \sum_{i=0}^{Nx-1} \sum_{j=1}^{Ny-1} C_{tt}(x_i, y_j, \tau) \tag{6.19}$$

6.4.8 Power spectrum of an energy density

The power spectrum of an energy density at time t, $E_{ff}(t)$, produced by a signal $f(\boldsymbol{r}, t)$ describes how this energy density distributes in the frequency domain. To compute this quantity, we can begin by writing the total energy density of the signal $f(\boldsymbol{r}, t)$:

$$E_{ff}(t) = \frac{1}{\mathcal{A}} \sum_{j=1}^{N_x} \sum_{k=1}^{N_y} |f(x_j, y_k, t)|^2 \Delta x \Delta y = \frac{1}{N_x N_y} \sum_{j=1}^{N_x} \sum_{k=1}^{N_y} |f(x_j, y_k, t)|^2, \tag{6.20}$$

where, we have assumed that f is discrete and a 2D variable, like all the quantities we can extract from our experiments, and $\mathcal{A} = L_x L_y$ is the area of the system with width $L_x = N_x \Delta x$ and height $L_y = N_y \Delta y$. We now introduce the Fourier decomposition of the zero-padded $f(x, y)$[1], which we denote with

[1] We zero-pad the functions to enhance the performance of the FFT computation (see Appendix D.3). Thus, the size of the input function is $N_x \times N_y$ and after the zero-padding the size of the output function is $M_x \times M_y$ with $M_x > N_x$ and $M_y > N_y$, and M_x and M_y powers of 2. The zero-padding is automatically performed by the MatLab function `fft2()` when it is introduced as `fft2(f,Mx,My)` [165], where `f` is the input function. `Mx` and `My` can be computed as `Mx=2^(nextpow2(size(f,2)))` and `My=2^(nextpow2(size(f,1)))`.

the superindex ZP, $f^{ZP}(x,y,t) = 1/M_x 1/M_y \sum_{j=1}^{M_x}\sum_{k=1}^{M_y} \tilde{f}(q_x^j, q_y^k, t)e^{i(q_x^j x + q_y^k y)}$, with $\tilde{f}$ the Fourier modes of f^{ZP} and $(q_x^j, q_y^k) = 2\pi/L(j,k)$ (see Appendix D), and obtain

$$E_{ff}(t) = \frac{1}{N_x N_y}\frac{1}{M_x M_y}\sum_{j=1}^{M_x}\sum_{k=1}^{M_y}|\tilde{f}|^2(q_x^j, q_y^k, t), \tag{6.21}$$

where we have applied the Parseval's theorem for Discrete Fourier Transform (DFT) (see Eq. D.22 in Appendix D.2). Now, we define the 2D energy density power spectrum $E_{ff}(q_x, q_y, t)$ as:

$$E_{ff}(t) = \sum_{j=1}^{M_x}\sum_{k=1}^{M_y} E_{ff}(q_x^j, q_y^k, t)\Delta q_x \Delta q_y, \tag{6.22}$$

plugging $\Delta q_x = 2\pi/L_x$ and $\Delta q_y = 2\pi/L_y$ and comparing Eq. 6.21 with Eq. 6.22, we can obtain the expression for the $E_{ff}(q_x^j, q_y^k)$

$$E_{ff}(q_x, q_y, t) = \frac{\mathcal{A}}{4\pi^2}\frac{1}{N_x N_y}\frac{1}{M_x M_y}|\tilde{f}(q_x, q_y, t)|^2. \tag{6.23}$$

Furthermore, if we have a time series of the quantity f, we can perform a temporal average, that we denote with $\langle\cdot\rangle$:

$$E_{ff}(q_x, q_y) = \frac{\mathcal{A}}{4\pi^2}\frac{1}{N_x N_y}\frac{1}{M_x M_y}\langle|\tilde{f}(q_x, q_y, t)|^2\rangle. \tag{6.24}$$

The time averaged energy power spectrum can be isotropic. In these cases, one can compute the angle-averaged power spectrum $E_{ff}(q)$, where q is the modulus of the wave vector $\boldsymbol{q} = (q_x^j, q_y^k)$. We define this quantity as:

$$E_{ff} = \sum_{l=1}^{M} E_{ff}(q_l)\Delta q. \tag{6.25}$$

Then, taking $\Delta q_x \Delta q_y = q\Delta\varphi\Delta q$ in Eq. 6.22, with φ the azimuth, and introducing Eq. 6.23, we arrive at

$$E_{ff}(q) = \frac{\mathcal{A}}{4\pi^2}\frac{1}{N_x N_y}\frac{1}{M_x M_y}\sum_{\varphi} q\langle|\tilde{f}(\varphi, q, t)|^2\rangle\Delta\varphi. \tag{6.26}$$

6.4.9 Kinetic energy power spectrum

To compute the kinetic energy power spectrum

$$\dot{F} = I(q) + D_s(q) + D_r(q) + D_{\text{ext}}^{\text{oil}}(q) + D_{\text{ext}}^{\text{water}}(q) + T_{\text{FA}}(q) + D_{\text{water}} + D_{\text{oil}}(q), \tag{6.27}$$

we first measure the flows $\mathbf{v}(x, y, t)$ within the AN film through PIV (see Methods Section 6.1.5). Afterwards, following what has been explained in Methods Section 6.4.8, we compute the 2D kinetic power spectrum $E(q_x, q_y, t)$ for each frame as:

$$E(q_x, q_y, t) = \frac{\mathcal{A}}{8\pi^2} \frac{1}{N_x N_y} \frac{1}{M_x M_y} |\tilde{\mathbf{v}}(q_x, q_y, t)|^2. \tag{6.28}$$

where we have used Eq. 6.24. Notice that the quantity in Eq. 6.24 is an **energy density per unit area**. $\tilde{\mathbf{v}}(q_x, q_y, t)$ is the discrete Fourier decomposition of size $M_x \times M_y$ of the velocity field $\mathbf{v}(x, y, t)$ of size $N_x \times N_y$ (see footnote in Page 132) obtained with the function `fft2()` in MatLab. We average all the 2D spectra to obtain a temporal-averaged spectrum and perform an angular average.

$$E(q) = \frac{\mathcal{A}}{8\pi^2} \frac{1}{N_x N_y} \frac{1}{M_x M_y} \sum_{\varphi} q \langle E(\varphi, q, t) \rangle \Delta\varphi, \tag{6.29}$$

where $\langle \cdot \rangle$ indicates the temporal average. The MatLab functions to compute the 2D and 1D kinetic energy spectrum are available here and here, respectively. You can also scan the QR in List of Codes.

The obtained $E(q)$ are fitted to Eq. 3.1, which we rewrite here:

$$E(q) = \frac{B q R_*^4 \, e^{-q^2 R_*^2/2} \left[I_0\left(q^2 R_*^2/2\right) - I_1\left(q^2 R_*^2/2\right) \right]}{\left[q + \eta_{\text{oil}}/\eta_{\text{n}} \tanh(q H_{\text{oil}}) + \eta_{\text{water}}/\eta_{\text{n}} \coth(q H_{\text{water}}) \right]^2}, \tag{6.30}$$

where B is a prefactor; R_* is the mean vortex radius; I_0 and I_1 are modified Bessel's functions of the first kind of order 0 and 1; η_{n} is the 2D AN's shear viscosity; η_{oil} and η_{water} are the 3D oil and water layers viscosities; and H_{oil} and H_{water} are the oil and water layers thicknesses. As fitting parameters we have B, R_*, and η_{n}. A good and reasonable convergence of the fitting can be hard to reach. Thus, we introduce the following starting fitting points:

- For B: the mean value of $E(q)$
- For R_*: the value extracted from the exponential fitting to the distribution of vortex areas (see Methods Section 6.4.5)
- For η_{n}: 10^{-6} Pa·s·m

The fittings are performed with *Mathematica* v10 [166].

6.4.10 Elastic energy power spectrum

The elastic energy power spectrum $F_{\mathrm{d}}(q)$ is computed as $E(q)$, but in this case, instead of the velocity field, we use the $\mathbf{Q}$ tensor.

$$F_{\mathrm{d}}(q) = A\frac{\mathcal{A}}{8\pi^2}\frac{1}{N_xN_y}\frac{1}{M_xM_y}\sum_{\varphi} q\left\langle\left[|\widetilde{\partial_x Q}_{xx}(\varphi,q,t)|^2+|\widetilde{\partial_x Q}_{xy}(\varphi,q,t)|^2+\right.\right.$$
$$\left.\left.|\widetilde{\partial_y Q}_{xy}(\varphi,q,t)|^2+|\widetilde{\partial_y Q}_{yy}(\varphi,q,t)|^2\right]\right\rangle\Delta\varphi, \tag{6.31}$$

where A is the elastic constant in the one-constant approximation, and $Q_{\alpha\beta}$ is the nematic tensor defined in Eq. 6.3. Note that this energy corresponds to the elastic contribution in the Landau-de-Gennes free energy [125], and that the elastic constant A, differs from the elastic constant in the Frank free energy $F_n = K/2\int(\partial_\alpha n_\beta)(\partial_\alpha n_\beta)$, by a factor of 2: $A = K/2$. All the derivatives are computed using Eq. 6.14.

6.4.11 Energy balance

To compute the energy balance, we include the different terms derived in Appendix C.1 and compute the respective energy spectra. To do so, as we did for $E(q)$ and $F_n(q)$, we refer to Eq. 6.26, but, in this case, we replace $|\tilde{f}(\varphi,q,t)|^2$ by the contraction of the terms involved in the energy term. To put an example, if we want to compute the power spectrum of the energy injection I, which is given by Eq. C.27 that we rewrite here:

$$I = \int \alpha v_{\alpha\beta}Q_{\alpha\beta}\mathrm{d}^2\mathbf{r}, \tag{6.32}$$

we will need to substitute $|\tilde{f}(\varphi,q,t)|^2$ by $\mathrm{Re}\left[\tilde{v}_{\alpha\beta}(\varphi,q,t)\tilde{Q}_{\alpha\beta}(\varphi,q,t)\right]$, where $\mathrm{Re}[\cdot]$ indicates the real part[1]. Then, the spectrum of the energy injection, $I(q)$ reads:

[1]When performing this calculus, it is better to specify in the code to only take the real part of the operation. If the sampling frequency is high enough, the result will be the same. However, when the sampling frequency and the length of the signal are limited, the output might have a non-vanishing imaginary part. $I(q)$ must be real because first, I is real and second because of the properties of the Fourier transform and complex numbers: since $\sum_{n=0}^{N-1} f(x_n)g(x_n) = \sum_{k=0}^{N-1} F(q_k)G^*(q_k) = \sum_{k=0}^{N-1} F^*(q_k)G(q_k)$, we can write $\sum_{n=0}^{N-1} f(x_n)g(x_n) = 1/2\sum_{k=0}^{N-1} F(q_k)G^*(q_k) + 1/2\sum_{k=0}^{N-1} F^*(q_k)G(q_k)$. Taking into account that $\mathrm{Re}[F^*(q_k)G(q_k)] = \mathrm{Re}[F(q_k)G^*(q_k)]$ and $\mathrm{Im}[F^*(q_k)G(q_k)] = -\mathrm{Im}[F(q_k)G^*(q_k)]$, we can then write $\sum_{n=0}^{N-1} f(x_n)g(x_n) = \mathrm{Re}\left[\sum_{k=0}^{N-1} F(q_k)G^*(q_k)\right]$.

$$I(q) = \alpha \frac{\mathcal{A}}{4\pi^2} \frac{1}{N_x N_y} \frac{1}{M_x M_y} \sum_{\varphi} q \mathrm{Re}\big[\langle 2\tilde{v}_{xx}(\varphi,q,t)\tilde{Q}^*_{xx}(\varphi,q,t) + 2\tilde{v}_{xy}(\varphi,q,t)\tilde{Q}^*_{xy}(\varphi,q,t)\rangle\big]\Delta\varphi, \tag{6.33}$$

where we have already applied the Einstein summation convention and the symmetries of $v_{\alpha\beta}$ and $Q_{\alpha\beta}$ ($v_{xx} = -v_{yy}, v_{xy} = v_{yx}, Q_{xx} = -Q_{yy}, Q_{xy} = Q_{yx}$). Proceeding analogously with the rest of the terms we obtain:

1. Shear dissipation, $D_s(q)$ (Eq. C.24)

$$D_s(q) = -\eta \frac{\mathcal{A}}{2\pi^2} \frac{1}{N_x N_y} \frac{1}{M_x M_y} \sum_{\varphi} q\langle 2|\tilde{v}_{xx}(\varphi,q,t)|^2 + 2|\tilde{v}_{xy}(\varphi,q,t)|^2\rangle\Delta\varphi \tag{6.34}$$

2. Rotational dissipation, $D_r(q)$ (Eq. C.25)

$$D_r(q) = -\gamma^{-1} \frac{\mathcal{A}}{4\pi^2} \frac{1}{N_x N_y} \frac{1}{M_x M_y} \sum_{\varphi} q\langle 2|\tilde{H}_{xx}(\varphi,q,t)|^2 + 2|\tilde{H}_{xy}(\varphi,q,t)|^2\rangle\Delta\varphi \tag{6.35}$$

3. Flow alignment energy transfer, $T_{\mathrm{FA}}(q)$ (Eq. C.26)

$$T_{\mathrm{FA}}(q) = \nu \frac{\mathcal{A}}{4\pi^2} \frac{1}{N_x N_y} \frac{1}{M_x M_y} \sum_{\varphi} q\mathrm{Re}\Big[\langle 2\tilde{v}_{xx}(\varphi,q,t)(\tilde{H}^*_{xx} - \widetilde{SH}^*_{xx})(\varphi,q,t) + 2\tilde{v}_{xy}(\varphi,q,t)(\tilde{H}^*_{xy} - \widetilde{SH}^*_{xy})(\varphi,q,t)\rangle\Big]\Delta\varphi \tag{6.36}$$

4. Dissipation due to the water 3D layer

$$D_{\mathrm{water}}(q) = -\eta_{\mathrm{water}} \frac{\mathcal{A}}{2\pi^2} \frac{1}{N_x N_y} \frac{1}{M_x M_y} \sum_{\varphi} \big\langle I_{1,\mathrm{water}}(q)\tilde{v}_{\alpha\beta}(\varphi,q,t)\tilde{v}^*_{\alpha\beta}(\varphi,q,t) + I_{2,\mathrm{water}}(q)|\tilde{\boldsymbol{v}}(\varphi,q,t)|^2\big\rangle\Delta\varphi, \tag{6.37}$$

with

$$I_{1,\mathrm{water}}(q) = -\frac{H_{\mathrm{water}}}{2}\mathrm{csch}^2(qH_{\mathrm{water}}) + \frac{1}{2q}\coth(qH_{\mathrm{water}}), \tag{6.38a}$$

$$I_{2,\mathrm{water}}(q) = \frac{1}{2}q^2 H_{\mathrm{water}}\,\mathrm{csch}^2(qH_{\mathrm{water}}) + \frac{1}{2}q\coth(qH_{\mathrm{water}})]. \tag{6.38b}$$

5. Dissipation due to the oil 3D layer

$$D_{\text{oil}}(q) = -\eta_{\text{oil}} \frac{\mathcal{A}}{2\pi^2} \frac{1}{N_x N_y} \frac{1}{M_x M_y} \sum_{\varphi} \big\langle I_{1,\text{oil}}(q) \tilde{v}_{\alpha\beta}(\varphi, q, t) \tilde{v}^*_{\alpha\beta}(\varphi, q, t) + I_{2,\text{oil}}(q) |\tilde{\boldsymbol{v}}(\varphi, q, t)|^2 \big\rangle \Delta\varphi. \tag{6.39}$$

In the case of the dissipation due to the oil layer, $I_{1,\text{oil}}(q)$ and $I_{2,\text{oil}}(q)$ depend on the experimental setup used. This is because in the open setup, the oil layer is in contact with the air, whereas in the flow cell arrangement, this layer is in contact with a substrate. Thus, in the former we can consider free boundary conditions and in the latter we can assume no-slip boundary conditions.

Open system (PDMS pool)

$$I_{1,\text{oil}}(q) = \frac{H_{\text{oil}}}{2} \operatorname{sech}^2(qH_{\text{oil}}) + \frac{1}{2q} \tanh(qH_{\text{oil}}) \tag{6.40a}$$

$$I_{2,\text{oil}}(q) = -\frac{1}{2} q^2 H_{\text{oil}} \operatorname{sech}^2(qH_{\text{oil}}) + \frac{1}{2} q \tanh(qH_{\text{oil}}). \tag{6.40b}$$

Closed system (Flow cell)

$$I_{1,\text{oil}}(q) = -\frac{H_{\text{oil}}}{2} \operatorname{csch}^2(qH_{\text{oil}}) + \frac{1}{2q} \coth(qH_{\text{oil}}), \tag{6.41a}$$

$$I_{2,\text{oil}}(q) = \frac{1}{2} q^2 H_{\text{oil}} \operatorname{csch}^2(qH_{\text{oil}}) + \frac{1}{2} q \coth(qH_{\text{oil}})]. \tag{6.41b}$$

Notice that these last two equations are the same as Eq. 6.38, but changing H_{water} and η_{water} by H_{oil} and η_{oil}.

To facilitate the computation of all these terms, we rewrite in Table 6.4 the meaning of the different terms appearing in the equations below.

The velocity field $\mathbf{v}$ obtained through PIV has a lower resolution than the $\mathbf{Q}$ tensor field, extracted from the birefringence imaging techniques described in Chapter 5. Consequently, we need to resize $\mathbf{Q}$. To do so, we interpolate $\mathbf{Q}$ using the coordinates of $\mathbf{v}$. All the derivatives are obtained using Eq. 6.14 and then filtered using Gaussian filter with standard deviations between 2 and 3 pixels. Since here we are computing Fourier decompositions, we could obtain the derivative by the corresponding multiplication of iq_x and iq_y. Nevertheless, we have found a better performance when the derivatives are calculated in the real space (see Appendix D.4).

Term	Description
$v_{xx} = \partial_x vx$	Term xx of the symmetric part of the deviatoric stress tensor
$v_{xy} = (\partial_x vy + \partial_y v_x)/2$	Term xy of the symmetric part of the deviatoric stress tensor
$H_{xx} = A\nabla^2 Q_{xx}$	Term xx of the molecular tensor
$H_{xy} = A\nabla^2 Q_{xy}$	Term xy of the molecular tensor
$S = 2\sqrt{Q_{xx}^2 + Q_{xy}^2}$	Scalar order parameter

Table 6.4: Meaning of the terms in Eqs. 6.32 to 6.41.

6

6.4.12 Filtering of the nematic director field

To filter the nematic orientational field, we cannot directly apply a conventional filter. This is because of the discontinuity at 0 and π. To overcome this problem, we can parameterize the orientation in terms of the $\mathbf{Q}$ tensor, that naturally contains the nematic symmetry. Hence, we first compute $\mathbf{Q}$ as

$$Q_{xx} = \mathbb{K} * \cos(2\theta)/2, \tag{6.42a}$$

$$Q_{xy} = \mathbb{K} * \sin(2\theta)/2, \tag{6.42b}$$

where $\mathbb{K}$ is the filter kernel and $*$ indicates a convolution. Usually, we apply a disk filter (or mean filter) or a gaussian filter. Then, we can obtain the order parameter S as

$$S = 2\sqrt{Q_{xx}^2 + Q_{xy}^2}, \tag{6.43}$$

and the nematic orientation

$$\theta = \text{atan}(Q_{xy}, 0.5S + Q_{xx}) \tag{6.44}$$

The corresponding MatLab code (winding.m) used to compute the winding number can be found in here. You can also scan the QR in List of Codes

Chapter 7

Conclusions

This thesis has experimentally addressed some open questions regarding 2D active nematic turbulence. Here, we list the main conclusions we have extracted from the present work:

- We have studied the onset of the primary bend instability, which leads to active nematic turbulence. In some experiments, we have been able to observe a cascade of instabilities prior to the final chaotic state. Interestingly, the characteristic length appearing during the first instability is still retained in the subsequent instabilities.
- The quantitative analysis of the orientational instability has demonstrated a quadratic or quasi-quadratic trend of the instability's leading growth rate with the associated wave number.
- To rationalize our experimental results, we have employed linear stability analyses that predict that the coupling of the AN with the two adjacent fluid layers, as happens in our experiments, endows the system with a wavelength selection mechanism. Moreover, according to this analysis, the selected wavelength follows the well-recognized scaling of the active length scale, ℓ_a, with the activity coefficient α and the elastic constant K: $\ell_a \sim \sqrt{K/\alpha}$. This highlights that the wavelength selected during the first instability is already an anticipation of the final characteristic wavelength.
- Although the theory allows us to have a taste of the possible mechanism of wavelength selection, it only partially captures some of our experimental results. This could also be attributed to our need for more accurate knowledge of most AN's material parameters.

- We have also studied some statistical properties of the AN in its fully developed turbulent regime. More particularly, we have measured the kinetic energy spectrum, $E(q)$ of the flows within the AN and have demonstrated the appearance of different scaling regimes.

- With our experimental measurements, we have confirmed scaling laws with universal exponents previously predicted by simulations and theory: a $E(q) \sim q^{-1}$ for intermediate q and a $E(q) \sim q^{-4}$ for large q. Moreover, we have discovered a new scaling regime at small q: $E(q) \sim q$.

- By controlling the viscosity of the oil above the AN, we have been capable of tuning the crossover between the different scaling regimes. The two extreme scalings, i.e., $E(q) \sim q$ and $E(q) \sim q^{-4}$ at small and large wave numbers, respectively, appear in all the experiments.

- Using a hydrodynamic theory that effectively introduces the coupling of the active film with the two adjacent passive layers, we have demonstrated that the newly unveiled scaling regime stems from such coupling. Moreover, this theory potentially predicts extra scaling regimes unseen in our experiments, but that could be observed in other experimental realizations of active fluids.

- The hydrodynamic theory correctly predicts the kinetic energy spectrum of the experiments performed at intermediate oil viscosities. Nonetheless, at low and high oil viscosities, the fitting of the theory fails. Therefore, we propose different features that could be included in new hydrodynamic theories devoted to eliciting the kinetic energy spectra for the full range of oil viscosities.

- From the fitting of the theory to the kinetic energy spectra obtained in the experiments with intermediate oil viscosities, we have inferred an unknown material parameter, namely the nematic viscosity. The latter appears to be constant for the range of validity of the theory.

- We have experimentally measured the different terms contributing to the free energy balance of the AN to assess the presence of energy cascades in 2D active nematic turbulence, as occurs in inertial turbulence. One of the biggest limitations we have envisaged during this project is, again, the lack of knowledge of most of the AN's material parameters. However, by exploiting some available parameters and predicted scaling relations, we have been able to obtain a free energy balance that, despite not being zero at all length scales, consistently integrates to zero over the whole range of the wave numbers. To evaluate whether the not-vanishing free

energy at all length scales is either a signature of an energy cascade or the result of experimental uncertainty, we have resorted to the computation of the energy balance from simulations of an isolated AN. We have observed that the obtained energy balance highly depends on the data treatment. Also, the balance does not completely vanish at all lengths, like in the experiments. Therefore, we cannot reach a firm conclusion on whether there are energy cascades in active nematic turbulence.

- For the last experiments devoted to investigating the energy cascades, we have engineered a new polarimetry technique coupled with fluorescence imaging. Such a technique is based on variable liquid crystal retarders that can be easily commanded with a computer. The acquisition of images at different retardance of the liquid crystal slab allows for the unambiguous determination of the local orientation of birefringent samples, such as the AN. Simultaneously, we acquire fluorescence images from which we can obtain the AN's velocity field.

- The temporal resolution we attain with the LC-based polarimeter substantially betters other similar and well-known commercial implementations. This setup will be of broad interest among the soft matter community.

- In addition to the LC-based polarimeter, we have implemented another polarimetry technique that exploits a polarization-sensitive camera. The advantage of this setup is that we only require one image to resolve the local orientation of a birefringent material. In this way, the temporal resolution is only limited by the camera's maximum frame rate. In addition, the retardance images generated with this technique are comparable to those obtained through epi-fluorescence imaging.

References

[1] Martínez-Prat, B., Ignés-Mullol, J., Casademunt, J. & Sagués, F. Selection mechanism at the onset of active turbulence. *Nat. Phys.* **15**, 362–366 (2019). (Cited on pages xix, 29, 30, 32, 33, 35, 45, 59, 125, and 126.)

[2] Ramaswamy, S. The Mechanics and Statistics of Active Matter. *Annu. Rev. Condens. Matter Phys.* **1**, 323–345 (2010). (Cited on page 1.)

[3] Marchetti, M. C. *et al.* Hydrodynamics of soft active matter. *Rev. Mod. Phys.* **85**, 1143–1189 (2013). (Cited on pages 1, 20, and 70.)

[4] Needleman, D. & Dogic, Z. Active matter at the interface between materials science and cell biology. *Nat. Rev. Mater.* **2** (2017). (Cited on page 1.)

[5] Doostmohammadi, A., Ignés-Mullol, J., Yeomans, J. M. & Sagués, F. Active nematics. *Nat. Commun.* **9** (2018). (Cited on pages 1 and 70.)

[6] Bowick, M. J., Fakhri, N., Marchetti, M. C. & Ramaswamy, S. Symmetry, Thermodynamics, and Topology in Active Matter. *Phys. Rev. X* **12**, 10501 (2022). (Cited on page 1.)

[7] Copenhagen, K., Alert, R., Wingreen, N. S. & Shaevitz, J. W. Topological defects promote layer formation in Myxococcus xanthus colonies. *Nat. Phys.* **17** (2020). (Cited on page 2.)

[8] Nédélec, F. J., Surrey, T., Maggs, A. C. & Leibler, S. Self-organization of microtubules and motors. *Nature* **389**, 305–308 (1997). (Cited on pages 1, 2, 9, 14, and 19.)

[9] Vicsek, T. & Zafeiris, A. Collective motion. *Phys. Rep.* **517**, 71–140 (2012). (Cited on page 1.)

[10] Surrey, T., Nédélec, F., Leibler, S. & Karsenti, E. Physical properties determining of motors and microtubules. *Science (80-.).* **292**, 1167–1171 (2001). (Cited on pages 1 and 14.)

[11] Huber, L., Suzuki, R., Krüger, T., Frey, E. & Bausch, A. R. Emergence of coexisting ordered states in active matter systems. *Science (80-.).* **361**, 255–258 (2018). (Cited on pages 1, 9, and 15.)

[12] Sciortino, A. & Bausch, A. R. Pattern formation and polarity sorting of driven actin filaments on lipid membranes. *Proc. Natl. Acad. Sci. U. S. A.* **118**, 1–8 (2021). (Cited on pages 1 and 9.)

[13] Senoussi, A. *et al.* Tunable corrugated patterns in an active nematic sheet. *Proc. Natl. Acad. Sci. U. S. A.* **116**, 22464–22470 (2019). (Cited on pages 1, 30, and 38.)

[14] Sokolov, A., Mozaffari, A., Zhang, R., De Pablo, J. J. & Snezhko, A. Emergence of Radial Tree of Bend Stripes in Active Nematics. *Phys. Rev. X* **9**, 31014 (2019). (Cited on page 1.)

[15] Tennenbaum, M., Liu, Z., Hu, D. & Fernandez-Nieves, A. Mechanics of fire ant aggregations. *Nat. Mater.* **15**, 54–59 (2016). (Cited on page 1.)

[16] Wensink, H. H. *et al.* Meso-scale turbulence in living fluids. *Proc. Natl. Acad. Sci. U.S.A.* **109**, 14308–14313 (2012). (Cited on pages 1, 25, 26, 27, 29, and 47.)

[17] Sanchez, T., Chen, D. T., Decamp, S. J., Heymann, M. & Dogic, Z. Spontaneous motion in hierarchically assembled active matter. *Nature* **491**, 431–434 (2012). (Cited on pages 1, 12, 14, 15, and 25.)

[18] Creppy, A., Praud, O., Druart, X., Kohnke, P. L. & Plouraboué, F. Turbulence of swarming sperm. *Phys. Rev. E - Stat. Nonlinear, Soft Matter Phys.* **92**, 032722 (2015). (Cited on pages 1, 25, 26, and 29.)

[19] Blanch-Mercader, C. *et al.* Turbulent Dynamics of Epithelial Cell Cultures. *Phys. Rev. Lett.* **120**, 208101 (2018). (Cited on pages 1, 25, 29, and 56.)

[20] Peng, Y., Liu, Z. & Cheng, X. Imaging the emergence of bacterial turbulence: Phase diagram and transition kinetics. *Sci. Adv.* **7** (2021). (Cited on page 1.)

[21] Bechinger, C. *et al.* Active particles in complex and crowded environments. *Rev. Mod. Phys.* **88** (2016). (Cited on page 3.)

[22] Ebbens, S. J. Active colloids: Progress and challenges towards realising autonomous applications. *Curr. Opin. Colloid Interface Sci.* **21**, 14–23 (2016). (Cited on page 3.)

[23] Purcell, E. M. Life at low Reynolds number. *Am. J. Phyiscs* **45**, 3–11 (1977). (Cited on pages 3 and 25.)

[24] Qiu, T. *et al.* Swimming by reciprocal motion at low Reynolds number. *Nat. Commun.* **5**, 1–8 (2014). (Cited on page 3.)

[25] Lauga, E. & Powers, T. R. The hydrodynamics of swimming microorganisms. *Reports Prog. Phys.* **72** (2009). (Cited on page 3.)

[26] Lauga, E. Life around the scallop theorem. *Soft Matter* **7**, 3060–3065 (2011). (Cited on page 3.)

[27] Elgeti, J., Winkler, R. G. & Gompper, G. Physics of microswimmers - Single particle motion and collective behavior: A review. *Reports Prog. Phys.* **78** (2015). (Cited on pages 3, 7, and 9.)

[28] Paxton, W. F. *et al.* Catalytic nanomotors: Autonomous movement of striped nanorods. *J. Am. Chem. Soc.* **126**, 13424–13431 (2004). (Cited on page 4.)

[29] Paxton, W. F., Sen, A. & Mallouk, T. E. Motility of catalytic nanoparticles through self-generated forces. *Chem. - A Eur. J.* **11**, 6462–6470 (2005). (Cited on page 4.)

[30] Kuron, M., Kreissl, P. & Holm, C. Toward Understanding of Self-Electrophoretic Propulsion under Realistic Conditions: From Bulk Reactions to Confinement Effects. *Acc. Chem. Res.* **51**, 2998–3005 (2018). (Cited on page 4.)

[31] Wang, Y. *et al.* Bipolar electrochemical mechanism for the propulsion of catalytic nanomotors in hydrogen peroxide solutions. *Langmuir* **22**, 10451–10456 (2006). (Cited on page 4.)

[32] Howse, J. R. *et al.* Self-Motile Colloidal Particles: From Directed Propulsion to Random Walk. *Phys. Rev. Lett.* **99**, 8–11 (2007). (Cited on page 5.)

[33] Wikipedia. Janus particles — Wikipedia, the free encyclopedia (2022). URL http://en.wikipedia.org/w/index.php?title=Janus%20particles&oldid=1100899882. [Online; accessed 22-September-2022]. (Cited on page 5.)

[34] Wikipedia. Janus — Wikipedia, the free encyclopedia (2022). URL http://en.wikipedia.org/w/index.php?title=Janus&oldid=1109791503. [Online; accessed 22-September-2022]. (Cited on page 5.)

[35] Nguyen, M.-L. Double herm. marble, roman copy after a greek original (2009). URL https://commons.wikimedia.org/wiki/File:Double_herm_Chiaramonti_Inv1395.jpg. [Online; accessed 22-September-2022]. (Cited on page 5.)

[36] Casagrande, C., Fabre, P., Raphaël, E. & Veyssié, M. «Janus beads»: Realization and behaviour at water/oil interfaces. *Epl* **9**, 251–255 (1989). (Cited on page 5.)

[37] Shields, C. W. & Velev, O. D. The Evolution of Active Particles: Toward Externally Powered Self-Propelling and Self-Reconfiguring Particle Systems. *Chem* **3**, 539–559 (2017). (Cited on page 6.)

[38] Palacci, J., Sacanna, S., Steinberg, A. P., Pine, D. J. & Chaikin, P. M. Living Crystals of Light-Activated Colloidal Surfers. *Science (80-.).* **339**, 936–939 (2013). (Cited on page 6.)

[39] Jiang, H. R., Yoshinaga, N. & Sano, M. Active motion of a Janus particle by self-thermophoresis in a defocused laser beam. *Phys. Rev. Lett.* **105**, 1–4 (2010). (Cited on page 6.)

[40] Dreyfus, R. *et al.* Microscopic artificial swimmers. *Nature* **437**, 862–865 (2005). (Cited on page 6.)

[41] Tierno, P., Golestanian, R., Pagonabarraga, I. & Sagués, F. Magnetically actuated colloidal microswimmers. *J. Phys. Chem. B* **112**, 16525–16528 (2008). (Cited on page 6.)

[42] Gao, W., Sattayasamitsathit, S., Manesh, K. M., Weihs, D. & Wang, J. Magnetically powered flexible metal nanowire motors. *J. Am. Chem. Soc.* **132**, 14403–14405 (2010). (Cited on page 6.)

[43] Tottori, S., Zhang, L., Peyer, K. E. & Nelson, B. J. Assembly, disassembly, and anomalous propulsion of microscopic helices. *Nano Lett.* **13**, 4263–4268 (2013). (Cited on page 6.)

[44] Sagués-Mestre, F. *Colloidal Active. Concepts, experimental realizations, and models* (CRC Press, Boca Raton, FL, 2022). (Cited on page 6.)

[45] Wadhwa, N. & Berg, H. C. Bacterial motility: machinery and mechanisms. *Nat. Rev. Microbiol.* **20**, 161–173 (2022). (Cited on pages 7 and 8.)

[46] Kearns, D. B. A field guide to bacterial swarming motility. *Nat. Rev. Microbiol.* **8**, 634–644 (2010). (Cited on page 7.)

[47] Bastos-Arrieta, J., Revilla-Guarinos, A., Uspal, W. E. & Simmchen, J. Bacterial biohybrid microswimmers. *Front. Robot. AI* **5**, 1–16 (2018). (Cited on page 7.)

[48] Tilney, L. G. & Portnoy, D. A. Actin filaments and the growth, movement, and spread of the intracellular bacterial parasite, Listeria monocytogenes. *J. Cell Biol.* **109**, 1597–1608 (1989). (Cited on page 8.)

[49] Team, T. B. 07.5 The Cytoskeleton MS. OpenStax CNX (2003). URL http://cnx.org/contents/609c7858-a692-4fb1-9c49-69462e3c739f@1. (Cited on page 8.)

[50] Pratt, C. W. & Cornely, K. *Essential Biochemistry* (Wiley, United States of America, 2018), 4$^{\text{th}}$ edn. (Cited on pages 8, 36, and 113.)

[51] Phillips, R., Kondev, J. & Theriot, J. *Physical Biology of the Cell* (Garland Science, Taylor & Francis Group, New York, 2008). URL http://www.worldcat.org/search?qt=worldcat_org_all&q=0815341636. (Cited on page 8.)

[52] Fritz-Laylin, L. K. The evolution of animal cell motility. *Curr. Biol.* **30**, R477–R482 (2020). (Cited on pages 9 and 10.)

[53] Sheetz, M. P. & Spudich, J. A. Movement of myosin-coated fluorescent beads on actin cables in vitro. *Nature* **303**, 31–35 (1983). (Cited on page 9.)

[54] Kron, S. J. & Spudich, J. A. Fluorescent actin filaments move on myosin fixed to a glass surface. *Proc. Natl. Acad. Sci. U. S. A.* **83**, 6272–6276 (1986). (Cited on page 9.)

[55] Sumino, Y. *et al.* Large-scale vortex lattice emerging from collectively moving microtubules. *Nature* **483**, 448–452 (2012). (Cited on pages 9 and 14.)

[56] Schaller, V., Weber, C., Semmrich, C., Frey, E. & Bausch, A. R. Polar patterns of driven filaments. *Nature* **467**, 73–77 (2010). (Cited on page 11.)

[57] Verde, F., Berrez, J.-M., Antony, C. & Karsenti, E. Taxol-induced Microtubule Asters in Mitotic Extracts of Xenopus Eggs : Requirement for Phosphorylated Factors and Cytoplasmic Dynem. *J. Cell Biol.* **112**, 1177–1187 (1991). (Cited on page 9.)

[58] Kumar, N., Zhang, R., De Pablo, J. J. & Gardel, M. L. Tunable structure and dynamics of active liquid crystals. *Sci. Adv.* **4**, 1–13 (2018). (Cited on page 9.)

[59] Cates, M. E. & Tailleur, J. Motility-induced phase separation. *Annu. Rev. Condens. Matter Phys.* **6**, 219–244 (2015). (Cited on page 11.)

[60] Schaller, V. & Bausch, A. R. Topological defects and density fluctuations in collectively moving systems. *Proc. Natl. Acad. Sci. U. S. A.* **110**, 4488–4493 (2013). (Cited on page 11.)

[61] Zhang, H. P., Be'er, A., Florin, E. L. & Swinney, H. L. Collective motion and density fluctuations in bacterial colonies. *Proc. Natl. Acad. Sci. U. S. A.* **107**, 13626–13630 (2010). (Cited on page 11.)

[62] Burbank, K. S. & Mitchison, T. J. Microtubule dynamic instability. *Curr. Biol.* **16**, 516–517 (2006). (Cited on page 14.)

[63] Mandelkow, E. M., Mandelkow, E. & Milligan, R. A. Microtubule dynamics and microtubule caps: A time-resolved cryo-electron microscopy study. *J. Cell Biol.* **114**, 977–991 (1991). (Cited on page 14.)

[64] Thoresen, T., Lenz, M. & Gardel, M. L. Reconstitution of Contractile Actomyosin Bundles. *Biophys. J.* **100**, 2698–2705 (2011). (Cited on page 14.)

[65] Nasirimarekani, V., Strübing, T., Vilfan, A. & Guido, I. Tuning the Properties of Active Microtubule Networks by Depletion Forces. *Langmuir* **37**, 7919–7927 (2021). (Cited on pages 14 and 15.)

[66] Ross, T. D. *et al.* Controlling organization and forces in active matter through optically defined boundaries. *Nature* **572**, 224–229 (2019). (Cited on page 14.)

[67] Roostalu, J., Rickman, J., Thomas, C., Nédélec, F. & Surrey, T. Determinants of Polar versus Nematic Organization in Networks of Dynamic Microtubules and Mitotic Motors. *Cell* **175**, 796–808.e14 (2018). (Cited on page 14.)

[68] Blackwell, R. *et al.* Microscopic origins of anisotropic active stress in motor-driven nematic liquid crystals. *Soft Matter* **12**, 2676–2687 (2016). (Cited on page 15.)

[69] Berezney, J., Goode, B. L., Fraden, S. & Dogic, Z. Extensile to contractile transition in active microtubule-actin composites generates layered asters with programmable lifetimes. *Proc. Natl. Acad. Sci. U. S. A.* **119** (2022). (Cited on page 15.)

[70] Lemma, B., Mitchell, N. P., Subramanian, R., Needleman, D. J. & Dogic, Z. Active Microphase Separation in Mixtures of Microtubules and Tip-Accumulating Molecular Motors. *Phys. Rev. X* **12**, 31006 (2022). (Cited on page 15.)

[71] Chew, W.-X., Henkin, G., Nédélec, F. & Surrey, T. Effects of microtubule length and crowding on active microtubule network organization. *bioRxiv* (2022). (Cited on page 15.)

[72] Giomi, L., Bowick, M. J., Mishra, P., Sknepnek, R. & Marchetti, M. C. Defect dynamics in active nematics. *Philos. Trans. R. Soc. A* **372**, 20130365 (2014). (Cited on pages 18, 30, and 185.)

[73] Endresen, K. D., Kim, M. S., Pittman, M., Chen, Y. & Serra, F. Topological defects of integer charge in cell monolayers. *Soft Matter* **17**, 5878–5887 (2021). (Cited on page 19.)

[74] Alert, R., Joanny, J. F. & Casademunt, J. Universal scaling of active nematic turbulence. *Nat. Phys.* **16**, 682–688 (2020). (Cited on pages 19, 27, 29, 47, 49, 52, 59, 76, 178, and 186.)

[75] Giomi, L. Geometry and topology of Turbulence in active nematics. *Phys. Rev. X* **5**, 031003 (2015). (Cited on pages 19, 25, 27, 38, 40, 47, 49, 51, 52, 56, 72, 128, 179, 185, and 186.)

[76] Rivera, M. K., Aluie, H. & Ecke, R. E. The direct enstrophy cascade of two-dimensional soap film flows. *Phys. Fluids* **26** (2014). (Cited on page 22.)

[77] Pope, S. B. *Turbulent Flows* (Cambridge University Press, 2000). (Cited on pages 21 and 22.)

[78] Livi, R. & Vulpani, A. (eds.) *The Kolmogorov legacy in physics* (Springer, Berlin, 2003). (Cited on pages 21 and 22.)

[79] Alexakis, A. & Biferale, L. Cascades and transitions in turbulent flows. *Phys. Rep.* **767-769**, 1–101 (2018). (Cited on pages 21, 22, 23, 24, and 69.)

[80] Aragón, J. L., Naumis, G. G., Bai, M., Torres, M. & Maini, P. K. Turbulent luminance in impassioned van Gogh paintings. *J. Math. Imaging Vis.* **30**, 275–283 (2008). (Cited on page 22.)

[81] Lees, A. & Aluie, H. Baropycnal work: A mechanism for energy transfer across scales. *Fluids* **4**, 1–17 (2019). (Cited on page 23.)

[82] Carbone, M. & Bragg, A. D. Is vortex stretching the main cause of the turbulent energy cascade? *J. Fluid Mech.* **883**, 1–13 (2020). (Cited on page 23.)

[83] Johnson, P. L. On the role of vorticity stretching and strain self-amplification in the turbulence energy cascade. *J. Fluid Mech.* **922**, 1–37 (2021). (Cited on page 23.)

[84] Boffetta, G. Energy and enstrophy fluxes in the double cascade of two-dimensional turbulence. *J. Fluid Mech.* **589**, 253–260 (2007). (Cited on page 23.)

[85] Boffetta, G. & Ecke, R. E. Two-dimensional turbulence. *Annu. Rev. Fluid Mech.* **44**, 427–451 (2011). (Cited on page 23.)

[86] Farazmand, M. M., Kevlahan, N. K. & Protas, B. Controlling the dual cascade of two-dimensional turbulence. *J. Fluid Mech.* **668**, 202–222 (2011). (Cited on page 23.)

[87] Kraichnan, R. H. Inertial ranges in two-dimensional turbulence. *Phys. Fluids* **10**, 1417–1423 (1967). (Cited on page 23.)

[88] Dombrowski, C., Cisneros, L., Chatkaew, S., Goldstein, R. E. & Kessler, J. O. Self-concentration and large-scale coherence in bacterial dynamics. *Phys. Rev. Lett.* **93**, 2–5 (2004). (Cited on page 25.)

[89] Thampi, S. P. & Yeomans, J. M. Active turbulence in active nematics. *Eur. Phys. J. Spec. Top.* **225**, 651–662 (2016). (Cited on page 25.)

[90] Lin, S. Z., Zhang, W. Y., Bi, D., Li, B. & Feng, X. Q. Energetics of mesoscale cell turbulence in two-dimensional monolayers. *Commun. Phys.* **4**, 1–9 (2021). (Cited on pages 25 and 26.)

[91] Guillamat, P., Ignés-Mullol, J. & Sagués, F. Control of active liquid crystals with a magnetic field. *Proc. Natl. Acad. Sci. U.S.A.* **113**, 5498–5502 (2016). (Cited on pages 25, 36, and 38.)

[92] Guillamat, P., Ignés-Mullol, J. & Sagués, F. Taming active turbulence with patterned soft interfaces. *Nat. Commun.* **8**, 1–8 (2017). (Cited on pages 25, 36, and 56.)

[93] Lemma, L. M., DeCamp, S. J., You, Z., Giomi, L. & Dogic, Z. Statistical properties of autonomous flows in 2D active nematics. *Soft Matter* **15**, 3264–3272 (2019). (Cited on pages 25, 36, 56, and 72.)

[94] Benzi, R., Patarnello, S. & Santangelo, P. Self-similar coherent structures in two-dimensional decaying turbulence. *J. Phys. A: Math. Gen.* **21**, 1221–1237 (1988). (Cited on pages 25 and 128.)

[95] Bratanov, V., Jenko, F. & Frey, E. New class of turbulence in active fluids. *Proc. Natl. Acad. Sci. U.S.A.* **112**, 15048–15053 (2015). (Cited on pages 27, 29, and 47.)

[96] Martínez-Prat, B. *et al.* Scaling Regimes of Active Turbulence with External Dissipation. *Phys. Rev. X* **11**, 031065 (2021). (Cited on pages 27, 40, 48, 51, 64, 65, 71, 72, 73, 75, and 174.)

[97] Carenza, L. N., Biferale, L. & Gonnella, G. Cascade or not cascade? Energy transfer and elastic effects in active nematics. *EPL* **132**, 44003 (2020). (Cited on pages 27 and 69.)

[98] Urzay, J., Doostmohammadi, A. & Yeomans, J. M. Multi-scale statistics of turbulence motorized by active matter. *J. Fluid Mech.* **822**, 762–773 (2017). (Cited on pages 27 and 69.)

[99] Słomka, J. & Dunkel, J. Spontaneous mirror-symmetry breaking induces inverse energy cascade in 3D active fluids. *Proc. Natl. Acad. Sci. U. S. A.* **114**, 2119–2124 (2017). (Cited on page 27.)

[100] Voituriez, R., Joanny, J. F. & Prost, J. Spontaneous flow transition in active polar gels. *Europhys. Lett.* **70**, 404–410 (2005). (Cited on pages 29, 36, 38, 159, 162, and 186.)

[101] Edwards, S. A. & Yeomans, J. M. Spontaneous flow states in active nematics: A unified picture. *Europhys. Lett.* **85** (2009). (Cited on pages 29, 39, 163, and 186.)

[102] Thampi, S. P., Golestanian, R. & Yeomans, J. M. Instabilities and topological defects in active nematics. *EPL* **105**, 1–6 (2014). (Cited on pages 29 and 30.)

[103] Aditi Simha, R. & Ramaswamy, S. Hydrodynamic fluctuations and instabilities in ordered suspensions of self-propelled particles. *Phys. Rev. Lett.* **89**, 058101 (2002). (Cited on page 29.)

[104] Duclos, G. *et al.* Spontaneous shear flow in confined cellular nematics. *Nat. Phys.* **14**, 728–732 (2018). (Cited on pages 30, 34, 162, and 186.)

[105] Sarfati, G., Maitra, A., Voituriez, R., Galas, J.-C. & Estevez-Torres, A. Crosslinking and depletion determine spatial instabilities in cytoskeletal active matter. *Soft Matter* **18**, 3793–3800 (2022). (Cited on page 30.)

[106] Najma, B. *et al.* Dual antagonistic role of motor proteins in fluidizing active networks (2021). arXiv:2112.11364. (Cited on page 30.)

[107] Giomi, L., Bowick, M. J., Ma, X. & Marchetti, M. C. Defect annihilation and proliferation in active Nematics. *Phys. Rev. Lett.* **110**, 228101 (2013). (Cited on pages 30 and 185.)

[108] Joanny, J. F. & Prost, J. Active gels as a description of the actin-myosin cytoskeleton. *HFSP J.* **3**, 94–104 (2009). (Cited on pages 36 and 38.)

[109] Thampi, S. P., Golestanian, R. & Yeomans, J. M. Velocity correlations in an active nematic. *Phys. Rev. Lett.* **111**, 118101 (2013). (Cited on page 36.)

[110] Schnitzer, M. J. & Block, S. M. Kinesin hydrolyses one ATP per 8-nm step. *Nature* **388**, 386–390 (1997). (Cited on page 36.)

[111] Tan, A. J. *et al.* Topological chaos in active nematics. *Nat. Phys.* **15**, 1033–1039 (2019). (Cited on page 36.)

[112] Henkin, G., DeCamp, S. J., Chen, D. T. N., Sanchez, T. & Dogic, Z. Tunable dynamics of microtubule-based active isotropic gels. *Philos. Trans. R. Soc. A* **372**, 20140142 (2014). (Cited on pages 38 and 112.)

[113] Ward, A. *et al.* Solid friction between soft filaments. *Nat. Mater.* **14**, 583–588 (2015). (Cited on page 38.)

[114] Kruse, K., Joanny, J. F., Jülicher, F., Prost, J. & Sekimoto, K. Generic theory of active polar gels: A paradigm for cytoskeletal dynamics. *Eur. Phys. J. E* **16**, 5–16 (2005). (Cited on pages 38, 47, 70, and 159.)

[115] Prost, J., Jülicher, F. & Joanny, J. F. Active gel physics. *Nat. Phys.* **11**, 111–117 (2015). (Cited on pages 38 and 159.)

[116] Gao, T., Blackwell, R., Glaser, M. A., Betterton, M. D. & Shelley, M. J. Multiscale polar theory of microtubule and motor-protein assemblies. *Phys. Rev. Lett.* **114**, 048101 (2015). (Cited on page 39.)

[117] Gao, T., Betterton, M. D., Jhang, A. S. & Shelley, M. J. Analytical structure, dynamics, and coarse graining of a kinetic model of an active fluid. *Phys. Rev. Fluids* **2**, 093302 (2017). (Cited on page 39.)

[118] Ellis, P. W. *et al.* Curvature-induced defect unbinding and dynamics in active nematic toroids. *Nat. Phys.* **14**, 85–90 (2018). (Cited on pages 40, 42, 43, 72, and 123.)

[119] Guillamat, P., Ignés-Mullol, J., Shankar, S., Marchetti, M. C. & Sagués, F. Probing the shear viscosity of an active nematic film. *Phys. Rev. E* **94**, 060602 (2016). (Cited on pages 49, 50, 56, and 72.)

[120] Thampi, S. P., Golestanian, R. & Yeomans, J. M. Active nematic materials with substrate friction. *Phys. Rev. E - Stat. Nonlinear, Soft Matter Phys.* **90**, 062307 (2014). (Cited on page 50.)

[121] Lubensky, D. K. & Goldstein, R. E. Hydrodynamics of monolayer domains at the air-water interface. *Physics of Fluids* **8**, 843–854 (1996). (Cited on pages 51 and 173.)

[122] Alert, R., Casademunt, J. & Joanny, J.-F. Active Turbulence. *Annu. Rev. Condens. Matter Phys.* **13**, 143–170 (2022). (Cited on pages 54 and 69.)

[123] Jülicher, F., Grill, S. W. & Salbreux, G. Hydrodynamic theory of active matter. *Reports Prog. Phys.* **81** (2018). (Cited on page 70.)

[124] de Gennes, P. G. & Prost, J. *The physics of liquid crystals* (Oxford University Press, New York, NY, 1993), 2nd edn. (Cited on pages 70, 71, 74, 160, 186, and 187.)

[125] Ravnik, M. & Žumer, S. Landau-de Gennes modelling of nematic liquid crystal colloids. *Liquid Crystals* **36**, 1201–1214 (2009). (Cited on pages 70, 135, and 186.)

[126] Thampi, S. P., Doostmohammadi, A., Golestanian, R. & Yeomans, J. M. Intrinsic free energy in active nematics. *EPL* **112**, 28004 (2015). (Cited on page 70.)

[127] Rivas, D. P., Shendruk, T. N., Henry, R. R., Reich, D. H. & Leheny, R. L. Driven topological transitions in active nematic films. *Soft Matter* **16**, 9331–9338 (2020). (Cited on page 72.)

[128] Hurd, A. J., Fraden, S., Lonberg, F. & Meyer, R. B. Field-Induced Transient Periodic Structures in Nematic Liquid Crystals: the Splay Frederiks Transition. *J. Phys. Paris* **46**, 905–917 (1985). (Cited on pages 72 and 73.)

[129] Taratuta, V. G., Hurd, A. J. & Meyer, R. B. Light-scattering study of a polymer nematic liquid crystal. *Phys. Rev. Lett.* **55**, 246–249 (1985). (Cited on pages 72 and 73.)

[130] Srajer, G., Fraden, S. & Meyer, R. B. Field-induced nonequilibrium periodic structures in nematic liquid crystals: Nonlinear study of the twist frederiks transition. *Phys. Rev. A* **39**, 4828–4834 (1989). (Cited on pages 72, 73, and 75.)

[131] Meyer, R. B. *et al.* Measurements of the anisotropic viscous and elastic properties of lyotropic polymer nematics. *Faraday Discuss. Chem. Soc.* **79**, 125–132 (1985). (Cited on pages 72 and 73.)

[132] Lee, S.-d. & Meyer, R. B. Computations of the phase equilibrium, elastic constants, and viscosities of a hard- rod nematic liquid crystal. *J. Chem. Phys.* **84**, 3443–3448 (1986). (Cited on page 72.)

[133] Lee, S.-d. The Leslie coefficients for a polymer nematic liquid crystal Cite. *J. Chem. Phys.* **88**, 5196–5201 (1988). (Cited on page 72.)

[134] Kleman, M. & Lavrentovich, O. D. *Soft Matter Physics : An Introduction* (Springer, 2001), 1st edn. (Cited on pages 73, 74, 93, and 160.)

[135] Robinson, P. C. & Davidson, M. E. Polarized Light Microscopy (2003). URL https://www.microscopyu.com/techniques/polarized-light/polarized-light-microscopy. (Cited on pages 79 and 81.)

[136] Oldenbourg, R. A new view on polarization microscopy. *Nature* **381**, 811–812 (1996). (Cited on page 80.)

[137] Shribak, M. & Oldenbourg, R. Techniques for fast and sensitive measurements of two-dimensional birefringence distributions. *Appl. Opt* **42**, 3009–3017 (2003). (Cited on page 80.)

[138] Mehta, S. B., Shribak, M. & Oldenbourg, R. Polarized light imaging of birefringence and diattenuation at high resolution and high sensitivity. *J. Opt.* **15** (2013). (Cited on page 80.)

[139] Gottlieb, D. & Arteaga, O. Mueller matrix imaging with a polarization camera: application to microscopy. *Opt. Express* **29**, 34723 (2021). (Cited on pages 82 and 96.)

[140] Thorlabs. *LCC25. Liquid Crystal Controller. Operating Manual* (2011). URL https://www.thorlabs.com/drawings/b15e4cb248648bfb-992819ED-089E-D9F2-6CD23151B32B7CF1/LCC25-Manual.pdf. (Cited on page 82.)

[141] Thorlabs. Software for the LCC25 Liquid Crystal Retarder Controller. Version 4.0.1 (2012). URL https://www.thorlabs.com/software_pages/viewsoftwarepage.cfm?code=LCC25. (Cited on page 82.)

[142] National Instruments. What is LabVIEW (2022). URL https://www.ni.com/en-gb/shop/labview.html. (Cited on pages 82 and 96.)

[143] National Instruments. Create and configure a LabVIEW SubVI (2022). URL https://knowledge.ni.com/KnowledgeArticleDetails?id=kA03q000000YK4VCAW&l=en-GB. (Cited on page 84.)

[144] National Instruments. NI-DAQmx Overview (2022). URL https://www.ni.com/docs/en-US/bundle/ni-daqmx/page/daqhelp/nidaqoverview.html. (Cited on page 84.)

[145] National Instruments. DataSocket simplifies live data Transfer for LabVIEW. URL https://www.ni.com/pdf/datasocket/us/datasocketarticle.pdf. (Cited on page 84.)

[146] Goldstein, D. H. *Polarized light* (CRC Press, Taylor & Francis Group, Boca Raton, FL, 2011), 3rd edn. (Cited on pages 86, 201, and 203.)

[147] Scharf, T. *Polarized light in liquid crystlas and polymers* (John Wiley & Sons, New Jersey, NJ, 2007). (Cited on pages 86 and 201.)

[148] Thorlabs. *Optical Power Meter Utility, Version 5.5* (2015). URL https://www.thorlabs.com/software_pages/ViewSoftwarePage.cfm?Code=PM100x. (Cited on page 88.)

[149] Edmund Optics. What are Beamsplitters? (2012). URL https://www.edmundoptics.com/knowledge-center/application-notes/optics/what-are-beamsplitters/. (Cited on page 89.)

[150] Cui, X. *et al.* Dichroism in Helicoidal Crystals. *J. Am. Chem. Soc.* **138**, 12211–12218 (2016). (Cited on page 91.)

[151] Subramanian, R. & Gelles, J. Two distinct modes of processive kinesin movement in mixtures of ATP and AMP-PNP. *J. Gen. Physiol.* **130**, 445–455 (2007). (Cited on page 109.)

[152] Jouybari, R. M., Sadeghi, A., Khansarinejad, B., Abbasian, S. S. & Abtahi, H. Production of recombinant streptavidin and optimization of refolding conditions for recovery of biological activity. *Reports Biochem. Mol. Biol.* **6**, 178–185 (2018). (Cited on page 109.)

[153] Vale, R. D. The molecular motor toolbox for intracellular transport. *Cell* **112**, 467 – 480 (2003). (Cited on page 110.)

[154] Hyman, A. A., Salser, S., Drechsel, D. N., Unwin, N. & Mitchison, T. J. Role of GTP hydrolysis in microtubule dynamics: Information from a slowly hydrolyzable analogue, GMPCPP. *Mol. Biol. Cell* **3**, 1155–1167 (1992). (Cited on page 111.)

[155] Kuznetsov, S. A. & Gelfand, V. I. Bovine brain kinesin is a microtubule-activated ATPase. *Proc. Natl. Acad. Sci. U.S.A.* **83**, 8530–8534 (1986). (Cited on page 113.)

[156] Lichtman, J. W. & Conchello, J. A. Fluorescence microscopy. *Nat. Methods* **2**, 910–919 (2005). (Cited on page 120.)

[157] Edelstein, A. D. *et al.* Advanced methods of microscope control using μManager software. *Journal of Biological Methods* **1**, 10 (2014). (Cited on page 120.)

[158] Willert, C. E. & Gharib, M. Digital particle image velocimetry. *Exp. Fluids* **10**, 181–193 (1991). (Cited on page 120.)

[159] Thielicke, W. & Stamhuis, E. J. PIVlab – Towards User-friendly, Affordable and Accurate Digital Particle Image Velocimetry in MATLAB. *J. Open Res. Softw* **2** (2014). (Cited on pages 120 and 122.)

[160] Thielicke, W. *The flapping flight of birds: Analysis and application.* Ph.D. thesis, University of Groningen (2014). (Cited on pages 120 and 122.)

[161] Raffel, M. *et al. Particle Image Velocimetry. A Practical Guide* (Springer International Publishing AG, Berlin, 2018), 3rd edn. (Cited on page 120.)

[162] Olson, T. *Applied Fourier Analysis* (Birkhäuser, New York, NY, 2017). (Cited on pages 121 and 193.)

[163] Ellis, P. W., Nambisan, J. & Fernandez-Nieves, A. Coherence-enhanced diffusion filtering applied to partially-ordered fluids. *Mol. Phys.* **118** (2020). (Cited on page 123.)

[164] Weickert, J. Coherence-enhancing diffusion filtering. *Int. J. Comput. Vis.* **31**, 111–127 (1999). (Cited on page 123.)

[165] MathWorks. 2-D fast Fourier transform - MATLAB. URL https://www.mathworks.com/help/matlab/ref/fft2.html. (Cited on page 132.)

[166] Inc., W. R. Mathematica, Version 10.0. Champaign, IL, 2014. (Cited on page 134.)

[167] Ross, T. D. *et al.* Controlling organization and forces in active matter through optically defined boundaries. *Nature* **572**, 224–229 (2019). (Cited on page 160.)

[168] Arfken, G., Weber, H. J. & Harris, F. E. *Mathematical methods for physicists. A comprehensive guide* (Elseiver, 2013), 7th edn. (Cited on pages 168, 169, 177, and 181.)

[169] Dunster, T. M. Bessel functions of purely imaginary order, with an application to second-order linear differential equations having a large parameter. *SIAM J. Math. Anal.* **21**, 995–1018 (1990). (Cited on page 168.)

[170] Brennen, C. E. An internet book on fluid dynamics (2006). URL http://brennen.caltech.edu/fluidbook/. (Cited on page 169.)

[171] Stone, H. A. & McConnell, H. M. Hydrodynamics of quantized shape transitions of lipid domains. *Proc. R. Soc. Lond. A* **448**, 97–11 (1995). (Cited on page 175.)

[172] Pozrikidis, C. *Boundary Integral and Singularity Methods for Linearized Viscous Flow* (Cambridge University Press, New York, NY, 1992). (Cited on page 177.)

[173] Stakgold, I. & Holst, M. *Green's functions and boundary value problems* (John Wiley & Sons, Hoboken, NJ, 2011), 3rd edn. (Cited on page 177.)

[174] James, J. F. *A student's guide to Fourier transforms* (Cambridge University Press, New York, NY, 2011), 3rd edn. (Cited on page 177.)

[175] Scherfgen, David. Integral Calculator (2022). URL https://www.integral-calculator.com/. (Cited on page 181.)

[176] Qmechanic. Leading terms in asymptotic expansion of modified bessel function of the first kind. Mathematics Stack Exchange. URL https://math.stackexchange.com/q/2792938. (version: 2018-05-24). (Cited on page 181.)

[177] Pearce, D. J. Activity Driven Orientational Order in Active Nematic Liquid Crystals on an Anisotropic Substrate. *Phys. Rev. Lett.* **122**, 227801 (2019). (Cited on pages 185 and 186.)

[178] Broughton, S. A. & Bryan, K. *Discrete Fourier Analysis and Wavelets* (John Wiley & Sons, Hoboken, NJ, 2018), 2nd edn. URL https://onlinelibrary.wiley.com/doi/abs/10.1002/9781119473329.fmatter. (Cited on page 193.)

[179] Stein, E. M. & Shakarchi, R. *Fourier Analysis: An Introduction* (Princeton University Press, 2003). (Cited on page 193.)

[180] Hansen, E. W. *Fourier transforms* (Wiley, New Jersey, 2014). (Cited on page 200.)

[181] Sunaina, Butola, M. & Khare, K. Calculating numerical derivatives using Fourier transform: Some pitfalls and how to avoid them. *Eur. J. Phys.* **39** (2018). (Cited on page 200.)

[182] Shipman, J. T., Wilson, J. D., Higgins, C. A. & Torres, O. *An Introduction to Physical Science* (Cengage Learning, Boston, MA, 2016), 14th edn. (Cited on page 201.)

[183] Stokes, G. G. On the composition and resolution of streams of polarized light from different sources. *Trans. Cambridge Philos. Soc.* **9**, 399–416 (1852). (Cited on page 204.)

[184] Schaefer, B., Collett, E., Smyth, R., Barrett, D. & Fraher, B. Measuring the Stokes polarization parameters. *Am. J. Phys.* **75**, 163–168 (2007). (Cited on page 205.)

Appendix A

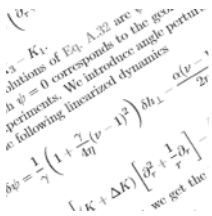

Stability of an extensile active nematic aster

A.1 Dynamic equations of an active nematic. Vectorial description in absence of defects

The dynamics of an isolated 2D active fluid with a velocity field $\vec{v}$ and a nematic director $\vec{n} = (\cos\theta \sin\theta)$ can be described using a hydrodynamic theory that accounts for conservation laws and symmetries within the system. An example of such theories is the so-called active gel theory [100, 114, 115]. In such theory, the momentum balance equation in the Einstein summation convention (see Info Box A.1) reads:

$$\rho(\partial_t + v_\beta \partial_\beta) v_\alpha = -\partial_\alpha P + \partial_\beta(\sigma_{\alpha\beta} + \sigma^{\mathrm{a}}_{\alpha\beta}), \tag{A.1}$$

where P is the pressure and acts as a Lagrange multiplier to enforces the incompressibility condition $\partial_\alpha v_\alpha = 0$. $\sigma_{\alpha\beta}$ and $\sigma^a_{\alpha\beta}$ are the symmetric and antisymmetric parts of the stress tensor, respectively. Since the system of interest here is at low Reynolds number, we can neglect the left hand side of Eq. A.1, which corresponds to the inertial forces, and momentum balance is reduced to force balance.

$$0 = -\partial_\alpha P + \partial_\beta(\sigma_{\alpha\beta} + \sigma^a_{\alpha\beta}), \tag{A.2}$$

This is the Stokes limit.The symmetric and the antisymmetric part of the stress tensor are defined by:

$$\sigma_{\alpha\beta} = 2\eta v_{\alpha\beta} + \frac{\nu}{2}(n_\alpha h_\beta + h_\alpha n_\beta - n_\gamma h_\gamma \delta_{\alpha\beta}) - \alpha q_{\alpha\beta}, \tag{A.3a}$$

$$\sigma^{\mathrm{a}}_{\alpha\beta} = \frac{1}{2}(n_\alpha h_\beta - h_\alpha n_\beta), \tag{A.3b}$$

where η is the shear viscosity, $v_{\alpha\beta} = 1/2(\partial_\alpha v_\beta + \partial_\beta v_\alpha)$ is the symmetric part of the strain rate tensor. ν is the flow alignment coefficient, which controls the coupling of the nematic field and the flow. $h_\alpha = -\delta F_n/\delta n_\alpha$ is the orientational field defined by the functional derivative of the Frank free energy F_n. The active term is controlled by the activity coefficient α. This term can be either positive or negative depending on the active stresses exerted by the active particles, here the kinesin clusters on the MT. In this formulation, if the stresses are extensile, as in the system of interest in this thesis, α is positive ($\alpha > 0$), whereas if the stresses are contractile, like in the actin-myosin system in [167], α is negative ($\alpha < 0$). $q_{\alpha\beta} = n_\alpha n_\beta - 1/2\delta_{\alpha\beta}$ is the nematic tensor. Note that in this theory the modulus of $\vec{n}$ is fixed at $|\vec{n}| = 1$ and there is not a scalar order parameter, thus topological defects are not considered. This approximation is good as far as the system is below the nematic/isotropic transition temperature [124]. The Frank free energy is given by

$$F_n = \int \left[\frac{K_1}{2}(\boldsymbol{\nabla} \cdot \vec{n})^2 + \frac{K_3}{2}(\vec{n} \times (\boldsymbol{\nabla} \times \vec{n}))^2 - h^0_\parallel \vec{n} \cdot \vec{n} \right] \mathrm{d}^2\vec{r}. \tag{A.4}$$

where K_1 and K_3 are the splay and bend elastic constants, respectively and $h^0_\parallel$ is a Lagrange multiplier that ensures $|\vec{n}| = 1$. This term can be neglected by parameterizing the director through the polar angle θ ($\vec{n} = (\cos\theta, \sin\theta)$) in such a way that the constraint $|\vec{n}| = 1$ is taken into account [134]. In this expression Eq. A.4, there is no twist term because it is for a 2D system. The molecular field then reads

$$h_x = K_1[\partial_x^2 n_x + \partial_x \partial_y n_y] + K_3[\partial_y^2 n_x - \partial_x \partial_y n_y] \tag{A.5}$$

$$h_y = K_1[\partial_y^2 n_y + \partial_x \partial_y n_x] + K_3[\partial_x^2 n_y - \partial_x \partial_y n_x], \tag{A.6}$$

where we have already not included the Lagrange multiplier.

Finally, the dynamics of the director field is given by:

$$\frac{D}{Dt} n_\alpha = (\partial_t + v_\beta \partial_\beta) n_\alpha + \omega_{\alpha\beta} n_\beta = \frac{1}{\gamma} h_\alpha - \nu v_{\alpha\beta} n_\beta, \tag{A.7}$$

with γ the rotational viscosity and $\omega_{\alpha\beta}$ the antisymmetric part of the strain rate constant or the vorticity tensor which reads:

$$\omega_{\alpha\beta} = \frac{1}{2}(\partial_\alpha v_\beta - \partial_\beta v_\alpha) \tag{A.8}$$

Infobox A.1: Einstein summation convention

The Einstein summation is a convention to simplify mathematical expressions including summations over vectors, matrices, and tensors. According to this convention:

1. Repeated indexes imply summation over.
2. Each index can appear in one term maximum twice.

Hence, for example the dot product of two 2D vectors can be written as:

$$\vec{a} \cdot \vec{b} = a_i b_i = a_1 b_1 + a_2 b_2$$

or, the contraction of two tensors, also known as Frobenius inner product or double dot product:

$$\boldsymbol{A} : \boldsymbol{B} = \mathrm{Tr}(\boldsymbol{A}\,\boldsymbol{B}^T) = a_{ij} b_{ij} = a_{11} b_{11} + a_{12} b_{12} + a_{21} b_{21} + a_{22} b_{22}$$

Within the theory of active gels, it is very common to use the one constant approximation ($K_1 = K_3 = K$), this leads Eq. A.4 to the following expression:

$$F_n = \int \frac{K}{2} (\boldsymbol{\nabla} \vec{n})^2 \mathrm{d}^2 \vec{r} = \int \frac{K}{2} (\partial_\alpha n_\beta)(\partial_\alpha n_\beta) = \int \frac{K}{2} |\boldsymbol{\nabla} \theta|^2 \mathrm{d}^2 \vec{r}. \tag{A.9}$$

In this case, the orientation or molecular field reads:

$$h_\alpha = -\frac{\delta F_n}{\delta n_\alpha} = K \nabla^2 n_\alpha \tag{A.10}$$

Usually h_α is written in terms of its parallel ($h_\parallel = \vec{n} \cdot \vec{h}$) and perpendicular ($h_\perp = \vec{n} \times \vec{h}$) components with respect to $\vec{n}$:

$$h_x = h_\parallel \cos\theta - h_\perp \sin\theta \tag{A.11a}$$
$$h_y = h_\parallel \sin\theta + h_\perp \cos\theta \tag{A.11b}$$
$$h_\perp = K \nabla^2 \theta \tag{A.11c}$$
$$h_\parallel = -K |\boldsymbol{\nabla} \theta|^2 \tag{A.11d}$$

Combining properly the components x and y of the dynamics of the director in

Eq. A.7 it is possible to arrive at the following simplified expressions:

$$\partial_t\theta = \frac{\partial_x v_y - \partial_y v_x}{2} + \frac{1}{\gamma}h_\perp + \frac{\nu}{2}\sin 2\theta(\partial_x v_x - \partial_y v_y) - \frac{\nu}{2}\cos 2\theta(\partial_x v_y + \partial_y v_x) - (\vec{v}\cdot\boldsymbol{\nabla})\theta \tag{A.12}$$

$$0 = \frac{1}{\gamma}h_\parallel - \nu\partial_x v_x\cos 2\theta - \frac{\nu}{2}\sin 2\theta(\partial_x v_y + \partial_y v_x) \tag{A.13}$$

In our experiments, we see how a radially aligned active nematic is unstable to bend perturbations that rapidly grow driven by active stresses. To study such instability, we start by the simplified picture of a linearly aligned active material following the scheme in [100, 104]

A.2 Linear stability analysis

Consider an active nematic film confined within a channel of length much larger than its width L. For an unconfined system $L \to \infty$. This geometry allows us to assume that the system is translationally invariant along the long axis, which we take as the x-direction. This implies that $\partial_x v_x = 0$, and, consequently, due to the incompressibility of the fluid $\partial_y v_y = 0$. Moreover, mass conservation entails that $v_y = 0$. Then, under these conditions, the force balance along the x axis reads

$$0 = \partial_y\sigma_{xy} + \partial_y\sigma^{\mathrm{a}}_{xy} \tag{A.14}$$

Also, if we assume hydrodynamic free boundary conditions, $\sigma_{xy}(y=0)+\sigma^{\mathrm{a}}_{xy}(y=0) = \sigma_{xy}(y=L)+\sigma^{\mathrm{a}}_{xy}(y=L) = 0$, the transverse stress must vanish:

$$0 = \sigma_{xy} + \sigma^{\mathrm{a}}_{xy} = \eta\partial_y v_x + \frac{\nu}{2}(h_\parallel\sin 2\theta + h_\perp\cos 2\theta) - \alpha\frac{\sin 2\theta}{2} + \frac{h_\perp}{2} \tag{A.15}$$

Taking Eq. A.13 and imposing the boundary conditions for this problem, the orientation dynamics read:

$$0 = \frac{1}{\gamma}h_\parallel - \nu\frac{\partial_y v_x}{2}\sin 2\theta, \tag{A.16}$$

$$\partial_t\theta = \frac{1}{\gamma}h_\perp - \frac{\partial_y v_x}{2}(\nu\cos 2\theta + 1). \tag{A.17}$$

Introducing Eq. A.16 into Eq. A.15

$$\partial_y v_x = \frac{-2h_\perp(\nu\cos 2\theta + 1) + 2\alpha\sin 2\theta}{4\eta + \nu^2\gamma\sin^2 2\theta}. \tag{A.18}$$

Now, inserting this last equation Eq. A.18 into Eq. A.17 we obtain a nonlinear differential equation for the angle θ

$$\partial_t\theta = \frac{h_\perp}{\gamma}\frac{4\eta+\gamma(\nu^2+2\nu\cos 2\theta+1)}{4\eta+\gamma\nu^2\sin^2 2\theta} - \frac{\alpha\sin 2\theta(\nu\cos 2\theta+1)}{4\eta+\gamma\nu^2\sin^2 2\theta}, \tag{A.19}$$

and, from Eq. A.11,

$$h_\perp = K\partial_y^2\theta. \tag{A.20}$$

The steady states of Eq. A.19 are then given by an homogeneous alignment with $\theta = 0$, $\theta = \pi/2$ and the angle θ_0 satisfying $(\nu\cos 2\theta_0 + 1) = 0$. The latter case is a stable configuration, independently to the material parameters of the system, therefore, we only focus on the former cases. Here, for the symmetry of the problem, the only wave numbers we can consider are those oriented along the y-direction (q_y). Hence, to study the stability of longitudinal (transversal) modulations, we have to take $\theta = \pi/2$ ($\theta = 0$). Longitudinal modulations result into bend-dominated deformations whereas transversal modulations produce splay-dominated deformations. For $\theta = \pi/2$, when the material is aligned along the y axis, we introduce angle perturbations $\theta = \pi/2 + \delta\theta$, whose linearized dynamics reads:

$$\partial_t\delta\theta = \frac{K}{\gamma}\left(1+\frac{\gamma}{4\eta}(\nu-1)^2\right)\partial_y^2\delta\theta - \frac{\alpha(\nu-1)}{2\eta}\delta\theta, \tag{A.21}$$

where we have used $\cos(2(\pi/2+\delta\theta)) \approx -1$, $\sin(2(\pi/2+\delta\theta)) \approx -2\delta\theta$ and $|\delta\theta| \ll 1$.

Considering that the solution of Eq. A.21 has the form of $\delta\theta(y,t) = Y(y)T(t)$, it is possible to see $\delta\theta(y,t) = \sum_{n=0}^{\infty}\delta\theta_n e^{\Omega t}\cos(q_n y)$. Then, the growth rate Ω takes the form

$$\Omega = -\frac{Kq_y^2}{\gamma}\left(1+\frac{\gamma}{4\eta}(\nu-1)^2\right) - \frac{\alpha(\nu-1)}{2\eta}. \tag{A.22}$$

Since $K > 0$ and $\gamma > 0$, the first term in Eq. A.22 is always negative and, thus, it damps any perturbation. In contrast, the second term can be either positive or negative depending on α and ν. For an extensile active system ($\alpha > 0$), as the one in our experiments, small-wave number longitudinal perturbations grow exponentially if $\nu < 1$. ν in our experiments should be negative since the MTs are rod-like ($\nu < 0$) and they should be in the flow-aligning regime ($|\nu| > 1$), i.e. they tend to align at a unique angle from the flow direction [101][1].

Finally, the critical wave number is given by

$$q_c = \left(-\frac{\gamma}{K}\frac{\alpha(\nu-1)}{2\eta}\right)^{1/2}\left(1+\frac{\gamma}{4\eta}(\nu-1)^2\right)^{-1/2} \tag{A.23}$$

[1] In this article by Edwards et al., the authors use the coefficient λ for the flow alignment parameter, which has the opposite sign of ν ($\nu = -\lambda$)

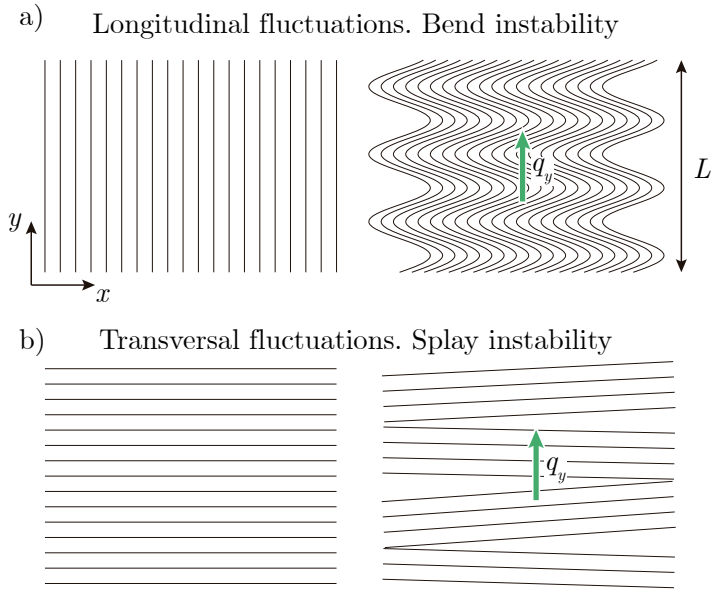

Figure A.1: Schematic representation of the two main fluctuations in aligned active fluids. **a**) Longitudinal fluctuations trigger the bending of an aligned active fluids. These fluctuations are seen in systems with extensile stresses. **b**) Transversal fluctuations that lead to splay deformations of an aligned active fluids. These fluctuations are seen in systems with contractile stresses. Both geometries are represented following the geometry for the problem here presented. The long axis is the x-axis, and y has a size of L, which, for an unconfined system $L \to \infty$. To study longitudinal (transversal) fluctuations we must consider an initial alignment along the y-axis (x-axis). The wave number q_y associated to the fluctuations is indicated as a green arrow.

and the wave number of maximum growth rate is $q^* = 0$.

A.3 Linear analysis with an axial symmetry

Before starting, I must mention that this stability analysis has been performed by Ricard Alert.

We start by considering a system with axial symmetry. Thus, the incompressibility condition using the polar coordinates r and φ looks

$$\frac{1}{r}\partial_r(rv_r) = 0, \tag{A.24}$$

which has a solution $v_r(r) = A/r$. In order to avoid divergence at the center, we impose $A = 0$ and, hence $\vec{v} = (0, v_\varphi$. We also write the director field in terms of the angle ψ with respect to the radial direction:

$$n_r = \cos\psi,\ n_\varphi = \sin\psi. \tag{A.25}$$

Using polar coordinates, the strain rate tensor reads (see Info Box A.3) $v_{r\varphi} = v_{\varphi r} = \frac{1}{2}\left(\partial_r v_\varphi - \frac{v_\varphi}{r}\right)$ and $\omega_{r\varphi} = -\omega_{\varphi r} = \frac{1}{2r}\partial_r(rv_\varphi) = \frac{1}{2}\left(\partial_r v_\varphi + \frac{v_\varphi}{r}\right)$.

As in the previous section, we compute the force balance along the φ direction taking into account the gradient of tensor in polar coordinates (see Info Box A.3):

$$0 = \frac{1}{r^2}\partial_r\left[r^2\left(\sigma_{\varphi r} + \sigma^{\mathrm{a}}_{\varphi r}\right)\right], \tag{A.26}$$

Hence, $\left(\sigma_{\varphi r} + \sigma^{\mathrm{a}}_{\varphi r}\right) = A/r^2$. As before, to avoid divergence at the center, we impose $A = 0$. Thus,

$$0 = \sigma_{\varphi r} + \sigma^{\mathrm{a}}_{\varphi r} = 2\eta v_{\alpha\beta} + \frac{\nu}{2}(h_\parallel \sin 2\psi + h_\perp \cos 2\psi) - \frac{\alpha \sin 2\psi}{2} - \frac{1}{2}h_\perp \tag{A.27}$$

and the dynamics of the director can be reduced to

$$0 = \frac{1}{\gamma}h_\parallel - \nu v_{r\varphi}\sin 2\psi, \tag{A.28}$$

$$\partial_t\psi = \frac{1}{\gamma}h_\perp - v_{r\varphi}\nu\cos 2\psi + \omega_{r\varphi}, \tag{A.29}$$

where, in this case, $h_\parallel = (h_r\cos\psi + h_\varphi\sin\psi)$ and $h_\perp = (-h_r\sin\psi + h_\varphi\cos\psi)$.

$$\partial_t\psi = \frac{1}{\gamma}h_\perp - v_{r\varphi}(\nu\cos 2\psi - 1) \tag{A.30}$$

Combining Eq. A.27 with Eq. A.28, we obtain the following expression for $v_{r\varphi}$:

$$v_{r\varphi} = \frac{-h_\perp(\nu\cos 2\psi - 1) + \alpha \sin 2\psi}{4\eta + \gamma\nu^2 \sin^2 2\psi}, \tag{A.31}$$

and introducing this last equation into Eq. A.29

$$\partial_t \psi = \frac{h_\perp}{\gamma}\frac{4\eta + \gamma(\nu^2 - 2\nu\cos 2\psi + 1)}{4\eta + \gamma\nu^2 \sin^2 2\psi} - \frac{\alpha \sin 2\psi(\nu\cos 2\psi - 1)}{4\eta + \gamma\nu^2 \sin^2 2\psi}. \tag{A.32}$$

To compute $h_\perp$, we need to write the Frank Free energy (Eq. A.4) in polar coordinates

$$F_n = \int_0^{2\pi}\int \left[\frac{K_1}{2}\left(\frac{1}{r}\partial_r(r\cos\psi)\right)^2 + \frac{K_3}{2}\left(\frac{1}{r}\partial_r(r\sin\psi)\right)^2\right] r dr d\varphi, \tag{A.33}$$

Thus,

$$h_r = -\frac{\delta F_n}{\delta n_r} = K_1\left[-\frac{1}{r}\sin\psi\partial_r\psi - \frac{1}{r^2}\cos\psi - \sin\psi\partial_r^2\psi - \cos\psi(\partial_r\psi)^2\right] \tag{A.34}$$

$$h_\varphi = -\frac{\delta F_n}{\delta n_\varphi} = K_3\left[\frac{1}{r}\cos\psi\partial_r\psi - \frac{1}{r^2}\sin\psi + \cos\psi\partial_r^2\psi - \sin\psi(\partial_r\psi)^2\right] \tag{A.35}$$

A

and

$$h_\perp = -\frac{\delta F_n}{\delta\psi} = (K + \Delta K\cos^2\psi)\left(\partial_r^2\psi + \frac{1}{r}\partial_r\psi\right) - \frac{\Delta K}{2}\sin 2\psi\left(\frac{1}{r^2} + (\partial_r\psi)^2\right), \tag{A.36}$$

where $K = K_1$ and $\Delta K = K_3 - K_1$.

Then, the stationary solutions of Eq. A.32 are $\psi = 0$ and $\psi = \pi/2$. Note that the steady state with $\psi = 0$ corresponds to the geometry of an aster, like the one we get in our experiments. We introduce angle perturbations $\delta\psi$ around $\psi = 0$ described by the following linearized dynamics

$$\partial_t\delta\psi = \frac{1}{\gamma}\left(1 + \frac{\gamma}{4\eta}(\nu - 1)^2\right)\delta h_\perp - \frac{\alpha(\nu - 1)}{2\eta}\delta\psi, \tag{A.37}$$

with

$$\delta h_\perp = \left[(K + \Delta K)\left[\partial_r^2 + \frac{1}{r}\partial_r\right] - \frac{\Delta K}{r^2}\right]\delta\psi. \tag{A.38}$$

Combining these last two equations, we get the following close dynamics

$$\left[\frac{\gamma}{1 + \frac{\gamma}{4\eta}(\nu - 1)^2}\right]\partial_t\delta\psi = (K + \Delta K)\left[\partial_r^2 + \frac{1}{r}\partial_r - \frac{n^2}{r^2} + \frac{1}{\ell^2}\right]\delta\psi. \tag{A.39}$$

Taking

$$n^2 = \frac{\Delta K}{K + \Delta K}, \text{ and } \frac{1}{\ell^2} = \frac{2\gamma}{4\eta + \gamma(\nu-1)^2}\frac{\alpha(\nu-1)}{K+\Delta K} \tag{A.40}$$

Notice that K and ΔK have units of N·m≡ Pa·m^3, γ and η of Pa·s·m, α of Pa·m, and ν is dimensionless. Hence, ℓ^2 has units of area and it can be either positive or negative depending on the sign of $\alpha(\nu-1)$.

As we did in the previous section, we consider that the solution to Eq. A.39 can be separated into the product of a function of t and a function of r such as $\delta\psi = X(r)T(t)$. Here, $T(t) = \sum_{n=0}^{\infty} T_n e^{\Omega_n t}$, which means that perturbations can grow or decay exponentially with a growth rate given by

$$\Omega = \frac{\Gamma}{\gamma}\left(1 + \frac{\gamma}{4\eta}(\nu-1)^2\right) \tag{A.41}$$

As for the function of r

$$(K + \Delta K)\left[\partial_r^2 + \frac{1}{r}\partial_r - \frac{n^2}{r^2} + \frac{1}{\lambda^2}\right] X(r) = 0 \tag{A.42}$$

with

$$\frac{1}{\lambda^2} = \frac{1}{\ell^2} - \frac{\Gamma}{K+\Delta K} \tag{A.43}$$

The solutions to Eq. A.42 are the two Bessel function $X(r) = B_n(r/\lambda)$ of order n and $-n$. To find Γ, and hence see the stability of the perturbations, we need to impose some boundary conditions. For this particular problem, we will assume that the aster at a given radius R is undistorted, this is $\delta\psi(R) = 0$. This picture corresponds to having an aster that merges with the rest of the active gel at $r = R$. This condition $B_n(R/\lambda) = 0$, sets a condition on the parameter λ, namely $z_m = R/\lambda$, where z_m is a zero of the Bessel function. This discretizes both λ and Ω, which are given by

$$\lambda_m = \frac{2\pi}{q_m} = \frac{z_m}{R}, \tag{A.44a}$$

$$\Omega_m = -\frac{K+\Delta K}{\gamma}\frac{q_m^2}{4\pi^2}\left(1 + \frac{\gamma(\nu-1)^2}{4\eta}\right) - \frac{\alpha(\nu-1)}{2\eta}, \tag{A.44b}$$

where the subindex m indicates the allowed discrete set of growth rates and wavelengths. Then, the growth rate of the fastest growing mode is

$$\Omega_1 = -\frac{K+\Delta K}{\gamma}\frac{z_1^2}{R^2}\left(1 + \frac{\gamma(\nu-1)^2}{4\eta}\right) - \frac{\alpha(\nu-1)}{2\eta}, \tag{A.45}$$

which happens for a finite wavelength $\lambda_1 = R/z_1$. In our experiments, $\alpha > 0$. Therefore, the aster disposition is unstable to small wave number perturbations if $\nu < 1$. We should recognize that the discretization of the relation dispersion is the result of the imposed boundary conditions rather than the geometry itself. Furthermore, even if we consider the discretization of the dispersion relation to be the selection mechanism of the wavelength, given that the most unstable mode is $\lambda_1 = R/z_1$, we would only see one turn of the director field. In other words, we would have seen only one kink in our experiments.

Infobox A.2: Bessel functions

Bessel functions are solutions to partial differential equations of the form:

$$x^2\frac{d^2y}{dx^2} + x\frac{dy}{dx} + (x^2 - n^2)y = 0 \tag{A.46}$$

These equations are widely used in physics, especially in problems involving radial or cylindrical geometries [168]. There are different kinds of Bessel functions, but the most studied are the Bessel function of the first kind $J_n(x)$

It is interesting to mention that the growth rate only depends on the bend elastic constant ($K + \Delta K = K_3$). This is because the aster geometry is a pure splay state. In contrast, if the initial distribution were a vortex, a pure bend geometry, the growth rate would only depend on the splay elastic constant. However, the spatial distribution of the perturbations depends on both elastic constants through the order of the Bessel function n. In fact, if $\Delta K \geq 0$, n is real and then the Bessel function $B_n(r/\lambda)$ is a Bessel function of the first kind $J_n(r/\lambda)$. Another possible solution to Eq. A.42 for real n could be a Bessel function of the second kind Y_n, but these type of functions diverge at 0. On the other hand, if $\Delta K < 0$, the order of the Bessel function $B_n(r/\lambda)$ becomes imaginary and then the solution is not a Bessel function of the first kind anymore. This is because these functions J_n are not real if n is imaginary. We, therefore, need to use another set of Bessel functions, which are a linear combination of Bessel functions of the first kind [169]

$$F_n(r) = \frac{1}{2}\sec(n\pi/2)\{J_n(r/\lambda) + J_{-n}(r/\lambda)\} \tag{A.47}$$

$$G_n(r) = \frac{1}{2}\mathrm{cosec}(n\pi/2)\{J_n(r/\lambda) - J_{-n}(r/\lambda)\} \tag{A.48}$$

Note that if $\Delta K = 0$, the relation between the growth rate and the wave

number given by A.44b is the same as in the problem with a linear geometry (Eq. A.22).

Infobox A.3: Operators in polar coordinates

Polar coordinates are very useful to mathematically describe systems with axial or radial symmetry. With this system, any point on a plane is represented with a distance (r) from a reference point and an angle (φ) from a reference angle.
Due to the new geometry, some operators can change from the cartesian coordinate system. Here we list some of the most important operators:

Operator	2D cartesian coordinate system	Polar coordinate system
Gradient $\boldsymbol{\nabla} F$ [168]	$\partial_x F \hat{e}_x + \partial_y F \hat{e}_y$	$\partial_r F \hat{e}_r + \frac{1}{r}\partial_\varphi F \hat{e}_\varphi$
Divergence of a vector $\boldsymbol{\nabla} \cdot \vec{f}$ [168]	$\partial_x f_x + \partial_y f_y$	$\frac{1}{r}\partial_r (r f_r) + \frac{1}{r}\partial_\varphi f_\varphi$
Curl of a vector $\boldsymbol{\nabla} \times \vec{f}$ [168]	$\partial_y f_x - \partial_x f_y$	$\frac{1}{r}(\partial_r (r f_\varphi) - \partial_\varphi f_r)$
Divergence of a tensor $\boldsymbol{\nabla} \cdot \boldsymbol{F}$	$\begin{pmatrix} \partial_x F_{xx} + \partial_y F_{yx} \\ \partial_x F_{xy} + \partial_y F_{yy} \end{pmatrix}$	$\begin{pmatrix} \partial_r F_{rr} + \frac{F_{rr}}{r} + \frac{1}{r}\partial_\varphi F_{\varphi r} - \frac{F_{\varphi\varphi}}{r} \\ \frac{1}{r}\partial_\varphi F_{\varphi\varphi} + \partial_r F_{r\varphi} + \frac{F_{r\varphi}}{r} + \frac{F_{\varphi r}}{r} \end{pmatrix}$
Symmetric part of the strain rate tensor [170]	$v_{\alpha\beta} = \frac{1}{2}(\partial_\alpha v_\beta + \partial_\beta v_\alpha)$	$v_{rr} = \partial_r v_r$ $v_{\varphi\varphi} = \frac{v_r}{r} + \frac{1}{r}\partial_\varphi v_\varphi$ $v_{r\varphi} = \frac{1}{2}(\partial_r v_\varphi - \frac{v_\varphi}{r} + \frac{1}{r}\partial_\varphi v_r)$ $v_{\varphi r} = v_{r\varphi}$
Antisymmetric part of the strain rate tensor [170]	$\omega_{\alpha\beta} = \frac{1}{2}(\partial_\alpha v_\beta - \partial_\beta v_\alpha)$	$\omega_{rr} = 0$ $\omega_{\varphi\varphi} = 0$ $\omega_{r\varphi} = \frac{1}{2}(\frac{1}{r}\partial_r (r v_\varphi) - \frac{1}{r}\partial_\varphi v_r)$ $\omega_{\varphi r} = -\omega_{r\varphi}$

A.4 Linear stability analysis with external dissipation

In our experiments, the coupling of the AN layer with the surrounding 3D layers is unavoidable. Thus, we assess whether this coupling can select a wavelength in the linear regime of the instability. We proceed as in Appendix A.2, but in the force balance equation we need to include two terms accounting for the viscous stresses produced by the passive layers, $\boldsymbol{f}^{\text{water}}$ and $\boldsymbol{f}^{\text{oil}}$:

$$0 = \partial_\beta \sigma_{\alpha\beta} + \partial_\beta \sigma^{\text{a}}_{\alpha\beta} + f^{\text{water}}_\alpha + f^{\text{oil}}_\alpha \tag{A.49}$$

with $\sigma_{\alpha\beta}$ and $\sigma^{\text{a}}_{\alpha\beta}$ defined in Eq. A.3, and

$$\boldsymbol{f}^{\text{water}} = -\eta_{\text{water}} \left.\frac{\partial \boldsymbol{u}^{\text{water}}_\parallel(\boldsymbol{r}, z)}{\partial z}\right|_{z=0^-} \tag{A.50a}$$

$$\boldsymbol{f}^{\text{oil}} = \eta_{\text{oil}} \left.\frac{\partial \boldsymbol{u}^{\text{oil}}_\parallel(\boldsymbol{r}, z)}{\partial z}\right|_{z=0^+} \tag{A.50b}$$

Here, we have considered that the velocity fields of the passive layers are planar, $\boldsymbol{u}(\boldsymbol{r}, z) = \boldsymbol{u}_\parallel(\boldsymbol{r}, z)$, with $\boldsymbol{r} = (x, y)$. With this geometry, the flow fields of the 3D layers are given by:

$$\boldsymbol{u}^{\text{ext}}(\boldsymbol{r}, z) = g^{\text{ext}}(z)\boldsymbol{v}(\boldsymbol{r}) \tag{A.51}$$

where $\boldsymbol{v}(\boldsymbol{r})$ is the velocity of the AN, and $g^{\text{ext}}(z)$ is a hydrodynamic function that describes how the flow penetrates into the external fluid layers. Like in Appendix A.2, we assume parallel alignment along the x axis of the active material with transversal invariance. Thus, $\partial_x v_x = \partial_y v_y = 0$, $v_y = 0$ and $f^{\text{ext}}_y = 0$. Then, the force balance along the x-direction has the form of:

$$\begin{aligned} 0 = \partial_y \sigma_{xy} + \partial_y \sigma^{\text{a}}_{xy} + f^{\text{water}}_x + f^{\text{oil}}_x = \\ \eta \partial_y^2 v_x - \alpha \cos 2\theta \partial_y \theta + \partial_y \frac{h_\perp}{2} + \frac{\nu}{2}\partial_y (h_\parallel \sin 2\theta + h_\perp \cos 2\theta) \\ + v_x \left(-\eta_{\text{water}}\, \partial_z g^{\text{water}}(z)\big|_{z=0^-} + \eta_{\text{oil}}\, \partial_z g^{\text{oil}}(z)\Big|_{z=0^+} \right) \end{aligned} \tag{A.52}$$

The dynamics of the orientational field, are the same as in Eqs. A.16 and A.17. Thus, the stationary solutions of Eqs. A.16, A.17 and A.52 are $\theta = 0$ or $\theta = \pi/2$ and $\boldsymbol{v} = \boldsymbol{0}$. In Appendix A.2, we have shown that extensile isolated active nematics are unstable to longitudinal perturbations, which, for this problem,

correspond to distortions of wavevector q_y around $\theta = \pi/2$. Thus, we now introduce angle and velocity perturbations $\delta\theta$ and $\delta\boldsymbol{v}$, respectively, around the $\theta = \pi/2$ and $\boldsymbol{v} = \mathbf{0}$ stationary point.

$$\partial_t \delta\theta = \frac{K}{\gamma}\partial_y^2\theta + \frac{\partial_y \delta v_x}{2}(\nu - 1) \tag{A.53}$$

$$\eta\partial_y^2\delta v_x = -\alpha\partial_y\delta\theta + \partial_y\frac{K\partial_y^2\delta\theta}{2}(\nu-1) - \delta v_x\left(-\eta_{\text{water}}\,\partial_z g^{\text{water}}(z)\big|_{z=0^-} + \eta_{\text{oil}}\,\partial_z g^{\text{oil}}(z)\Big|_{z=0^+}\right) \tag{A.54}$$

Combining Eqs. A.53 and A.54

$$\partial_t\delta\theta = \frac{K}{\gamma}\partial_y^2\delta\theta + \frac{(\nu-1)}{2}\frac{[-\alpha + K/2(\nu-1)\partial_y^2]\partial_y^2\delta\theta}{\eta\partial_y^2 + (-\eta_{\text{water}}\,\partial_z g^{\text{water}}(z)|_{z=0^-} + \eta_{\text{oil}}\,\partial_z g^{\text{oil}}(z)|_{z=0^+})}. \tag{A.55}$$

The solution to this last Eq. A.55, must be of the form $\delta\theta = \sum_q \delta\tilde{\theta}e^{(\Omega t + iq_y y)}$, which is the Fourier decomposition of $\delta\theta$. We can take g^{water} and g^{oil} from Eq. B.11, which are the prefactors of $\tilde{\boldsymbol{v}}(\boldsymbol{q})$. Thus, we get

$$\Omega = -\frac{K}{\gamma}q_y^2\left(1 + \frac{1}{4}\frac{\gamma(\nu-1)^2q_y^2}{\eta q_y^2 + \eta_{\text{water}}\,q_y\coth(q_yH_{\text{water}}) + \eta_{\text{oil}}\,q_y\tanh(q_yH_{\text{water}})}\right) - \frac{1}{2}\frac{\alpha(\nu-1)q_y^2}{\eta q_y^2 + \eta_{\text{water}}\,q_y\coth(q_yH_{\text{water}}) + \eta_{\text{oil}}\,q_y\tanh(q_yH_{\text{water}})}. \tag{A.56}$$

As aforementioned, our system is extensile, implying that $\alpha > 0$. Therefore, in the presence of 3D fluid layers coupled to the 2D active layer, the latter can suffer from flowing instabilities with longitudinal modulations if $\nu < 1$. More interestingly, the dispersion relation in Eq. A.56 showcases that the presence of a fluid 3D passive layer endows the system with a wavelength selection mechanism at a linear regime.

A

Appendix B

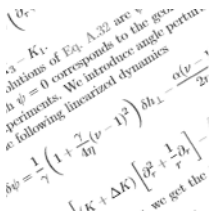

Hydrodynamic theory of active turbulence with external dissipation

B.1 Hydrodynamic Green's function

In practice, active nematics are not isolated systems. For instance, in our experiments, an active nematic film is in contact with a thicker layer of water, and an even thicker layer of oil. The water layer is underneath the active film and supported by a solid substrate (a glass microscope slide), and the oil layer is in contact with the air (see Fig. B.1). Thus, flows within the active layer induce flows in both passive layers, which in turn modify or influence the flows in the active film. This is why the kinetic energy spectrum of our active nematic can be significantly modified by these two layers. To account for this, we can add to the force balance equation in Eq. A.2 the viscous force densities exerted by the water and the oil layers, $\boldsymbol{f}_{\text{water}}$ and $\boldsymbol{f}_{\text{oil}}$, respectively:

$$\mathbf{0} = \eta_n \nabla^2 \boldsymbol{v} - \boldsymbol{\nabla} P + \boldsymbol{f}_{\text{water}} + \boldsymbol{f}_{\text{oil}} + \boldsymbol{f}. \tag{B.1}$$

Here, for compactness, we have grouped the stresses arising from the orientational order of the nematic film, including elastic, flow-alignment, and active stresses into $\boldsymbol{f}$. Note that, as in Appendix A.1, we have neglected the inertia terms.

Now, as in [121], we introduce the Green's function $G_{\alpha\beta}$ that gives the response of the active nematic layer coupled with the two passive fluid layers

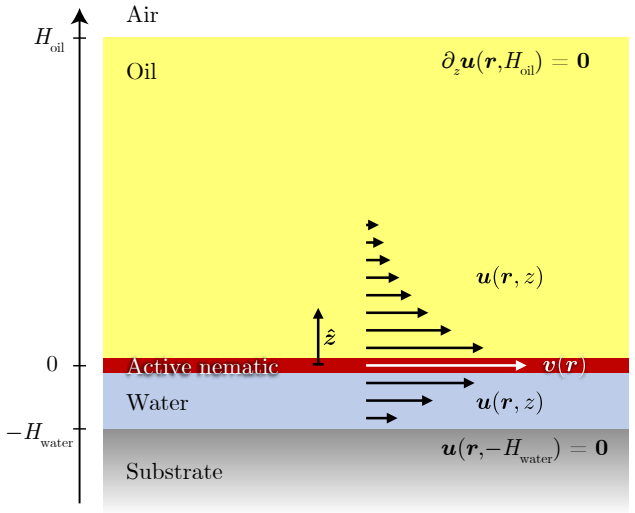

Figure B.1: Schematic represetation of the experimental setup and flow fields (side view). The thicknesses of the fluid layers are not to scale. The actual thickness of the active nematic film is $h \approx 2$ µm, whereas the thicknesses of the passive fluid layers are $H_{\mathrm{water}} \approx 40$ µm and $H_{\mathrm{oil}} \approx 3$ mm. We treat the active nematic as a two-dimensional film. White and black arrows represent the flow fields in the active nematic film and in the passive fluid layers, respectively. The flow is planar, and it penetrates into the oil and water layers, respectively in contact with the air and a substrate. Thus, we assume free boundary conditions at $z = H_{\mathrm{oil}}$ and no-slip boundary conditions at $z = -H_{\mathrm{water}}$. Here, we represent flow penetration according to Eq. B.11 for a planar wave number $q/(2\pi) = 5 \cdot 10^{-3}$ µm^{-1}, which lies in the range of our experimental measurements. Image adapted from [96] under Creative Commons Attribution 4.0 International license.

B

to a point force applied to the active layer. Similarly, we can also introduce Green's functions for the pressure, H_α, and the forces exerted by the passive layers, $F^{\mathrm{water}}_{\alpha\beta}$ and $F^{\mathrm{oil}}_{\alpha\beta}$. Thus, we can write

$$\eta_n \nabla^2 G_{\alpha\beta}(\boldsymbol{r}, \boldsymbol{r}') - \partial_\alpha H_\beta(\boldsymbol{r}, \boldsymbol{r}') + F^{\mathrm{water}}_{\alpha\beta}(\boldsymbol{r}, \boldsymbol{r}') + F^{\mathrm{oil}}_{\alpha\beta}(\boldsymbol{r}, \boldsymbol{r}') = -\delta_{\alpha\beta}\, \delta(\boldsymbol{r} - \boldsymbol{r}'). \quad \text{(B.2)}$$

where $\delta_{\alpha\beta}$ is the Kronecker delta. The Green's function $G_{\alpha\beta}$ must also obey the incompressibility condition

$$\partial_\alpha G_{\alpha\beta} = 0. \quad \text{(B.3)}$$

To obtain the velocity field, we need to sum all the contributions from the forces at each point $\boldsymbol{r}'$

$$v_\alpha(\boldsymbol{r}) = \int G_{\alpha\beta}(\boldsymbol{r} - \boldsymbol{r}') f_\beta(\boldsymbol{r}') \mathrm{d}\boldsymbol{r}'. \quad \text{(B.4)}$$

where the greek indices indicate spatial components, and summation over repeated indices (see Info Box A.1). Note that in Eq. B.4, the forces applied by the passive fluids do not appear explicitly, nevertheless, they will be included implicitly in $G_{\alpha\beta}$. To get rid of the integral, we can introduce the Fourier decomposition of the velocity

$$\boldsymbol{v}(\boldsymbol{r}) = \frac{1}{(2\pi)^2} \int \tilde{\boldsymbol{v}}(\boldsymbol{q}) e^{i\boldsymbol{q}\cdot\boldsymbol{r}} \mathrm{d}^2\boldsymbol{q}, \tag{B.5}$$

and invoke the convolution theorem

$$\tilde{v}_\alpha(\boldsymbol{q}) = \tilde{G}_{\alpha\beta}(\boldsymbol{q}) \tilde{f}_\beta(\boldsymbol{q}). \tag{B.6}$$

To find the Green's function, we need to obtain first the viscous stresses exerted by the water and oil layers on the active film

$$\boldsymbol{f}_{\text{water}}(\boldsymbol{r}) = -\eta_{\text{water}} \left.\frac{\partial \boldsymbol{u}_\parallel(\boldsymbol{r}, z)}{\partial z}\right|_{z=0^-}, \tag{B.7a}$$

$$\boldsymbol{f}_{\text{oil}}(\boldsymbol{r}) = \eta_{\text{oil}} \left.\frac{\partial \boldsymbol{u}_\parallel(\boldsymbol{r}, z)}{\partial z}\right|_{z=0^+}, \tag{B.7b}$$

with $\boldsymbol{u}(\boldsymbol{r}, z)$ the three-dimensional flow field of the passive fluids, and $\parallel$ denotes the components along the active film's plane, which is at $z = 0$. Furthermore, the viscous flows in the passive layers must obey the Stokes equation

$$\eta_{\text{water}} \nabla^2 \boldsymbol{u} - \boldsymbol{\nabla} p = \boldsymbol{0}, \qquad -H_{\text{water}} < z < 0, \tag{B.8a}$$

$$\eta_{\text{oil}} \nabla^2 \boldsymbol{u} - \boldsymbol{\nabla} p = \boldsymbol{0}, \qquad 0 < z < H_{\text{oil}}, \tag{B.8b}$$

where p is the three-dimensional pressure. These flows are induced by the hydrodynamic coupling with the active film, thus velocity continuity entails that at the interface all three fluids have the same velocity $\boldsymbol{u}_\parallel(\boldsymbol{r}, 0^+) = \boldsymbol{u}_\parallel(\boldsymbol{r}, 0^-) = \boldsymbol{v}(\boldsymbol{r})$. We also consider these passive fluids to be incompressible, $\boldsymbol{\nabla} \cdot \boldsymbol{v} = 0$, thus, as shown in [171], the pressure p inside the surrounding fluids becomes constant, $\boldsymbol{\nabla} p = \boldsymbol{0}$, and the out-of-plane component of the velocity vanishes everywhere, $u_z = 0$, *i.e.* the flow in the surrounding layers is planar $\boldsymbol{u} = \boldsymbol{u}_\parallel(\boldsymbol{r}, z)$. This simplifies significantly Eq. B.8. In fact, they take the form of the Laplace equation and the components of $\boldsymbol{u}$ become harmonic.

$$\eta_{\text{water}} \nabla^2 \boldsymbol{u}_\parallel = \boldsymbol{0}, \qquad -H_{\text{water}} < z < 0, \tag{B.9a}$$

$$\eta_{\text{oil}} \nabla^2 \boldsymbol{u}_\parallel = \boldsymbol{0}, \qquad 0 < z < H_{\text{oil}}, \tag{B.9b}$$

To obtain the Green's function $G_{\alpha\beta}$ in Fourier space, we need to solve Eq. B.9 in terms of the Fourier modes in 2d.

$$\eta_{\text{water}}(\partial_z^2 - q^2)\tilde{\boldsymbol{u}}_{\parallel} = \boldsymbol{0}, \qquad -H_{\text{water}} < z < 0, \tag{B.10a}$$

$$\eta_{\text{oil}}(\partial_z^2 - q^2)\tilde{\boldsymbol{u}}_{\parallel} = \boldsymbol{0}, \qquad 0 < z < H_{\text{oil}}, \tag{B.10b}$$

The solutions to Eq. B.10 should have the form of $\tilde{\boldsymbol{u}}_{\parallel}(\boldsymbol{q}, z) = A^{\text{water/oil}}(\boldsymbol{q})\cosh(qz) + B^{\text{water/oil}}(\boldsymbol{q})\sinh(qz)$. Assuming no-slip boundary conditions of the water layer at the contact with the solid substrate, $z = -H_{\text{water}}$, $\boldsymbol{u}_{\parallel}(\boldsymbol{r}, -H_{\text{water}}) = \boldsymbol{0}$ and no-shear-stress boundary conditions of the oil layer at the contact with the air, $z = H_{\text{oil}}$, $\partial_z \boldsymbol{u}_{\parallel}(\boldsymbol{r}, z)|_{z=H_{\text{oil}}} = 0$ and imposing $\boldsymbol{u}_{\parallel}(\boldsymbol{r}, 0^+) = \boldsymbol{u}_{\parallel}(\boldsymbol{r}, 0^-) = \boldsymbol{v}(\boldsymbol{r})$, the solutions to Eq. B.10 become

$$\tilde{\boldsymbol{u}}_{\parallel}(\boldsymbol{q}, z) = [\cosh(qz) + \coth(qH_{\text{water}})\sinh(qz)]\tilde{\boldsymbol{v}}(\boldsymbol{q}), \qquad -H_{\text{water}} < z < 0, \tag{B.11a}$$

$$\tilde{\boldsymbol{u}}_{\parallel}(\boldsymbol{q}, z) = [\cosh(qz) - \tanh(qH_{\text{oil}})\sinh(qz)]\tilde{\boldsymbol{v}}(\boldsymbol{q}), \qquad 0 < z < H_{\text{oil}}. \tag{B.11b}$$

Plugging this equation into the Fourier decomposition of Eq. B.7

$$\tilde{\boldsymbol{f}}_{\text{water}}(\boldsymbol{q}) = -\eta_{\text{water}}\, q\, \tilde{\boldsymbol{v}}(\boldsymbol{q})\coth(qH_{\text{water}}) \tag{B.12a}$$

$$\tilde{\boldsymbol{f}}_{\text{oil}}(\boldsymbol{q}) = -\eta_{\text{oil}}\, q\, \tilde{\boldsymbol{v}}(\boldsymbol{q})\tanh(qH_{\text{water}}) \tag{B.12b}$$

Note that we are looking for the Green's functions $F_{\alpha\beta}^{\text{water}}$ and $F_{\alpha\beta}^{\text{oil}}$. We can thus substitute $\tilde{\boldsymbol{v}}$ by $\tilde{G}_{\alpha\beta}$

$$\tilde{F}_{\alpha\beta}^{\text{water}}(\boldsymbol{q}) = -\eta_{\text{water}}\, q\, \tilde{G}_{\alpha\beta}(\boldsymbol{q})\coth(qH_{\text{water}}) \tag{B.13a}$$

$$\tilde{F}_{\alpha\beta}^{\text{oil}}(\boldsymbol{q}) = -\eta_{\text{oil}}\, q\, \tilde{G}_{\alpha\beta}(\boldsymbol{q})\tanh(qH_{\text{water}}) \tag{B.13b}$$

Now we have to find the Green's function for the pressure H_α. Thus, we convert Eq. B.2 to the Fourier space

$$-\eta_{\text{n}} q^2 \tilde{G}_{\alpha\beta} - iq_\alpha \tilde{H}_\beta + \tilde{F}_{\alpha\beta}^{\text{water}} + \tilde{F}_{\alpha\beta}^{\text{water}} = -\delta_{\alpha\beta} \tag{B.14}$$

Applying the gradient $(i\boldsymbol{q}\cdot)$ and taking into account the incompressibility condition $q_\alpha \tilde{v}_\alpha = 0$

$$q^2 \tilde{H}_\beta = -iq_\alpha \delta_{\alpha\beta} = -iq_\beta \tag{B.15}$$

Thus, inserting Eq. B.15 into Eq. B.14 and solving for $\tilde{G}_{\alpha\beta}$

$$\tilde{G}_{\alpha\beta} = \frac{\delta_{\alpha\beta} - q_\alpha q_\beta / q^2}{\eta_{\text{n}} q^2 + \eta_{\text{water}}\, q\, (\boldsymbol{q})\coth(qH_{\text{water}}) + \eta_{\text{oil}}\, q \tanh(qH_{\text{water}})} \tag{B.16}$$

Infobox B.1: Green's functions

A Green's function $G(x, x_0)$ at a point x_0 of a linear differential operator $\mathcal{L}$ is the solution of

$$\mathcal{L}G(x, x_0) = \delta(x - x_0), \tag{B.17}$$

where δ denotes the Dirac delta function.
To have a more physical idea, we can imagine a given field $u(x)$, whose response to a force $f(x)$ is defined by a linear operator $\mathcal{L}$,

$$\mathcal{L}u(x) = f(x). \tag{B.18}$$

If the force $f(x)$ is a point force, which can be described by a Dirac delta function, the field $u(x)$ will take the form of the Green's function of $\mathcal{L}$ with particular boundary conditions [168, 172, 173].
One could consider that the force or the source $f(x)$ is distributed into many small point sources at different points, whose contributions can be added up to obtain $u(x)$ [173]. Hence, the interest in Green's functions relies on the fact that they provide a way to find the solution to partial differential equations as

$$u(x) = \sum_{n=1}^{N} g(x, x_0) f(x_0) \Delta x_0. \tag{B.19}$$

If $n \to \infty$

$$u(x) = \int g(x, x_0) f(x_0) \mathrm{d}x_0. \tag{B.20}$$

B

B.2 Kinetic energy spectrum

The kinetic energy per unit mass density E of a two-dimensional AN reads

$$E = \frac{1}{2} \int \boldsymbol{v}^2 \mathrm{d}^2\boldsymbol{r}. \tag{B.21}$$

Introducing the Fourier decomposition as in Eq. B.5, and applying the Parseval's theorem [174], we can obtain the following expression for the kinetic energy spectrum $E(\boldsymbol{q})$

$$\langle E \rangle = \frac{1}{2} \int \frac{1}{(2\pi)^2} \langle |\tilde{\boldsymbol{v}}(\boldsymbol{q}|) \rangle^2 \mathrm{d}^2\boldsymbol{q} = \mathcal{A} \int E(\boldsymbol{q}) \mathrm{d}^2 q, \tag{B.22}$$

where $\mathcal{A}$ is the area of the system, and $\langle\cdot\rangle$ indicates a time average. If the velocity correlations of the system are isotropic, we can angle-average $E(\boldsymbol{q})$ as

$$E(q) = \int_0^{2\pi} qE(q,\varphi)\mathrm{d}\varphi = \frac{1}{4\pi\mathcal{A}} q\langle|\tilde{\boldsymbol{v}}(q)\rangle \tag{B.23}$$

with q and φ the modulus and the azimuth of the wave number $\boldsymbol{q}$, respectively.

To derive an analytical expression of the power spectrum, we need to invoke Eqs. B.6 and B.16, that lead to

$$\begin{aligned}\langle|\tilde{\boldsymbol{v}}(\boldsymbol{q})|^2\rangle &= \langle|\tilde{G}_{xx}\tilde{f}_x + \tilde{G}_{xy}\tilde{f}_y|^2\rangle + \langle|\tilde{G}_{yy}\tilde{f}_y + \tilde{G}_{yx}\tilde{f}_x|^2\rangle \\ &= \frac{1}{q^2\Lambda^2(q)}\left\langle q_y^2|\tilde{f}_x|^2 + q_x^2|\tilde{f}_y|^2 - q_xq_y(\tilde{f}_x\tilde{f}_y^* + \tilde{f}_y\tilde{f}_x^*)\right\rangle,\end{aligned} \tag{B.24}$$

where we have introduced the notation

$$\Lambda(q) \equiv \eta_\mathrm{n}q^2 + \eta_\mathrm{oil}q\tanh(qH_\mathrm{oil}) + \eta_\mathrm{water}q\coth(qH_\mathrm{water}). \tag{B.25}$$

Now, to find a closed-form expression for the velocity, we need to eliminate the source force density f. To this aim, we can utilize the force-balance condition for an isolated active nematic, i.e. without external fluids:

$$\eta_\mathrm{n}\nabla^2\boldsymbol{v}_\mathrm{i} - \boldsymbol{\nabla}P_\mathrm{i} + \boldsymbol{f} = \boldsymbol{0}. \tag{B.26}$$

Here, the subscript i indicates that the active nematic film is isolated. As it was mentioned before, $\boldsymbol{f}$ accounts for the force density due to elastic, flow-alignment, and active stresses. The source force must be equal for both the isolated and the not-isolated film, as far as we ignore flow alignment. In this limit, $\boldsymbol{f}$ is not modified by the velocity field.

As in [74], to eliminate the pressure, we take the curl of Eq. B.26 and introduce the vorticity field $\omega = \hat{z}\cdot(\boldsymbol{\nabla}\times\boldsymbol{v})$

$$\nabla^2\omega_\mathrm{i} = -\frac{1}{\eta_\mathrm{n}}\hat{\boldsymbol{z}}\cdot(\boldsymbol{\nabla}\times\boldsymbol{f}). \tag{B.27}$$

This equation in Fourier space is given by

$$-q^2\tilde{\omega}_\mathrm{i}(\boldsymbol{q}) = \frac{i}{\eta_\mathrm{n}}(q_y\tilde{f}_x - q_x\tilde{f}_y). \tag{B.28}$$

Therefore, the vorticity spectrum of an isolated active nematic reads

$$\langle\tilde{\omega}_\mathrm{i}(\boldsymbol{q})\,\tilde{\omega}_\mathrm{i}(\boldsymbol{q})^*\rangle = \langle|\tilde{\omega}_\mathrm{i}(\boldsymbol{q})|^2\rangle = \frac{1}{\eta_\mathrm{n}^2q^4}\left\langle q_y^2|\tilde{f}_x|^2 + q_x^2|\tilde{f}_y|^2 - q_xq_y(\tilde{f}_x\tilde{f}_y^* + \tilde{f}_y\tilde{f}_x^*)\right\rangle. \tag{B.29}$$

Comparing this last equation to Eq. B.24, we find the following expression, that relates the velocity power spectrum of an active nematic in contact with two passive layers to the vorticity spectrum of an isolated active layer

$$\langle|\tilde{\boldsymbol{v}}(\boldsymbol{q})|^2\rangle = \frac{\eta_{\mathrm{n}}^2 q^2}{\Lambda^2(q)}\langle|\tilde{\omega}_{\mathrm{i}}(\boldsymbol{q})|^2\rangle. \tag{B.30}$$

To obtain an expression for $\langle|\tilde{\omega}_{\mathrm{i}}(\boldsymbol{q})|^2\rangle$, we can draw on the mean-field theory by Giomi [75]. In this theory, Giomi proposed as an ansatz that the vorticity was decomposed into the superposition of N uncorrelated vortices with mean vorticity ω_v. Making use of simulations, the author observed that this mean vorticity was independent of the vortex size and that the vortex areas followed an exponential distribution with a characteristic area $a_* = \pi R_*^2$, with R_* the mean vortex radius. With these assumptions, Giomi found the following closed-form expression for the vorticity spectrum of an isolated active nematic layer

$$\langle|\tilde{\omega}_{\mathrm{i}}(\boldsymbol{q})|^2\rangle = \frac{N\omega_{\mathrm{v}}^2 R_*^4}{8\pi^2} e^{-q^2R_*^2/2}\left[I_0\left(\frac{q^2R_*^2}{2}\right) - I_1\left(\frac{q^2R_*^2}{2}\right)\right], \tag{B.31}$$

where I_0 and I_1 are modified Bessel's functions of the first kind of order 0 and 1, respectively. Hence, plugging this last result to Eq. B.30 and ,

$$E(q) = \frac{BqR_*^4\, e^{-q^2R_*^2/2}\left[I_0\left(q^2R_*^2/2\right) - I_1\left(q^2R_*^2/2\right)\right]}{\left[q + \eta_{\mathrm{oil}}/\eta_{\mathrm{n}}\tanh(qH_{\mathrm{oil}}) + \eta_{\mathrm{water}}/\eta_{\mathrm{n}}\coth(qH_{\mathrm{water}})\right]^2}, \tag{B.32}$$

where $B = N\omega_{\mathrm{v}}^2/(32\pi^3\mathcal{A})$, which is independent of the wave number q. The ratios between the 2D viscosity of the active nematic and the 3D viscosities of the external fluid layers define two viscous lengths:

$$\ell_{\mathrm{water}} = \eta_{\mathrm{n}}/\eta_{\mathrm{water}} \qquad , \qquad \ell_{\mathrm{oil}} = \eta/\eta_{\mathrm{oil}}. \tag{B.33}$$

B.3 Predicted scaling regimes

To extract the scaling regimes predicted by Eq. B.32, we must analyze the asymptotic behaviors of the functions involved, which I here list for $x \to 0$ and $x \to \infty$.

For $x \to 0$

1. Function e^{-x}

$$e^{-x} \approx 1 - x \tag{B.34}$$

2. Function $I_0(x)$

$$I_0(x) = \frac{1}{\pi}\int_0^\pi e^{x\cos\theta}\mathrm{d}\theta \approx \frac{1}{\pi}\int_0^\pi (1 + x\cos\theta)\mathrm{d}\theta = 1 \tag{B.35}$$

3. Function $I_1(x)$

$$I_1(x) = \frac{1}{\pi}\int_0^\pi e^{x\cos\theta}\cos\theta\mathrm{d}\theta \approx \frac{1}{\pi}\int_0^\pi (\cos\theta + x\cos^2\theta)\mathrm{d}\theta = \frac{x}{2} \tag{B.36}$$

4. Function $\tanh x$

$$\tanh x = \frac{e^x - e^{-x}}{e^x + e^{-x}} \approx x \tag{B.37}$$

5. Function $\coth x$

$$\coth x = \frac{e^x + e^{-x}}{e^x - e^{-x}} \approx \frac{1}{x} \tag{B.38}$$

Applying Eqs. B.34 to B.36, it is possible to see that the numerator of Eq. B.32 for small q scales as:

$$qe^{-q^2}[I_0(q^2) - I_1(q^2)] \sim q \tag{B.39}$$

For $x \to \infty$

1. Function e^{-x}

$$e^{-x} \approx 0 \tag{B.40}$$

2. Function I_0 (see Info Box B.2)

$$I_0(x) \approx \frac{e^x}{\sqrt{2\pi x}}\left(1 + \frac{1}{8x}\right) \tag{B.41}$$

3. Function I_1

$$I_1(x) \approx \frac{e^x}{\sqrt{2\pi x}}\left(1 - \frac{3}{8x}\right) \tag{B.42}$$

4. Function $\tanh x$

$$\tanh x = \frac{e^x - e^{-x}}{e^x + e^{-x}} \approx 1 \tag{B.43}$$

5. Function $\coth x$

$$\coth x = \frac{e^x + e^{-x}}{e^x - e^{-x}} \approx 1 \tag{B.44}$$

Applying Eqs. B.40 to B.42, we can see that the numerator of the right-hand side of Eq. B.32 for large q scales as:

$$qe^{-q^2}[I_0(q^2) - I_1(q^2)] \approx qe^{-q^2}\frac{e^{q^2}}{\sqrt{2\pi q}}\frac{2}{q^2} \sim q^{-2} \tag{B.45}$$

Infobox B.2: Asymptotic expansion of modified Bessel functions of the first kind

To find the asymptotic behavior of a modified Bessel function of the first kind, we first need to introduce the full mathematical definition:

$$I_n(x) = \frac{1}{\pi}\int_0^{\pi} \mathrm{d}\theta e^{x\cos\theta}\cos(n\theta). \tag{B.46}$$

Thanks to Taylor's series, we know that for $x \to 0$, $e^x \approx 1 + x + x^2/2$ and $\cos x \approx 1 - x^2/2 + x^4/24$. To be able to apply such expansions, we can conveniently change variables $\theta = t/\sqrt{x}$. Thus,

$$I_n(x) = \frac{1}{\pi}\int_0^{\pi\sqrt{x}} \frac{\mathrm{d}t}{\sqrt{x}} \exp\left(x\left(\cos\left(t/\sqrt{x}\right)\right)\right)\cos\left(nt/\sqrt{x}\right). \tag{B.47}$$

For large x, we can apply the expansions and cut at order x^{-1}, so we are left with:

$$\begin{aligned} I_n(x) \approx \frac{1}{\pi\sqrt{x}}\int_0^{\pi\sqrt{x}} \mathrm{d}t \exp\left(x - \frac{t^2}{2} + \frac{t^4}{24x}\right)\left(1 - \frac{n^2t^2}{2x}\right) = \\ \frac{e^x}{\pi\sqrt{x}}\int_0^{\pi\sqrt{x}} \mathrm{d}t \exp\left(-\frac{t^2}{2}\right)\left(1 + \frac{t^4}{24x}\right)\left(1 - \frac{n^2t^2}{2x}\right). \end{aligned} \tag{B.48}$$

Finally, we can integrate this expression (we have used the integral calculator in [175]). Note that we can use as integrations limits 0 and ∞ because we are looking at the asymptotic behavior ($\pi\sqrt{x} \to \infty$). Moreover, $\mathrm{erf}(x) = 2/\sqrt{x}\int_0^x e^{-t^2}\mathrm{d}t$, where erf is Gauss' error function [168], rapidly goes to 1.

$$I_n(x) \approx \frac{e^x}{\sqrt{2\pi x}}\left(1 + \frac{1}{8x} - \frac{n^2}{2x}\right) \tag{B.49}$$

To derive this expression, I have used as a guide the post in [176]

Now, to simplify the analysis, we can imagine there is only one external fluid, and therefore, only one viscous length $\ell_v = \eta_n/\eta_{\text{ext}}$. With this simpler configuration, we can still capture the effects of external fluid layers on the active film. Within this framework, we can identify three different scenarios:

1. The thick-layer limit, $qH \gg 1$
2. The thin-layer limit, $qH \ll 1$, with free boundary conditions (in contact with air)
3. The thin-layer limit, $qH \ll 1$, with no-slip boundary conditions (in contact with a substrate)

We will now discuss scenario by scenario, and utilize all the asymptotic behaviors above listed to find the predicted scalings for each situation.

1. **The thick-layer limit,** $qH \gg 1$

In this case, Eq. B.32 becomes

$$E(q) = \frac{BqR_*^4\, e^{-q^2R_*^2/2}\left[I_0\left(q^2R_*^2/2\right) - I_1\left(q^2R_*^2/2\right)\right]}{\left[q + 1/\ell_v\right]^2}, \tag{B.50}$$

Here, the boundary conditions are unimportant because both functions $\tanh(qH)$ and $\coth(qH)$ are ≈ 1. Therefore, for $qR_* \ll 1$ and $q\ell_v \gg 1$

$$E(q) \sim \frac{q}{q^2} \sim q^{-1}. \tag{B.51}$$

For $qR_* \ll 1$ and $q\ell_v \ll 1$

$$E(q) \sim \frac{q}{1/\ell_v^2} = q^1. \tag{B.52}$$

For $qR_* \gg 1$ and $q\ell_v \ll 1$

$$E(q) \sim \frac{q^{-2}}{1/\ell_v^2} = q^{-2}. \tag{B.53}$$

For $qR_* \gg 1$ and $q\ell_v \gg 1$

$$E(q) \sim \frac{q^{-2}}{q^2} = q^{-4}. \tag{B.54}$$

2. The thin-layer limit, $qH \ll 1$**, with free boundary conditions (in contact with air)**

The term that accounts for the coupling of the AN with a 3D layer with free boundary condition, is the term with $\tanh(qH)$. Therefore, we can neglect the term containing $\coth(qH)$, that accounts for the 3D fluid with no-slip boundary conditions. Moreover, in this thin-layer limit, we can use Eq. B.37, and, then, Eq. B.32 becomes

$$E(q) = \frac{BqR_*^4\, e^{-q^2R_*^2/2}\left[I_0\left(q^2R_*^2/2\right) - I_1\left(q^2R_*^2/2\right)\right]}{\left[q + qH/\ell_v\right]^2}, \tag{B.55}$$

Thus, for $qR_* \ll 1$ and $q\ell_v \gg 1$

$$E(q) \sim \frac{q}{q^2} \sim q^{-1}. \tag{B.56}$$

For $qR_* \ll 1$ and $q\ell_v \ll 1$

$$E(q) \sim \frac{q}{q^2} = q^{-1}. \tag{B.57}$$

For $qR_* \gg 1$ and $q\ell_v \ll 1$

$$E(q) \sim \frac{q^{-2}}{q^2} = q^{-4}. \tag{B.58}$$

For $qR_* \gg 1$ and $q\ell_v \gg 1$

$$E(q) \sim \frac{q^{-2}}{q^2} = q^{-4}. \tag{B.59}$$

3. The thin-layer limit, $qH \ll 1$, with no-slip boundary conditions (in contact with a substrate)

Finally, in this case, analogously to what we did above, we can neglect the term with $\tanh(qH)$ and keep the one containing $\coth(qH)$, and use the asymptotic behavior shown in Eq. B.38. Then, Eq. B.32 becomes

$$E(q) = \frac{BqR_*^4\, e^{-q^2R_*^2/2}\left[I_0\left(q^2R_*^2/2\right) - I_1\left(q^2R_*^2/2\right)\right]}{\left[q + 1/(qH\ell_v)\right]^2}, \tag{B.60}$$

Thus, for $qR_* \ll 1$ and $q\ell_v \gg 1$

$$E(q) \sim \frac{q}{q^2} \sim q^{-1}. \tag{B.61}$$

For $qR_* \ll 1$ and $q\ell_v \ll 1$

$$E(q) \sim \frac{q}{q^{-2}} = q^3. \tag{B.62}$$

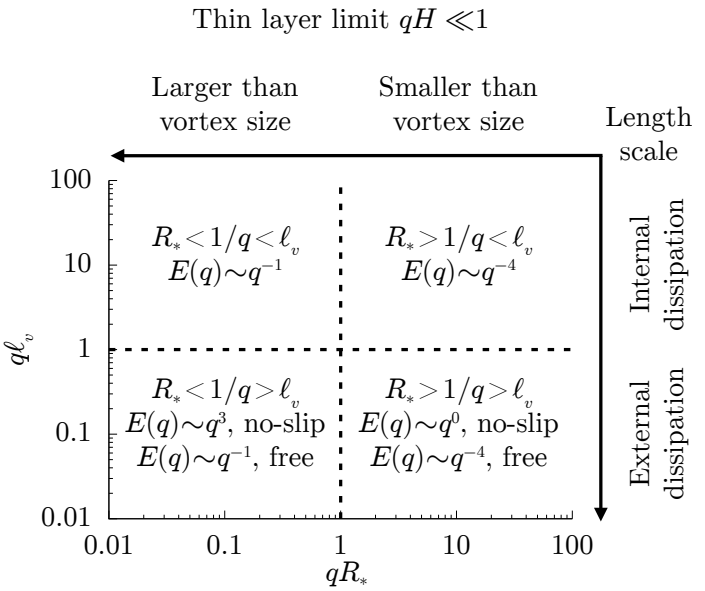

Figure B.2: Scaling regimes of turbulent flows in an active nematic film in contact with a thin external fluid layer. The different regimes are predicted at length scales $(2\pi/q)$ either larger or smaller than the mean vortex radius R_*, the viscous length $\ell_v = \eta_n/\eta_{ext}$, and the thickness H of the external fluid layer. This figure summarizes the scalings in the thin-layer limit $qH \ll 1$; see Section 3.3 and Fig. 3.4 for the predictions in the thick-layer limit $qH \ll 1$.

B

For $qR_* \gg 1$ and $q\ell_v \ll 1$

$$E(q) \sim \frac{q^{-2}}{q^{-2}} = q^0. \tag{B.63}$$

For $qR_* \gg 1$ and $q\ell_v \gg 1$

$$E(q) \sim \frac{q^{-2}}{q^2} = q^{-4} \tag{B.64}$$

Appendix C

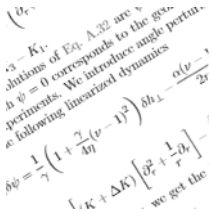

Derivation of the energy balance

C.1 Constitutive equations of the active nematic

In this chapter, instead of parametrizing the nematic field with the nematic director as in Appendix A.1, we utilize the traceless tensor $\mathbf{Q} = S(\mathbf{nn}^T - \mathbf{I}/2)$, used for instance in the models in [72, 75, 107, 177] based on the Beris-Edwards theory of nematohydrodynamics. To help to understand the derivation of the energy balance, I write again the Navier-Stokes equation written in Eq. A.1.

$$\rho(\partial_t + \boldsymbol{v}\cdot\boldsymbol{\nabla})v_\alpha = -\partial_\beta P\delta_{\alpha\beta} + \partial_\beta(\sigma_{\alpha\beta} + \sigma^{\mathrm{a}}_{\alpha\beta}) = \partial_\beta\sigma'_{\alpha\beta}, \tag{C.1}$$

where we have used the Einstein summation convention (see Info Box A.1). As said before, P is the pressure, $\delta_{\alpha\beta}$ is the Kronecker delta, and $\sigma_{\alpha\beta}$ and $\sigma^a_{\alpha\beta}$ are the symmetric and antisymmetric parts of the stress tensor, respectively. We also consider the active fluid to be incompressible, this requires $\partial_\alpha v_\alpha = 0$. Within this framework, the symmetric and the antisymmetric parts of the stress tensor are defined in terms of the $Q_{\alpha\beta}$ as:

$$\sigma_{\alpha\beta} = 2\eta v_{\alpha\beta} + \nu H_{\alpha\beta} - \alpha Q_{\alpha\beta} + \sigma^E_{\alpha\beta}, \tag{C.2a}$$

$$\sigma^{\mathrm{a}}_{\alpha\beta} = Q_{\alpha\gamma}H_{\gamma\beta} - H_{\alpha\gamma}Q_{\gamma\beta}, \tag{C.2b}$$

where η is the shear viscosity, $v_{\alpha\beta} = 1/2(\partial_\alpha v_\beta + \partial_\beta v_\alpha)$ is the symmetric part of the strain rate tensor (shear tensor). ν is the flow alignment coefficient, which controls the coupling of the nematic field and the flow. $H_{\alpha\beta} = -\delta F_{LdG}/\delta Q_{\alpha\beta}$

is the orientational field that governs the relaxational dynamics of the nematic phase and is obtained from the two-dimensional Landau-de Gennes free energy. α is the active coefficient, which is positive ($\alpha > 0$) for extensile systems, and negative ($\alpha < 0$) for contractile systems. Note that in some articles, the activity coefficient (α, sometimes in the literature it appears as ζ [74], or as $\zeta\Delta\mu$ [100, 104]) and the flow alignment coefficient (ν, sometimes in the literature it appears as λ [75, 101, 177]) change their sign, depending on the way they are expressed in the force balance equations (Eqs. C.1 to C.2b). Finally, $\sigma^E_{\alpha\beta}$ is the Ericksen stress defined in Eq. C.13c (see Info Box C.1), which, in general, is not a symmetric tensor. Nevertheless, if we consider the elastic constants to be equal, this stress tensors turns out to be symmetric [124]. This is why we have only included it in the symmetric part of the total stress tensor. Given that the Ericksen stress includes higher order of the derivatives of $Q_{\alpha\beta}$ compared to other terms in the stress tensor, it is most times neglected, as for instance in [75] or in previous chapter Appendix A.1. The Landau-de-Gennes free energy required to compute both $H_{\alpha\beta}$ and $\sigma^E_{\alpha\beta}$ is defined as

$$F_{\mathrm{LdG}} = \int \left[\frac{A}{2}(\partial_\alpha Q_{\beta\gamma})(\partial_\alpha Q_{\beta\gamma}) + \frac{B}{2} Q_{\alpha\beta}Q_{\alpha\beta} + \frac{C}{4}(Q_{\alpha\beta}Q_{\alpha\beta})^2 \right] \mathrm{d}^2\mathbf{r}, \tag{C.3}$$

where A is the single elastic constant, which differs from the elastic constant K in the active gel theory (Appendix A.1), by a factor of 2, $A = K/2$. B and C are nematic material parametters that control the nematic/isotropic transition [125]. The first term is the analogue to the Frank free energy F_n defined in Eq. A.4, in fact, if S were homogeneous and $S = 1$, this term and the F_n would be the same.

For the sake of simplicity, we can neglect the two last terms in Eq. C.3. This approximation is good as far as the system is well bellow the nematic/isotropic transition, when S is almost everywhere close to 1. S will only go to 0 at the defects. Then, the Landau-de Gennes free energy is only given by the distortion term (F_d)

$$F_{\mathrm{LdG}} \approx F_d = \int \frac{A}{2}(\partial_\alpha Q_{\beta\gamma})(\partial_\alpha Q_{\gamma\beta})\, \mathrm{d}^2\mathbf{r}. \tag{C.4}$$

Therefore, the molecular field $H_{\alpha\beta}$ reads

$$H_{\alpha\beta} = A\nabla^2 Q_{\alpha\beta}. \tag{C.5}$$

Infobox C.1: The Ericksen stress tensor

If the molecules of a liquid crystal are displaced while retaining their initial orientation, the total free energy changes [124]. The stress tensor used to describe such change can be defined as:

$$\sigma^d_{\alpha\beta} = -\partial_\alpha Q_{\beta\gamma} \frac{\delta F_{\mathrm{LdG}}}{\delta \partial_\epsilon Q_{\beta\gamma}}. \tag{C.6}$$

To obtain the expression for this tensor assuming equal elastic constants, we can start by applying the Einstein's summation convention (see Info Box A.1) to Eq. C.4

$$\begin{aligned} F_d = \frac{A}{2}\int_{\mathcal{A}} &[(\partial_x Q_{xx})^2 + (\partial_x Q_{xy})^2 + (\partial_x Q_{yx})^2 + (\partial_x Q_{yy})^2 \\ &+(\partial_y Q_{xx})^2 + (\partial_y Q_{xy})^2 + (\partial_y Q_{yx})^2 + (\partial_y Q_{yy})^2]\mathrm{d}^2\mathbf{r} \end{aligned} \tag{C.7}$$

From this we can see that:

$$\frac{\delta F_d}{\delta \partial_\beta Q_{\gamma\epsilon}} = A\partial_\beta Q_{\gamma\epsilon} \tag{C.8}$$

Then, $\sigma^d_{\alpha\beta}$ reads:

$$\sigma^d_{\alpha\beta} = -\partial_\alpha Q_{\gamma\epsilon}\frac{\delta F_d}{\delta \partial_\beta Q_{\gamma\epsilon}} = -A\partial_\alpha Q_{\gamma\epsilon}\partial_\beta Q_{\gamma\epsilon} \tag{C.9}$$

Thus, applying this formula to each term of the tensor and taking into account the symmetries $Q_{xx} = -Q_{yy}$ and $Q_{xy} = Q_{yx}$:

$$\begin{aligned} \sigma^d_{xx} &= -A[(\partial_x Q_{xx})^2 + (\partial_x Q_{xy})(\partial_x Q_{yx}) + (\partial_x Q_{yx})(\partial_x Q_{xy}) + (\partial_x Q_{yy})^2] \\ &= -2A[(\partial_x Q_{xx})^2 + (\partial_x Q_{xy})^2] \end{aligned} \tag{C.10a}$$

$$\begin{aligned} \sigma^d_{xy} = \sigma^d_{yx} = -A[&(\partial_x Q_{xx})(\partial_y Q_{xx}) + (\partial_x Q_{xy})(\partial_y Q_{yx}) + (\partial_x Q_{yx})(\partial_y Q_{xy}) \\ &+(\partial_x Q_{yy})(\partial_y Q_{yy})] = -2A[(\partial_x Q_{xx})(\partial_y Q_{xx}) + (\partial_x Q_{xy})(\partial_y Q_{yx})] \end{aligned} \tag{C.10b}$$

$$\begin{aligned} \sigma^d_{yy} &= -A[(\partial_y Q_{xx})^2 + (\partial_y Q_{xy})(\partial_y Q_{yx}) + (\partial_y Q_{yx})(\partial_y Q_{xy}) + (\partial_y Q_{yy})^2] \\ &= -2A[(\partial_y Q_{xx})^2 + (\partial_y Q_{xy})^2] \end{aligned} \tag{C.10c}$$

This tensor is symmetric and has a trace. Since we are assuming that our active fluid is incompressible, we are only interested in the traceless part of the stress. Thus, we can take the trace:

$$\mathrm{Tr}\{\boldsymbol{\sigma}^E\} = -2A[(\partial_x Q_{xx})^2 + (\partial_x Q_{xy})^2 + (\partial_y Q_{xx})^2 + (\partial_y Q_{xy})^2], \quad \text{(C.11)}$$

and write the stress as a combination of the traceless stress and $\mathrm{Tr}\{\boldsymbol{\sigma}^d\}$, which will be absorbed by the isotropic pressure. This new tensor is the so-called Ericksen stress tensor and is given by

$$\sigma^E_{\alpha\beta} = \sigma^d_{\alpha\beta} - \frac{\mathrm{Tr}\{\boldsymbol{\sigma}^d\}\delta_{\alpha\beta}}{2}. \quad \text{(C.12)}$$

Thus,

$$\sigma^E_{xx} = -A[(\partial_x Q_{xx})^2 + (\partial_x Q_{xy})^2 - (\partial_y Q_{xx})^2 - (\partial_y Q_{xy})^2] \quad \text{(C.13a)}$$

$$\sigma^E_{xy} = -2A[(\partial_x Q_{xx})(\partial_y Q_{xx}) + (\partial_x Q_{xy})(\partial_y Q_{yx})] \quad \text{(C.13b)}$$

$$\sigma^E_{yy} = -\sigma^E_{xx} \quad \text{(C.13c)}$$

Finally, the dynamics of the nematic orientation tensor

$$(\partial_t + \boldsymbol{v}\cdot\nabla)Q_{\alpha\beta} = -\nu S v_{\alpha\beta} + Q_{\alpha\gamma}\omega_{\gamma\beta} - \omega_{\alpha\gamma}Q_{\gamma\beta} + \gamma^{-1}H_{\alpha\beta} \quad \text{(C.14)}$$

where $\omega_{\alpha\beta} = (\partial_\alpha v_\beta - \partial_\beta v_\alpha)/2$ is the antisymmetric part of the strain rate tensor (the vorticity tensor), and γ is the rotational viscosity.

C.2 Rate change of the free energy of an active nematic

To obtain the energy balance of the 2D active nematic neglecting the two surrounding passive fluid layers, we can compute the rate change of the free energy $\dot{F} = \dot{U} - T\dot{\Omega}$, where U is the internal energy, T the temperature, and Ω the entropy (not to be confused with the growth rate Ω). In this case, we use the free Helmholtz energy because we consider the AN is at constant temperature and volume.

Then, the free energy stored in our active nematic is given by

$$F = \int \left[\frac{1}{2}\rho|\boldsymbol{v}|^2 + F_d\right] \mathrm{d}^2\mathbf{r} \quad \text{(C.15)}$$

where the first term accounts for the kinetic energy and the second term for the elastic energy due to distortions. Then, the energy change rate reads

$$\dot{F} = \frac{\mathrm{d}}{\mathrm{d}t}\int \left[\frac{1}{2}\rho|\boldsymbol{v}|^2 + F_d\right] \mathrm{d}^2\mathbf{r}. \tag{C.16}$$

To derive the kinetic energy term, we apply the chain rule

$$\frac{\mathrm{d}}{\mathrm{d}t}\frac{1}{2}\rho|\boldsymbol{v}| = \frac{\mathrm{d}}{\mathrm{d}t}\frac{1}{2}\rho v_\alpha v_\alpha = \rho v_\alpha \frac{\mathrm{d}}{\mathrm{d}t}v_\alpha \tag{C.17}$$

Here, $\mathrm{d}/\mathrm{d}t$ is the material derivative, $\mathrm{d}v_\alpha/\mathrm{d}t = (\partial_t + \boldsymbol{v}\cdot\boldsymbol{\nabla})v_\alpha$. Now, we insert the force balance equation Eq. C.1 and integrate by parts, neglecting the surface term. In this way, we obtain the following expression:

$$\frac{\mathrm{d}}{\mathrm{d}t}\int \frac{1}{2}\rho|\boldsymbol{v}|^2\,\mathrm{d}^2r = \int v_\alpha \partial_\beta \sigma'_{\alpha\beta}\mathrm{d}^2\mathbf{r} = -\int \partial_\beta v_\alpha \sigma'_{\alpha\beta}\mathrm{d}^2\mathbf{r}. \tag{C.18}$$

For the purpose of the derivation, it is convenient to separate the velocity gradient into a symmetric and an antisymmetric part, which actually correspond respectively to the symmetric and the antisymmetric parts of the strain rate tensor ($\partial_\beta v_\alpha = v_{\alpha\beta} - \omega_{\alpha\beta}$). In this way, we just need to contract $v_{\alpha\beta}$ and $\omega_{\alpha\beta}$ with the symmetric and the antisymmetric parts of $\sigma'_{\alpha\beta}$, respectively.

$$\begin{aligned}\frac{\mathrm{d}}{\mathrm{d}t}\int \frac{1}{2}\rho|\boldsymbol{v}|^2\,\mathrm{d}^2r = \int [&-2\eta v_{\alpha\beta}v_{\alpha\beta} - \nu v_{\alpha\beta}H_{\alpha\beta} + \alpha v_{\alpha\beta}Q_{\alpha\beta} \\ &-v_{\alpha\beta}\sigma^E_{\alpha\beta} + \omega_{\alpha\beta}(Q_{\alpha\gamma}H_{\gamma\beta} - H_{\alpha\gamma}Q_{\gamma\beta})]\mathrm{d}^2\mathbf{r}\end{aligned} \tag{C.19}$$

Here, the incompressible condition has caused the pressure term to drop, $Pv_{\alpha\beta}\delta_{\alpha\beta} = P(\partial_x v_x + \partial_y v_y) = 0$:

Now, to obtain the distortion energy, we take the left-hand term in Eq. C.3 and apply the chain rule

$$\frac{\mathrm{d}}{\mathrm{d}t}\int F_d\,\mathrm{d}^2\mathbf{r} = \int \frac{A}{2}\frac{\mathrm{d}}{\mathrm{d}t}(\partial_\alpha Q_{\beta\gamma})(\partial_\alpha Q_{\beta\gamma})\,\mathrm{d}^2\mathbf{r} = \int \frac{A}{2}2(\partial_\alpha Q_{\beta\gamma})\frac{\mathrm{d}}{\mathrm{d}t}(\partial_\alpha Q_{\beta\gamma})\,\mathrm{d}^2\mathbf{r}, \tag{C.20}$$

integrating by parts and neglecting the surface term:

$$-\int A(\partial_\alpha\partial_\alpha Q_{\beta\gamma})\frac{\mathrm{d}}{\mathrm{d}t}Q_{\beta\gamma}\,\mathrm{d}^2\mathbf{r} = -\int A(\nabla^2 Q_{\beta\gamma})\frac{\mathrm{d}}{\mathrm{d}t}Q_{\beta}\gamma\,\mathrm{d}^2\mathbf{r}. \tag{C.21}$$

Combining this last equation with Eqs. C.5 and C.14

$$\frac{\mathrm{d}}{\mathrm{d}t}\int F_d\,\mathrm{d}^2\mathbf{r} = \int -H_{\alpha\beta}\frac{\mathrm{d}}{\mathrm{d}t}Q_{\alpha\beta}\,\mathrm{d}^2\mathbf{r} = \int H_{\alpha\beta}\left[\nu S v_{\alpha\beta} - Q_{\alpha\gamma}\omega_{\gamma\beta} + \omega_{\alpha\gamma}Q_{\gamma\beta} - \gamma^{-1}H_{\alpha\beta}\right]\,\mathrm{d}^2\mathbf{r}. \tag{C.22}$$

Thus, adding all the contributions from Eqs. C.19 and C.22

$$\dot{F} = \int \left[-2\eta v_{\alpha\beta}v_{\alpha\beta} - \nu v_{\alpha\beta}H_{\alpha\beta}(1-S) + \alpha v_{\alpha\beta}Q_{\alpha\beta} - v_{\alpha\beta}\sigma^E_{\alpha\beta} - \gamma^{-1}H_{\alpha\beta}H_{\alpha\beta}\right]\mathrm{d}^2\mathbf{r} \tag{C.23}$$

From this final result, we can extract the different contributions to dissipation:

$$D_s = \int 2\eta v_{\alpha\beta}v_{\alpha\beta}\mathrm{d}^2\mathbf{r}, \tag{C.24}$$

$$D_r = \int \gamma^{-1}H_{\alpha\beta}H_{\alpha\beta}\mathrm{d}^2\mathbf{r}, \tag{C.25}$$

$$T_{\mathrm{FA}} = \int \nu v_{\alpha\beta}H_{\alpha\beta}(S-1)\mathrm{d}^2\mathbf{r}, \tag{C.26}$$

$$I = \int \alpha v_{\alpha\beta}Q_{\alpha\beta}\mathrm{d}^2\mathbf{r}. \tag{C.27}$$

$$T_{\mathrm{el}} = \int v_{\alpha\beta}\sigma^E_{\alpha\beta}\mathrm{d}^2\mathbf{r}. \tag{C.28}$$

C.3 Dissipation in the external fluid layers

To account for the viscous dissipation in the external fluid layers, we can add to the fee energy in Eq. C.15 the contributions to the kinetic energy of the external layers:

$$\int \left[\frac{1}{2}\rho|\boldsymbol{v}|^2 + F_d\right]\,\mathrm{d}^2\mathbf{r} + \int \frac{1}{2}|\boldsymbol{u}_{\mathrm{oil}}|^2\mathrm{d}^3\mathbf{r} + \frac{1}{2}|\boldsymbol{u}_{\mathrm{water}}|^2\mathrm{d}^3\mathbf{r} \tag{C.29}$$

The entropy production due to these two last terms is then given by

$$\dot{F}_{\mathrm{water}} = \frac{\mathrm{d}}{\mathrm{d}t}\int \frac{1}{2}|\boldsymbol{u}_{\mathrm{water}}|^2\mathrm{d}^3\mathbf{r} = \int u_{\alpha,\mathrm{water}}\frac{\mathrm{d}}{\mathrm{d}t}u_{\alpha,\mathrm{water}}\mathrm{d}^3\mathbf{r} \tag{C.30}$$

$$\dot{F}_{\mathrm{oil}} = \frac{\mathrm{d}}{\mathrm{d}t}\int \frac{1}{2}|\boldsymbol{u}_{\mathrm{oil}}|^2\mathrm{d}^3\mathbf{r} = \int u_{\alpha,\mathrm{oil}}\frac{\mathrm{d}}{\mathrm{d}t}u_{\alpha,\mathrm{oil}}\mathrm{d}^3\mathbf{r} \tag{C.31}$$

Now, introducing the Navier-Stokes equations of the two passive fluids

$$(\partial_t + \boldsymbol{u}_{\text{water}} \cdot \boldsymbol{\nabla}) u_{\alpha,\text{water}} = -\partial_\beta P \delta_{\alpha\beta} + 2\eta_{\text{water}} \partial_\beta u_{\alpha\beta,\text{water}}, \tag{C.32}$$

$$(\partial_t + \boldsymbol{u}_{\text{oil}} \cdot \boldsymbol{\nabla}) u_{\alpha,\text{oil}} = -\partial_\beta P \delta_{\alpha\beta} + 2\eta_{\text{oil}} \partial_\beta u_{\alpha\beta,\text{oil}}, \tag{C.33}$$

where $u_{\alpha\beta} = (\partial_\alpha u_\beta + \partial_\beta u_\alpha)/2$ is the symmetric part of the shear stress tensor, we obtain

$$\dot{F}_{\text{water}} = \int u_{\alpha,\text{water}} [-\partial_\beta P \delta_{\alpha\beta} + 2\eta_{\text{water}} \partial_\beta u_{\alpha\beta,\text{water}}] \mathrm{d}^3\mathbf{r}, \tag{C.34a}$$

$$\dot{F}_{\text{oil}} = \int u_{\alpha,\text{oil}} [-\partial_\beta P \delta_{\alpha\beta} + 2\eta_{\text{oil}} \partial_\beta u_{\alpha\beta,\text{oil}}] \mathrm{d}^3\mathbf{r} \tag{C.34b}$$

The pressure term drops due to the incompressibility condition ($\int u_\alpha(-\partial_\alpha P \delta_{\alpha\beta}) \mathrm{d}^3\mathbf{r} = \int \partial_\beta u_{\alpha,\text{oil}} P \delta_{\alpha\beta} \mathrm{d}^2\mathbf{r} = \int (\partial_x u_x + \partial_y u_y + \partial_z u_z) P \mathrm{d}^3\mathbf{r} = 0$). Hence, we are left with

$$\dot{F}_{\text{water}} = \int -2\eta_{\text{water}} u_{\alpha\beta,\text{water}} u_{\alpha\beta,\text{water}} \mathrm{d}^3\mathbf{r}, \tag{C.35a}$$

$$\dot{F}_{\text{oil}} = \int -2\eta_{\text{oil}} u_{\alpha\beta,\text{oil}} u_{\alpha\beta,\text{oil}} \mathrm{d}^3\mathbf{r}, \tag{C.35b}$$

where we have integrated by parts and substituted $\partial_\beta u_\alpha u_{\alpha\beta} = u_{\alpha\beta} u_{\alpha\beta}$, which is given by

$$u_{\alpha\beta} u_{\alpha\beta} = u_{xx}^2 + u_{yy}^2 + 2(u_{xy}^2 + u_{xz}^2 + u_{yz}^2) \tag{C.36}$$

The term u_{zz} does not appear because the flows in our surrounding layers are planar (see Appendix B.1), $\boldsymbol{u} = \boldsymbol{u}_\parallel(\boldsymbol{r}, z)$, where $\boldsymbol{r}$ is the position vector on the plane of the active fluid film.

Now, we need the expressions for $\boldsymbol{u}_{\parallel,\text{water}}(\boldsymbol{r}, z)$ and $\boldsymbol{u}_{\parallel,\text{oil}}(\boldsymbol{r}, z)$. In Appendix B.1, we have found the solutions in the Fourier space of these two quantities (Eq. B.11). These solutions have the following form

$$\tilde{\boldsymbol{u}}_{\parallel,\text{water}}(\boldsymbol{q}, z) = f_{\text{water}}(q, z) \tilde{\boldsymbol{v}}(\boldsymbol{q}) \tag{C.37a}$$

$$\tilde{\boldsymbol{u}}_{\parallel,\text{oil}}(\boldsymbol{q}, z) = f_{\text{oil}}(q, z) \tilde{\boldsymbol{v}}(\boldsymbol{q}) \tag{C.37b}$$

where $\tilde{\boldsymbol{v}}(\boldsymbol{q})$ is the velocity field of the active 2D layer, and $f_{\text{water}}(q, z)$ and $f_{\text{oil}}(q, z)$ are hydrodynamic functions characterizing the penetration of the flow into the water and oil fluid layers, respectively, and are given by Eq. B.12a and Eq. B.12b. Therefore, we decompose Eq. C.35 into its Fourier modes and apply the Parseval's theorem (Eq. D.22)

$$\mathcal{F}[\dot{F}_{\text{water}}] = -\frac{\eta_{\text{water}}}{2\pi^2} \int \mathrm{d}z \int \mathrm{d}^2\boldsymbol{q}\, \tilde{u}_{\alpha\beta,\text{water}} \tilde{u}^*_{\alpha\beta,\text{water}} \tag{C.38a}$$

$$\mathcal{F}[\dot{F}_{\text{oil}}] = -\frac{\eta_{\text{oil}}}{2\pi^2} \int \mathrm{d}z \int \mathrm{d}^2\boldsymbol{q}\, \tilde{u}_{\alpha\beta,\text{oil}} \tilde{u}^*_{\alpha\beta,\text{oil}}, \tag{C.38b}$$

with $\tilde{\boldsymbol{u}}(\boldsymbol{q},z)=\iint \boldsymbol{u}(\boldsymbol{r},z)e^{-i\boldsymbol{q}\cdot\boldsymbol{r}}\mathrm{d}^2\boldsymbol{r}$ and $\boldsymbol{u}(\boldsymbol{r},z)=1/(2\pi)^2\iint \tilde{\boldsymbol{u}}(\boldsymbol{q},z)e^{i\boldsymbol{q}\cdot\boldsymbol{r}}\mathrm{d}^2\boldsymbol{q}$ and combine this equation with Eq. C.37b:

$$\mathcal{F}[\dot{F}_{\mathrm{water}}]=-\frac{\eta_{\mathrm{water}}}{2\pi^2}\int \mathrm{d}z\int \mathrm{d}^2\boldsymbol{q}\,\left[f^2_{\mathrm{water}}(q,z)\tilde{v}_{\alpha\beta}\tilde{v}^*_{\alpha\beta}+(\partial_z f_{\mathrm{water}})^2|\tilde{\boldsymbol{v}}|^2\right], \tag{C.39a}$$

$$\mathcal{F}[\dot{F}_{\mathrm{oil}}]=-\frac{\eta_{\mathrm{oil}}}{2\pi^2}\int \mathrm{d}z\int \mathrm{d}^2\boldsymbol{q}\,\left[f^2_{\mathrm{water}}(q,z)\tilde{v}_{\alpha\beta}\tilde{v}^*_{\alpha\beta}+(\partial_z f_{\mathrm{oil}})^2|\tilde{\boldsymbol{v}}|^2\right], \tag{C.39b}$$

We first integrate over z. In the case of the water layer we need to integrate from $-H_{\mathrm{water}}$ to 0, and in the case of the oil layer, from 0 to H_{oil}.

$$I_{1,\mathrm{water}}=\int_{-H_{\mathrm{water}}}^{0} f^2_{\mathrm{water}}(q,z)\,\mathrm{d}z=-\frac{H_{\mathrm{water}}}{2}\mathrm{csch}^2(qH_{\mathrm{water}})+\frac{1}{2q}\coth(qH_{\mathrm{water}}), \tag{C.40a}$$

$$I_{1,\mathrm{oil}}=\int_{0}^{H_{\mathrm{oil}}} f^2_{\mathrm{oil}}(q,z)\,\mathrm{d}z=\frac{H_{\mathrm{oil}}}{2}\mathrm{sech}^2(qH_{\mathrm{oil}})+\frac{1}{2q}\tanh(qH_{\mathrm{oil}}), \tag{C.40b}$$

$$\begin{aligned} I_{2,\mathrm{water}}&=\int_{-H_{\mathrm{water}}}^{0}(\partial_z f_{\mathrm{water}})^2(q,z)\,\mathrm{d}z=\\ &\int_{-H_{\mathrm{water}}}^{0} q^2[\sinh(qz)+\coth(qH_{\mathrm{water}})\sinh(qz)]^2\,\mathrm{d}z=\\ &\frac{1}{2}q^2H_{\mathrm{water}}\,\mathrm{csch}^2(qH_{\mathrm{water}})+\frac{1}{2}q\coth(qH_{\mathrm{water}})], \end{aligned} \tag{C.41a}$$

$$\begin{aligned} I_{2,\mathrm{oil}}&=\int_{0}^{H_{\mathrm{oil}}}(\partial_z f_{\mathrm{oil}})^2(q,z)\,\mathrm{d}z=\\ &\int_{0}^{H_{\mathrm{oil}}} q^2[\sinh(qz)-\tanh(qH_{\mathrm{oil}})\sinh(qz)]^2\,\mathrm{d}z=\\ &-\frac{1}{2}q^2H_{\mathrm{oil}}\,\mathrm{sech}^2(qH_{\mathrm{oil}})+\frac{1}{2}q\tanh(qH_{\mathrm{oil}}), \end{aligned} \tag{C.41b}$$

Thus, the shear dissipation in the external fluids per unit area, read

$$D_{\mathrm{water}}(\boldsymbol{q})=-\frac{\eta_{\mathrm{water}}}{2\pi^2}\left[I_{1,\mathrm{water}}\tilde{v}_{\alpha\beta}\tilde{v}^*_{\alpha\beta}+I_{2,\mathrm{water}}|\tilde{\boldsymbol{v}}|^2\right], \tag{C.42a}$$

$$D_{\mathrm{oil}}(\boldsymbol{q})=-\frac{\eta_{\mathrm{oil}}}{2\pi^2}\left[I_{1,\mathrm{oil}}\tilde{v}_{\alpha\beta}\tilde{v}^*_{\alpha\beta}+I_{2,\mathrm{oil}}|\tilde{\boldsymbol{v}}|^2\right], \tag{C.42b}$$

Appendix D

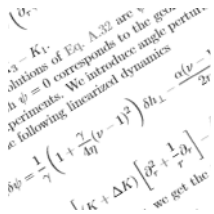

Fourier analysis

Throughout this thesis, we have extensively used Fourier analysis to extract information from experimental data. Due to the different conventions used in Fourier analysis found in the literature, we have encountered some hassles when comparing my experiments with theoretical works. To this aim, we here write a brief introduction to Fourier analysis applied to experimental data, which we think would have been very useful at the beginning of this thesis.

D.1 Fourier analysis

Fourier analysis is based on representing a given function as a sum of sines and cosines [162, 178, 179]. Likewise, we can apply Euler's formula $\cos(qx) + i\sin(qx) = e^{iqx}$, and represent this sum of sines and cosines as a sum of exponential functions. There exist four different Fourier analyses depending on the type of function one is dealing with [162]:

1. Fourier series → for continuous and periodic functions on a finite interval $[a, b]$
2. Fourier transform → for continuous functions on a infinite interval. This is the limit of a Fourier series with an interval $[a, b] = (-\infty, +\infty)$
3. Discrete Fourier Transform DFT → for discontinuous and finite or periodic on a finite interval functions
4. Discrete-time Fourier series → for discontinuous functions on a infinite interval.

The formulas for each Fourier analysis can be found in Table D.1.

Input function	Output function	
	Discrete	Continuous
Continuous	Fourier series $F[n] = \frac{1}{L}\int_{-L/2}^{L/2} f(x)e^{\frac{-i2\pi nx}{L}}\mathrm{d}x$ $f(x) = \sum_{-\infty}^{+\infty} F[n]e^{\frac{i2\pi nx}{L}}$	Fourier transform $F(q) = \int_{-\infty}^{+\infty} f(x)e^{-iqx}\mathrm{d}x$ $f(x) = \frac{1}{2\pi}\int_{-\infty}^{+\infty} F(q)e^{iqx}\mathrm{d}q$
Discrete	Discrete Fourier transform $F[q_k] = \sum_{n=0}^{N-1} f[x_n]e^{-iq_k x_n}$ $f(x_n) = \frac{1}{N}\sum_{k=0}^{N-1} F[q_k]e^{iq_k x_n}$ with $x_n = \frac{nL}{N}$ and $q_k = \frac{2\pi k}{L}$	Discrete-time Fourier Transform $F(q) = \sum_{n=-\infty}^{+\infty} f[n]e^{-iqn}$ $f[n] = \frac{1}{2\pi}\int_{-\pi}^{+\pi} F(q)e^{iqn}\mathrm{d}q$

Table D.1: The four types of Fourier analyses - The different Fourier analyses are classified depending on the continuity of the input (real space) and output (frequency space) functions

At this point, we should warn that there is no standard convention for Fourier transforms. Physicists tend to use:

$$\begin{cases} F_{\mathrm{P}}(q) = \int_{-\infty}^{+\infty} f(x)e^{-iqx}\mathrm{d}x \\ f(x) = \frac{1}{2\pi}\int_{-\infty}^{+\infty} F_{\mathrm{P}}(q)e^{iqx}\mathrm{d}q \end{cases} \tag{D.1}$$

Mathematicians mainly use

$$\begin{cases} F_{\mathrm{M}}(\tilde{\nu}) = \int_{-\infty}^{+\infty} f(x)e^{-2\pi i\tilde{\nu}x}\mathrm{d}x \\ f(x) = \int_{-\infty}^{+\infty} F_{\mathrm{M}}(q)e^{2\pi i\tilde{\nu}x}\mathrm{d}\tilde{\nu} \end{cases} \tag{D.2}$$

Finally, engineers prefer

$$\begin{cases} F_{\mathrm{E}}(q) = \frac{1}{\sqrt{2\pi}}\int_{-\infty}^{+\infty} f(x)e^{-iqx}\mathrm{d}x \\ f(x) = \frac{1}{\sqrt{2\pi}}\int_{-\infty}^{+\infty} F_{\mathrm{E}}(q)e^{iqx}\mathrm{d}q \end{cases} . \tag{D.3}$$

$\tilde{\nu}$ and q are both wave numbers, but they differ by a factor of 2π, $q = 2\pi\tilde{\nu}$. Thus, $\tilde{\nu}$ gives the number of wavelengths per unit distance, whereas q gives the

number of radians per unit distance. The relation between the different Fourier transforms are:

$$F_{\mathrm{P}}(q) = 2\pi F_{\mathrm{M}}(2\pi\tilde{\nu}) \tag{D.4a}$$

$$F_{\mathrm{P}}(q) = \sqrt{2\pi} F_{\mathrm{E}}(q) \tag{D.4b}$$

D.2 Useful identities and theorems

In this section, we will list the different theorems and properties of Fourier analysis. Given that the observables in our experiments are discrete, we will mainly focus on the DFT and FFT, the algorithm we use (in Matlab) to compute DFT. As a final remark, we will use $\mathcal{F}$ to denote the Fourier decomposition, in this case DFT, and $\mathcal{F}^{-1}$ the inverse Fourier transform.

Convolution theorem

$$\mathcal{F}[f(x_n)g(x_n)](q_k) = \frac{1}{N} F(q_l) * G(q_l) = \frac{1}{N} \sum_{l=0}^{N-1} F(q_l) G(q_k - q_l) \tag{D.5}$$

Proof:

We start by writing the Fourier transform of $f(x_n)g(x_n)$ as given in Table D.1:

$$\mathcal{F}[f(x_n)g(x_n)](q_k) = \sum_{n=0}^{N-1} f(x_n)g(x_n)e^{-ix_n q_k} \tag{D.6}$$

now, we write $f(x)$ in terms of its Fourier decomposition, $F(q_l)$:

$$\mathcal{F}[f(x_n)g(x_n)](q^k) = \sum_{n=0}^{N-1} \left(\frac{1}{N} \sum_{l=0}^{N-1} F(q_l) e^{iq_l x_n} \right) g(x_n) e^{-iq_k x_n}. \tag{D.7}$$

Rearranging Eq. D.7:

$$\mathcal{F}[f(x_n)g(x_n)](q_k) = \frac{1}{N} \sum_{l=0}^{N-1} F(q_l) \sum_{n=0}^{N-1} g(x_n) e^{-i(q_k - q_l)x_n}. \tag{D.8}$$

$$\mathcal{F}[f(x_n)g(x_n)](q_k) = \frac{1}{N} \sum_{l=0}^{N-1} F(q_l) G(q_k - q_l) = \frac{1}{N} F(q_l) * G(q_l) \tag{D.9}$$

Cross-correlation theorem

$$C_{fg} = \sum_{n=0}^{N-1} f(x_n + x_m) g(x_n) = \mathcal{F}^{-1}[F(q_k) G^*(q_k)] \tag{D.10}$$

$\mathcal{F}^{-1}$ indicates the inverse DFT.

Proof

We start by writing the cross-correlation of two discrete functions $f(x_n)$ and $g(x_n)$

$$C_{fg} = \sum_{n=0}^{N-1} f(x_n + x_m) g(x_n), \tag{D.11}$$

now, we introduce the Fourier decomposition of both functions:

$$C_{fg} = \sum_{n=0}^{N-1} \left(\frac{1}{N} \sum_{k=0}^{N-1} F(q_k) e^{iq_k(x_n + x_m)} \right) \left(\frac{1}{N} \sum_{l=0}^{N-1} G^*(q_l) e^{-iq_l x_n} \right). \tag{D.12}$$

Rearranging this last equation:

$$C_{fg} = \frac{1}{N^2} \sum_{k=0}^{N-1} \sum_{l=0}^{N-1} F(q_k) G^*(q_l) e^{iq_k x_m} \left(\sum_{n=0}^{N-1} e^{i(q_k - q_l) x_n} \right), \tag{D.13}$$

and now identifying that the term within the parenthesis is $N\delta_{kl}$ (see Info Box D.1, Eq. D.21), we can arrive at:

$$C_{fg} = \frac{1}{N} \sum_{k=0}^{N-1} F(q_k) G^*(q_k) e^{iq_k x_m} = \mathcal{F}^{-1}[F(q_k) G^*(q_k)]. \tag{D.14}$$

D

Wiener-Khinchin or auto-correlation theorem

$$C_{ff} = \sum_{n=0}^{N-1} |f(x_n + x_m)|^2 = \mathcal{F}^{-1}[|F(q_k)|^2] \tag{D.15}$$

This is the special case of the cross-correlation theorem in Eq. D.10 $f(x_n) = g(x_n)$, we have the Wiener-Khinchin or auto-correlation theorem:

Infobox D.1: The Kronecker delta δ_{kl} and its discrete Fourier transform

The Kronecker delta is a function of two integer numbers, i and j, defined by:

$$\delta_{kl} = \begin{cases} 0 & \text{if } k \neq l \\ 1 & \text{if } k = l. \end{cases} \tag{D.16}$$

This equation can also be defined in an exponential form as:

$$\delta_{kl} = \frac{1}{N} \sum_{n=0}^{N-1} e^{2\pi i \frac{n}{N}(k-l)} \tag{D.17}$$

To derive this last equation, we can make use of the geometric series:

$$\sum_{n=0}^{N-1} ar^n = a\frac{1-r^N}{1-r}. \tag{D.18}$$

Taking $r = e^{\frac{2\pi i}{N}(k-l)}$, we can arrive at:

$$\sum_{n=0}^{N-1} e^{2\pi i \frac{n}{N}(k-l)} = \frac{1 - e^{2\pi i(k-l)}}{1 - e^{\frac{2\pi i}{N}(k-l)}} = \frac{1 - \cos(2\pi(k-l)) - i\sin(2\pi(k-l))}{1 - \cos\left(\frac{2\pi}{N}(k-l)\right) - i\sin\left(\frac{2\pi}{N}(k-l)\right)}, \tag{D.19}$$

where we have used the Euler's formula. Taking into account that k and l are integers and $(k, l) \in [0, N-1]$, this last equation goes to 0 if $k \neq l$. When $k = l$

$$\sum_{n=0}^{N-1} e^{2\pi i \frac{n}{N}(k-l)} = \sum_{n=0}^{N-1} 1 = N \qquad \text{for } k = l. \tag{D.20}$$

This is the same as writing

$$\sum_{n=0}^{N-1} e^{2\pi i \frac{n}{N}(k-l)} = N\delta_{kl}. \tag{D.21}$$

Thus, we have proofed Eq. D.17. This last Eq. D.21 will be useful to derive some properties of the DFT.

Parseval's theorem

$$\sum_{n=0}^{N-1} f(x_n)g(x_n) = \frac{1}{N}\sum_{k=0}^{N-1} F(q_k)G^*(q_k) \tag{D.22}$$

Proof

As before, we start by writing the discrete functions $f(x_n)$ and $g(x_n)$ in terms of their Fourier transforms, $F(q_k)$ and $G(q_k)$, respectively:

$$\sum_{n=0}^{N-1} f(x_n)g(x_n) = \sum_{n=0}^{N-1}\left(\frac{1}{N}\sum_{k=0}^{N-1} F(q_k)e^{iq_k x_n}\right)\left(\frac{1}{N}\sum_{l=0}^{N-1} G^*(q_l)e^{-iq_l x_n}\right), \tag{D.23}$$

with some rearrangements and applying Eq. D.21:

$$\sum_{n=0}^{N-1} f(x_n)g(x_n) = \frac{1}{N^2}\sum_{k=0}^{N-1}\sum_{l=0}^{N-1} F(q_k)G^*(q_l)\left(\sum_{n=0}^{N-1} e^{i(q_k-q_l)x_n}\right) = \frac{1}{N}\sum_{k=0}^{N-1} F(q_k)G^*(q_k). \tag{D.24}$$

D.3 DFT and zero-padding

Zero padding is a technique consisting of extending with zeros a discrete signal $f(x_n)$ with length N to a signal with a length M, with $M > N$. Zero-padding is generally used to produce a function with a size equal to the next power of two of the original size. For instance, if the original signal has size $N = 20$, the output signal after zero-padding will be $M = 32$. The zeros are added to the end of the signal, and if the FFT is computed with zero-padding, the corresponding Inverse Fast Fourier Transform (iFFT) is also padded with zeros (see Fig. D.1a). In fact, one could zero-pad the function `f` and then introduce it to `FFT` in Matlab as:

```
N=numel(f);
f(end+1:2^nextpow2(N))=0; Zero-padding manually
M=numel(f);
F=fft(f,M);
```

and the result would be the same as in

```
N=numel(f);
M=2^nextpow2(N);
F=fft(f,M);
```

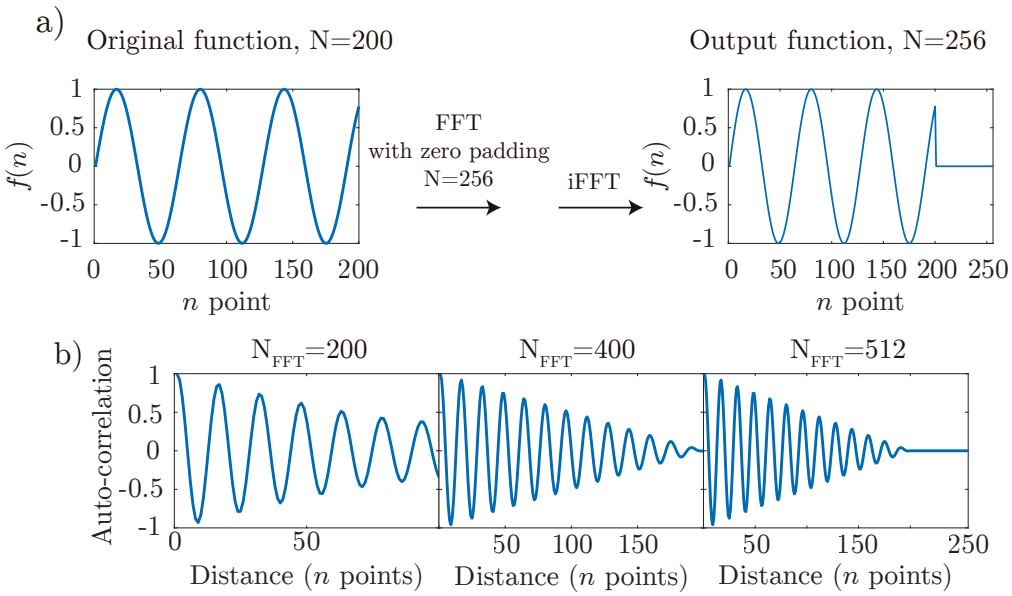

Figure D.1: Zero-padding-a) Effect of the zero-padding in the inverse FFT. **b**) Auto-correlation functions using the Wiener-Khinchin theorem (Eq. D.10) with different sizes of the FFT (N_{FFT}). The different sizes are obtained through zero-padding.

The motivations of this technique are, first, to improve the efficiency of FFT calculations because computing the FFT of signals with a size equal to the next power of two is faster; second, to improve the visual resolution of the spectrum [180].

We should remark that when computing cross-correlations, convolutions, or auto-correlations, zero-padding turns out to be very useful because it provides the DFT with enough space to place all the data from the computation. As an example, imagine we have a function of size N, if we compute the auto-correlation of a function `f` in Matlab using the Wiener-Khinchin theorem with the following script

```
function [aut]=autocorr(f)
    F=fft(f);
    N=length(F);
    aut_sym=ifftshift(ifft(abs(F).^2));
    aut=aut_sym(N/2+1:end); % aut_sym is symmetric from respect
    % to x=N/2, so we take the second half.
    aut=aut/aut_sym(N/2+1); % Rescale the data with the maximum
    % (which corresponds to the amplitude of the mode q=0 and of f.^2
end
```

the output function `aut` will have size `N`/2. This is like if we would have cut the auto-correlation function in the half, we would not see correlations at distances larger than a half of the signal size. To overcome this problem, we can specify that we want the DFT to be the size of `2*N` or larger, for example we can use `2^nextpow2(2*N)` (Fig. D.1b).

D.4 Some tips

Here, I list some tips that could be useful when computing DFT:

1. Convolutions are computationally expensive, therefore it is better to compute the Fourier transform of a product of two functions as $\mathcal{F}[f(x)g(x)]$ instead of using the convolution theorem (Eq. D.5).

2. Extending the continuous Fourier transform derivative identity (multiplication by iq) to the discrete case, can lead to artifacts. In [181], a modified wave number is proposed, but we think the best option is to differentiate the functions in the real space and then compute the FFT.

3. Applying the Eq. D.22 directly in Matlab (or in another program) can produce complex results. Hence, we must specify that we want to only keep the real part by adding `real()`.

Appendix E

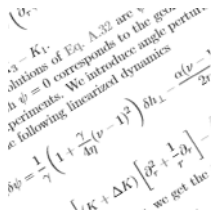

Mueller Calculus

Mueller calculus is a method to predict light polarization mediated by optical elements. This framework describes light using a 4×1 vector: the Stokes vector, whose elements are the so-called Stokes parameters obtained from the Poincare sphere. To better understand the Stokes vector formalism, we first introduce polarized light and the polarization ellipse. Afterward, we derive the Stokes vector from the polarization ellipse, and finally, we illustrate how to compute light modulation mediated by optical devices with the Mueller calculus.

E.1 Polarized light

Light is composed of electromagnetic waves that oscillate perpendicularly to the direction of propagation. Generally, a beam coming from a light source, like the sun or a bulb, has no preferred direction of oscillation, i.e., waves composing the beam are randomly oriented. Such light is said to be unpolarized. In contrast, if all the waves vibrate in the same plane, the light is linearly polarized. By convention, the polarization of an electromagnetic wave refers to the direction of oscillation of the electric field. Finally, there is partially polarized light, which is between the linearly polarized and the unpolarized light [146, 147, 182]. Apart from the linear polarization, two more polarization states exist: the circular and the elliptical (see Fig. E.1), with the latter being the most general one since linear and circular polarizations can be thought of as particular cases of the elliptical one.

Regardless of the state of polarization of monochromatic light, any polarization can be described as the sum of orthogonal waves ($\mathbf{E_x} = \hat{i}E_x$ and $\mathbf{E_y} = \hat{j}E_y$,

with $\hat{i}$ and $\hat{j}$ orthogonal unitary vectors), hence:

$$\mathbf{E}(z,t) = \hat{i}E_{0x}\cos(\omega t - qz + \delta_x) + \hat{j}E_{0y}\cos(\omega t - kz + \delta_y) \tag{E.1}$$

where ω is the angular frequency, q the wavenumber, x and y subscripts refer to components in the x and y directions, E_{0x} and E_{0y} are the maximum amplitudes, and δ_x and δ_y are the phase constants. The last four parameters should depend on time t if the light is not monochromatic.

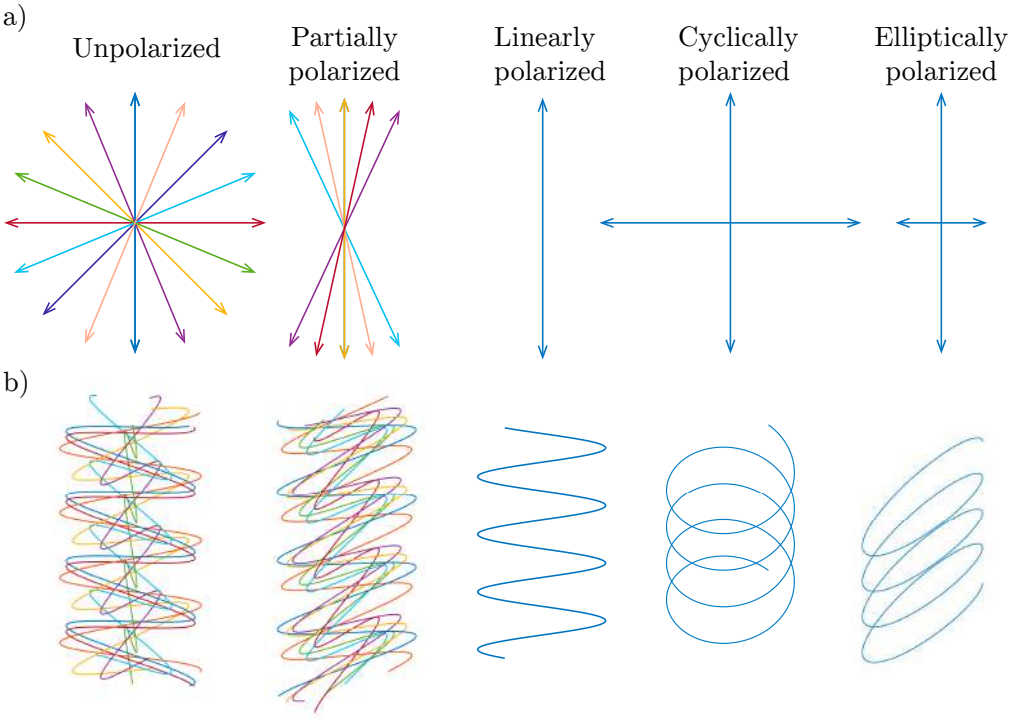

Figure E.1: Light polarization. Direction of oscillation of different polarization states (**a**) and illustration of the corresponding waves (**b**).

In the most general case, $\mathbf{E}(z,t)$ is an elliptic wave that would be seen as an ellipse in a hypothetical visualization from any point at the z-axis (the propagation direction). This hypothetical ellipse is known as the polarization ellipse (see Fig. E.2a) and is mathematically described as:

$$\frac{E_x^2}{E_{0x}^2} + \frac{E_y^2}{E_{0y}^2} - 2\frac{E_x}{E_{0x}}\frac{E_y}{E_{0y}}\cos\delta = \sin^2\delta \tag{E.2}$$

with $\delta = \delta_y - \delta_x$ (phase shift or retardance).

The polarization ellipse can be fully parametrized with two angles: ψ and χ and called the orientation angle and the ellipticity angle, respectively (Fig. E.2b). Both angular parameters can be written in terms of E_{0x}, E_{0y} and δ:

$$\tan 2\psi = \frac{2E_{0x}E_{0y}\cos\delta}{E_{0x}^2 - E_{0y}^2} \tag{E.3}$$

$$\sin 2\chi = \frac{2E_{0x}E_{0y}\sin\delta}{E_{0x}^2 + E_{0y}^2} \tag{E.4}$$

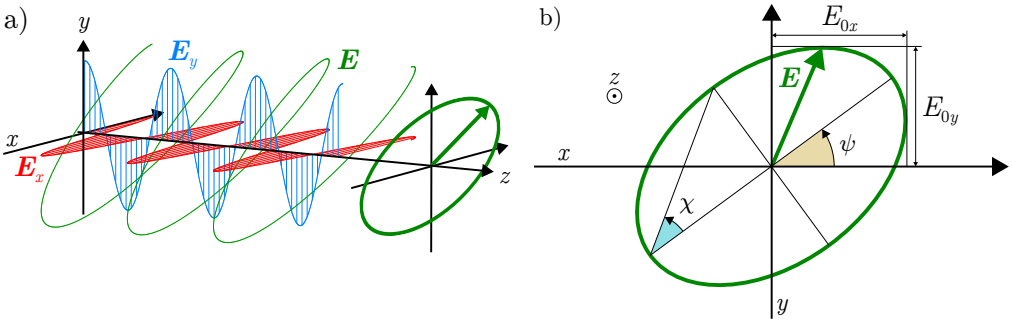

Figure E.2: The polarization ellipse. **a**) Representation of an elliptical electromagnetic wave (**E**, green light), which is the combination of a wave oscillating along the x-axis ($\mathbf{E}_x$, in red) and the y-axis ($\mathbf{E}_y$, in blue). The corresponding polarization ellipse is also sketched. This ellipse would correspond to the wave as seen from the x-axis. **b**) Polarization ellipse of **a** with the orientation angle (ψ) and the ellipticity angle (χ) also represented. $\mathbf{E}_{0x}$ and $\mathbf{E}_{0y}$ are the amplitudes of E_x and E_y.

In general, polarization ellipses are doubly degenerated given that they describe two possible waves: one rotating clockwise and another counter-clockwise. Thus, together with the ellipse, a chirality (or handedness) should also be specified. By convention, handedness is to be given as if the observer was looking toward the light source [146].

Description of polarized light in terms of the polarization ellipse is handy, as it enables the study of different polarization states with only one equation. Nevertheless, it has two significant limitations. The first one is that it can describe neither unpolarized nor partially polarized light, and, in practice, light is mainly partially polarized. The second limitation is that it is impossible to experimentally observe the ellipse as the period of a single rotation is of the order of 10^{-15} s [146]. Hence, it is an idealization of light, and the polarization ellipse can only be applied to an instant of time. To overcome these limitations,

in 1852, Sir G. G. Stokes [183] showed that, time averaging the polarization ellipse, it is possible to obtain four different parameters, which, this time, are measurable and can also be applied to unpolarized light. Such parameters are now called the Stokes parameters, whose derivation from the polarization ellipse we show in the next section.

E.2 Stokes parameters

To derive the Stokes parameters, we need to time average the equation of the polarization ellipse (Eq. E.2) at a given point z, that, for the sake of simplicity, we take $z = 0$ and consider a monochromatic wave. In this way E_{0x}, E_{0y} and δ do not change with time. The time-averaged equation for the polarization ellipse is written as:

$$\frac{\langle E_x^2(t)\rangle}{E_{0x}^2} + \frac{\langle E_y^2(t)\rangle}{E_{0y}^2} - 2\frac{\langle E_x(t)E_y(t)\rangle}{E_{0x}E_{0y}}\cos\delta = \sin^2\delta \tag{E.5}$$

with

$$E_x(z=0,t) = E_{0x}\cos(\omega t + \delta_x) \tag{E.6a}$$
$$E_y(z=0,t) = E_{0y}\cos(\omega t + \delta_y) \tag{E.6b}$$

Time-averaged quantities $\langle E_x^2(t)\rangle$, $\langle E_y^2(t)\rangle$ and $\langle E_x(t)E_y(t)\rangle$ can be computed as:

$$\langle E_\alpha(t)E_\beta(t)\rangle = \frac{1}{T}\int_0^T E_\alpha(t)E_\beta(t)dt \qquad \alpha,\beta = x,y \tag{E.7}$$

Thus, applying Eq. E.7 for $E_x^2(t)$, $E_y^2(t)$, and $E_x(t)E_y(t)$ and using Eq. E.6:

$$\langle E_x^2(t)\rangle = \frac{E_{0x}}{2}, \tag{E.8}$$
$$\langle E_y^2(t)\rangle = \frac{E_{0y}}{2}, \tag{E.9}$$
$$\langle E_x(t)E_y(t)\rangle = \frac{E_{0x}E_{0y}}{2}\cos\delta. \tag{E.10}$$

Substituting Eqs. E.8 to E.10 into Eq. E.2:

$$\frac{E_{0x}^2}{2E_{0x}^2} + \frac{E_{0y}^2}{2E_{0y}^2} - \frac{2E_{0x}E_{0y}\cos^2\delta}{2E_{0x}E_{0y}} = \sin^2\delta \tag{E.11}$$

Stokes parameters are obtained from this last equation but rearranged. One of these parameter is light intensity ($I^2 = E_{0x}^2 + E_{y0}^2$). Therefore, we need to

rearrange Eq. E.11 in such a way that we obtain a $E_{0x}^2 + E_{y0}^2$ term. One way to do this is by multiplying everything by $4E_{0x}^2 E_{0y}^2$ and adding and subtracting $E_{0x}^4 + E_{0y}^4$ to the left-hand side of Eq. E.11. Doing this and grouping the terms leads to:

$$(E_{0x}^2 + E_{0y}^2)^2 - (E_{0x}^2 - E_{0y}^2)^2 - (2E_{0x}E_{0y}\cos\delta)^2 = (2E_{0x}E_{0y}\sin\delta)^2 \tag{E.12}$$

Each of these parameters between parenthesis gives one Stokes parameter:

$$S_0 = E_{0x}^2 + E_{0y}^2, \tag{E.13}$$

$$S_1 = E_{0x}^2 - E_{0y}^2, \tag{E.14}$$

$$S_2 = 2E_{0x}E_{0y}\cos\delta, \tag{E.15}$$

$$S_3 = 2E_{0x}E_{0y}\sin\delta, \tag{E.16}$$

and all together form the four-element Stokes vector $\mathbf{S}$. Notice that each element has a physical meaning: S_0 gives the total intensity, S_1 the amount of linear horizontal or vertical polarization, S_2 the amount of 45^o or -45^o polarization, and S_3 the amount of right or left circular polarization. The exciting thing about these parameters is they all can be experimentally measured [184] because they are light intensities.

Note that Eqs. E.13 to E.16 define polarized light (they have been derived from the polarization ellipse). Nonetheless, Stokes parameters can still be used for partially polarized and unpolarized light, but a degree of polarization (P) should be added. P is defined as the ratio between light intensity coming from polarized light ($I_{\text{polarized}}$) and the total intensity (I_{total}):

$$P = \frac{I_{\text{polarized}}}{I_{\text{total}}} = \frac{\sqrt{S_1^2 + S_2^2 + S_3^2}}{S_0} \tag{E.17}$$

For polarized light $P = 1$, for partially polarized $1 > P > 0$ and for unpolarized $P = 0$.

For unpolarized and polarized beams, the Stokes vectors ($\mathbf{S}_{UP}$ and $\mathbf{S}_P$) are represented by:

$$\mathbf{S}_{UP} = \begin{pmatrix} S_0 \\ 0 \\ 0 \\ 0 \end{pmatrix} \quad , \quad \mathbf{S}_P = \begin{pmatrix} S_0 \\ S_1 \\ S_2 \\ S_3 \end{pmatrix} \tag{E.18}$$

Then, partially polarized light can be represented as a linear combination of these two vectors, whose contributions are given by $(1 - P)$ and P: $\mathbf{S}_{PP} = (1 - P)\mathbf{S}_{UP} + P\mathbf{S}_P$.

E.3 Mueller calculus

Polarization of light can be easily modulated with optical devices, like linear polarizers[1] or retarders[2] (or compensators). These transformations can be readily anticipated with the Mueller calculus, which assumes that the Stokes vector of the emergent light ($\mathbf{S}_{\text{out}}$) can be represented as a linear combination of the Stokes parameters of the incident light Stokes vector ($\mathbf{S}_{\text{in}}$). Such combination is given by a 4×4 matrix called a Mueller matrix. Thus, if a beam of light crosses different optical elements $1, 2, ..., N-1$ like it is represented in Fig. E.3, the resultant Stokes vector can be found as:

$$\mathbf{S}_{\text{out}} = \mathbf{M}_N \mathbf{M}_{N-1} \cdots \mathbf{M}_2 \mathbf{M}_1 \mathbf{S}_{\text{in}} \tag{E.19}$$

where $\mathbf{S}_{\text{in}}$ and $\mathbf{S}_{\text{out}}$ are the Stokes vectors of the incident and the resultant light, respectively, and $\mathbf{M}_1$, $\mathbf{M}_2$,..., $\mathbf{M}_{N-1}$, $\mathbf{M}_N$ are the Mueller matrices of element $1, 2, ..., N-1$ and N.

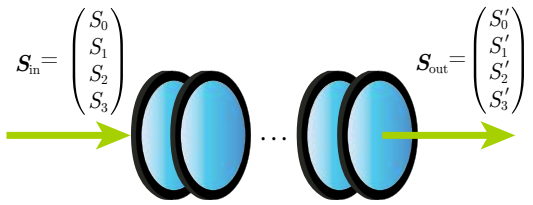

Figure E.3: Light polarization with optical devices - Diagram showing a beam with a Stokes vector $\mathbf{S}_{\text{in}}$ crossing different optical elements with Mueller matrices $\mathbf{M}_1$, $\mathbf{M}_2$,..., $\mathbf{M}_{N-1}$, $\mathbf{M}_N$. The emergent beam comes out with a different polarization characterized by a stokes vector $\mathbf{S}_{\text{out}}$.

Any Mueller matrix can be obtained by solving the linear system of equations relating $\mathbf{S}_{\text{in}}$ and $\mathbf{S}_{\text{out}}$. For an example, see Info Box E.1

Infobox E.1: How to obtain the Mueller matrix of a horizontal linear polarizer (LHP)

Here, we obtain the Mueller matrix of a LHP. We start by writing the

E

[1] Polarizers block out any wave oscillating in a direction different from their principle axis.
[2] Retarders induce a phase shift (or retardance) between two orthogonal waves. They are composed of birefringent materials.

Stokes vector of the incident light:

$$\mathbf{S}_{\text{in}} = \begin{pmatrix} S_0 \\ S_1 \\ S_2 \\ S_3 \end{pmatrix} = \begin{pmatrix} E_{0x}^2 + E_{0y}^2 \\ E_{0x}^2 - E_{0y}^2 \\ 2E_{0x}E_{0y}\cos\delta \\ 2E_{0x}E_{0y}\sin\delta \end{pmatrix} \tag{E.20}$$

Now, since a LHP filters out any wave of light not oscillating along the x direction, the only wave that crosses the polarizer is E_x. Consequently, the Stokes vector of the emergent light is then represented as:

$$\mathbf{S}_{\text{out}} = \begin{pmatrix} S'_0 \\ S'_1 \\ S'_2 \\ S'_3 \end{pmatrix} = \begin{pmatrix} E_{0x}^2 \\ E_{0x}^2 \\ 0 \\ 0 \end{pmatrix} \tag{E.21}$$

Thus, we need to solve the linear system:

$$\begin{pmatrix} E_{0x}^2 \\ E_{0x}^2 \\ 0 \\ 0 \end{pmatrix} = \begin{pmatrix} m_{11} & m_{12} & m_{13} & m_{14} \\ m_{21} & m_{22} & m_{23} & m_{24} \\ m_{31} & m_{32} & m_{33} & m_{34} \\ m_{41} & m_{42} & m_{43} & m_{44} \end{pmatrix} \begin{pmatrix} E_{0x}^2 + E_{0y}^2 \\ E_{0x}^2 - E_{0y}^2 \\ 2E_{0x}E_{0y}\cos\delta \\ 2E_{0x}E_{0y}\sin\delta \end{pmatrix} \tag{E.22}$$

We finally get:

$$\mathbf{M}_{\text{LHP}} = \frac{1}{2}\begin{pmatrix} 1 & 1 & 0 & 0 \\ 1 & 1 & 0 & 0 \\ 0 & 0 & 0 & 0 \\ 0 & 0 & 0 & 0 \end{pmatrix} \tag{E.23}$$

This is the Mueller matrix for a LHP.

Usually, tabulated Mueller matrices $\mathbf{M}$ for optical devices are written taking as reference frame the fast axis of the device . Hence, if the fast axis of the optical device is oriented at an angle α with respect to the horizontal (the frame of work), one should:

1. Change the frame reference from x, y to x', y' of the Stokes vector of the input light using a rotation matrix $\mathbf{R}(\alpha)$, where α is the angle of rotation.

2. Multiply the Mueller matrix by the rotated Stokes vector.
3. Change back the frame reference from x', y' to x, y with the rotating matrix $\mathbf{R}(-\alpha)$.

This is the same as computing a new Mueller matrix for the rotated device as:

$$\mathbf{M}(\alpha) = \mathbf{R}(-\alpha)\mathbf{M}\mathbf{R}(\alpha) \tag{E.24}$$

The rotation matrix $\mathbf{R}(\alpha)$ is written as:

$$\mathbf{R}(\alpha) = \begin{pmatrix} 1 & 0 & 0 & 0 \\ 0 & \cos 2\alpha & \sin 2\alpha & 0 \\ 0 & -\sin 2\alpha & \cos 2\alpha & 0 \\ 0 & 0 & 0 & 1 \end{pmatrix} \tag{E.25}$$

In Table E.1 there is a list of different Mueller matrices.

E.4 Mueller calculus for the fast adaptive polarimetry based on liquid crystal compensators for birefringence measurements (Section 5.1)

As we already explained in Section 5.1, we have assembled a setup composed by the following optical elements:

1. Light source
2. LHP
3. LCR (with variable retardance ψ controlled with a computer)
4. QWP (fast axis at 0^{o})
5. Sample
6. QWP (fast axis at 45^{o})
7. VLP
8. Detector (camera)

In order to predict light modulation with this setup, we performed the appropriate Mueller calculus. Considering that the samples imaged with this setup were going to be birefringent, we took as the sample's Mueller matrix the one for a linear retarder (Eq. E.28) rotated at an angle α:

$$\mathbf{M}_{\text{sample}}^{\alpha,\delta} = \mathbf{R}(-\alpha)\mathbf{M}_{\text{LR}}^{0,\delta}\mathbf{M}(\alpha) \tag{E.31}$$

Optical device	Mueller matrix
Linear hotizontal polarizer (LHP) (fast axis at 0°)	$\mathbf{M}_{\mathrm{LHP}} = \frac{1}{2}\begin{pmatrix} 1 & 1 & 0 & 0 \\ 1 & 1 & 0 & 0 \\ 0 & 0 & 0 & 0 \\ 0 & 0 & 0 & 0 \end{pmatrix}$ (E.26)
Linear vertical polarizer (LVP) (fast axis at 90°)	$\mathbf{M}_{\mathrm{LVP}} = \frac{1}{2}\begin{pmatrix} 1 & -1 & 0 & 0 \\ -1 & 1 & 0 & 0 \\ 0 & 0 & 0 & 0 \\ 0 & 0 & 0 & 0 \end{pmatrix}$ (E.27)
Linear retarder with retardance δ (LR) (fast axis at 0°)	$\mathbf{M}_{\mathrm{LR}}^{0,\delta} = \begin{pmatrix} 1 & 0 & 0 & 0 \\ 0 & 1 & 0 & 0 \\ 0 & 0 & \cos\delta & \sin\delta \\ 0 & 0 & -\sin\delta & \cos\delta \end{pmatrix}$ (E.28)
Quarter wave plate (retardance $\delta = \pi/2$) (QWP) (fast axis at 0°)	$\mathbf{M}_{\mathrm{QWP}} = \begin{pmatrix} 1 & 0 & 0 & 0 \\ 0 & 1 & 0 & 0 \\ 0 & 0 & 0 & 1 \\ 0 & 0 & -1 & 0 \end{pmatrix}$ (E.29)
Half wave plate also ideal mirror (retardance $\delta = \pi$) (HWP) (fast axis at 0°)	$\mathbf{M}_{\mathrm{HWP}} = \begin{pmatrix} 1 & 0 & 0 & 0 \\ 0 & 1 & 0 & 0 \\ 0 & 0 & -1 & 0 \\ 0 & 0 & 0 & -1 \end{pmatrix}$ (E.30)

Table E.1: Mueller matrices for some optical devices

The Mueller calculus for the setup is shown in the following Eq. E.32. For the sake of clarity, we have also included the name of each device above the corresponding matrix.

Emergent light | Linear vertical polarizer | QWP fast axis at 45°

$$\mathbf{S}_{\text{out}} = \begin{pmatrix} S_0' \\ S_1' \\ S_2' \\ S_3' \end{pmatrix} = \frac{1}{2}\begin{pmatrix} 1 & -1 & 0 & 0 \\ -1 & 1 & 0 & 0 \\ 0 & 0 & 0 & 0 \\ 0 & 0 & 0 & 0 \end{pmatrix} \begin{pmatrix} 1 & 0 & 0 & 0 \\ 0 & 0 & 0 & -1 \\ 0 & 0 & 1 & 0 \\ 0 & 1 & 0 & 0 \end{pmatrix}$$

Sample

$$\begin{pmatrix} 1 & 0 & 0 & 0 \\ 0 & \cos^2 2\alpha + \sin 2\alpha^2 \cos\delta & (1-\cos\delta)\cos 2\alpha \sin 2\alpha & -\sin 2\alpha \sin\delta \\ 0 & (1-\cos\delta)\cos 2\alpha \sin 2\alpha & \sin^2 2\alpha + \cos^2 2\alpha \cos\delta & \cos 2\alpha \sin\delta \\ 0 & \sin 2\alpha \sin\delta & -\cos 2\alpha \sin\delta & \cos\delta \end{pmatrix}$$

QWP fast axis at 0° | LCR fast axis at 45°with retardance ψ

$$\begin{pmatrix} 1 & 0 & 0 & 0 \\ 0 & 1 & 0 & 0 \\ 0 & 0 & 0 & 1 \\ 0 & 0 & -1 & 0 \end{pmatrix} \begin{pmatrix} 1 & 0 & 0 & 0 \\ 0 & \cos\psi & 0 & -\sin\psi \\ 0 & 0 & 1 & 0 \\ 0 & \sin\psi & 0 & \cos\psi \end{pmatrix}$$

Linear horizontal polarizer | Incident light

$$\frac{1}{2}\begin{pmatrix} 1 & 1 & 0 & 0 \\ 1 & 1 & 0 & 0 \\ 0 & 0 & 0 & 0 \\ 0 & 0 & 0 & 0 \end{pmatrix} \begin{pmatrix} S_0 \\ 0 \\ 0 \\ 0 \end{pmatrix} \tag{E.32}$$

The detector (the camera) only detects light intensity. Accordingly, the only Stokes parameter we are interested in is S_0', which corresponds to the total light intensity (I). For this system of optical elements I is written as:

$$I = \begin{pmatrix} 1 & 0 & 0 & 0 \end{pmatrix} \cdot \mathbf{S}_{\text{out}} = \frac{1}{4} S_0' (1 + \sin 2\alpha \sin\delta \cos\psi - \cos 2\alpha \sin\delta \sin\psi) \tag{E.33}$$

Therefore, by acquiring images at different values of ψ (retardance of the LCR) and fitting the data to an equation as:

$$I = a + b\cos\psi + c\sin\psi, \tag{E.34}$$

it is possible to obtain the fast axis of a birefringent sample (oriented at α) and its retardance (δ):

$$\alpha = \frac{1}{2}\text{atan2}\left(\frac{b}{-c}\right) \tag{E.35}$$

$$\delta = \arcsin\left(\frac{\sqrt{b^2+c^2}}{a}\right) \tag{E.36}$$

Note that this α will be perpendicular to the optical axis if the birefringence is positive. Furthermore, this orientation is set with respect to the light; hence it has to be corrected in order to reference it with respect to the camera.

E.4.1 Calibration

In this section, we explain and show the pertinent Mueller calculus we perform to calibrate all the optical devices of the polarimeter described in Section 5.1. Then, we describe how to minimize misalignments once the instrument is mounted. Before starting, we should remark that all the angles are with respect to the lab frame of reference.

E.4.1.1 Fast axis determination

In Section 5.2.4, we explain how we calibrate all the optical elements of the LCR-based polarimeter. In this section, we show the corresponding Mueller calculus.

1. Linear polarizers → The Mueller calculus for the setup shown in Fig. 5.6a is given by:

$$I(\alpha) = I_0 \begin{pmatrix} 1 & 0 & 0 & 0 \end{pmatrix} \mathbf{M}(-\alpha)\mathbf{M}_{\text{LHP}}\mathbf{M}(\alpha)\mathbf{M}_{\text{LHP}} \begin{pmatrix} 1 \\ 0 \\ 0 \\ 0 \end{pmatrix} = \frac{I_0}{2}(\cos 2\alpha + 1) = I_0 \cos^2\alpha \tag{E.37}$$

where I_0 is the light intensity coming out from the light source. Thus, the orientation with minimum light intensity is 90°. Note that Eq. E.37 coincides with the Malus's law.

2. Linear retarders (QWP and LCR) → To calibrate a LR (or linear compensator) with a fast axis oriented at α and a retardance δ, we use the setup shown in Fig. 5.6b, whose Mueller calculus reads:

$$I(\alpha,\delta) = I_0 \begin{pmatrix} 1 & 0 & 0 & 0 \end{pmatrix} \mathbf{M}_{\mathrm{LP}}^{90^o} \mathbf{M}_{\mathrm{LR}}^{-\alpha,\delta} \mathbf{M}_{\mathrm{Mirror}} \mathbf{M}_{\mathrm{LR}}^{\alpha,\delta} \mathbf{M}_{\mathrm{LHP}} \begin{pmatrix} 1 \\ 0 \\ 0 \\ 0 \end{pmatrix} \tag{E.38}$$

$$= \frac{I_0}{4}\Big[(\cos 2\delta - 1)(\cos 4\alpha - 1)\Big]$$

where the superscripts of the Mueller matrices indicate the orientation of the fast axis of each device with respect to the lab frame reference (horizontal). Note that, with this arrangement, the beam crosses the LR from one side, hits the mirror, changes the direction, and strikes back the LR, but this time on the opposite side to the one it hit first. Consequently, if the angle of the rotation matrix of LR is the first time α, the second time, it will be $-\alpha$. This is why one of the Mueller matrices has as an orientation angle $-\alpha$.

Since the compensators we want to calibrate are QWP and the variable LCR, which can be configure to be a QWP, we can simplify Eq. E.38 by substituting $\delta = \pi/2$, which is the retardance for a QWP:

$$I(\alpha) = \frac{I_0}{2}(1 - \cos 4\alpha) = \sin^2(2\alpha) \tag{E.39}$$

The light intensity depends on the $\cos(4\alpha)$. Thus, there is not one only minimum or maximum. The minima are at $\alpha^{\min} = 0^{\mathrm{o}}, 90^{\mathrm{o}}$, and the maxima $\alpha^{\max} = 45^{\mathrm{o}}, 135^{\mathrm{o}}$. Thus, for the calibration of these devices, we take as a first reference the fast axis provided by the manufacturer. From there, we search for the minimum or maximum light intensity, depending on the desired orientation (0^{o} or 45^{o}, respectively).

E.4.1.2 Instrument calibration

Finally, after the assembly of the setup, it is convenient to calibrate the whole assembly in order to minimize as much as possible light aberrations due to misalignments. For the sake of simplicity, we assume that the alignment errors of the QWPs and the variable LCR are larger than the ones of the LHP and the LVP. Therefore, we neglect the latter ones. We also neglect the errors in the retardation of the compensators.

Let us suppose we have an optical device with a Mueller matrix $\mathbf{M}$ and with a deviation from its theoretical alignment of Δ. Then, the Mueller matrix $\mathbf{M}^{\Delta}$

that accounts for this deviation can be written as:

$$\mathbf{M}^{\Delta} = \mathbf{R}(-\Delta)\mathbf{M}\mathbf{R}(\Delta) = \begin{pmatrix} 1 & 0 & 0 & 0 \\ 0 & \cos 2\Delta & -\sin 2\Delta & 0 \\ 0 & \sin 2\Delta & \cos 2\Delta & 0 \\ 0 & 0 & 0 & 1 \end{pmatrix} \mathbf{M} \begin{pmatrix} 1 & 0 & 0 & 0 \\ 0 & \cos 2\Delta & \sin 2\Delta & 0 \\ 0 & -\sin 2\Delta & \cos 2\Delta & 0 \\ 0 & 0 & 0 & 1 \end{pmatrix} \tag{E.40}$$

if we consider $\Delta \to 0$, we can simplify Eq. E.40 to:

$$\mathbf{M}^{\Delta} = \mathbf{R}(-\Delta)\mathbf{M}\mathbf{R}(\Delta) \approx \begin{pmatrix} 1 & 0 & 0 & 0 \\ 0 & 1 & -2\Delta & 0 \\ 0 & 2\Delta & 1 & 0 \\ 0 & 0 & 0 & 1 \end{pmatrix} \mathbf{M} \begin{pmatrix} 1 & 0 & 0 & 0 \\ 0 & 1 & 2\Delta & 0 \\ 0 & -2\Delta & 1 & 0 \\ 0 & 0 & 0 & 1 \end{pmatrix} \tag{E.41}$$

Note that for an optical device with a theoretical orientation of α and a deviation Δ from this angle α, we should rotate twice the Mueller matrix $\mathbf{M}$:

$$\mathbf{M}^{\alpha+\Delta} = \mathbf{R}(-\alpha)\mathbf{R}(-\Delta)\mathbf{M}\mathbf{R}(\Delta)\mathbf{R}(\alpha) \tag{E.42}$$

Applying Eq. E.42 to the Mueller calculus of our setup without a sample and supposing that the only sources of error come from misalignments in the QWPs and the LCR:

$$\begin{aligned} I(\psi, \Delta_0, \Delta_1, \Delta_2) = \begin{pmatrix} 1 & 0 & 0 & 0 \end{pmatrix} \cdot \mathbf{M}_{\mathrm{LP}}^{90} \cdot \mathbf{M}_{\mathrm{QWP}}^{45+\Delta_2} \cdot \mathbf{M}_{\mathrm{QWP}}^{0+\Delta_1} \cdot \mathbf{M}_{\mathrm{LCR}}^{45+\Delta_0} \cdot \mathbf{M}_{\mathrm{LP}}^{0} \cdot \mathbf{S}_{\mathrm{in}} = \\ I_0[(4\Delta_0^2 + \cos\psi)(-2\Delta_2^2 + 2\Delta_1\Delta_2 + \Delta_1) + \Delta_2 \sin\psi(4\Delta_1\Delta_2 + 1) \\ -2\Delta_0(\cos\psi - 1)(-4\Delta_1^2\Delta_2 + 4\Delta_1\Delta_2^2 + 1/2) + 1/2] \end{aligned} \tag{E.43}$$

where Δ_0, Δ_1 and Δ_2 are the deviations of the variable LCR, the first QWP (the one oriented at 0°), and the second QWP (the one oriented at 45°), respectively. ψ is the retardance of the variable LCR. Assuming $\Delta_0 \sim \Delta_1 \sim \Delta_2 \to 0$, we can neglect the second order terms and write a simpler form of Eq. E.43:

$$I(\psi, \Delta_0, \Delta_1, \Delta_2) \approx \frac{I_0}{2}\left[(\Delta_1 - \Delta_0)\cos\psi + \Delta_2 \sin\psi + \frac{1}{2}\right] \tag{E.44}$$

We obtain Δ_2 by combining the light intensities at $\psi = \pi/2$ and $\psi = 3\pi/2$:

$$\Delta_2 = \frac{1}{2}\frac{I(\pi/2) - I(3\pi/2)}{I(\pi/2) + I(3\pi/2)} \tag{E.45}$$

and $(\Delta_1 - \Delta_0)$ with the light intensities at $\psi = 0$ and $\psi = \pi$:

$$(\Delta_1 - \Delta_0) = \frac{1}{2}\frac{I(0) - I(\pi)}{I(0) + I(\pi)} \tag{E.46}$$

Observe that the two deviations Δ_0 and Δ_1 cannot be isolated from each other. This is why we have to minimize them by trial and error.

E.5 Mueller calculus for the fast adaptive polarimetry with a polarization camera (Section 5.3)

In this case, the setup presented in Section 5.3 is comprised of the following optical elements

1. Light source
2. LHP
3. QWP (fast axis at 45°)
4. Sample
5. Polarization camera with pixels divided into four different linear polarizers with polarizing angles: 0°, 45°, 90°, and 135°.

In this sense, we can perform four different Mueller calculus for each subpixel:

$$I^{\beta}(\alpha, \delta) = \begin{pmatrix} 1 & 0 & 0 & 0 \end{pmatrix} \mathbf{M}^{\beta}_{\text{LP}} \mathbf{M}^{\alpha,\delta}_{\text{sample}} \mathbf{M}^{45}_{\text{QWP}} \mathbf{M}^{0}_{\text{LP}} \tag{E.47}$$

where β is the orientation of the subpixel's polarizing axis (0°, 45°, 90°, or 135°) and α and δ are the sample's fast axis orientation and retardance, respectively. $\mathbf{M}^{\alpha,\delta}_{\text{sample}}$ is defined in Eq. E.31. To compute $\mathbf{M}^{\beta}_{\text{LP}}$ we use Eq. E.28 and Eq. E.26. Therefore, the detected light intensity for each pixel is described as:

$$I^{0}(\alpha, \delta) = \frac{I_0}{2}(1 + \sin 2\alpha \sin \delta), \tag{E.48a}$$

$$I^{45}(\alpha, \delta) = \frac{I_0}{2}(1 + \cos 2\alpha \sin \delta), \tag{E.48b}$$

$$I^{90}(\alpha, \delta) = \frac{I_0}{2}(1 - \sin 2\alpha \sin \delta), \tag{E.48c}$$

$$I^{135}(\alpha, \delta) = \frac{I_0}{2}(1 - \cos 2\alpha \sin \delta). \tag{E.48d}$$

Proper combination of these last equations allows us to extract α and δ:

$$\alpha = \frac{1}{2} \operatorname{atan} 2 \left(\frac{I^0 - I^{90}}{I^{45} - I^{135}} \right), \tag{E.49}$$

$$\delta = \operatorname{asin}\left(\frac{2\sqrt{(I^0 - I^{90})^2 + (I^{45} - I^{135})^2}}{I^0 + I^{90} + I^{45} + I^{135}}\right) \tag{E.50}$$

E.5.1 Instrument calibration

As we explained previously, it is highly advisable to calibrate the instrument after its assembly, obviously after the calibration of each device as presented in Section 5.2.4 with the corresponding Mueller calculus shown in Appendix E.4.1. In the case of the present arrangement, there are fewer optical devices than in the previous one, which eases the calibration. Moreover, we can include the error in the alignment of the linear polarizer, which was misregarded in the other setup.

Then, assuming that the LP and the QWP have an error Δ_1 and Δ_2 in their alignments, we can perform the following Mueller calculus:

$$I^{\beta}(\Delta_1, \Delta_2) = \begin{pmatrix} 1 & 0 & 0 & 0 \end{pmatrix} \mathbf{M}_{\mathrm{LP}}^{\beta} \mathbf{M}_{\mathrm{QWP}}^{45+\Delta_2} \mathbf{M}_{\mathrm{LP}}^{0+\Delta_1}, \tag{E.51}$$

where $\mathbf{M}_{\mathrm{QWP}}^{45+\Delta_2}$ and $\mathbf{M}_{\mathrm{LP}}^{0+\Delta_1}$ are obtained using Eq. E.42. Thus, the light intensity reaching each pixel is described by:

$$I^0(\Delta_1, \Delta_2) = I_0\left(\frac{1}{2} - 2\Delta_1\Delta_2 + 2\Delta_2^2\right), \tag{E.52a}$$

$$I^{45}(\Delta_1, \Delta_2) = I_0\left(\frac{1}{2} + \Delta_1 - \Delta_2\right), \tag{E.52b}$$

$$I^{90}(\Delta_1, \Delta_2) = I_0\left(\frac{1}{2} + 2\Delta_1\Delta_2 - 2\Delta_2^2\right), \tag{E.52c}$$

$$I^{135}(\Delta_1, \Delta_2) = I_0\left(\frac{1}{2} - \Delta_1 + \Delta_2\right). \tag{E.52d}$$

Omitting the terms with order higher than 1:

$$I^0(\Delta_1, \Delta_2) = \frac{I_0}{2}, \tag{E.53a}$$

$$I^{45}(\alpha, \delta) = I_0\left(\frac{1}{2} + \Delta_1 - \Delta_2\right), \tag{E.53b}$$

$$I^{90}(\Delta_1, \Delta_2) = \frac{I_0}{2}, \tag{E.53c}$$

$$I^{135}(\alpha, \delta) = I_0\left(\frac{1}{2} - \Delta_1 + \Delta_2\right). \tag{E.53d}$$

Combining these last equations we can find the following relation to assess how well the LR and QWP are aligned:

$$\Delta_1 - \Delta_2 = \frac{I^{45}(\Delta_1, \Delta_2) - I^{135}(\Delta_1, \Delta_2)}{I^{45}(\Delta_1, \Delta_2) + I^{135}(\Delta_1, \Delta_2) + I^{0}(\Delta_1, \Delta_2) + I^{90}(\Delta_1, \Delta_2)} \tag{E.54}$$

Appendix F

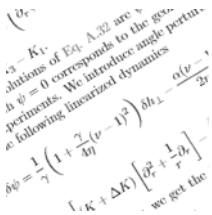

Budget for the multimodal microscopes with polarimetry and fluorescence

Designator	Component	Units	Price/unit	Price	Manufacturer, Reference
1" Lens Tube	SM1 lens tube, 1" Thread Depth	1	13.34	13.34	Thorlabs, SM1L10
1.5" Lens Tube	SM2 Lens Tube, 1.5" Thread Depth	1	28.9	28.9	Thorlabs, SM2L15
2" Lens tube	SM1 Lens Tube, 2.00" Thread Depth	1	15.45	15.45	Thorlabs, SM1L20
2.5" Lens Tube	Lens Tube Spacer, 2.5" Long	1	20.56	20.56	Thorlabs, SM1S25
1" Mirror mount	Elliptical mirror Kinematic Mount	1	189.13	189.13	Thorlabs, KCB1E/M
1" Spacer	SM1 Lens Tube Spacer, 1" Long	1	12.41	12.41	Thorlabs, SM1S10
1" Tube coupler	SM1 (1.035"-40) Coupler, External Threads	1	18.63	18.63	Thorlabs, SM1T3
2" Tube coupler	SM2 Coupler, External threads	1	35.04	35.04	Thorlabs, SM2T2
2" Mirror mount	Right-Angle Kinematic Mirror Mount with Tapped Cage Rod Holes	1	162.11	162.11	Thorlabs, KCB2/M
Adapter tube	Adapter with External SM1 Threads and Internal SM2 Threads	2	24.1	48.2	Thorlabs, SM1A2

Adapter tube	Adapter with External SM2 Threads and Internal SM1 Threads	2	24.7	49.4	Thorlabs, SM2A6
Cage plate	SM1-Threaded 30 mm Cage Plate, 0.35” Thick	3	16.53	49.59	Thorlabs, CP33/M
Camera	Camera Blackfly GigE Teledyne	1	689.00	689.00	Teledyne, BFLY-PGE-50S5M-C
Camera	Fluorescence camera Qimaging ExiBlue	1	5000	5000	Local supplier
Clamp	Right angle clamp for 66 mm Rails	2	49.9	99.8	Thorlabs, XT66RA1
Condenser	2” Aspheric condenser	1	42.6	42.6	Thorlabs, ACL50832U
Elliptical mirror, 1”	Broadband Dielectric Elliptical Mirror	1	110.67	110.67	Thorlabs, BBE1-E02
Field lens	Achromatic Doublet (f=200 mm, 1” diameter) with SM1-Threaded Mount	2	98.81	197.62	Thorlabs, AC254-200-A-ML
Fluorescence block	Fluorescence Filter Cube	1	359.8	359.8	Thorlabs, DFM1/M
Fluorescence filter set	Cy5 Fluoresecence filter set	1	740.00	740.00	Edmund optics, 67-010

Focus stage	Travel Manual Translation Stage for 30 mm Cage Systems	1	430.52	430.52	Thorlabs, CT1A
Focus stage	Translation Stage with Standard Micrometer	1	280.29	280.29	Thorlabs, PT1A
LC controller	Liquid Crystal compensator controller	1	1309.7	1309.7	Thorlabs, LCC25
LED	660 nm LED module with SM1 thread	1	217.78	217.78	Thorlabs, M660L4
LED Driver	T-Cube LED Driver	1	301.46	301.46	Thorlabs, LEDD1B
Locking SM2-Threaded Kinematic Mirror Mount	Locking SM2-Threaded Kinematic Mirror Mount	1	200.63	200.63	Thorlabs, KC2-T/M
Mirror 2”	Broadband Dielectric Mirror (2” diameter)	1	142.29	142.29	Thorlabs, BB2-E02
Mount adapter	Adapter External C-Mount Threads and Internal SM1 Threads	4	18.14	72.56	Thorlabs, SM1A9
Mounting plate	Vertical Mounting Plate for 34 mm & 66 mm Optical Rails	1	35.8	35.8	Thorlabs, XT66P1

Objective	Nikon, CFI 60 10x objective, 7mm WD	2	173.6	347.2	Local supplier
Plate adapter	Adapter to couple 30mm and 60 mm cage assemblies	3	39.32	117.96	Thorlabs, LCP33/M
Platform	66 mm Double dovetail rail, L=500 mm	1	45.38	45.38	Thorlabs, XT66DP-500
Polarizer	Linear polarizer (1" diameter)	2	91.75	183.5	Thorlabs, LPVISE100-A
Power Supply	Power Supply Unit	1	34.23	34.23	Thorlabs, KPS201
Quarter-wave plate	Polymer Zero-Order Quarter-Wave Plate (670 nm, 1" diameter)	2	273.23	546.46	Thorlabs, WPQ10E-670
Rail	66 mm Construction Rail, L = 1000 mm	1	149.58	149.58	Thorlabs, XT66-1000
Rail-to-cage braquet 30 mm	Snap-On 30 mm Cage Mounting Bracket for 66 mm Rails	3	49.43	148.29	Thorlabs, RCA2
Rail-to-cage plate 30 mm	SM1-Threaded 30 mm Cage Plate for 66 mm Rails	4	49.43	197.72	Thorlabs, RCA1
Rods 1" (Pack of 4)	Aluminium rods 1" (Pack of 4)	2	17.97	35.94	Thorlabs, ER1-P4
Rods 3" (Pack of 4)	Aluminium rods 3" (Pack of 4)	3	23.48	70.44	Thorlabs, ER3-P4

Rods 4”	Aluminium rods 4”	2	6.64	13.28	Thorlabs, ER4
Rods 6”	Aluminium rods 6”	2	8.1	16.2	Thorlabs, ER6
Rods 6” (pack of 4)	Aluminium rods 6” (pack of 4)	2	30.78	61.56	Thorlabs, ER6-P4
Rotating mount	30 mm Cage Rotation Mount for Ø1” Optics, SM1 Threaded	5	81.42	407.1	Thorlabs, CRM1T/M
Sample holder	XY translation stage and sample holder	1	341.02	341.02	Thorlabs, XYF1/M
Screws	Stainless Steel Cap Screw, 12 mm Long (Pack of 25)	1	8.02	8.02	Thorlabs, SH6MS12
Variable LC retarder	Compensated Half-Wave LC Retarder	1	756.18	756.18	Thorlabs, LCC1411-A
TOTAL PRICE (EUR)				**14353.34**	

Table F.1: Budget for the total assembly of the variable LCR-based polarimeter. The prices of the items were checked on 15 June 2022. Some deviations from the final price might be possible. VAT not included.

Designator	Component	Units	Price/unit	Price	Manufacturer, Reference
1” Lens Tube	SM1 lens tube, 1” Thread Depth	1	13.34	13.34	Thorlabs, SM1L10
1.5” Lens Tube	SM2 Lens Tube, 1.5” Thread Depth	1	28.9	28.9	Thorlabs, SM2L15
1” Spacer	SM1 Lens Tube Spacer, 1” Long	1	12.41	12.41	Thorlabs, SM1S10
1” Tube coupler	SM1 (1.035”-40) Coupler, External Threads	1	18.63	18.63	Thorlabs, SM1T3
2” Lens tube	SM1 Lens Tube, 2.00” Thread Depth	1	15.45	15.45	Thorlabs, SM1L20
2” Mirror mount	Right-Angle Kinematic Mirror Mount with Tapped Cage Rod Holes	1	162.11	162.11	Thorlabs, KCB2/M
2” Tube coupler	SM2 Coupler, External threads	1	35.04	35.04	Thorlabs, SM2T2
2.5” Lens Tube	Lens Tube Spacer, 2.5” Long	1	20.56	20.56	Thorlabs, SM1S25
Adapter tube	Adapter with External SM1 Threads and Internal SM2 Threads	2	24.1	48.2	Thorlabs, SM1A2

Adapter tube	Adapter with External SM2 Threads and Internal SM1 Threads	2	24.7	49.4	Thorlabs, SM2A6
Cage plate	SM1-Threaded 30 mm Cage Plate, 0.35" Thick	3	16.53	49.59	Thorlabs, CP33/M
Camera	Polarization camera	1	3759.47	3759.47	SVS-Vistek, exo253ZU3
Camera	Fluorescence camera Qimaging ExiBlue	1	5000	5000	Local supplier
Condenser	2" Aspheric condenser	1	42.6	42.6	Thorlabs, ACL50832U
Field lens	Achromatic Doublet (f=200 mm, 1" diameter) with SM1-Threaded Mount	2	98.81	197.62	Thorlabs, AC254-200-A-ML
Fluorescence block	Fluorescence Filter Cube	1	359.8	359.8	Thorlabs, DFM1/M
Fluorescence filter set	Cy5 Fluoresecence filter set	1	740	740	Edmund optics, 67-010
Focus stage	Travel Manual Translation Stage for 30 mm Cage Systems	1	430.52	430.52	Thorlabs, CT1
Focus stage	Translational Stage with Standard Micrometer	1	280.29	280.29	Thorlabs, PT1

LED	660 nm LED module with SM1 thread	1	217.78	217.78	Thorlabs, M660L4
LED Driver	T-Cube LED Driver	1	301.46	301.46	Thorlabs, LEDD1B
Locking SM2-Threaded Kinematic Mirror Mount	Locking SM2-Threaded Kinematic Mirror Mount	1	200.63	200.63	Thorlabs, KC2-T/M
Mirror 2”	Broadband Dielectric Mirror (2” diameter)	1	142.29	142.29	Thorlabs, BB2-E02
Mount adapter	Adapter External C-Mount Threads and Internal SM1 Threads	4	18.14	72.56	Thorlabs, SM1A9
Mounting plate	Vertical Mounting Plate for 34 mm & 66 mm Optical Rails	1	35.8	35.8	Thorlabs, XT66P1
Objective	Nikon, CFI 60 10x objective, 7mm WD	2	173.6	347.2	Local supplier
Plate adapter	Adapter to couple 30mm and 60 mm cage assemblies	3	39.32	117.96	Thorlabs, LCP33/M
Polarizer	Linear polarizer (1” diameter)	1	91.75	91.75	Thorlabs, LPVISE100-A
Power Supply	Power Supply Unit	1	34.23	34.23	Thorlabs, KPS201

Quarter-wave plate	Polymer Zero-Order Quarter-Wave Plate (670 nm, 1" diameter)	1	273.23	273.23	Thorlabs, WPQ10E-670
Rail	66 mm Construction Rail, L = 1000 mm	1	149.58	149.58	Thorlabs, XT66-1000
Rail-to-cage braquet 30 mm	Snap-On 30 mm Cage Mounting Bracket for 66 mm Rails	3	49.43	148.29	Thorlabs, RCA2
Rail-to-cage plate 30 mm	SM1-Threaded 30 mm Cage Plate for 66 mm Rails	4	49.43	197.72	Thorlabs, RCA1
Rods 1" (Pack of 4)	Aluminium rods 1" (Pack of 4)	2	17.97	35.94	Thorlabs, ER1-P4
Rods 3" (Pack of 4)	Aluminium rods 3" (Pack of 4)	2	23.48	46.96	Thorlabs, ER3-P4
Rods 4"	Aluminium rods 4"	2	6.64	13.28	Thorlabs, ER4
Rods 6"	Aluminium rods 6"	2	8.1	16.2	Thorlabs, ER6
Rods 6" (pack of 4)	Aluminium rods 6" (pack of 4)	2	30.78	61.56	Thorlabs, ER6-P4
Rotating mount	30 mm Cage Rotation Mount for Ø1" Optics, SM1 Threaded	2	81.42	162.84	Thorlabs, CRM1T/M
Sample holder	XY translation stage and sample holder	1	341.02	341.02	Thorlabs, XYF1/M

Screws	Stainless Steel Cap Screw, 12 mm Long (Pack of 25)	1	8.02	8.02	Thorlabs, SH6MS12
TOTAL PRICE (EUR)				**14280.23**	

Table F.2: Budget for the total assembly of the polarimeter with a polarized camera. The prices of the items were checked on 15 June 2022. Some deviations from the final price might be possible. VAT not included.

Appendix G

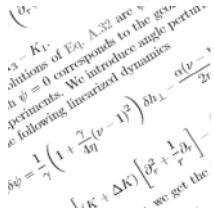

Detailed protocol for the K401 expression

K401 Expression protocol for dummies

Berta Martínez-Prat[1] and Laura Casas-Ferrer[2]

[1] *bmartinezprat@gmail.com*
[2] *lauracasas6@gmail.com*

December 4, 2018

The following protocol explains the expression of the *Drosophila Melanogaster* heavy chain kinesin-1, K401-BCCP-6His [1] in *Escherichia Coli* via the WC2 plasmid, from The Gelles Laboratory (Brandeis University, MA, USA). **The molecular weight of the protein is 140 kDa** (120 kDa K401 + 20 kDa BCCP)

Products

- HEPES
- LB (Lennox)
- LB-Agar (Lennox)
- KOH (1M) (to adjust pH)
- Mili-Q water
- $MgCl_2{\cdot}6H_2O$ (M_w= 203.30 g/mol)
- Isopropyl β-D-1-thiogalactopyranoside[2] (IPTG) (1 M, in water)
- ATP (-20^{o}C)
- Lysozyme[3] (-20^{o}C)
- Imidazole (M_w= 68.08 g/mol)
- DTT (500 mM, in water)
- Chloroamphenicol - CHAM (5 mg/mL, in ethanol)
- Ampicillin - AMP (100 mg/mL)
- E Coli with the WC2 plasmid containing the gene to express our protein.[4]
- Protease Inhibitor Cocktails (PIC). [5]
- Phenylmethane sulfonyl fluoride[6] (PMSF) (200 mM, in isopropanol)
- Biotin (M_w=244,31 g/mol)
- Sucrose (M_w=342.30 g/mol)
- β-mercaptoethanol (14.3 M, pure liquid) (Work with it under the hood)

Buffers

- **preHEPES buffer** (500 mL)
  50 mM HEPES (pH=7.2, adjust pH with 1M KOH) (5.95 g)
  4 mM $MgCl_2{\cdot}6H_2O$ (0.407 g)

- **HEPES buffer** (Using the 500 mL preHEPES buffer)
  10 mM β-Mercaptoethanol (350 μL)
  50 μM ATP (0.0138 g)

  For the protein purification:

[1] Truncated at residue 401, fused to biotin carboxyl carrier protein (BCCP) and labelled with six histidine tags
[2] To induce protein expression
[3] It is also known as muaramidase and it can be found in our inmune system. It damages the gram-positive bacterial cell wall.
[4] In the group SOC&SAM they are in the -85^{o}C freezer inside the second box at the central drawer. It is a small tube with an orange cap with a yellowish solid (because they are frozen in glycerol).
[5] To avoid protein degradation by endogenous proteases (i.e. by the bacteria themselves).
[6] A serine protease ihibitor

G

- **Washing buffer** (100 mL)
  100 mL HEPES buffer
  20 mM Imidazole (0.136 g)

- **Elution buffer** (50 mL)
  50 mL HEPES buffer
  500 mM Imidazole (1.702 g)

- **Sucrose storage solution**
  The expressed K401-BCP-6His must be stored in a 36% sucrose HEPES solution with 2mM of DTT. Such solution can be prepared by just dissolving the sucrose and the DTT (from the 500 mM DTT stock solution) in the final solution obtained during the expression and once the kinesin has been tested.

Day 1

Isolating a bacteria colony (Streaking) → This step ensures the homogeneity of the protein since only cloned cells will be collected to perform the preculture[7].

1. **First hour in the morning** Prepare the LB-agar broth (35 g LB-agar/1 L of MiliQ water) and autoclave it. Not a large volume is needed (∼15 mL/plate).

2. While one waits for the LB broth to be autoclavated, it is possible to start preparing the preHEPES buffer and LB broth (without agar) (2x(1L in a 3L flask)[8]). This LB broth will be the **harvest LB broth**. You can prepare extra LB broth for the pre-culture (day 2) (for example 500 mL in a 500 mL glass bottle). You could maybe steal it from the biochemistry lab. The preHEPES buffer and the LB broth must be autoclaved as well. Before and after the autoclave, they can be stored at 4^oC.

3. Prepare the plates to streak out the bacteria later. To prepare three plates (one blank, that will be the control, and two to streak the bacteria).
   Careful! For all the following steps, you must work under the sterile hood [9]:

   - If the LB-agar is not liquid, melt it in the microwave (∼10-15 min at low power). Leave it opened under the sterile hood until it is cold enough to handle it.
   - Transfer 50 mL of the LB-agar to a 50 mL sterile falcon and add the antibiotics: 25 μL of stock chloroamphenicol + 25 μL of stock ampicillin (Final concentrations: 2.5 μg/mL of chloroamphenicol and 50 μg/mL of ampicillin).
   - Drain the LB-agar with the antibiotics (∼15 mL) to the plates (petri dishes) and let them sit until they gel (∼10 min). The plates can be stored sealed with parafilm until the streaking at 4^oC.

4. Streak out the E. Coli. Again under the sterile hood. *This should be done in the afternoon in order to proceed the next morning (∼16 hours later. Maximum 18 hours).*

   - It is convenient to prepare different plates with different dilutions of the stock of cells. To this aim, the cells can be diluted with LB broth (without agar). For example, drain 1 mL of LB broth in a 1.5 mL eppendorf and add the cells from the stock by dipping the inoculation loop[10] (Fig. 1) in the tube with the cells and then introducing it in the eppendorf with the LB. From this first dilution, more dilutions can be prepared[11].
   - Dip an inoculating loop (Fig. 1) in one of the eppendorfs with the cells and spread them as it is shown in Fig. 2

5. Let the bacteria proliferate for 16 hours (18 maximum) in an oven at 37^oC.

[7] In the stock of cells there can be both transformed cells with the desired gene and non-transformed cells, those which have been successfully transformed, will survive the antibiotics and hence proliferate

[8] It is important that the flask is at least 3 times the volume of the broth so the bacteria have O_2 during the harvest (day 3). The harvest will be performed in the same containers

[9] At least two minutes before using it, the UV light should be turned on and once starting working, turned off. When finishing to use the hood, the UV light must be switched on again to sterilize the hood again.

[10] If the loop is metallic, it should be previously sterilized with the bunsen flame. Advice: It is better to use an inoculation loop with a big loop (like the ones at the left of Fig. 1)

[11] In our case we just made one dilution and streaked three plates: one with the dilution, another one without diluting the cells and a blank.

Figure 1: Inoculation loop

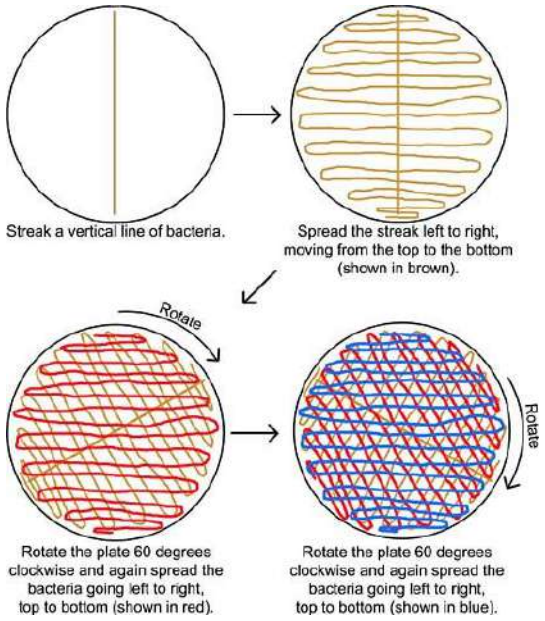

Figure 2

Day 2

1. Take out the plates from the oven and keep them at 4^oC until the pre-culture. The bacterial colonies should have proliferate within the 16 hours and different dots, each one corresponding to a single colony, should be seen. If the streaked bacteria suspension was too concentrated, you will see a continuum. It is possible to either try to grab one isolated colony, in the case there is any, or streak the bacteria again. If more than 24 hours are needed for the colonies to appear, do not use them.

   Pre-culture The addition of the reagents must be done under the sterile hood *This should be done in the afternoon in order to proceed the next morning (∼16 hours later. Maximum 18 hours).*

2. Fill two 50 mL sterile falcons with 10 mL of autoclavated LB (with a serological pipette). It is important not to fill too much the falcon since the bacteria need O_2 to live.

3. Add the two antibiotics (cloroamphenicol and ampicillin), 5 μL of each stock (Final concentrations are: 2.5 μg/mL of cloroamphenicol and 50 μg/mL of ampicillin).

4. Collect one of the colonies with a micropipette (the tips should be sterile) and add it to one of the falcons

G

with the LB.[12] Do the same with another colony and the other falcon.

5. Leave the falcons at 37^{o}C and 220 rpm overnight (∼16 hours, maximum 18 hours). The resultant broths will be the **pre-cultures**.

   →*Hereinafter, all the steps will be done by duplicate, i.e. for the two **pre-cultures** and the two **harvest LB broth**.*

Day 3

Any time of the day, degase [13] the preHEPES buffer.

Harvest and protein expression

1. Take out the **pre-cultures** from the chamber at 37^{o}C and leave them at 4^{o}C as the other things are prepared. The **pre-cultures** should look turbid and yellowish.
2. Add 500 μL of each stock of antibiotics (cloroamphenicol and ampicillin) to the 3L flasks containing the (already autoclavated) **harvest LB broth**. Add as well 0.0244 g of biotin to each container. (Final concentrations are: 2.5 μg/mL of cloroamphenicol, 50 μg/mL of ampicillin and 24.4 μg/mL of biotin)
3. Transfer 10 mL of **pre-cultures** to one of the **harvest LB broth**.
4. Read the OD_{600} as zero[14].
5. Let the harvest broths at 37^{o}C and 120 rpm until the OD_{600}s reach 0.6 A.U. of absorbance, when the bacterial density will be the optimal one for the protein expression. Measure the OD_{600} every hour. The growth of the OD_{600} is a power of 2[15], in this way, if the OD_{600} is around 0.3 A.U., the 0.6 A.U. will be reached when the bacteria divide one more time, this is after ∼30 min. In our case, we had to wait for ∼4 hours (this depends on the amount of **pre-culture** transferred to the **harvest LB broth**).
6. Once the OD_{600} is 0.6 A.U., leave the flasks for 15 minutes at 4^{o}C and afterwards add $1/1000_{th}$ of the volume of IPTG (i.e. 1 mL of IPTG stock to our 1 L broth). The IPTG induces the overexpression of the protein of interest encoded in our plasmid, in our case, the kinesin.
7. Leave the broths with the IPTG at 22^{o}C and 140 rpm overnight (∼12-20 hours).

Day 4

From this point, working under the hood is not needed.

Centrifugation and lysis

1. Transfer the broths to plastic centrifuge bottles and centrifuge them at 4,000 rpm and 4^{o}C[16] for 30 min. After the centrifugation, there should be a pellet (a solid) corresponding to the precipitated bacteria (with the protein inside).
2. During the centrifugation, prepare the HEPES buffer by adding 350 μL of β-mercaptoethanol and 0.0138 g of ATP to the autoclavated and degased preHEPES buffer. (Final concentrations are: 10 mM of β-mercaptoethanol and 50 μM of ATP).
3. Transfer 50 mL of HEPES buffer to two 50 mL falcons and add 500 μL of both PIC and PMSF (final concentration: 1mM). Leave the falcons in ice. This will make the Full lysis buffer.
4. Once the centrifugation is over, remove the supernatant[17] and transfer the pellets to the falcons with 20 mL of the Full lysis buffer. Resuspend the pellet using a vortex.

[12] To collect the colony it is convenient to mark it beforehand. In this way it will be easier to identify it when working under the hood. Moreover, to collect the colony you can press the micropipette and suction it. Afterwards, add it to the LB broth pippeting and releasing the volume several times.

[13] Degase solution using a vacuum pump and a stirrer for 30 minutes

[14] Transfer 1 mL of your broth to a cuvette and read the absorbance at 600 nm.

[15] It is a power of 2 because every bacterium divides into 2 bacteria in one life cycle.

[16] The low temperature is to avoid the heating of the centrifuge due to the high reached velocities. Vacuum is performed as well in order to reduce the friction with the air and have a properly operation.

[17] You can use the 3 L flasks used for the harvest to collect the supernatant and then disinfect them with bleach

5. Put the falcons at -80^o for 30 min.

6. Anneal the falcons in a beaker with water at 4^o for 20 min.

7. Add the lysozyme and leave the suspensions in ice at 4^o.

8. Sonicate the suspensions with a probe type sonicator for two cycles (per suspension) of 90' alternating 10' of sonication and 10' of rest (i.e. 5 times sonicating for 10' with 10' pauses between them). [18].

9. Transfer the suspensions to two centrifuge tubes and centrifuge them at 20,000 rpm for 20 min to get the **supernatants**.

Figure 3: Result of the high-speed centrifugation.

Protein purification

1. During the highspeed centrifugation, prepare the buffers for the Ni-NTA column. We have used a 1 mL column.

   – Take $\sim$ 150 mL of HEPES buffer and adjust the pH>7.5 with KOH (in our case 1 M). The pH must be >7.5 adjusted in order to prevent the His·Tag protonation. From the pH-adjusted HEPES buffer prepare in 50 mL falcons:

   - 50 mL of HEPES buffer (You can split the volume into 2x25 mL).
   - 25 mL of Wash buffer.
   - 50 mL of Elution buffer.

   Ni·NTA column

   The flow velocity during all the process should be $\sim$2 mL/min. The buffers used must be previously degased.
   In order to test whether the protein purification has been successful or not, it is possible to perform an electrophoresis in polyacrilamide gel with Coomassie Blue as indicator (See more in page 8).

[18] Important! Keep the samples in ice during all the procedure to avoid heating during the sonication, as it could denature the proteins.

Figure 4: Ni NTA column. The column is connected to a peristaltic pump that allows the fluid to flow.

2. Equilibrate the Ni-NTA cartridge with the HEPES buffer by letting flow $\sim$ 5 mL of buffer (5 times the volume of the column, which is 1 mL).
3. Load the column with the two centrifugated supernatants. You should make all the volume of both supernatants completely flow through the column.
4. Make 10 mL of wash buffer flow.
5. Collect the sample with the elution buffer. It is possible to check when the protein has completely flowed through the column by using coomassie blue (Fig. 5)[19] In this way, the protein will be as concentrated as possible.

Figure 5: Drops of Coomassie blue (with SDS that denaturalizes the proteins) mixed with the eluate candidate to contain the protein. The eluate was collected when there had flowed: 3, 4 and 5 mL of elution buffer through the column.

6. Recondition the Ni·NTA column following the protocol described by the manufacturer. In our case, the refurbishment consisted on making flow:
   - 5-10 mL of Protein wash buffer (7 M Urea + 400 mM Imidazol degased at pH=8.0)
   - 5-10 mL of water
   - 5-10 mL of purge buffer (50 mM $NaPO_4$, 300 mM NaCl, 100 mM EDTA degased at pH=8.0)

[19]In a piece of parafilm, put 18 μL of the pendling drop when the protein is being eluated and add 2 μL of coomassie blue stain. Mix with the pipette and wait: if it becomes blue, it means that the sample contains protein.(Fig. 5).

– 20 mL Degased MiliQ water
– Nikel reload (>100 mM $NiSO_4$ degased). Reflux for 20 minutes.
– 20 mL Degased MiliQ water

Removing the imidazol

In order to get rid of the imidazol coming from the elution of the protein, a PD10 column was utilized. PD10 is a molecular exclusion column that will allow us to replace the elution buffer (with imidazol) with hepes buffer (without imidazol).

Figure 6

7. Equilibrate the column with ∼25 mL of HEPES buffer.
8. Load the column with 2.5 mL of the solution containing the protein. If the sample is less than 2.5 mL, add HEPES buffer until reaching 2.5 mL.
9. Eluate the protein with 3.4 mL of HEPES buffer.
10. Recondition of the column with water.

Protein reconcentration

It might be eventually necessary to concentrate more the protein to have a higher activity. It is convenient to try first of all to prepare the active gel and if the activity is not high enough, it is possible to concentrate more the protein suspension with a Centricon centrifugal filter. It consist on a falcon-like tube with a display that contains a membrane splitting the falcon into two different parts: an upper one which contains the protein and the lower one which collects the solvent as the protein suspension gets more concentrated. As it is said in ref. [1] (Millipore, 2005): *Concentration is achieved by ultrafiltering the sample solution through an anisotropic membrane. Centrifugal force drives solvents and low molecular weight solutes through the membrane into the filtrate vial. Retained macrosolutes are above the membrane inside the sample reservoir. As the sample volume is diminished, retained solute concentration increases. For recovery, the sample is transferred to the retentate vial by placing the vial over the sample reservoir, inverting the device, then centrifuging briefly.*

Figure 7

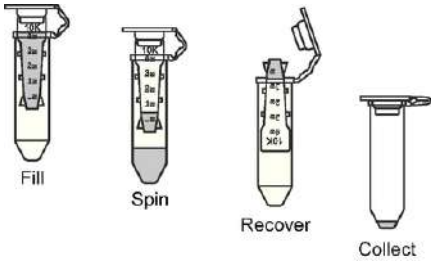

Figure 8

Polyacrilamide gel electrophoresis (SDS-PAGE)

An electrophoresis in polyacrylamide gel can be performed in order to test the presence of the protein of interest and to probe if there are any other proteins contaminating the sample.

SDS-PAGE is a method of separating molecules based on the difference of their molecular weight. At the pH at which gel electrophoresis is carried out the SDS molecules are negatively charged and bind to proteins in a set ratio, approximately one molecule of SDS for every 2 amino acids. In this way, the detergent provides all proteins with a uniform charge-to-mass ratio. By binding to the proteins the detergent destroys their secondary, tertiary and/or quaternary structure denaturing them and turning them into negatively charged linear polypeptide chains. When subjected to an electric field in PAGE, the negatively charged polypeptide chains travel toward the anode with different mobility. Their mobility, or the distance traveled by molecules, is inversely proportional to the logarithm of their molecular weight. [2]

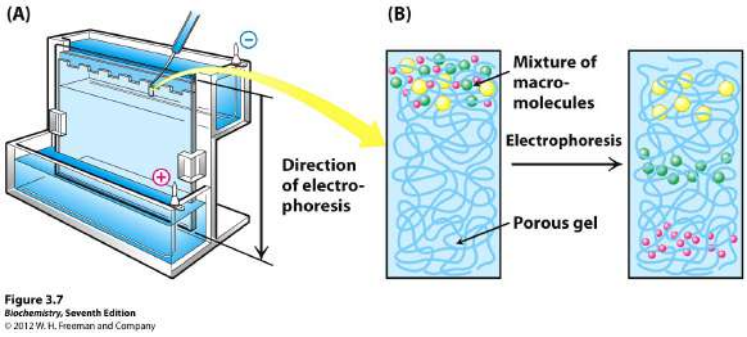

Figure 9: SDS-PAGE cuvette

IMPORTANT! Read this part before performing the Ni column procedure, as you will need to take 4 samples of 20 μL each one at 4 different stages of the purification:

– Raw extract - it is the protein solution BEFORE passing it through the column.

G

- Flow through - it is the protein solution AFTER passing it through the column.
- Wash - it is the sample that we get AFTER passing the washing buffer, that should contain a mixture of proteins, but NOT OUR PROTEIN OF INTEREST.
- Elution - it is the sample that we get AFTER passing the elution buffer, that should contain ONLY OUR PROTEIN OF INTEREST.
- PD10 - it is the sample that we get AFTER filtering our eluate (4) through the PD10 column. It should contain ONLY OUR PROTEIN OF INTEREST.

The standard procedure for the polyacrylamide electrophoresis is the following one:

1. Prepare the polyacrylamide gels:
   - Running gel

     This gel allows to separate the proteins according to their molecular weight. It can be prepared in a 15 mL falcon.
     - 9.9 mL of acrylamide.
     - 1.13 mL of Milli-Q H_2O
     - 3.75 mL of Tris Buffer 1.5 M pH=8.8
     - 150 μL of 10% SDS
     - 75 μL of 10% APS
     - 7.5 μL of TEMED
   - Stacking gel

     The stacking gel will concentrate the proteins before they start flowing inside the running gel. It can be prepared in a 15 mL falcon.
     - 3.13 mL of Milli-Q H_2O
     - 0.62 mL acrylamide
     - 1.25 mL of Tris buffer 1.5 M pH=6.8
     - 50 μL of 10% APS
     - 5 μL of TEMED
2. Pour the running gel in the electrophoresis cuvette until it reaches the front line. Wait until it has completely polymerized (15-20 min). Then add isopropanol[20] with a Pasteur pipette to make up the gel and pour the solvent in the sink.
3. Pour the stacking gel in the electrophoresis cuvette, over the (already gel) running gel, until it reaches the top and bursts.
4. Put the 1 cm comb in the cuvette and let it polymerize (1h).
5. Take out the comb carefully and proceed to load the wells as it is shown in the picture. You have to add 10 μL of coomassie blue in 20 μL of the samples and load them with a 1 μl automatic pipette or a hamilton pipette. Don't forget the MW marker!
6. Fill the electrophoresis cuvette with Running Buffer, close it and connect it at 120 V 48 A for 30 min. By that time the protein front should have reached the middle of the gel, if it hasn't, leave it for another half an hour.
7. Change to 140 V and leave it during another 40 minutes. By that time the proteins should be visibly separated.
8. Take the gel out from the cuvette carefully and put it in a rocker with Milli-Q H_2O during 10 min to eliminate the excess of coomassie blue. The result should be similar to the one that is shown in Fig. 10, with a thick line at the height corresponding to 110,000 Da, which is the molecular weight of the protein of interest.

[20] Isopropanol eliminates bubbles from the meniscus and protects the gel solution of the radical scavenger oxygen.

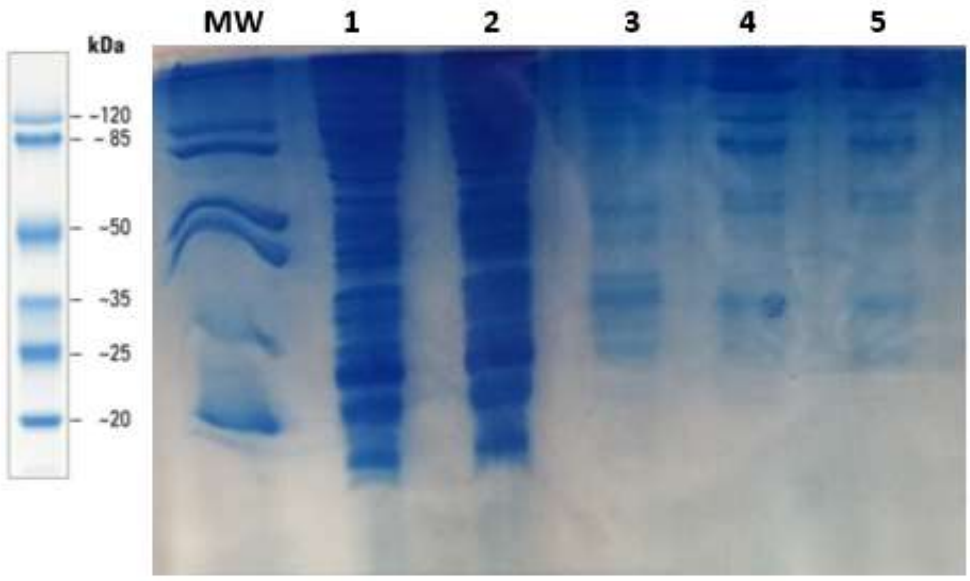

Figure 10

References

[1] Millipore, "CENTRICON Centrifugal Filter Devices User Guide" (2005)

[2] "Polyacrylamide gel electrophoresis". From Wikipedia. Accessed: 18th December 2018